Understanding Unsteady Flow and Modeling Water Quality Dynamics in the Coastal Systems under Various Hydrological and Climate Scenarios

by

Janesh Devkota

A dissertation submitted to the Graduate Faculty of
Auburn University
in partial fulfillment of the
requirements for the Degree of
Doctor of Philosophy

Auburn, Alabama
August 2, 2014

Keywords: Age of water, recirculation, salt flux, Eulerian decomposition, Isohaline method

Approved by

Xing Fang, Chair, Professor, Civil Engineering
T. Prabhakar Clement, Professor, Civil Engineering
Jose G. Vasconcelos, Assistant Professor, Civil Engineering
Jeyhoon (Jay) M. Khodadadi, Alumni Professor, Mechanical Engineering
Hanqin Tian, Professor, School of Forestry and Wildlife Sciences

Abstract

Three dimensional hydrodynamic Environmental Fluid Dynamics Code (EFDC) model was used to simulate flow, temperature, dye, age of tracer, and salinity in the Alabama coastal systems. The study area Perdido Bay and Wolf Bay (PBWB) estuarine system was considered for the study of age of water / tracer, and water and salt flux exchange, and tidal Mobile River was considered to study the possible flow and thermal recirculation of warm water from the discharge canal to the intake canal of a power plant.

The PBWB system is a shallow estuarine system connected to the Gulf of Mexico through three open boundaries; Perdido Pass, Dolphin Pass, and the Gulf Intracoastal Waterway (GIWW). Perdido EFDC model was developed for the PBWB system and was calibrated and validated against observed data (water surface elevations, temperatures, and salinity measurements) under measured river inflows, tides, and atmospheric parameters as boundary conditions. Age of a water parcel, an abstract quantity was calculated to understand the pollutant pathway and pollutant distribution in PBWB. Several numerical experiments were designed and performed to study the age of water under different hydrological (inflow) and climate change (sea level rise) conditions. The age of water was less than 20 and 160 days for numerical experiments with dye released from all rivers under high and low flows. For model experiments with dye release from Wolf Bay tributaries and mean inflows, age of water in the lower Perdido Bay was around 50–70 days and age increased at middle and upper Perdido Bay locations.

The calibrated Perdido EFDC model using 2008–2009 data was then used to study the water and salt exchange at five selected cross sections in the PBWB system. Eulerian and isohaline decomposition methods were used to investigate the subtidal (low pass filtered) water and salt flux at the cross sections. From the Eulerian decomposition method, it was found that tidal oscillatory transport (F_T) was dominant at Perdido Pass and Dolphin Pass and shear dispersive transport (F_E) was dominant at the Perdido Pass complex, Wolf-Perdido canal and lower Perdido Bay. Incoming and outgoing flows and salinity classes at all the cross sections were calculated using isohaline methods. In Perdido Pass, the average incoming salinity to Perdido Bay was 33 psu and outgoing salinity to the Gulf of Mexico was 27.7 psu. The multi-linear regression was performed to establish the relationship of incoming and outgoing inflows at the cross sections with river inflows, water surface elevations at open boundaries, and wind stresses.

Two three-dimensional EFDC models were developed for tidal Mobile River to study the possible recirculation of warm water from the discharge canal back to the intake canal of a power plant. The domain of the study area was the Mobile River segment from the USGS Bucks gaging station to the downstream towards Mobile Bay at the intersection of I-65 Bridge for model calibration. The calibrated model was extended approximately 13 km upstream of the USGS Bucks station to simulate unsteady flow, dye, and temperature distributions under different upstream inflows and downstream harmonic tides. Velocity profiles and distributions of flow, dye, and temperature at various locations were analyzed. It was found that the recirculation of warm water could only occur under small river inflows (50 m^3 s^{-1} or smaller) when the downstream tides control the flow pattern in Mobile River.

Acknowledgments

I would like to deeply thank to my academic advisor, Dr. Xing Fang, for providing me the opportunity to purse my PhD degree under his guidance. I really appreciate his support, continuous encouragement, patience and guidance he has shown towards me in accomplishing my goals. He is an excellent professional researcher as well a very good human being who will always remain as an inspiration throughout my life.

I am also equally thankful to my graduate committee members; Dr. T. Prabhakar Clement, Dr. Jose G. Vasconcelos, and Dr. Jay Khodadadi; University Reader Dr. Hanqin Tian for their valuable time to review my dissertation and provide the insights and suggestions on my research problems and motivating me which substantially improved my research and study.

I would also like to acknowledge my friends Manoj KC, Nirajan Dhakal, Liping Jiang, Sushban Shrestha, Gang Chen, Man Zhang, and Thomas Weems during my research in Auburn University. Thanks are due to Auburn University's Water Resources Center and Alabama Power Company for funding my study.

Finally, I would like to express my sincere gratitude and appreciation to my wife Shovana Devkota and my family who have supported me tirelessly throughout my study period. Without your love, care, and encouragement I would not have been capable of completing this study. I am blessed to be surrounded by such a good support system at home, at school, and at work.

Table of Contents

Abstract ..... **ii**

Acknowledgments ..... **iv**

Table of Contents ..... **v**

List of Tables ..... **viii**

List of Figures ..... **x**

List of Abbreviations ..... **xiv**

Chapter 1. Introduction **1**
1.1 Background 1
1.2 Study Areas 4
1.2.1 Wolf Bay and Perdido Bay 4
1.2.2 Mobile River 7
1.3 Research Objectives 10
1.4 Methods and Models Used in the Study 12
1.4.1 Numerical Grids Generation 12
1.4.2 Modifying EFDC Code to Compute Age of Water 13
1.4.3 Validation of Age of Water 15
1.4.4 Program Development Implementing Lanczos Filter 16
1.4.5 Code Development for Salt Flux using Eulerian and Isohaline Methods 16
1.4.6 Multi-linear Regression Analysis for Flows from Isohaline Method 17
1.5 Organization of Dissertation 17

Chapter 2. Response Characteristics of the Perdido and Wolf Bay System to Inflows and Sea Level Rise **21**
2.1 Abstract 21
2.2 Introduction 22
2.3 Materials and Methods 26
2.3.1 Study Area 26
2.3.2 Hydrodynamic Simulation Model Used 27
2.3.3 Model Grid Generation 30
2.3.4 Atmospheric Forcing 31
2.3.5 Boundary Conditions 32
2.4 Model Calibration Results 33
2.4.1 Water Level Calibration 33

2.4.2 Salinity Calibration 34
2.4.3 Water Temperature Calibration 35
2.5 Model Applications: Predictions on Water age 36
2.5.1 Introduction on the Age of Water 36
2.5.2 Prediction of Water Ages under Various Inflow Scenarios 40
2.5.2.1 Dye release from all rivers 42
2.5.2.2 Dye release from streams that flow into Wolf Bay 45
2.6 Model Application under Projected Sea Level Rises 46
2.6.1 Projection of Sea Level Rises 46
2.6.2 Projected Salinity Distributions under Sea Level Rise Scenarios 47
2.6.3 Projected Age Distributions under Sea Level Rise Scenarios 49
2.7 Conclusions 51

Chapter 3. Quantification of Water and Salt Exchanges in Perdido Bay and Wolf Bay system 66
3.1 Abstract 66
3.2 Introduction 67
3.3 Materials and Methods 70
3.3.1 Study Area 70
3.3.2 Hydrodynamic Model 72
3.3.3 Theoretical Formulation for Eulerian Decomposition Method 73
3.3.4 Theoretical Formulation of Isohaline Salt Flux Method 76
3.4 Results 78
3.4.1 Salinity Distributions in Perdido Bay. 79
3.5 Water and Salt Exchange in the PBWB System 83
3.5.1 Eulerian Flux Decomposition 84
3.5.1.1 Exchange through Perdido Pass 85
3.5.1.2 Exchange through the Perdido Pass complex and Dolphin Pass 87
3.5.1.3 Exchange through the Wolf-Perdido canal and the lower Perdido Bay 89
3.5.2 Isohaline Flux Method 90
3.5.2.1 Flow exchanges through cross sections 91
3.5.2.2 Salinity exchanges through cross sections 93
3.5.2.3 Linear regressions of total exchange flows (TEF) 97
3.6 Summary and Conclusions 99

Chapter 4. Numerical Simulation of Flow Dynamics in a Tidal River under various Upstream Hydrological Conditions 118
4.1 Abstract 118
4.2 Introduction 119
4.3 Materials and Methods 123
4.3.1 Study Area 123
4.3.2 Numerical Model 124
4.4 Model Setup 127
4.4.1 Boundary Conditions 127
4.4.2 Atmospheric Forcing 128
4.5 Model Calibration Results 129
4.5.1 Model Evaluation Criteria 130

4.5.2 Water Level Calibration 131
4.5.3 Temperature Calibration 132
4.5.4 Velocity Calibration 133
4.6 Model Applications under Different Inflow Scenarios 133
4.6.1 Discharge Distributions under Different Scenarios 137
4.6.2 Velocity Distributions under Different Upstream Inflows 142
4.6.3 Dye Distributions under Different Upstream Inflows 143
4.6.4 Temperature Distributions under Different Inflows 149
4.7 Conclusion 154

Chapter 5. Conclusions and Recommendations 173
5.1 Summary and Conclusions 173
5.2 Limitations of the Study 179
5.3 Future Study 181

Appendix A: Calibration Parameters in EFDC model 185
A.1 Calibration Parameters and their Range 186

Appendix B. Age of Water Theory 188
B.1 Age Averaging Hypothesis and Age of Tracer 193
B.2 Special Case: Passive Tracer 196

References 198

List of Tables

Table 2.1 Observed and modeled tidal amplitude (m) and phase (hr) of harmonic constituents of surface water elevations at the Blue Angels Park 54

Table 2.2 Observed and modeled surface means of salinities (ppt) in 2008–2009 and error parameters at nine monitoring stations (Fig. 2.1) 54

Table 2.3 Observed and modeled means of surface water temperatures in 2008-2009 and error parameters calculated at six monitoring stations (Fig. 2.1) 55

Table 2.4 A summary of inflow conditions and dye release locations used in the model scenario simulations..... 55

Table 3.1 Statistical summary of river inflows into Wolf Bay and Perdido Bay and filtered water surface elevations at GIWW (Gulf Intracoastal Waterway, west boundary), the Gulf of Mexico (south boundary), and Big Lagoon (east boundary)..... 102

Table 3.2 Statistical summary of the differences (Observed - Modeled) and absolute differences (|Observed - Modeled|) between observed and modeled subtidal water surface elevations (m) at the monitoring stations Terry Cove and Blue Angeles Park..... 103

Table 3.3 Statistical summary of Q_F (m^3 s^{-1}) and F_S (kg s^{-1}) computed using Eulerian decomposition method through five cross sections (Fig. 3.1): Perdido Pass (section A-A), the Perdido Pass complex (section B-B), Dolphin Pass (section C-C), the Wolf-Perdido canal (section D-D), and the lower Perdido Bay (section E-E) 104

Table 3.4 Correlation coefficients of F_E (kg s^{-1}), F_S (kg s^{-1}), Q_F (m^3 s^{-1}), Q_{in} (m^3 s^{-1}), Q_{out} (m^3 s^{-1}), F_{in} (kg s^{-1}), and F_{out} (kg s^{-1}) through different cross sections (Fig. 3.1). 105

Table 3.5 Statistical summary of the filtered incoming (Q_{in}, m^3 s^{-1}) and outgoing flows (Q_{out}, m^3 s^{-1}) through five cross sections (Fig. 3.1): Perdido Pass, the Perdido Pass complex, Dolphin Pass, the Wolf-Perdido canal, and the lower Perdido Pass..... 105

Table 3.6 Statistical summary of the filtered incoming (s_{in} in psu) and outgoing salinity (s_{out} in psu) through five cross sections (Fig. 3.1): Perdido Pass, Dolphin Pass, the Perdido Pass complex, the Wolf Perdido canal, and the lower Perdido Bay..... 106

Table 4.1 Statistical summary of the differences (Observed - Modeled) and absolute differences (|Observed - Modeled|) between observed and modeled water surface elevations (m) at the monitoring stations WS1 and WS2 (Fig. 4.1). 157

Table 4.2 Statistical summary of the differences (Observed - Modeled) and absolute differences (|Observed - Modeled|) between observed and modeled water temperatures (^{o}C) at the temperature monitoring stations T1 and T2 (Fig. 4.1). 157

Table 4.3 Statistical summary of model performance evaluation of water surface elevation (m) time series at the WS1 and WS2 stations and water temperature (^{o}C) time series at the T1 and T2 stations. 158

Table 4.4 Statistical summary of observed and filtered flow rate ($m^3 s^{-1}$) at Bucks gauging station in 2011 and from 2008 to 2012. 158

Table 4.5 Statistical summary of simulated dye concentrations (arbitrary units) in the surface and bottom layers at W1, Cell E, and the discharge exit (Fig. 4.2) under 50 $m^3 s^{-1}$, 100 $m^3 s^{-1}$, and 250 $m^3 s^{-1}$ inflows from upstream. 159

Table 4.6 Statistical summary of simulated dye concentrations (arbitrary units, greater than 0.01 i.e. 1% released dye) in the surface and bottom layers at W1, Cell E, and the discharge exit (Fig. 4.2) for the calibration run (measured inflows from upstream). 160

Table A.1 Calibration parameters used in Perdido EFDC model, EFDC model for Mobile River and the calibration range for calibration parameters 186

Table A.2 Temperature calibration parameters used in Perdido EFDC model, EFDC model for Mobile River 187

List of Figures

Fig. 1.1 Geographic location of Wolf Bay and Perdido Bay and adjacent Gulf of Mexico and major rivers in Wolf Bay and Perdido Bay 6

Fig. 1.2 Geographical location of the Mobile River showing the upstream and downstream boundaries for EFDC model, the intake canal and the discharge canal of a power plant 9

Fig. 2.1 Geographical location of Wolf Bay and Perdido Bay showing the monitoring stations managed by Alabama Department of Environment Management (ADEM), Florida Department of Environmental Protection (FDEP), National Oceanic and Atmospheric Administration (NOAA), and Alabama Water Watch (AWW). GIWW stands for the Gulf Intracoastal Waterway, and the two weather stations used are shown 56

Fig. 2.2 EFDC computational grid system showing bathymetry (bottom elevation in m below mean sea level) of Wolf Bay, Perdido Bay, and a portion of the Gulf of Mexico. 57

Fig. 2.3 Measured and observed water levels at the Blue Angels Park and Terry Cove monitoring stations for the model calibration run 58

Fig. 2.4 Time-series plots of modeled surface and bottom salinities (lines) against observed salinities (dots) near the surface at nine monitoring stations in Wolf Bay and Perdido Bay 59

Fig. 2.5 Time-series plots of modeled surface and bottom water temperatures (lines) against observed surface temperatures (dots) at six monitoring stations (Fig. 2.1) in Wolf Bay and Perdido Bay 60

Fig. 2.6 Simulated dye concentrations plotted with analytical solutions for two idealized advection-diffusion experiments: (a) pulse dye release (b) continuous dye release. Age of water profiles calculated from the EFDC model at t = 5 min, 10 min, and 30 min for continuous release are given in (c) as solid lines, and the dots from left to right represent the age of dye calculated from the instantaneous pulse release at t = 2 min, 5 min, 10 min, and 15 min, respectively 61

Fig. 2.7 Simulated age distributions in the Perdido and Wolf Bay system from all freshwater streams with constant tracer releases using (a) 2-year inflows, (b) 7Q10 low inflows, (c) mean inflows from 1998 to 2010, and (d) measured or SWAT simulated inflows in 2008–2009 62

Fig. 2.8 Simulated age distributions in Wolf Bay and Perdido Bay when tracer is released only from streams in Wolf Bay watershed using (a) and (d) 2-year inflows, (b) and (e) 7Q10 low inflows, (c) and (f) mean inflows (1998–2010). Fig. 2.8a, 2.8b, and 2.8c were simulated under observed water levels, and Fig. 2.8d, 2.8e, and 2.8f are projected under the 2100 sea level rise (S.L.R.) scenario at the open boundaries (the Gulf, GIWW, and Dolphin Pass, Fig. 2.2)..... 63

Fig. 2.9 Time series plots of mass-weighted salinities in the upper Perdido Bay, middle Perdido Bay, and Wolf Bay under the base run (2008 observed sea level) and the 2050 and 2100 sea level rise scenarios 64

Fig. 2.10 Projected change on the age (2100 – Past) in Wolf Bay and Perdido Bay when tracer is released only from streams in Wolf Bay watershed for (a) 2-year inflows, (b) 7Q10 low inflows, and (c) mean inflows from 1998 to 2010..... 65

Fig. 3.1 EFDC model domain for Wolf Bay and Perdido Bay showing the colored contours of bottom elevation and five cross sections (A–A, B–B, C–C, D–D, and E–E) where water and salt fluxes were calculated. A centerline from Perdido Pass to Perdido River is represented using a series of dots for studying the salinity profile. 108

Fig. 3.2 Modeled and observed filtered water surface elevations at station (a) Blue Angels Park and (b) Terry Cove from October 27, 2008 (Julian Day 300) to July 3, 2009 (Julian Day 184)..... 109

Fig. 3.3 Simulated salinity profile contour plots through the centerline (Fig. 3.1) from Perdido Pass to Perdido River during **low flows** from upstream under (a) ebb tide (15:00 April 25, 2009) (b) lowest water surface elevation (21:00 April 25, 2009), and (c) flood tide (05:00 April 26, 2009) at the Gulf of Mexico..... 110

Fig. 3.4 Simulated salinity profile contour plots through the centerline (Fig. 3.1) from Perdido Pass to Perdido River during **high flows** from upstream rivers in Perdido Bay under (a) ebb tide (21:00 March 30, 2009), (b) the lowest water surface elevation (02:00 March 31, 2009) , and (c) flood tide (08:00 March 31, 2009) at the Gulf of Mexico. ... 111

Fig. 3.5 Time series of (a) discharge Q_R (m^3 s^{-1}) from Perdido River and Styx River, (b) water surface elevation (WSE, m) at the Gulf of Mexico (solid line) and Big Lagoon (dashed line), (c) volumetric flow rate Q_F (m^3 s^{-1}), (d) salt transport rate F_S (kg s^{-1}), and (e) cross-sectional average salinity s_0 (psu) at Perdido Pass and Dolphin Pass. Positive and negative fluxes in (c) and (d) indicate flow into and out of the Perdido Bay. 112

Fig. 3.6 (a) Salt transport rate F_S (kg s^{-1}) and river flow flux component $Q_F s_o$, (b) salt transport components F_E and F_T through the cross section A-A (Perdido Pass), (c) subtidal estuarine exchange flow u_E (m s^{-1}), and (d) salinity s_E (psu) in the surface and bottom layers at the deepest channel cell of Perdido Pass..... 113

Fig. 3.7 Shear dispersion (F_E) and tidal oscillatory salt transport (F_T) through four cross sections (Fig. 3.1): (a) Perdido Pass complex (section B-B), (b) Dolphin Pass (section C-C), (c) Wolf-Perdido canal (section D-D), and (d) Lower Perdido Bay (section E-E)... 114

Fig. 3.8 Low-pass filtered isohaline total exchange flow (TEF) transport (Q_{in} and $-Q_{out}$ in $m^3 s^{-1}$) through five cross sections (Fig. 3.1): (a) Perdido Pass (section A-A), (b) Perdido Pass complex (section B-B), (c) Dolphin Pass (section C-C), (d) Wolf-Perdido canal (section D-D), and (e) Lower Perdido Bay (section E-E)..... 115

Fig. 3.9 Low-pass filtered isohaline total exchange flow (TEF) salinity (s_{in} and s_{out} in *psu*) through five cross sections (Fig. 3.1): (a) Perdido Pass (section A-A), (b) Perdido Pass complex (section B-B), (c) Dolphin Pass (section C-C), (d) Wolf-Perdido canal (section D-D), and (e) lower Perdido Bay (section E-E)..... 116

Fig. 3.10 Q_{out} calculated from EFDC model output (solid) and predicted (dashed) from regression equations (Table 3.6) through three cross sections (Fig. 3.1): (a) Perdido Pass (section A-A), (b) Perdido Pass complex (section B-B), and (c) lower Perdido Bay (section E-E). 117

Fig. 4.1 (a) Geographic location of the study area including the location of weather station, (b) satellite images showing monitoring stations (WS1, WS2, T1, and T2), downstream (I-65), and upstream boundary locations for calibration (Upstream-1) and for sensitivity runs (Upstream-2), and (c) model domain showing channel bathymetry 161

Fig. 4.2 The EFDC model grid with bottom elevation zoomed to show the intake canal and discharge canal. Withdrawal locations (W1 and W2) and discharge points (R1 and R2) for the power plant are shown along with three locations (Cell D, Cell E, and Cell F) where velocity profiles were studied in detail. At the Cell E and discharge exit point, dye concentration and water temperatures were studied. 162

Fig. 4.3 Time-series plot of observed and modeled water surface elevations (m) at the monitoring station WS1 from 26 April to 28 August 2011 (Julian day 115 to 240). 163

Fig. 4.4 Time-series plots of observed and modeled water surface temperature (°C) at the shallow depth of the temperature monitoring station T1 from 26 April to 28 August 2011 (Julian day 115 to 240). 164

Fig. 4.5 Time-series plots of observed (dashed lines) and simulated (solid lines) depth-averaged velocities at the downstream of the EFDC model on 29–30 June and 24–25 August 2011 165

Fig. 4.6 (a) Location of the three cross sections *A*, *B*, and *C* (used in Figs. 4.6 and 4.7) from the intake canal to the discharge canal. Simulated discharges through the bottom layer (solid lines) and the surface layer (dashed lines) at the cross section *A* under (b) 50 $m^3 s^{-1}$, (c) 250 $m^3 s^{-1}$, and (d) 900 $m^3 s^{-1}$ inflows from upstream, respectively. 166

Fig. 4.7 Time series of simulated discharges ($m^3 s^{-1}$) at the (a) downstream of the intake canal (cross section *B* in Fig. 4.6a), and (b) upstream of the discharge canal (cross section *C* in Fig. 4.6a) for numerical experiments with 50 $m^3 s^{-1}$ (top panels), 250 $m^3 s^{-1}$ (middle panels), and 900 $m^3 s^{-1}$ (bottom panels) inflows from upstream, respectively. 167

Fig. 4.8 Simulated velocity profiles at the Cell D (top panels), Cell E (middle panels) and Cell F (bottom panels) for numerical experiments with upstream inflow 50 m^3s^{-1} and 100 m^3s^{-1} under ebb tide (left panels) and flood tide (right panels) from the downstream boundary. 168

Fig. 4.9 Time series of (a) water surface elevation (WSE) at the downstream boundary (b) air temperature (°C), and (c) simulated dye concentration at R1 and R2 (Fig. 2) from Julian day 151 to 181 (1–30 June) under three different inflows (50, 100, and 250 m^3 s^{-1}). 169

Fig. 4.10 Time series of simulated dye concentrations in the surface layer (right panels) and bottom layer (left) at the withdrawal location W1, Cell E, and discharge exit under 50 m^3 s^{-1}, 100 m^3 s^{-1}, and 250 m^3 s^{-1} inflows with temperature rises, and 50 m^3 s^{-1} inflows without temperature rises in the intakes/discharges 1 and 2. 170

Fig. 4.11 Simulated three-dimensional temperature distributions at (a) 11:00 and (c) 22:00 on 16 June, and two-dimensional temperature profile contours along the river centerline of the Mobile River in the vicinity of the intake canal and discharge canal at (b) 11:00 and (d) 22:00 on 16 June under 50 m^3 s^{-1} inflow from upstream. 171

Fig. 4.12 Time series of simulated surface and bottom temperatures at the withdrawal location W1 under (a) 50 m^3 s^{-1}, (b) 250 m^3 s^{-1}, and (c) 900 m^3 s^{-1} inflows from upstream, respectively, with time series of measured temperatures at the downstream (I-65 bridge) and upstream (Bucks station) boundaries from 151–181 Julian days (1–30 June)..... 172

Fig. B.1 Concentration distribution function of a fluid parcel in the age direction (Delhez and Deleersnijder 2002) 189

List of Abbreviations

AU	Auburn University
ADCP	Acoustic Doppler Current Profiler
ADEM	Alabama Department of Environmental Management
ASCE	American Society of Civil Engineers
AWW	Alabama Water Watch
BJECC	British Journal of Environment and Climate Change
CH3D	Curvilinear-grid Hydrodynamics 3D model
EFDC	Environmental Fluid Dynamics Code
FDEP	Florida Department of Environmental Protection
GIS	Geographic Information System
GIWW	Gulf Intracoastal Waterway
HSJ	Hydrological Sciences Journal
NOAA	National Oceanographic and Atmospheric Administration
PSU	Practical Salinity Unit
SWAT	Soil and Water Assessment Tool
TVD	Total Variation Diminishing
USEPA	United States Environmental Protection Agency
USGS	United States Geological Survey
VMS	Velocity mapping software

Chapter 1. Introduction

1.1 Background

During the recent years, rapid urbanization and exploitation of natural resources has led to massive land use changes, resulting in the reduction of forest soils and increase in developed areas (Deng et al. 2009). According to UN Atlas of the Oceans, the 44% of the world population reside within 150 km of seas and oceans and in US alone 53% of the population lives near coast (Small et al. 2000; Tralli et al. 2005). The large population living near coastal zone justifies the need for integrated coastal management, i.e., management of natural resources and their uses with emphasis on cooperation, coordination and multiple uses of resources. The major threats near the coasts and estuaries are eutrophication, effects of deforestation, habitat destruction, harmful algal blooms, loss of wetlands, sea-level rise, climate change, increased risks to human health, reduced biodiversity, etc. The most serious stress factors in the estuarine environment are pollution inputs (e.g. nutrient enrichment, organic carbon loading, and chemical contaminants) and several other anthropogenic factors such as habitat loss and alteration, overfishing, freshwater diversions etc. (Kennish 2002). The ever increasing demand of industrial cooling water for power, desalination, chemical, and other industrial plants due to rapid urbanization and socioeconomic development also impose a serious threat on the health of coastal water bodies. Elevated water temperatures and residual chlorine (anti-fouling agent) are major threats from thermal discharges of coastal power plants

(Langford 1990; Chuang et al. 2009). The thermal and radioactive discharges from power plants into aquatic environment have become the subject of lively debate as an ecological concern (Ilus 2009). Heat as a separate pollutant was first brought into the public eye in the UK around 50 years ago, very few research programs dealing specifically with the effects of thermal discharges were originated anywhere in the world before the early 1950s (Ilus 2009). By the mid-1960s there were many research projects concerned with thermal discharges in the UK, USA, USSR and Europe, and the term “thermal pollution” was taken into general use.

Estuaries are partly enclosed coastal water bodies which act as bridges between marine environment (sea) and land where the balance of freshwater from rivers and the salt water from the ocean results in the productive ecosystem (Bales et al. 2006). The transport of dissolved substances and suspended particles takes place during the interaction of riverine and marine systems. Phytoplankton growth and variations of nutrients in lakes or estuaries are connected with the discharge from the inflow rivers and tributaries (Shen and Haas 2004). Harmful algal blooms (HABs) found in coastal waters are caused by circulation, river flow, and anthropogenic nutrient loadings leading to eutrophication (Sellner et al. 2003). The dynamic forcing in the estuarine system such as tides, river inflows, winds, solar radiation etc. results in the spatial and temporal variability of salinity, temperature, and nutrients in the estuary. Floods from the tributaries after heavy rainfall events result in reduced salinity because of flushing of large amount of inflows from upstream rivers. Similarly, drought caused after a long period of no or very little rainfall can result in higher salinity in an estuary system because of the salt water intrusion from downstream without much counterbalancing

momentum from upstream inflow. To understand the contaminant or dissolved substances fate and transport in the estuary, it is important to estimate the travel time required for the dissolved substances introduced from the tributaries to the given location of the estuary. The concept of the age of water is used in this study to understand the transport of the substances in the estuary. The age of water is defined as the time elapsed since the water parcel under the consideration departed the region in which its age is defined to be zero (Zimmerman 1976; Shen and Lin 2006). Age of water can also be defined as the time interval between the entrance of a pollutant discharge into a waterbody and arrival at a location of interest within the waterbody.

The exchanges of fresh water and salt water are of primary importance in determining the character of environment in studies of ecology of tidal estuaries (Ketchum 1951). The salinity structure in an estuary provides the basic habitat for life and have a big impact on water quality (MacCready and Geyer 2001). The distribution of any material dissolved or suspended in water is determined by circulation and interaction of fresh and salt water. Tides carry salinity and other substances (e.g., nutrient, sediment, etc.) in and out of the estuary as well as mix them over the entire estuary. Saline water can intrude landward due to the difference in density between the freshwater and the seawater and due to tidal movement. The salinity intrusion itself can reach a farther distance from the coastline, especially when the river flow is small. Salinity intrusion affects every water-use activity in the estuary, e.g., domestic, agricultural, industrial and other uses. Therefore, it is important to understand the circulation and exchange of salt and freshwater in estuary because water-borne material transported by advection contributes significantly to the balance of material budgets (Engqvist and Stenstrom

2009). The exchanges in the estuary are over short periods of time to the tidal oscillations and over longer period of time to the fluctuations of river flow (Ketchum 1951).

The rapid urbanization has led to an increase in power demands and has resulted in the regulation of many power plant operations. Among different types of cooling systems used, once through cooling systems were initially most popular and widespread systems used for electricity generation purposes. The once-through cooling system withdraws the ambient water from the intake canal and releases warmer water into the discharge canal connecting to nearby water body. Colder water cools the steam more effectively and allows more efficient electricity generation. The warmer water released into the river systems may result in changes in the biological communities reflecting the loss of temperature-sensitive species, invasion of pest species or diseases, increased period of oxygen stress etc. On the other hand, the efficient operation of the power plant requires the cooling system to withdraw the coldest water possible. Usually, in once-through cooling systems there is a concern about the possible recirculation of the warm water released from cooling plant to the intake canal which withdraws water for the cooling purposes.

1.2 Study Areas

1.2.1 Wolf Bay and Perdido Bay

The Perdido Bay and Wolf Bay (PBWB) system (Fig. 1.1) is an estuarine system that lies in an area of submergence on the north flank of the active Gulf coast and is shallow to moderately deep inshore water body oriented along a northeast-southwest axis (Livingston 2003). Wolf Bay is located on the Gulf of Mexico in Baldwin County, Alabama, nestled between Perdido Bay to the east and Mobile Bay to the west. The Wolf

Bay watershed covers about 44,700 acres, which is approximately 23% forest, 27% urban/suburban, 27% agricultural, 16% wetlands and 7% other uses. The streams that flow into Wolf Bay include Wolf Creek, Sandy Creek, Miflin Creek, Graham Creek, Owens Bayou, and Hammock Creek and combined flow into Wolf Bay ranged from 0.95 to 15.37 $m^3 s^{-1}$ with mean flow of 1.95 $m^3 s^{-1}$ during 2008–2009 period. In April 2007, Wolf Bay was granted "Outstanding Alabama Water" (OAW) status by the Alabama Department of Environmental Management (ADEM). OAW is the highest of seven levels of waterbody classifications established by ADEM. OAW classification signifies "high quality waters that constitute an outstanding Alabama resource of exceptional recreational and ecological significance".

The surface area of Perdido Bay is approximately 130 km^2 with an average depth of 2.6 m (Schropp et al. 1991; Macauley et al. 1995). Perdido River is the dominant source of freshwater inflows to the Bay (Fig. 1.1). Elevenmile Creek watershed including Eightmile Creek (Fig. 1.1) accounts for 10% of the freshwater inflow to the Bay and receives an industrial wastewater discharge from the International (formerly Champion) Paper Company pulp and paper mill (Macauley et al. 1995). Perdido Pass is the primary pathway of salt water to Perdido Bay and controls salinity distributions in Perdido Bay (Livingston 2003). Perdido Bay connects to Wolf Bay through the Gulf Intercostal Waterway (GIWW) and to Pensacola Bay through Dolphin Pass (Fig. 1.1). The U.S Army Corps of Engineers (USCOE) maintains the Perdido Pass navigation channel as part of the GIWW (USACE 1976; Livingston 2003). The width of Perdido Pass ranges from 200 to 500 m, and depth is around 5 m.

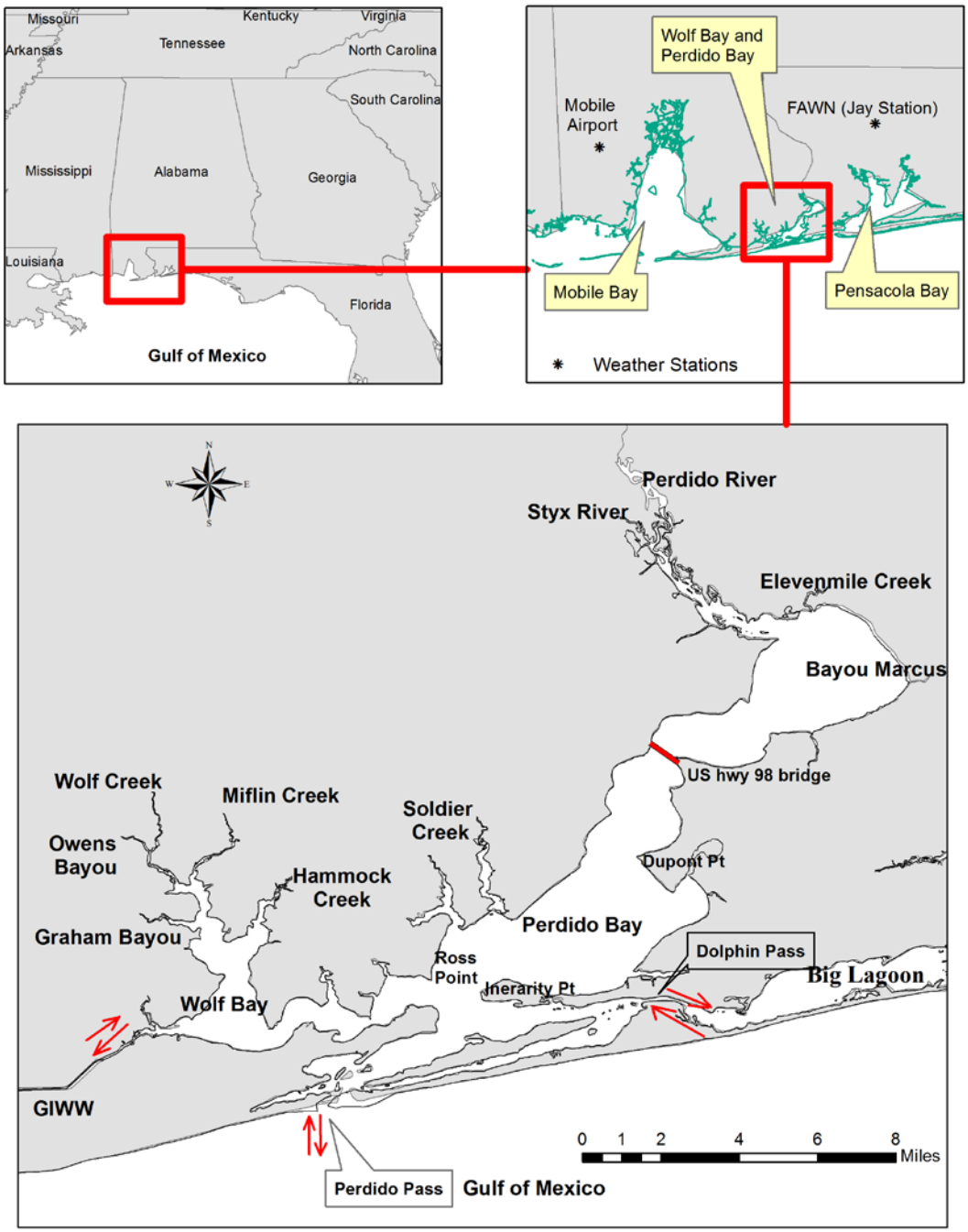

Fig. 1.1 Geographic location of Wolf Bay and Perdido Bay and adjacent Gulf of Mexico and major rivers in Wolf Bay and Perdido Bay

1.2.2 Mobile River

The Mobile River is a tidally influenced river in the southern Alabama, USA. The Mobile River is formed from Tombigbee River and Alabama River and is approximately 72.4 km long before it discharges into the Mobile Bay and the Gulf of Mexico (Fig. 1.2). The study area in Mobile River is a river segment between the confluence of Mobile River and Tensaw River and the river cross section of the Mobile River at the intersection of Mobile River and I-65 Bridge. I-65 Bridge on the Mobile River is located approximately 33.8 km upstream from the Mobile Bay. Fig. 1.2 shows the geographical location of Mobile River showing the upstream and downstream boundary of the EFDC model, the intake canal and the discharge canal of a power plant. The power plant is a once-through cooling power plant in the vicinity of the Mobile River. The cooling water for the power plant is withdrawn from the deep depth of the intake canal and the warm water from the power plant is returned to the surface of the discharge canal and then to the Mobile River. Mobile River is highly tidally dominant during the summer period and the dominant tidal constituents observed at monitoring stations in study area are consistent to constituents of tides in Mobile Bay. However, during spring when the river flows are large, then the higher momentum from the river inflows flushes the water towards Mobile River and prevents the tidal oscillation in the study area.

The astronomical tides of the Mobile Bay cause significant tidal cycles of water levels at Bucks station (period of 24.84 hours). Because of the tidal effects during the summer season, there is a possibility of warm water discharged into the discharge canal reaching the intake canal because of the downstream tides. In the once-through cooling system located in the vicinity of Mobile River, it is very important to eliminate the

recirculating flow from the discharge canal back to the intake canal. Recirculation is the common problem found in the once-through cooling systems. For the scenario studies, the simulation domain is extended from the USGS Bucks gaging station to where the Mobile River splits into two branches (Fig. 1.2). The simulation domain for model calibration was 10.6 miles of the Mobile River, and the extended simulation domain for the scenario study covers 18.6 miles of the Mobile River (Fig. 1.2).

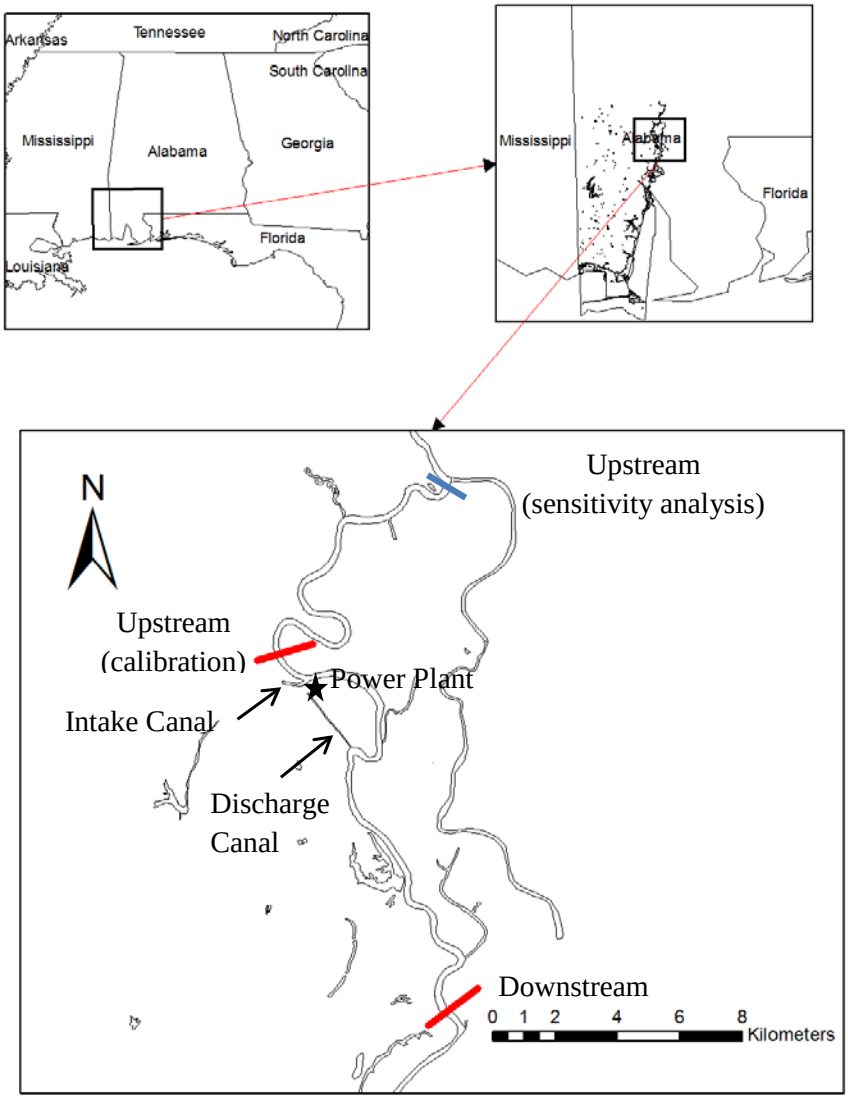

Fig. 1.2 Geographical location of the Mobile River showing the upstream and downstream boundaries for EFDC model, the intake canal and the discharge canal of a power plant.

1.3 Research Objectives

Estuaries and tidally-influenced rivers can have very complex unsteady flow and water quality dynamics because of unique morphological characteristics (bathymetry) and interactions of freshwater inflows from upstream and surrounding watersheds and salt water intrusion from downstream due to the connection to an ocean or gulf. It is very difficult to track the changes and understand dynamics in the water body using a few monitoring stations or solving couple of simple equations. A numerical model is required to analyze and understand the dynamics of flow, salinity, currents, and temperature in the water body. The principal objectives of this research are to develop three three-dimensional unsteady hydrodynamic models as effective tools to understand and quantify the complex dynamics and transport phenomenon in Wolf Bay, Perdido Bay, and Mobile River under various hydrological and climate scenarios. The specific objectives are as follows:

1. Development of three-dimensional hydrodynamic model including Wolf Bay, Perdido Bay and part of the Gulf of Mexico to determine (quantify) age of water and long term transport timescale in Wolf Bay and Perdido Bay under different inflow conditions and climate change (sea level rise) scenarios.
2. Use of Eulerian decomposition method and the isohaline flux method for quantifying water and salt exchange between Wolf Bay and Perdido Bay and between Perdido Bay and the Gulf of Mexico under different inflows and tidal variations.
3. Development of three-dimensional hydrodynamic models in Mobile River to quantify under what inflows from upstream river the recirculation of warmer

water from a power plant could happen in the Mobile River system under typical operation conditions of the power plant and harmonic tides at downstream.

The focus of proposed study deals with the use of the three-dimensional Environmental Fluid Dynamics Code (EFDC) model to understand the unsteady flows and tides in estuaries and impacts caused due to the various hydrological and sea-level rise scenarios. The first two objectives are related to a study on "Impacts of human activities and climate change on water resource and ecosystem health in the coastal Wolf Bay Basin: A Coastal Diagnostic and Forecast System (CDFS) for integrated assessment" funded by Auburn University Water Resources Center. The goal of the study was to build a coastal diagnostic and forecast system linking models of land use, water use, water quality, watershed hydrology, groundwater, river and estuary hydrodynamics, and ecosystems (upland, riparian, wetland and stream) for evaluating and predicting how changing human and climate impacts influence water quantity and quality, and further affect the ecological and economic well-being of Wolf Bay watershed inhabitants and visitors.

The third objective is to investigate complex interactions of freshwater inflows and tides in the Mobile River. It is related to complex temperature dynamics resulted from cooling water withdrawals and thermal discharges from a power plant in addition to interactions between upstream inflows and downstream tides.

For all three objectives, very complex three-dimensional flow and water quality dynamics were studied using three-dimensional EFDC model. It is impossible to use simpler two dimensional or one-dimensional models to solve the problems for the study. For Mobile River study, one may think one-dimensional model such as HEC-RAS

(references) can be used to quantify what inflows can result recirculation of warmer water under harmonic downstream boundary. There was strong temperature (i.e., density) stratification in Mobile River when warmer water (about 10 ^{o}C warmer than ambient river temperature) was released from the discharge canal to the river system. HEC-RAS is a cross-sectionally averaged one-dimensional flow model that does not handle the density stratification.

1.4 Methods and Models Used in the Study

There were several new concepts and advanced methods that were used to accomplish the research objectives described in three phases presented in Chapter 2 – Chapter 3. In Chapter 2, age of water /tracer concept was used and the Dynamic Solutions International (DSI) LLC version of EFDC was modified to incorporate the computation of age concentration equation. In Chapter 3, i.e., studying flow and salt exchange, Lanczos filter (Walters and Heston 1982) was implemented and R code (Team 2005) were written to compute different flow and flux components using Eulerian and Isohaline method. The intellectual contributions and general methodology used in different phases are described below.

1.4.1 Numerical Grids Generation

The study performed involved with using EFDC model as model framework or simulation engine. To develop a site-specific three-dimensional numerical model involves creating numerical grids, assigning appropriate boundary conditions (river inflows, water surface elevation / harmonic constituents at open boundaries), obtaining

accurate bathymetry (bottom elevations), collecting atmospheric data, and identifying/gathering measured data for model calibration and validation. In any numerical modeling study, the first and foremost thing is to create a grid of good resolution to represent the study area adequately. The study areas considered in our study are complex in topography and do not have a fixed geometry. Meandering rivers and complex shorelines formed due to river and ocean interaction require special attention to represent the simulation domains correctly in the model. Therefore, the three dimensional model developments for the study had various challenges and took a lot of effort including grid generations and collecting / preparing appropriate input data for initial and time-dependent boundary conditions. The model grids need to be orthogonal and should have minimum orthogonal deviations. The model grids and number of horizontal layers used in all the phases of the study were modified and revised several times until the numerical model error was reduced to minimum.

The curvilinear orthogonal grids for the Perdido EFDC model and the Mobile River EFDC model were developed using the Delft RGFGRID module (Deltares 2010) with GIS shoreline data (shapefiles) as input and imported into the EFDC using EFDC-Explorer 6 (Craig 2011). The horizontal model grids developed for the Perdido EFDC model were based on the 1983 North American Vertical Datum (NAVD) and the Universal Transverse Mercator (UTM) projection.

1.4.2 Modifying EFDC Code to Compute Age of Water

This is the intellectual contribution by the author which allows the DSI-EFDC model to solve the dye concentration equation and age concentration equation to compute age of

water/tracer. During the study, some modifications were done into the EFDC code to incorporate the computation of age concentration for the research presented in Chapter 2. Some of the subroutines were modified based on the suggestions from Dr. Jian Shen from Virginia Institute of Marine Sciences. He has used the age of water concept to calculate age of water in the several studies such as Chesapeake Bay (Shen and Wang 2007), tidal Rappahannock River (Gong et al. 2009), tidal James River (Shen and Lin 2006), etc. using EFDC and CH3D (Curvilinear-grid Hydrodynamics 3D model) model (Sheng 1990). The age concentration is the product of the dye concentration and the time elapsed which would be discussed in detail in Chapter 2.

To obtain the dye concentration and age concentration in the system, we need to solve two transport equations; dye concentration equation (Eq. 2.10) and age concentration equation (Eq. 2.11). The dye module and sediment module (cohesive sediment) were used to solve these two equations in EFDC. As we were not simulating real sediment, density was defined only as a function of temperature and salinity. The settling velocity was also defined to be zero. The advantage of sediment transport not being used in the model simulation was explored for modeling the age concentration by modifying the EFDC source code. It should be noted that the cohesive sediment chosen in the code has nothing to do with the real suspended sediment. Therefore, the basic algorithm that was used while calculating the age concentration is to find out the dye concentration at each time step and then solve for the age concentration. The modifications that were made are as follows:

a) Turn off the density as a function of the sediment (CALBUOY.FOR).

b) The code modified to calculate the age concentration is as follows:

*SED(L,K,1)=SED(L,K,1)+DELT*DYE(L,K)*

In EFDC model, each grid is represent by *I*, *J*, and *K* notations to represent the *X* coordinate, *Y* coordinate, and *Z* (vertical) coordinate. A single variable *L* also can be used to represent (*I*, *J*) in the model. In the above equation *SED(L, K, 1)* represents the suspended sediment concentration, *L* represents the cell ID in EFDC model, *K* represents the layer of the grid cells, and "1" in the parenthesis represents only one type of cohesive sediment is simulated in the model.

At the end of the simulation, the code computes the dye concentration and age concentration at each grid cells. Then, the mean age of water is determined by dividing the age concentration by dye concentration (Eq. 2.12).

1.4.3 Validation of Age of Water

Age of water computed as the ratio of age concentration and dye concentration were validated for the 1-D rectangular channel problem. I have developed a visual basic program to implement the total variation diminishing numerical scheme (Shu and Osher 1988). The scheme was used to solve differential equations for the dye concentration and age concentration, and results were compared with modeled output from the EFDC model after implementing the dye and age concentration equations. The results obtained from both the methods were exactly the same which imply the appropriate implementation of governing equations for dye concentration and age concentration computation in EFDC model. Finally, the age of water computed for the continuous dye

release in a rectangular channel was also validated with the age computed using pulse release of dye (details are given in Chapter 2).

1.4.4 Program Development Implementing Lanczos Filter

The data analysis requires advanced technical background in fluid mechanics, hydrodynamics, turbulent flow, heat transfer, and water quality modeling and dynamics. R programming language was used to perform all the data analysis for the study. For paper 3 (phase 3 of the study), I had to use the low pass filter (performing time averaging of a variable over a fixed time period, e.g., 48 hours) in order to separate the repeating patterns from the tides to understand the residual velocity, salinity, and water surface elevation. A Butterworth low pass filter (Selesnick and Burrus 1998) was first used as a low pass filter, but this method resulted in the time shifting of the modified residual vector. Finally, a Lanczos filter (Walters and Heston 1982) was implemented in the study which didn't result in any time shifting. The output of Lanczos filter implemented in my R program was verified by comparing the filtered series of discharges at USGS Bucks gaging station (02470629) from my program to the filtered series given and reported in the USGS website where the Godin filter (Godin 1972) were used (http://waterdata.usgs.gov/nwis/uv/?site_no=02470629&agency_cd=USGS). Kim and Park (2012) also used Lanczos filter for the modeling study of water and salt exchange in Mobile Bay estuary. This is another intellectual contribution which helped to calculate subtidal salt and flow exchange in Phase 2.

1.4.5 Code Development for Salt Flux using Eulerian and Isohaline Methods

Eulerian decomposition method and isohaline method require a lot of computations using the output of salinity, velocity, depth of all cross-sectional cells from EFDC model. Functions were created in R programming language to input the salinity, velocity, depth and compute various flux components such as subtidal flow rate Q_F, salt transport rate F_S, shear dispersion transport rate F_E, and tidal oscillatory salt transport rate F_T for each cross section. The computation of flux components from the functions were validated by calculating the same components for smaller time period using excel. Similarly, separate code was written to solve the isohaline equations from 3.8 to 3.12 in the phase 3 to compute incoming flow (Q_{in}), outgoing flow (Q_{out}), incoming salinity (s_{in}), and outgoing salinity (s_{out}), and incoming and outgoing salt flux (F_{in}, F_{out}) through a cross section.

1.4.6 Multi-linear Regression Analysis for Flows from Isohaline Method

Multi-linear regression analysis was performed using R program (calling predefined powerful regression functions in the R library) to explore the correlations and relations of Q_{in} and Q_{out} at all five cross sections with influencing factors: river inflows, water surface elevations at open boundaries, and wind stresses. It was very closely examined that what parameters would be used for the model fitting between dependent parameters Q_{in} and Q_{out} and independent variables.

1.5 Organization of Dissertation

This dissertation is organized into 5 chapters. Chapters two to four are organized in journal paper format prepared for British Journal of Environment and Climate Change (BJECC), and the International Association of Hydrological Sciences (IAHS). Chapter

two (Paper 1) has already been published in British Journal of Environment and Climate Change and Chapter four (Paper 2) has already been accepted for publication in Hydrological Sciences Journal (HSJ) of IAHS respectively by the time this dissertation was written. Chapter three has been submitted to HSJ and is under review by the time this dissertation was written. Literature review for the study is given in Chapters two to four for corresponding journal papers. The references for all three papers were combined, sorted, and listed at the end of the dissertation.

Chapter two deals with determining age of water and long term transport timescale in Wolf Bay and Perdido Bay under different inflow conditions from upstream rivers and sea level rise scenarios due to climate change. A three dimensional hydrodynamic model, EFDC was developed for Wolf Bay and Perdido Bay to simulate flow velocities, temperature, dye, and age of water. The work of this chapter has been published in British Journal of Environment and Climate Change as Paper 1:

Devkota, J., Fang, X., and Fang, V. Z. 2013. Response characteristics of Perdido and Wolf Bay system to inflows and sea level rise. British Journal of Environment and Climate Change, 3(2), 229-256.

A part of the work has also been accepted as the conference paper and oral presentation:

Devkota, Janesh; Fang, Xing (2014). “Age of water and salt exchange in Wolf Bay and Perdido Bay”. World Environment and Water Resources Congress. 2014, ASCE/EWRI, Portland, OR.

Chapter three deals with the use of calibrated EFDC model presented in paper 1 or Chapter two to study the flow and salt exchange at various locations in Wolf Bay and

Perdido Bay. Eulerian and isohaline flux methods are applied to the EFDC model to calculate flow and salt exchange. The regression equations were also developed to find out the relationship between the net outflow/inflow with the boundary conditions such as river inflows, tidal water surface elevations, and wind. The work of this chapter is a journal paper submitted to Hydrological Sciences Journal under review as Paper 3:

Devkota, Janesh and Fang, Xing. "Quantification of water and salt exchange in the Perdido Bay and Wolf Bay system". Hydrological Sciences Journal (Under review).

A part of this work has been accepted as the conference paper and oral presentation:

Devkota, Janesh, Fang, Xing (2014). "Age of water and salt exchange in Wolf Bay and Perdido Bay". World Environment and Water Resources Congress. 2014, ASCE/EWRI, Portland, OR.

Chapter four deals with the development of hydrodynamic model EFDC in Mobile River, model calibration, and results analysis performed to determine the possible recirculation of warm water from the discharge canal to the intake canal of the power plant (Fig. 1.2). Several sensitivity model runs were made. Dye, velocity, discharge, and temperature were studied in detail to determine the flow conditions under which the recirculation occur. The work of chapter four is a journal paper accepted for the publication as Paper 2:

Devkota, Janesh and Fang, Xing (2014). "Numerical simulation of flow dynamics in a tidal river under various upstream hydrologic conditions". Hydrological Sciences Journal, In press.

The work of chapter four is also accepted as the conference paper and two oral presentations:

Janesh Devkota, Xing Fang, William E. Garrett, Jr., and Jonathan Ponstein (2011). **"**Advantages and challenges of thermal discharge modeling in rivers using three dimensional hydrodynamic and temperature models". An oral presentation at the Third Thermal Ecology and Regulation Workshop, October 11–12, 2011, Maple Grove, MN.

Devkota, Janesh and Fang, Xing (2014). "Numerical simulations of flow dynamics in a tidal river under changing hydrologic conditions". World Environmental and Water Resources Congress 2014, ASCE/EWRI, Portland, OR.

Chapter five summarizes the study performed as conclusions and provides limitations of the study and the future study in this area.

Appendix A discusses about the calibration parameters and calibration procedure used in the calibration of Perdido EFDC model and EFDC model for Mobile River. The calibration parameters used in the EFDC models and the literature values are also listed.

Appendix B expands the theory of age of water that is briefly discussed in Chapter 2. The detailed procedure of calculating the age of water/tracer and implementing in the numerical model is explained.

Chapter 2. Response Characteristics of the Perdido and Wolf Bay System to Inflows and Sea Level Rise

2.1 Abstract

The Perdido and Wolf Bay system in Alabama, USA, is an estuarine system linking the freshwater from the Perdido and Wolf Bay watersheds and the tidal saltwater from the Gulf of Mexico through Perdido Pass, Dolphin Pass, and the Gulf Intracoastal Waterway. A three dimensional hydrodynamic model using Environmental Fluid Dynamics Code (EFDC) was developed and used to analyze complex and dynamic flow, salinity, and temperature distributions in the system. The external driving forces for the model include the river discharges from natural and urban watersheds, atmospheric winds, and astronomical tidal elevations at the open boundaries where flow exchange takes place. Simulated water surface elevation, temperature, and salinity were compared against the field data at several observation stations in 2008 and 2009 with good agreement (coefficient of determination R^2 = 0.92 between the measured and the modeled water surface elevations). The calibrated EFDC model was used to examine responses of the system to high, mean, and low inflows from streams and the sea level rise in the open boundaries under climate change. The concept of the age of water was applied to understand pollutant transport in the system. The age of water reveals dynamic and complex interactions between tides from the Gulf of Mexico and inflows from the streams. The age of water is less than 20 days under the 2-year high inflows and up to 160 days under 7Q10 low inflows. Under mean inflow conditions, the age of the tracer

released from Wolf Bay is 50–70 days in the lower Perdido Bay and larger than that in the upper Perdido Bay, indicating a strong interaction between tides and inflows, which results in recirculation of flow and pollutants. The age of water is projected to increase up to 60 days under estimated sea level rise scenarios.

2.2 Introduction

The principal external forcings that control estuarine processes are tides, winds, and freshwater inflows from upstream watersheds and surrounding rural/urban watersheds. The freshwater inflows produce a net seaward transport of nutrients and pollutants into an estuary, while the tides lead to periodic seaward and landward transport or exchange (Jiang and Shen 2009). This periodic transport process affects the salinity in an estuary and the flushing time of pollutants in the estuary. Salinity in an estuary varies temporally with rising and falling tides and seasonal changes in sea level and ocean salinity. The estuarine salinity distribution is a result of the interplay among the buoyancy flux from riverine inflow, the advection by tides, the estuarine circulation, and the wind mixing (Warner et al. 2005). Human activities such as urbanization can influence salinity distributions in an estuary by altering freshwater inflows through upstream hydraulic control structures, increasing urban runoff from impervious areas, and modifying the estuarine morphometry. Alteration of estuarine morphometry includes channel deepening, construction of coastal structures, etc. The Perdido Bay estuary has experienced channel deepening near the Perdido Pass (Fig. 2.1) for navigational purposes in the past, which could influence salinity distribution and the ecosystem in the Bay. Several studies have been conducted to understand hydrodynamics and salinity transport

(Bales et al. 2006; Xu et al. 2008; Jiang and Shen 2009), sediment transport (Gong and Shen 2009; Liu and Huang 2009), and water quality (Tetra Tech Inc. 1998; Li et al. 2009) in estuaries under past climate conditions.

Estuaries are the most productive systems in nature. The balance of fresh water and saline water in an estuary results in a productive ecosystem (Bales et al. 2006). The transport of dissolved substances and suspended particles takes place during the interaction of riverine inflows and coastal tides. Phytoplankton growth and variations of nutrients in lakes or estuaries are connected to the discharge from upstream rivers and tributaries (Shen and Haas 2004). Harmful algal blooms found in coastal waters are caused by circulation, river inflows, and anthropogenic nutrient loadings, such as urbanization; algal blooms lead to eutrophication (Sellner et al. 2003). It is essential to find the travel time required for the dissolved substances, e.g. nutrients introduced from the inflow tributaries, to travel to a given location of an estuary. The travel time is useful for planning strategies for water-quality restoration of an estuary. In this paper, the age of water was used as a time scale parameter for understanding mass exchange and transport process in an estuary. The age of a water parcel is defined as the time elapsed since the water parcel under consideration departed from the region in which its age is defined to be zero (Zimmerman 1976; Shen and Lin 2006). The age determined in this study is the time elapsed since a dissolved substance was discharged into the upstream rivers of an estuary.

Several studies related to the age of water, flushing time, and residence time have been conducted to understand mixing and transport processes (Shen and Haas 2004; Shen and Lin 2006; Huang and Liu 2009). Flushing time, residence time, and age of water are

three common transport timescales used to measure retention of water or scalar quantities. Pollutant residence time (Chapra 1997) for any pollutant with chemical/biological decay and settling is beyond the scope of the study. Flushing time of an estuary is commonly defined as the time needed to replace the freshwater already in the estuary (freshwater volume) at the rate of freshwater inflow (Dyer 1973). It represents the average time required to remove a parcel of freshwater (or conservative tracer) from an upstream location in an estuary to the sea. Flushing time is used to describe the flushing rate or removal rate of pollutants in a waterbody without identifying the underlying physical processes or their spatial distribution. Residence time for a substance is the mean amount of time that particles of the substance or water parcels stay or "reside" in a system (Chapra 1997). Zimmerman (1976) defined residence time as the time required for the water parcel to reach to the outlet after arriving at a particular location in a waterbody for the first time. Age of water is the compliment of the residence time. Age of water is defined as the time interval between the entrance of a pollutant discharge into a waterbody and arrival at a location of interest within the waterbody.

River inflow is one of the dominant factors that influences water age distribution (Shen and Lin 2006). Density-induced circulation substantially contributes to long-term transport in a downstream estuary, where stratification persists. Flushing time affects a wide range of hydrodynamic and water quality processes in an estuary (Ji et al. 2007). Shen and Haas (2004) developed and applied a three-dimensional numerical model for the York River estuary in order to calculate the age of water and residence time in the estuary. They reported that it took about 2 and 3 months for the dissolved substances

discharged into the system at the headwaters of the tributaries to be transported to the mouth of the estuary under high and mean inflow conditions, respectively.

Model studies were conducted to understand the salinity distribution as a result of the change in wind directions in the Perdido Bay and Wolf Bay estuary (Xia et al. 2011a). Xia et al. (2011b) studied the response of a Gulf of Mexico estuary plume to wind forcing using the particle tracking approach. The present study was conducted to support the overall objective of understanding the impacts of human activities and climate change on water resources and ecosystem health in the Wolf Bay basin. To understand the flow dynamics in Wolf Bay under extreme climate conditions such as flood and drought, sea level rise, and future climate changes a high spatial resolution three-dimensional hydrodynamic model was developed. Because there was not adequate data to quantify the flow exchange between Wolf Bay and Perdido Bay, the study area was expanded from Wolf Bay to the Perdido River and Bay system (Fig. 2.1). The expanded study area included Wolf Bay as well as the upper, middle, and lower Perdido Bay. The river and estuary system of the Wolf Bay includes various nutrients and sediment inputs from natural and urban watersheds and salt water from Perdido Bay with direct connection to the Gulf of Mexico. In order to understand the impacts of climate and land use changes on the ecosystem of the Wolf Bay watershed, it is crucial for water resources managers to be able to quantify and understand the movement and distribution of any water quality constituents or pollutants in the river and estuary system. A three-dimensional (3D) Environmental Fluid Dynamics Code (EFDC) model was developed, calibrated, and applied to study the hydrodynamics in Wolf Bay and Perdido Bay and understand the

estuarine system response to assumed high, low, and mean inflows from upstream rivers and estimated sea level rises under future climate scenarios.

2.3 Materials and Methods

2.3.1 Study Area

The numerical model study was conducted for the Perdido and Wolf Bay system (Fig. 2.1). Perdido Bay is a relatively small, shallow estuary connected to the Northern Gulf of Mexico and to the eastern part of Mobile Bay in the USA. The surface areas of Perdido Bay and Wolf Bay are approximately 130 and 14.7 km^2 with an average depth of 2.6 and 1.9 m (Schropp et al. 1991; Macauley et al. 1995), respectively. The major freshwater inflows into the upper Perdido Bay are the Perdido River, Styx River, Elevenmile Creek, and Bayou Marcus (Fig. 2.1). The Perdido River is the dominant source of the freshwater inflows to the Bay. The Elevenmile Creek watershed including the Eightmile Creek accounts for about 10% of the freshwater inflows to the Bay and receives an industrial wastewater discharge from the International (formerly Champion) Paper Company's pulp and paper mill (Macauley et al. 1995). Perdido Bay is connected to the Gulf of Mexico through a narrow outlet (200 to 500 m wide, around 5 m deep) called Perdido Pass, to the Big Lagoon on the east through Dolphin Pass, and to Mobile Bay on the west through the Gulf Intracoastal Waterway (GIWW) as shown in Fig. 2.1. Because of its small size, the Perdido and Wolf Bay system features dynamic changes in water quality in response to large inflows due to heavy rainfall events, strong winds, and tides from the Gulf. Flow characteristics and dynamics in the Perdido and Wolf Bay system are affected by tidal fluctuations associated with astronomical and meteorological forces (Grubbs and Pittman

1997) and inflows from upstream rivers, but interactions among these forcing factors on estuary mixing and circulation dynamics have not been well studied yet. The diurnal tidal range in Perdido Pass is 0.2 m (Xia et al. 2011b). Perdido Bay has a small tidal range (<0.5m) (Macauley et al. 1995; Flemer et al. 1998).

2.3.2 Hydrodynamic Simulation Model Used

The 3D hydrodynamic EFDC model was used to develop a site-specific model for understanding the hydrodynamics and transport (temperature, dye, and salinity) in the Perdido and Wolf Bay system (Fig. 2.1). The EFDC model solves three-dimensional continuity, momentum, and free surface equations of motion (Hamrick 1992b) and uses the Mellor and Yamada level 2.5 turbulence closure scheme (Mellor and Yamada 1982). The EFDC model has been applied to many study areas: Virginia's James and York River estuaries (Hamrick 1995), the entire Chesapeake Bay estuarine system (Hamrick 1994), and Morro Bay, California (Ji et al. 2001). The EFDC model has also been used to study the water age and residence time (Shen and Haas 2004; Shen and Lin 2006; Huang et al. 2009). The U.S. Environmental Protection Agency (EPA), Region 4, contracted Tetra Tech, Inc. to develop the hydro version of EFDC (EFDC-Hydro), which is publicly available. The EFDC version from the Dynamic Solutions-International, LLC (EFDC-DSI) was used for the study (http://efdc-explorer.com/). The momentum and continuity equations used in EFDC are (Hamrick 1992b):

$$\partial_t(m_x m_y Hu) + \partial_x(m_y Huu) + \partial_y(m_x Hvu) + \partial_z(m_x m_y wu) - m_x m_y f_c Hv = \quad (2.1)$$
$$-m_y H\partial_x(p + gH + gz_b^*) - m_y(\partial_x h - z\partial_x H)\partial_z p + m_x m_y \partial_z(H^{-1}A_v\partial_z u) + Q_u$$

$$\partial_t(m_x m_y Hv) + \partial_x(m_y Huv) + \partial_y(m_x Hvv) + \partial_z(m_x m_y wv) - m_x m_y f_c Hu = \quad (2.2)$$
$$-m_y H\partial_y(p + gH + gz_b^*) - m_x(\partial_y h + z\partial_y H)\partial_z p + m_x m_y \partial_z(H^{-1}A_v\partial_z v) + Q_v$$

$$\partial_z p = -gHb = -gH(\rho - \rho_0)\rho_0^{-1} \quad (2.3)$$

$$\partial_t(m_x m_y H) + \partial_x(m_y Hu) + \partial_y(m_x Hv) + \partial_z(m_x m_y w) = Q_H \quad (2.4)$$

$$m_x m_y f_c = m_x m_y f - u\partial_y m_x + v\partial_x m_y \quad (2.5)$$

where u and v are the horizontal velocities in the curvilinear-orthogonal horizontal coordinates (x, y); w is the vertical velocity in the stretched vertical coordinate z; p is the excess pressure above the reference density hydrostatic pressure divided by the reference density, ρ_0 (Eq. 3); z_s^* is the free surface elevation; z_b^* is the bottom or topography elevation; $H\,(= z_s^* - z_b^*)$ is the total water column depth in a grid; A_v is the horizontal eddy or turbulent viscosity; f_c is the Coriolis parameter; Q_u and Q_v represent additional forces or momentum sources and sinks, including horizontal turbulent momentum diffusion, vegetation resistance, and wave Reynolds stress due to high frequency gravity waves; Q_H is the source/sink term used to represent direct rainfall, evaporation, groundwater interaction, water withdrawals, and point and nonpoint source discharges; m_x and m_y are dimensionless scale factors for curvilinear horizontal coordinates. The sigma coordinate z is dimensionless, $z = 0$ at the bottom topography, and $z = 1$ at the free surface for all grids, but water depth H is a function of time and location and solved by the EFDC.

The generic transport equation in EFDC for a dissolved or suspended constituent C (Hamrick 1992b) is:

$$\partial_t(m_x m_y HC) + \partial_x(m_y HuC) + \partial_y(m_x HvC) + \partial_z(m_x m_y wC) = \quad (2.6)$$
$$m_x m_y \partial_z(H^{-1}\partial_z A_b C + \sigma C) + m_x m_y H R_C + Q_C$$

where A_b is the vertical turbulent or eddy diffusivity; σ is the settling velocity, which is zero for a dissolved constituent or tracer modeled in this study; and R_C is the reactive sources and sinks. The horizontal turbulent diffusion and external sources and sinks associated with volumetric withdrawals and discharges are accounted for using Q_C.

The transport of dynamically active constituents such as salinity, temperature, and suspended sediment is coupled with the momentum equations through an equation of state and the hydrostatic approximation (2.3), which is valid for the shallow Perdido and Wolf Bay system.

The second moment turbulence closure model developed by Mellor and Yamada (1982) and modified by Galperin et al. (1988b) and Blumberg et al. (1992) is used in the EFDC model to relate vertical turbulent viscosity and diffusivity to the turbulent intensity q, a turbulent length scale l, and a Richardson number R_q:

$$A_v = \phi_v ql = 0.4(1+8R_q)ql(1+36R_q)^{-1}(1+6R_q)^{-1} \quad (2.7)$$

$$K_b = \phi_b ql = 0.5ql(1+36R_q)^{-1} \quad (2.8)$$

$$R_q = -gH\partial_z bl^2 H^{-2} q^{-2} \quad (2.9)$$

where ϕ_v and ϕ_b account for reduced and enhanced vertical mixing or transport in stable and unstable vertically density-stratified environments.

2.3.3 Model Grid Generation

Computational grid development is an important step of any two- or three-dimensional hydrodynamic modeling. A model grid is the result of balancing spatial resolution, a site conceptual model, and modeling objectives against the computational time and resources. High resolution grids can produce great horizontal and vertical detail, but if the model run times are excessive, then the model is limited due to its inability to produce enough model runs to perform adequate calibration and validation and develop useful results from various model input scenarios.

A curvilinear grid was used to develop an EFDC model for the Perdido and Wolf Bay system, and the model is called “Perdido EFDC model”. The curvilinear orthogonal grids for the Perdido EFDC model were developed using the Delft RGFGRID module (Deltares 2010) with GIS shoreline data (shapefiles) as input and imported into the EFDC using EFDC-Explorer 6 (Craig 2011). The horizontal model grids developed for the Perdido EFDC model were based on the 1983 North American Vertical Datum (NAVD) and the Universal Transverse Mercator (UTM) projection. The Perdido EFDC model has a total of 4878 curvilinear horizontal grids and 4 layers in the vertical direction, i.e., a total of 19512 3D cells. Fig. 2.2 shows the computational grid with bathymetry of Perdido Bay and Wolf Bay. The grid sizes of the Perdido EFDC model ranged from 27 m to 1200 m. The typical water depths in the simulation domain ranged from 0.16 m to 7.1 m in the estuary and from 9.7 m to 18.6 m in a small portion of the Gulf of Mexico that connects to the estuary (Fig. 2.2). The horizontal layer thickness ranged from < 0.1 m to 1.77 m in the estuary to produce high resolution simulation results along the depth in the estuary. There are 847 grids extended from the Perdido Pass into the Gulf of Mexico;

therefore, appropriate boundary conditions in the Gulf can be used. The bathymetry data for the Perdido and Wolf Bay system including the portion of the Gulf of Mexico were obtained from the NOAA web site (http://www.ngdc.noaa.gov/mgg/bathymetry/hydro.html).

2.3.4 Atmospheric Forcing

The Perdido EFDC model uses meteorological data as input to model the surface heat exchange between the water surface and the atmosphere. The meteorological parameters required for the EFDC model (Hamrick 1992b) are atmospheric pressure (millibars), solar radiation (W/m^2), precipitation (m/day), evaporation (m/day), relative humidity (fraction), cloud cover (fraction), dry bulb temperature (^oC), wind speed (m/s), and wind direction. The 15-minute meteorological data were available from two weather stations near the study area. One set of the data is from the Mobile Regional Airport (~40 miles northwest of the Bay, Fig. 2.1) and obtained from the Southeast Regional Climate Center (SERCC), and the other set of the data is from Jay station (~25 miles northeast of the Bay, Fig. 2.1) and obtained from the Florida Automated Weather Network (FAWN). Meteorological parameters from the two stations were in good agreement with one another. The data from FAWN did not have atmospheric pressure and cloud cover data, and these missing data were filled in by the Mobile Regional Airport data. Therefore, combined 15-minute meteorological data from FAWN and SERCC were used for the Perdido EFDC model as the atmospheric forcing boundary.

2.3.5 Boundary Conditions

There are three open boundaries (the Gulf of Mexico, Dolphin Pass, and GIWW, Fig. 2.1) in the study area where flow exchanges take place. The open boundary used in the Gulf allows the EFDC to appropriately model the flow exchanges between the Gulf and the estuary through Perdido Pass (Fig. 2.1). Input data at the open boundaries for the Perdido EFDC model were combined data from the nearest available observation stations. Measured water surface elevation and water temperature at the Dauphin Island station from NOAA were used as the open boundary in the Gulf of Mexico to represent tidal influences. The boundary in the Gulf of Mexico is relatively far from the estuary, and a constant salinity of 34 ppt was used as salinity boundary condition. The open boundary at Dolphin Pass, which connects Perdido Bay with the Big Lagoon (Fig. 2.1), included measured water surface elevation at the Pensacola Gulf station from the US Army Corps of Engineers (USACE) and observed salinity and temperature at the 33010H24 (Fig. 2.1) monitoring station (Galvez Landing on Innerarity Island) from FDEP. The open boundary at the GIWW included measured water surface elevations at the NOAA's Gulf Shores station on the GIWW, measured water temperatures at Dauphin Island (NOAA 8735180 station), and measured salinity at the Orange Beach Waterfront Park (OBWP) monitoring station from ADEM.

Freshwater is discharged into the Perdido and Wolf Bay system through several rivers and tributaries. The discharge data for the four rivers flowing into Perdido Bay (Fig. 2.1) were obtained from the closest US Geological Survey (USGS) gaging stations. The major rivers that discharge into Wolf Bay are Wolf Creek, Miflin Creek, Owens Bayou, Graham Bayou, and Hammock Creek (Wang 2010). The freshwater inflow data

for the rivers flowing into Wolf Bay were obtained from the output of the Soil Water Assessment Tools (SWAT) watershed modeling system provided by Wang (Wang 2010), because only a short period of measured discharges is available for Wolf Creek and none for other streams. For the freshwater inflows from all streams, a constant low salinity of 0.5 ppt was used. Water temperature boundary conditions for the rivers discharging into the Perdido and Wolf Bay system were calculated using the regression equation that correlates stream temperature with air temperature (Pilgrim et al. 1998).

2.4 Model Calibration Results

The Perdido EFDC model was calibrated from September 17, 2008 (Julian day 260) to July 14, 2009 (Julian day 560) against observed data. The hydrodynamic model was calibrated for water surface elevation, water temperature, and salinity using observed data collected at various monitoring stations (Fig. 2.1) throughout Wolf Bay and Perdido Bay.

2.4.1 Water Level Calibration

In any hydrodynamic modeling, flow calibration is a very essential step, because all the other parameters such as temperature, salinity, and dissolved oxygen are directly related to the flow simulations. The inaccurate flow patterns simulated by the model may introduce errors in all the other model parameters. Simulated and observed water levels at the NOAA's Blue Angels Park tidal station were in good agreement in both amplitude and phase (Fig. 2.3): the coefficient of determination (R^2) is 0.92 between the measured and the modeled water surface elevations. The average absolute difference between observed and simulated water surface elevation at Blue Angels Park is 0.04 m. Table 2.1 shows the amplitude and the phase of harmonic constituents derived from measured and

modeled surface water elevations at Blue Angels Park. The dominant harmonic constituents in Perdido Bay are K1 and O1, which are Lunisolar diurnal constituents. The constituent K1 shows the effect of the Sun's declination. O1 shows the effect of the Moon's declination and accounts for the diurnal tides. Diurnal tides occur once a day.

Errors in water surface elevation might have occurred because of the large inflows from the rivers in the upstream of Perdido Bay. The Blue Angels Park monitoring station (Fig. 2.1) is located in the upper Perdido Bay where the flow is influenced by the freshwater inflows from rivers such as the Perdido River, Styx River, Bayou Marcus, and Elevenmile Creek. Ji et al. (2007) reported that a large amount of freshwater inflows can cause a sudden change in elevation, which then propagates downstream like a wave. Simulated and observed water surface elevations at Terry Cove (Fig. 2.1) in Perdido Pass were in good agreement with an average absolute difference of 0.07 m. There were no velocity measurements available to compare with modeled velocity at any monitoring station in the study area.

2.4.2 Salinity Calibration

Salinity measurements for model calibration were available at 11 monitoring stations operated by ADEM, FDEP, and AWW in Perdido Bay and Wolf Bay as shown in Fig. 2.1. The frequencies of data collections varied from weekly to monthly. Most of the salinity data were measured near the water surface; therefore, the top layer salinity from the Perdido EFDC model was compared with measurements, and statistical error parameters (Table 2.2) were derived. The time series of modeled surface and bottom salinities were plotted against observed salinity data at nine monitoring stations in Perdido Bay and Wolf Bay (Fig. 2.4).

The modeled surface salinity values were in reasonable agreement with the observed salinity data (Fig. 2.4 and Table 2.2). The average coefficient of determination (R^2) was 0.7, and the root mean squared error (RMSE) was 3.2 ppt. Observed data and model results indicate that salinity was relatively high in 2008, because there were lower freshwater inflows due to drier climate conditions in the Perdido and Wolf watershed. However, in 2009, the salinity was relatively lower because of high inflows from the rivers due to wet climate conditions. The Perdido EFDC model predicted the spatial variability of the salinity well (Fig. 2.4). In some monitoring stations such as 04012032, it seems that the model tended to under-predict the salinity. Because salinities in an estuary are affected by many factors, such as the local freshwater inflow, runoff, wind, and local circulation, some discrepancies can be expected (Wang et al. 2010). Ji et al. [14] indicated that simulated freshwater runoff in the St. Lucie estuary, Florida, could significantly influence salinity, especially during the wet season.

2.4.3 Water Temperature Calibration

Simulated water temperatures in Perdido Bay and Wolf Bay were compared with observed data at six monitoring stations from AWW and FDEP (Fig. 2.5). Observed water temperatures from AWW and FDEP were measured at 0.30 m and 0.15 m from the surface, respectively. Using these observed data, modeled temperatures in the surface layer were calibrated. Observed temperature data from AWW and FDEP were available in weekly to monthly intervals, and combined data from both sources were used for model calibration and calculation of statistical error parameters. Simulated temperature variation in Perdido Bay and Wolf Bay matched well with the observed data sets in all the calibration stations. The average Nash Sutcliffe coefficient (NSE) for the six

calibration stations is 0.78, and the average R^2 is 0.87 (Table 2.3). The blue and red lines in Fig. 2.5 are the modeled temperatures in the bottom and surface layers, respectively, and they indicate that there were very weak stratifications on temperature at these monitoring stations.

2.5 Model Applications: Predictions on Water age

2.5.1 Introduction on the Age of Water

Water age is an important and useful time-scale parameter that can be used to assess mixing and water quality dynamics in a waterbody (Zimmerman 1976; Deleersnijder et al. 2001; Shen and Haas 2004; Shen and Lin 2006; Gong et al. 2007; Gong et al. 2009; Li et al. 2011a; Li et al. 2011b). The amount of nutrients discharged into an estuary and the transport time required for these nutrients to reach a given location contribute to algal blooms in an estuary. As a result, retention time and time required to remove pollutants out of an estuarine system are critical to the water quality in the system. Traditionally, the flushing time concept has been used to quantify the entire waterbody. The limitation of flushing time to quantify estuary transport processes without high degree of spatial variations has been recognized (Shen and Haas 2004). Flushing time is an integrative system measure, whereas both the residence time and the age of water are local measures (i.e., spatially variable within the domain) (Monsen et al. 2002). In this paper, the water age concept has been used to understand the transport mechanism of a dissolved conservative (no growth and decay) substance from multiple sources (inflows) and to understand complex interactions between tides and inflows from natural and urban watersheds.

Delhez et al. (1999) studied the age of a particle of sea water and defined water age as the time elapsed since the particle under consideration left the region in which its age is prescribed to be zero. Delhez et al. (1999) formulated a method to compute spatially- and temporally-varying age distributions in a real system based on the tracer concentration and age concentration. This method has been successfully used to find the age of water in the York River (Shen and Haas 2004), in the tidal James River (Shen and Lin 2006) using EFDC models, and in the Chesapeake Bay using the CH3D model (Shen and Wang 2007) and to find the age of river-borne sediment transport in the tidal York River estuary using the EFDC (Gong and Shen 2010).

Assuming there is only one tracer or pollutant discharged into the estuary and no other sources and sinks of the tracer in the estuary, the transport equations for calculating the tracer and the age concentrations can be written as follows (Delhez et al. 1999):

$$\frac{\partial c(t,\vec{x})}{\partial t} + \nabla(uc(t,\vec{x}) - K\nabla c(t,\vec{x})) = 0 \tag{2.10}$$

$$\frac{\partial \alpha(t,\vec{x})}{\partial t} + \nabla(u\alpha(t,\vec{x}) - K\nabla \alpha(t,\vec{x})) = c(t,\vec{x}) \tag{2.11}$$

where c is the tracer or dye concentration, α is the age concentration, u is the velocity field, K is the diffusivity tensor, t is the time, and $\vec{x}$ is the distance vector. The mean age "a" of a set of particles or tracers in a fluid parcel (Delhez et al. 1999) can be calculated as follows:

$$a(t,\vec{x}) = \frac{\alpha(t,\vec{x})}{c(t,\vec{x})} \tag{2.12}$$

Equations (2.10) through (2.12) were used to compute the age of water parcels using the EFDC with specified initial and boundary conditions.

Fig. 2.6 (a) and (b) show simulated dye concentrations (red lines) for two case studies against corresponding analytical solutions (blue dashed lines) in order to verify the modeling of the age of water using the EFDC. The first case (Fig. 2.6a) is an ideal one-dimensional channel flow where a 0.5 kg pulse of dye is released into the channel with steady flow and constant diffusivity. The second case (Fig. 2.6b) is the same channel where a certain amount of conservative material is continuously released into the channel's upstream end, where x = 0. Fig. 2.6a shows the EFDC simulated dye concentrations, which matched well with the analytical solution (Chapra 1997) for the first case at time t = 2 min, 5 min, 10 min, and 15 min after the pulse is released. Fig. 2.6b shows that the simulated dye concentrations matched well with the analytical solution (Chapra 1997) for the second case at t = 5 min, 10 min, and 30 min for the continuous release. For both cases, dye concentration released is 1 mg/L, diffusivity is 1 m^2/s, steady flow velocity is 0.42 m/s, and the channel is 1 m wide, 5 m deep and 500 m long in the flow direction.

Age concentration in the EFDC is calculated by using the equation (11) proposed by Delhez et al. (1999). Age of water (equation 12) was calculated as the ratio of the age concentration and dye concentration and is plotted on Fig. 2.6c. The solid lines in Fig. 2.6c represent the age of water profile as a function of distance at t = 5 min, 10 min, and 30 min due to the continuous dye release at the upstream end (the case in Fig. 2.6b). The age of water/dye/tracer/pollutant at the release point (upstream boundary) is always assumed to be zero; therefore, the age of water increases with distance and varies with time when the time is shorter than the travel time of dye passing through the simulation domain. When the time is large enough, e.g., at 30 minutes, the system has reached the

equilibrium state, i.e., the dye concentration is constant everywhere. Therefore, the numerical experiment with the constant dye release from the source provides useful information on the spatial variation of the age of water/dye after the equilibrium state is reached when the EFDC is run for a long simulation time. For a pulse release, simulated dye concentration (Eq. 2.10, Fig. 2.6a), age concentration (Eq. 2.11), and age of water/dye (Eq. 2.12) change with time and location (distance). The age of a dye at a channel location for a pulse release was calculated by tracking 50% of the dye mass passing the location (Huang et al. 2009). Solid dots in Fig. 2.6c represent the age of water/dye at t = 2 min, 5 min, 10 min, and 15 min calculated from a pulse release experiment (Fig. 2.6a). The age profile represented by solid dots and the age profile at t = 30 min from the continuous release match very well. Therefore, the age profile determined for the steady or equilibrium state well characterizes spatial variation of travel time of a water/dye/pollutant from both pulse and constant releases. In this paper, the age of water computed by the calibrated Perdido EFDC model is used as a useful time-scale parameter to assess complex mixing and water quality dynamics in the Perdido and Wolf Bay system under different combinations of several external forcing factors.

2.5.2 Prediction of Water Ages under Various Inflow Scenarios

The amount of nutrients discharged into an estuary and the transport time required for these nutrients to be exported to the ocean, along with other biogeochemical processes, play important roles in the eutrophication processes of an estuary (Shen and Haas 2004). In natural water bodies, it is essential to understand the effects of extreme weather conditions on salinity and nutrients. In this study, return period flow, mean flow, and low flow (*i.e.*, 7Q10) were chosen to represent extreme inflow conditions from upstream rivers, including streams from urban watersheds. Numerical experiments were performed to study the impact of the flushing due to the high inflows, mean inflows, and low inflows from upstream rivers into Perdido Bay and Wolf Bay, which are freshwater inflows but interact with tides from the Gulf of Mexico (Fig. 2.1).

Return period is a statistical measurement representing the average recurrence interval over an extended period of time. The 2-year flow (m^3/s) for an Alabama river can be calculated based on the national flood-frequency program (Mason et al. 1998) as a function of the drainage area (A in square miles):

$$Q_2 = 169A^{0.616} \quad \text{For 2 year recurrence interval} \tag{2.13}$$

The drainage areas for the Perdido River and the Styx River are 394 and 192 $mile^2$, and the corresponding 2-year flows are 190 and 122 m^3/s. Other streams have drainage areas ranging from 2.1 (Owen Bayou) to 27.8 (Elevenmile Creek) $mile^2$ and 2-year flows ranging from 5.5 to 37.1 m^3/s.

The 7Q10 low flow in a stream represents the minimum 7-day flow that occurs, on average, over a 10-year interval, and it is generally accepted as the critical low flow for water quality engineering studies (Chapra 1997). The 7Q10 low flows for the streams

in Wolf Bay and Perdido Bay were determined using low-flow frequency analysis (1997) and ranged from 0.02 to 5.69 m^3/s. The mean flows were calculated from the flow data of streams in Wolf Bay and Perdido Bay from 1998–2010. The mean flows calculated for freshwater streams ranged from 0.13 to 19.17 m^3/s.

A conservative tracer without decay was used to diagnose the variation of the transport properties, both spatially and temporally, in Wolf Bay and Perdido Bay. The tracer with a concentration of 1 (arbitrary units) was continuously released into the freshwater streams of the estuary. The open boundary conditions (Gulf of Mexico, Dauphin Pass, and GIWW, Fig. 2.1) were assumed to have a zero tracer concentration such that the incoming tracer concentration into the system from the Gulf was zero.

To better understand the transport processes in the Perdido and Wolf system, model runs were categorized into three groups (Table 2.4) by where the tracer was released from: (1) all the streams, (2) streams flowing into Wolf Bay, and (3) the two major rivers flowing into Perdido Bay (Perdido River and Styx River). Only simulation results for group (1) and (2) are reported here (Table 2.4). Each group of the simulations included four flow scenarios: base inflows, high inflows, low inflows, and mean inflows (Table 2.4). The base inflow scenario has inflows from streams that were either measured or simulated using the SWAT model in 2008 and 2009 (the model calibration period). Combined inflows from all streams into Perdido Bay ranged from 11.2 to 631.4 m^3/s with a mean flow of 35.2 m^3/s, and combined inflows from all streams into Wolf Bay ranged from 1.3 to 21.9 m^3/s with a mean flow of 2.7 m^3/s during the 2008–2009 simulation period.

For all the scenario runs, the model was run for 600 days from March 1, 2008 (Julian day 60) to October 21, 2009 (Julian Day 660 starting from January 1, 2008) so that the estuary system would reach the dynamic equilibrium condition. All other forcing boundary conditions (meteorological forcing parameters, salinity, temperature, water surface elevations at open boundaries) were from 2008–2009 observations. It should be noted that age distribution in an estuary varies with time and space and is a function of tide, freshwater discharge, salinity, and wind in the estuary..

2.5.2.1 Dye release from all rivers

Numerical experiments were performed to evaluate the age distributions in Wolf Bay and Perdido Bay with the conservative dye release from all the rivers. The age of water distribution in the system would explain the time required for the conservative pollutants to reach any particular location. Fig. 2.7 shows simulated vertically-averaged age distributions in the Perdido and Wolf system under dynamic equilibrium conditions using 2-year inflows, 7Q10 inflows, mean inflows, and inflows in 2008–2009 (base) from all the rivers. Age of water was computed at the end of the simulation for all the model runs. The age at a prior time could be different, since the age is dependent on variations of freshwater inflows, tides, and other forcing conditions (Shen and Wang 2007).

The vertically-averaged age of water (tracer) at the dynamic equilibrium corresponding to 2-year inflows is 0–4 days in Wolf Bay (Fig. 2.7a, 2-day increment contours), 0–16 days in Perdido Bay, 4–8 days in the navigation channel connecting Wolf Bay and Perdido Bay, and 8–10 days in the Perdido Bay complex. The areas with an age of water greater than 10 days in the system represent low flushing zones under high inflow conditions (Fig. 2.7a). These areas have less flow circulation due to special local

bathymetry and shoreline geometry that allow the areas to avoid strong interactions between tidal influences from the Gulf and upstream inflows. In general, the larger freshwater inflows lead to a short flushing time in the Perdido and Wolf system (Ji 2008).

Fig. 2.7(b) with 10-day increment contours shows the age distribution due to 7Q10 low inflows from all the streams. The age varies from 20–30 days in Wolf Bay and 30–80 days in the navigation channel connecting Wolf Bay and Perdido Bay. This means that during low inflow conditions the age of water is much higher than that during high inflow conditions (2-year return period). The water age ranges from 40–90 days in the upper Perdido Bay, 90–110 days in the middle and lower Perdido Bay, and 60–90 days in the Perdido Pass complex. Fig. 2.7(b) indicates that, under low inflow conditions, tidal influences from the Gulf force a tracer released from upstream rivers to stay in the system much longer (more than 3 months).

Fig. 2.7(c) with 10-day increment contours shows the age distribution due to mean inflows from all the streams. During mean inflow conditions, the simulated age of water is less than that under 7Q10 low inflow conditions. Because the mean inflows are greater compared to 7Q10 low inflows, the dye is transported more rapidly throughout the Perdido and Wolf Bay system. The vertically-averaged age ranges from 10–30 days in the upper Perdido Bay and 40–50 days in the middle Perdido Bay. The age varies from 50–60 days in the lower Perdido Bay and 40–50 days in the Perdido Pass complex. The age in Wolf Bay is smaller than that in Perdido Bay. In the navigation channel, the age of water varies from 20–30 days. Fig. 2.7(c) indicates that a pollutant flowing into Wolf Bay would be transported out via the GIWW within 30 days, and the residual pollutant from

Wolf Bay and Perdido Bay would be transported out of the system in 40–50 days under the mean inflow conditions.

Fig. 2.7(d) with 10-day increment contours shows the age distribution under measured inflows from streams in the Perdido Bay watershed and SWAT simulated inflows from streams in the Wolf Bay watershed in 2008–2009. The age of water in the system is slightly higher than that under mean inflow conditions. In the upper Perdido Bay, the age varies from 40–50 days. The larger age at the middle and lower Perdido Bay (50–65 days) indicates that the materials would take a longer amount of time to be flushed out of the system in these regions. It would take about 35–50 days for the materials to flush out of the system from Perdido Pass. The age distributions under the long-term (1998–2010) mean inflows are representative of the age distributions under the 2008–2009 inflow conditions (base) (Fig. 2.7); therefore, simulation results of the age distribution under 2008–2009 inflow conditions are not given in the following discussion (Figs. 2.8 and 2.10).

These numerical experiment results indicate interesting underlying flow dynamics in the Perdido and Wolf Bay system. It should be noted that the age of water is not the time necessary for a single particle to reach the location examined from its release point, but rather, it should be interpreted as the time needed for a marked change in the characteristics of the source to significantly affect the conditions at the location (Shen and Wang 2007). Deleersnijder et al. (2001) discussed the concept of age in marine modeling, stated that the age reported is the mean age of a set of particles in a fluid parcel, and defined the age as the mass-weighted, arithmetic average of the ages of the particle considered.

2.5.2.2 Dye release from streams that flow into Wolf Bay

In order to understand how dye/nutrients/pollutants from streams that go into Wolf Bay can be transported over time within the Perdido and Wolf Bay system, three numerical experiments were conducted, and simulated distributions of the age of water (dye) are presented in Fig. 2.8 for three scenarios. These three numerical experiments have the same inflow and open boundary conditions as the first three model runs presented in Fig. 2.7, but the dye or tracer is only released from streams that flow into Wolf Bay (Wolf Creek, Miflin Creek, Owens Bayou, Graham Bayou and Hammock Creek). Results presented in Fig. 2.8a, 2.8b, and 2.8c are from model runs under observed water levels at the open boundaries (the Gulf of Mexico, GIWW, and Dolphin Pass, Fig. 2.2).

For 2-year inflows (Fig. 2.8a, 2-day increment contours), it was found that the dye released into Wolf Bay does not reach most parts of Perdido Bay. This indicates that the 2-year inflows from the rivers into Perdido Bay are much larger compared to the tidal flows from the Gulf through Perdido Pass.

For the experiment with low inflows (7Q10) from all the streams, the dye is projected to appear in the lower, middle and upper Perdido Bay. This is because under the low inflow scenario, the tides from the Gulf are driving forces that control the fate and transport of the contaminants in the system. Therefore, when freshwater inflows from all streams are small, contaminants that are present in the Wolf Bay freshwater sources can reach Perdido Bay. The higher water age values in the upper and middle Perdido Bay indicate that it will take a substantially longer (150 days) time for the materials in Wolf Bay to reach the upstream portion of Perdido Bay. However, higher discharges from the streams of Perdido Bay can flush the materials out of the system.

The dye from streams that flow into Wolf Bay under mean inflows (Fig. 2.8c) can be transported to the Perdido Pass complex quicker than if it was under 7Q10 low inflows (Fig. 2.8b). The lower age of the tracer in the upper Perdido Bay indicates that the tracer from streams in Wolf Bay is transported into the area by tides from the Gulf and then flushed back by inflows from streams in the Perdido Bay watershed (Perdido River and Styx River). The larger age of the tracer in the middle and lower Perdido Bay indicates the existence of a low flushing zone where dynamic interactions between tides from the Gulf and inflows from streams in the Perdido Bay watershed are strong and complex. Therefore, in the middle and lower Perdido Bay, there are some tracers with a relatively larger age, as a result of flow recirculation due to the complex interactions and some relatively new tracers from Wolf Bay, but the mean age of all particles in a water parcel is larger than that in the upper Perdido Bay.

2.6 Model Application under Projected Sea Level Rises

2.6.1 Projection of Sea Level Rises

Emissions of greenhouse gases are causing global warming, resulting in glacier melting and sea level rise (Bhuiyan and Dutta 2012). As the sea level rises, the interaction between the freshwater and saltwater increases, and the saltwater intrusion can play a more dominant and pivotal role in the estuary. Thus, it can cause various restoration issues and threats to humans and species residing in the estuary. Therefore, analysis and understanding of the response of an estuary such as the Perdido and Wolf Bay system to sea level rise is essential in order to keep the estuary safe and productive.

Various researchers have studied the projection of sea level rise and its associated causes. In this paper, we have used the procedure proposed by Titus and Narayanan (1995) for the US EPA:

$$Local(t) = Normalized(t) + (t - 1990) \times Trend \quad (2.14)$$

where *t* is the year after 1990, *Normalized(t)* is the normalized projection of the sea level rise at year *t* if current trends simply continue, and *Trend* is the historic rate of sea level rise derived from observations at the site. In this study, 1990 was replaced by 2008 in Eq. (2.14), because the base model run used observed water surface elevations at the Gulf of Mexico in 2008 and 2009. The procedure (Titus and Narayanan 1995) estimates sea level rise by extrapolating all trends other than those due to global warming; this avoids counting the portion of the historical trend caused by global warming twice.

The *trend* of 2.4 mm/year (Titus and Narayanan 1995), measured at Pensacola, Florida, the closest station where the *Trend* was measured, was used to study the impact of sea level rise on the Perdido and Wolf Bay system. The median and 1% high normalized projections of the sea level rise at Pensacola are 0.10 and 0.35 m in 2050 and 0.25 and 0.92 m in 2100, respectively. Therefore, projected sea level rise in 2100 is 0.47 m (1.54 feet) and has a one percent chance of exceeding 1.14 m (3.74 feet). Similarly, projected sea level rise in 2050 is 0.2 m (0.66 feet) and has a one percent chance of exceeding 0.45 m (1.48 feet).

2.6.2 Projected Salinity Distributions under Sea Level Rise Scenarios

To understand the impact of sea level rise on salinity in Perdido Bay and Wolf Bay, the EFDC simulation runs were performed under two sea level rise scenarios: predicted sea level rise in 2050 and in 2100. The base run is the EFDC run with measured sea level

elevations at the model boundaries and observed atmospheric conditions from 2008 to 2009. All simulation runs were performed from Julian day 260 (September 17) to Julian day 560 (July 14) because of available data for the base run. For the 2050 and 2100 scenario runs, projected water surface elevations at the open boundaries (the Gulf of Mexico, Dolphin Pass, and GIWW, Fig. 2.1) were the observed elevations of the base run increased by 0.2 m and 0.47 m, respectively. Other boundary conditions were the same as the base run.

Fig. 2.9 shows the time series plots of mass-weighted salinities in three areas (the upper Perdido Bay, the middle Perdido Bay, and Wolf Bay) for the base run, the 2050 scenario, and the 2100 scenario. The mass-weighted salinity refers to the average salinity for all cells in a selected area, such as Wolf Bay. The upper Perdido Bay is the area north of the US Hwy 98 Bridge (Fig. 2.2), and the middle Perdido Bay is the area between the US Highway 98 Bridge and the DuPont Point (Fig. 2.2). The mass-weighted salinity in an area, as opposed to the salinity in single cells, provides the overall and representative characteristic in the area. The sea level rise scenarios project a higher impact on salinity in the upper Perdido Bay, a lower impact in the middle Perdido Bay, and almost no impact in Wolf Bay. For the 2050 and 2100 sea level rise scenarios, the average increases of salinity from the base conditions are projected to be 1.3 and 2.7 ppt in the upper Perdido Bay, 1.0 and 2.1 ppt in the middle Perdido Bay, 0.3 and 0.6 ppt in Wolf Bay, respectively. The maximum projected increase in salinity is 4.3 ppt and occurs in the upper Perdido Bay. In the middle Perdido Bay, the impact of sea level rise is also distinct; however, it has more temporal fluctuations, thereby showing the effect of tides at the open boundaries. Wolf Bay is least impacted by the sea level rise, meaning that the sea

level rise at the boundaries will have minimum impact in Wolf Bay in terms of salinity. The flow from the Gulf of Mexico boundary is the main contributor to the salinity increase in Perdido Bay.

In Fig. 2.9, from Julian day 452 to 482 days, the salinity in the upper Perdido Bay is almost the same for all three scenarios. From Julian day 452 (March 27) to 462 (April 6), the average inflow from the Perdido watershed is 263.3 m^3/s (the peak discharge is 631.4 m^3/s and occurs on March 29), and these high inflows are projected to flush or push the saline water towards the downstream direction, thereby replacing the saline water with the freshwater. However, during the same period, there are some increases in salinity in the middle Perdido Bay due to the projected sea level rises. This is because inflow momentum diminishes in the middle Perdido Bay.

2.6.3 Projected Age Distributions under Sea Level Rise Scenarios

To understand the impact of projected sea level rises on the age of water, three numerical experiments for three inflow scenarios presented in Figs. 2.8a, 2.8b, and 2.8c were conducted under the 2050 and 2100 sea level rise scenarios. Projected distributions of the age of water (dye) for the 2100 scenario are presented in Figs. 2.8d, 2.8e, and 2.8f for easy comparison. For the results in Fig. 2.8, the dye or tracer is only released from streams flowing into Wolf Bay.

Under 2-year high inflow conditions, the dye distribution projected under the 2100 sea level rise scenario at the open boundaries (Fig. 2.8d) is almost the same as that under the historic sea level conditions (Fig. 2.8a). The large inflows into Perdido Bay have a higher momentum and push the water towards the lower Perdido Bay (Fig. 2.2)

against tidal flow. As a result, large inflows prohibit the dye from Wolf Bay from entering into Perdido Bay (only a small portion of the lower Perdido Bay appears to have the dye/tracer) under both historic and projected sea level rise conditions.

Projected change on the water age (2100 – Past) shown in Fig. 2.10 is the difference of the water age between projected under the 2100 sea level rise scenario at the open boundaries (Fig. 2.8d, 2.8e, and 2.8f) and simulated under the historic (past) sea level conditions (Fig. 2.8a, 2.8b, and 2.8c). Under 2-year high inflow conditions, projected change on the water age is less than 10 days (Fig. 2.10a, 2-day increment contours) with increase occurring only in a small part of the lower Perdido Bay. This increase of water age indicates that the dye is projected to travel a little further upstream under the 2100 sea level rise scenario (Fig. 2.8d) in comparison to under the historical sea level conditions (Fig. 2.8a).

Under low inflow (7Q10) conditions from all the streams, the dye is projected to reach the lower Perdido Bay relatively faster (30-90 days, Fig. 2.8e) under the 2100 sea level rise scenario in comparison to under the historic sea level conditions (Fig. 2.8b). However, the age projected in some areas of the middle and upper Perdido Bay is much higher (130–160 days), indicating a complex interaction between increased tidal flow due to sea level rises and freshwater inflows from upstream watersheds of Perdido Bay. It is projected to take about 50–60 more days for the dye to reach those areas (Fig. 2.10b) under the 2100 scenario in comparison to under historic conditions. The trapping or circulation of some dye during the interaction of flows from the rivers and the open boundaries is the reason why the age is large in those areas. In the areas near freshwater rivers flowing into Perdido Bay, the negative values of the age difference (Fig. 2.10b)

indicate that the dye is projected to reach those areas faster under the 2100 scenario in comparison to under the historic sea level conditions (2008–2009) and under the 7Q10 low inflow conditions. Overall, the model simulation under the 2100 scenario helped us identify the complex dynamics of the system and the momentum, which is increased from the tidal boundaries and pushes the water towards the upstream portion of Perdido Bay.

Projected age distributions for mean inflow conditions (Fig. 2.8f, 5-day increment contours) have a similar spatial pattern under the 2100 sea level rise scenario at the open boundaries in comparison to under the historic sea level conditions (Fig. 2.8c). The age of water is projected to increase by 5–10 days for large portions of the middle and upper Perdido Bay. However, in the headwater areas near Perdido Bay, the age is projected to increase by up to 20 days for mean inflow conditions under the 2100 scenario (Fig. 2.10c).

2.7 Conclusions

A three-dimensional hydrodynamic EFDC model was developed for the Perdido and Wolf Bay system and calibrated against observed water level, salinity, and temperature measurements at several monitoring stations with good agreement. The Perdido EFDC model was applied to understand the response of the system to different inflow conditions and sea level rise scenarios. The major findings of the study are as follows:

a. The Perdido EFDC model developed for the study is able to model and predict the spatial and temporal distributions of flow and salinity in the estuary that has flow contribution from several natural and urban streams and tidal influences from the Gulf of Mexico.

b. The age of water as an auxiliary variable is a useful time-scale parameter to provide insights on transport and mixing dynamics of a tracer or pollutant in an estuary. Its application to the Perdido and Wolf Bay system reveals complex interaction between various forcing factors, such as inflows from upstream rivers and tides from the Gulf.

c. The numerical experiments performed to study the age of water in the system indicated that it would take about 60 days for the substances that are discharged into the system to completely flush out of the system under historic mean (from 1998 to 2010 data) and 2008–2009 inflow conditions. Under 2-year high inflow conditions, simulated age of water is significantly less (about 14 days). Under 7Q10 low inflow conditions, simulated age of water is up to 140 days (more than 3 months); therefore, any pollutant that enters into the system under low inflows can stay in the system for a long period of time. Nutrients flowing into the system can lead to algal blooms and local eutrophication, because the interaction between low inflows and tides from the Gulf forces nutrients to stay in the estuary.

d. Under projected sea level rises in 2050 and 2100, salinity in the upper Perdido Bay is projected to increase up to 4.3 ppt, and the projected change on the age of water is less than 10 days in Perdido Bay under high inflows (2-year return period) and up to 60 days under low inflows (7Q10). Projected impact on salinity and the age of water in Wolf Bay due to sea level rise is small and not significant.

The common pollution problems that estuaries face are over-enrichment of nutrients, pathogen contamination, toxic chemicals, and alteration of freshwater inflow. The age of water study performed for the Perdido and Wolf Bay system gives water

quality managers a good idea about residence time, the time that pollutants remain in a waterbody before they are completely flushed out. The study of the impact of sea level rise on salinity and the age of water provides valuable information for developing management strategies. A future study that investigates impacts of tsunamis and hurricanes on salinity and the age of water in the Perdido and Wolf Bay system will give a better understanding on the influences of extreme events to the system.

Table 2.1 Observed and modeled tidal amplitude (m) and phase (hr) of harmonic constituents of surface water elevations at the Blue Angels Park

Constituent	Amplitude (m)		Phase (hr)	
	Observed	Modeled	Observed	Modeled
M2	0.007	0.006	6.6	6.7
S2	0.004	0.005	2.2	3.3
N2	0.001	0.000	12.3	1.5
K2	0.002	0.002	7.0	7.3
K1	0.082	0.084	0.1	0.8
O1	0.082	0.070	15.7	16.8
P1	0.018	0.012	2.8	5.2

Table 2.2 Observed and modeled surface means of salinities (ppt) in 2008–2009 and error parameters at nine monitoring stations (Fig. 2.1)

Station (Fig. 2.1)	**Observed Mean (ppt)**	**Modeled Mean (ppt)**	**R^2**	**RMSE [1] (ppt)**	**Number of observed data**
Kee Avenue	8.6	9.2	0.84	2.3	22
Spanish Cove	8.9	10.0	0.79	2.4	23
Bear Point	16.2	14.9	0.77	2.5	16
33010G10	15.1	13.9	0.83	2.6	39
04012041	15.7	14.8	0.72	2.7	12
04012042	14.7	14.4	0.64	3.0	12
33010C14	8.6	7.9	0.53	3.9	29
04012032	18.7	15.6	0.65	4.4	10
04012020	11.6	8.7	0.48	5.0	9

[1] *RMSE stands for the root mean squared error.*

Table 2.3 Observed and modeled means of surface water temperatures in 2008-2009 and error parameters calculated at six monitoring stations (Fig. 2.1)

Station	**Observed Mean**	**Modeled Mean (ºC)**	**NSE**	**R^2**	**RMSE (ºC)**	**Number of observed data**
04012032	21.8	22.3	0.92	0.94	1.6	10
04012041	20.9	21.5	0.84	0.87	2.1	13
04012042	21.0	20.5	0.83	0.89	2.1	12
33010G10	19.0	19.7	0.64	0.84	2.5	37
33010C14	17.2	17.6	0.74	0.76	2.7	27
04012020	22.1	20.2	0.75	0.92	2.9	9

Table 2.4 A summary of inflow conditions and dye release locations used in the model scenario simulations

Simulation	Flow	Dye Release Locations
Case 1	2008-2009 inflows	All streams
Case 2	2-year inflows (high inflows)	All streams
Case 3	Mean inflows	All streams
Case 4	7Q10 inflows (low inflows)	All streams
Case 5	2008-2009 inflows	Wolf , Miflin, Owens, Graham, Hammock
Case 6	2-year inflows	Wolf , Miflin, Owens, Graham, Hammock
Case 7	Mean inflows	Wolf , Miflin, Owens, Graham, Hammock
Case 8	7Q10 inflows (low inflows)	Wolf , Miflin, Owens, Graham, Hammock

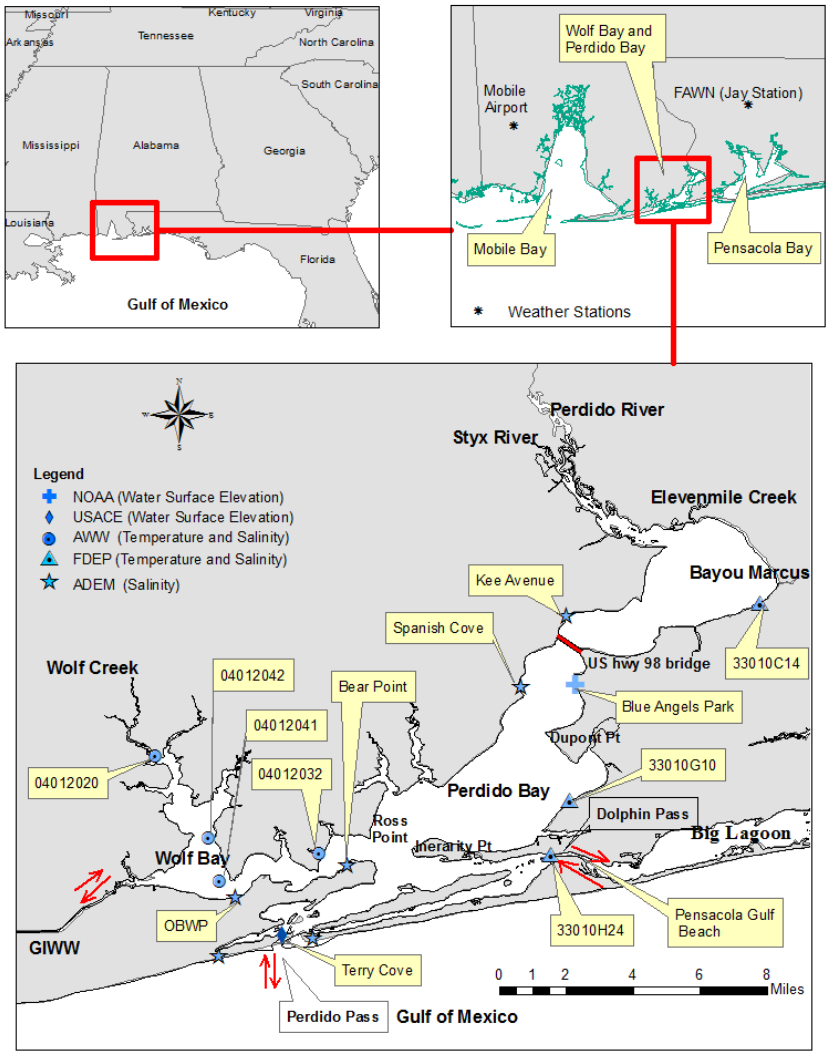

Fig. 2.1 Geographical location of Wolf Bay and Perdido Bay showing the monitoring stations managed by Alabama Department of Environment Management (ADEM), Florida Department of Environmental Protection (FDEP), National Oceanic and Atmospheric Administration (NOAA), and Alabama Water Watch (AWW). GIWW stands for the Gulf Intracoastal Waterway, and the two weather stations used are shown

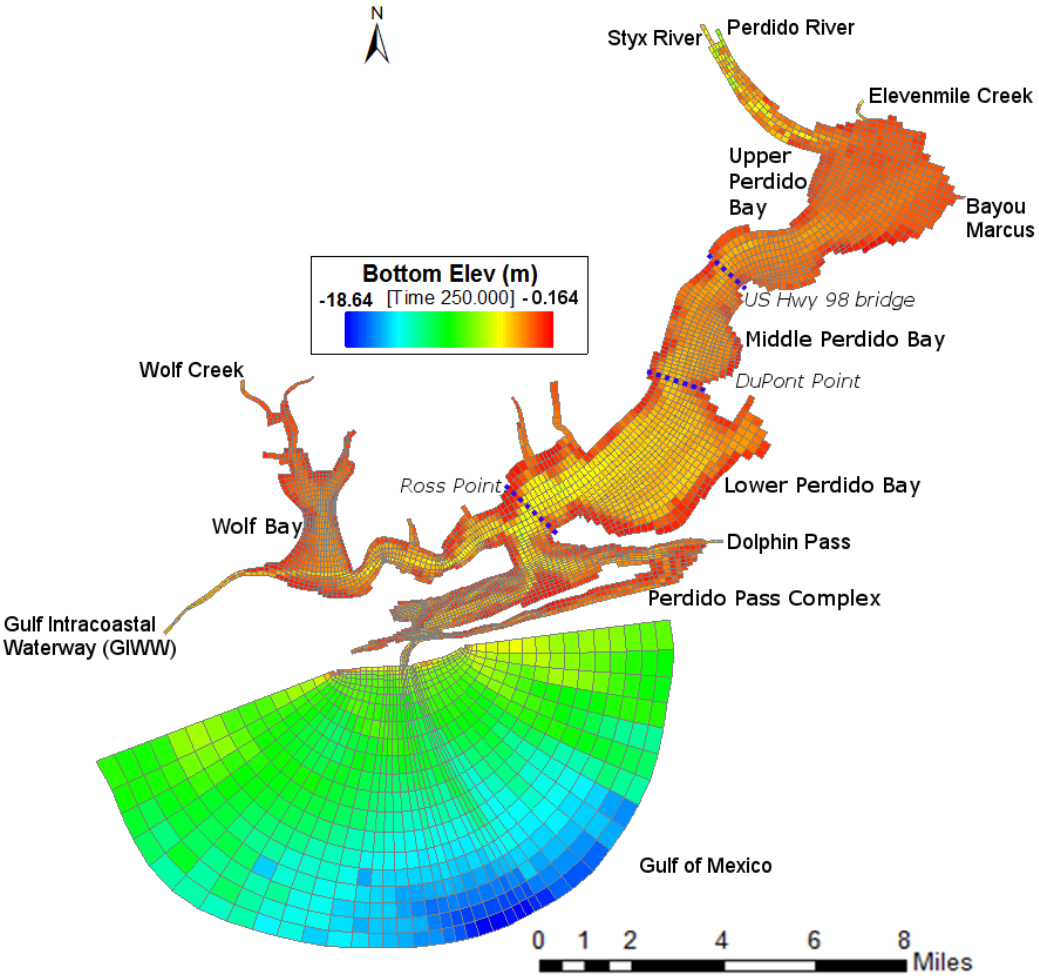

Fig. 2.2 EFDC computational grid system showing bathymetry (bottom elevation in m below mean sea level) of Wolf Bay, Perdido Bay, and a portion of the Gulf of Mexico

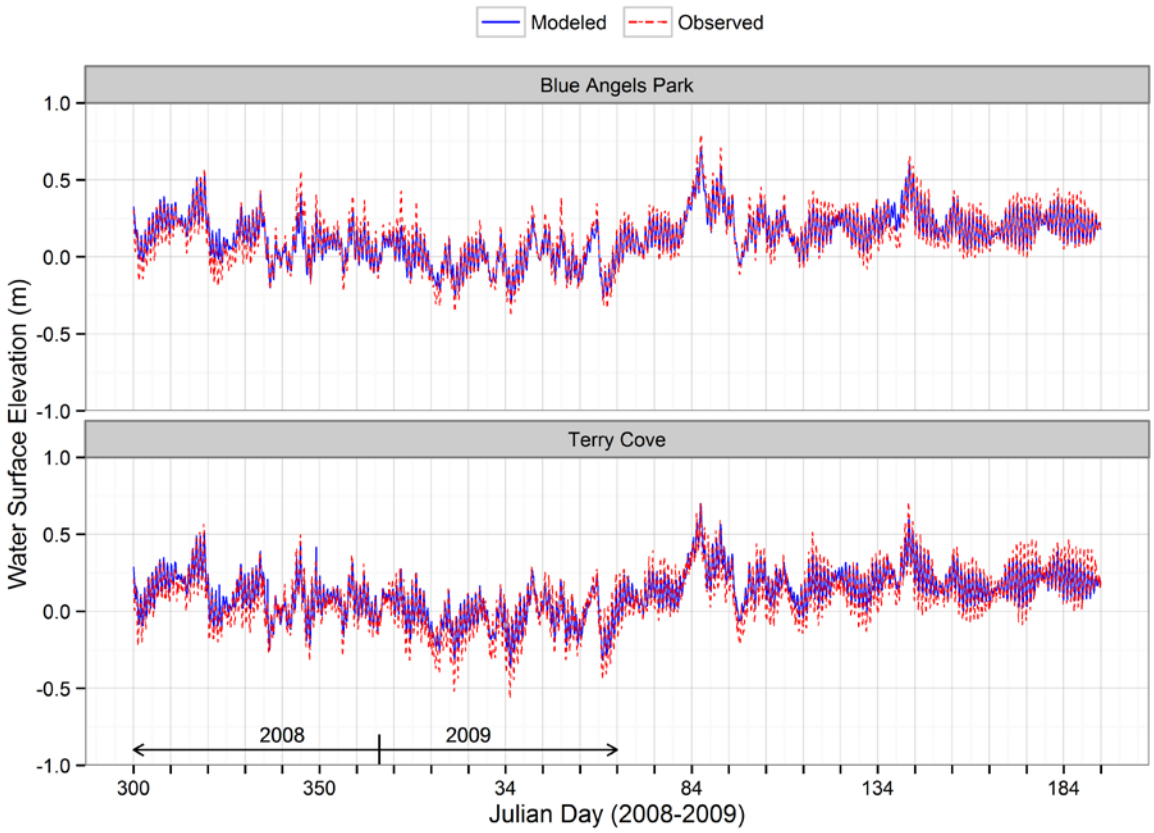

Fig. 2.3 Measured and observed water levels at the Blue Angels Park and Terry Cove monitoring stations for the model calibration run

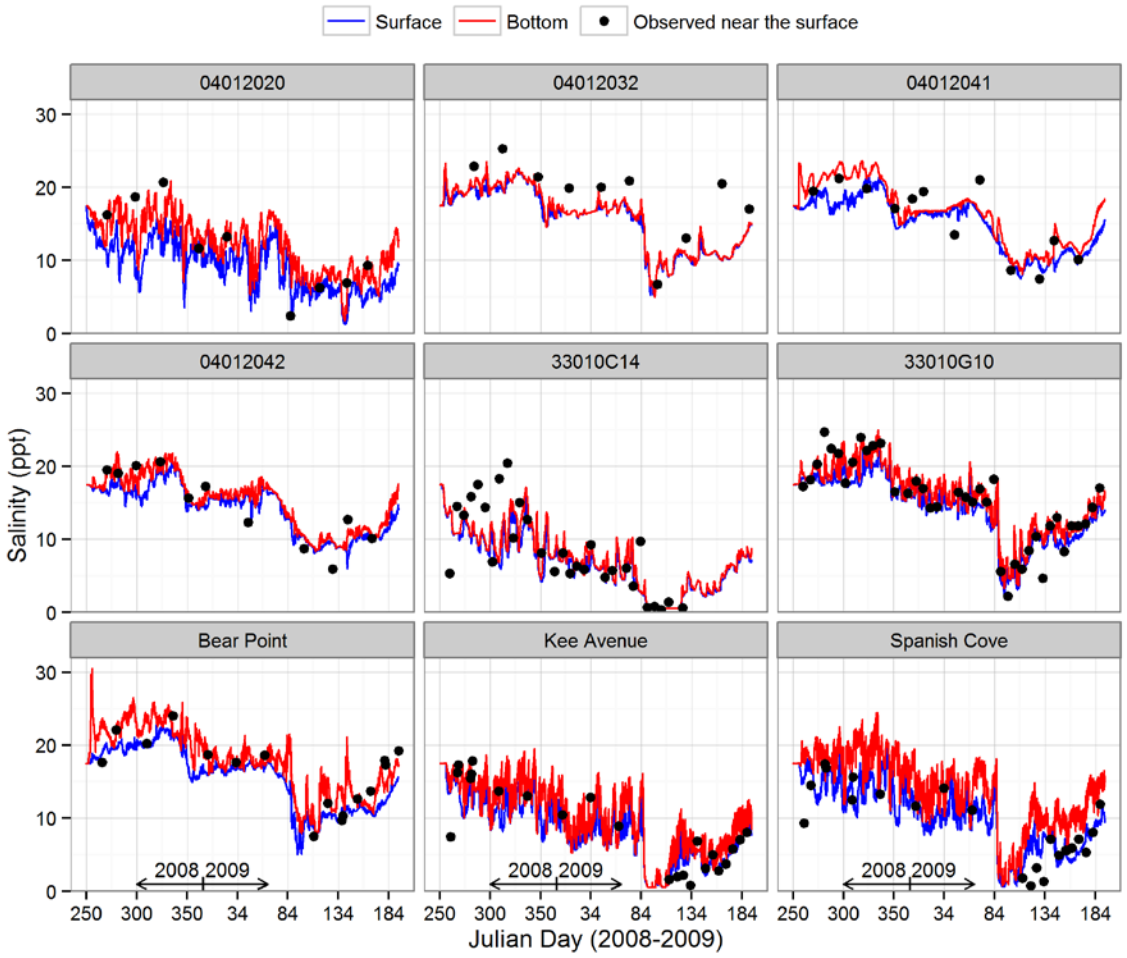

Fig. 2.4 Time-series plots of modeled surface and bottom salinities (lines) against observed salinities (dots) near the surface at nine monitoring stations in Wolf Bay and Perdido Bay

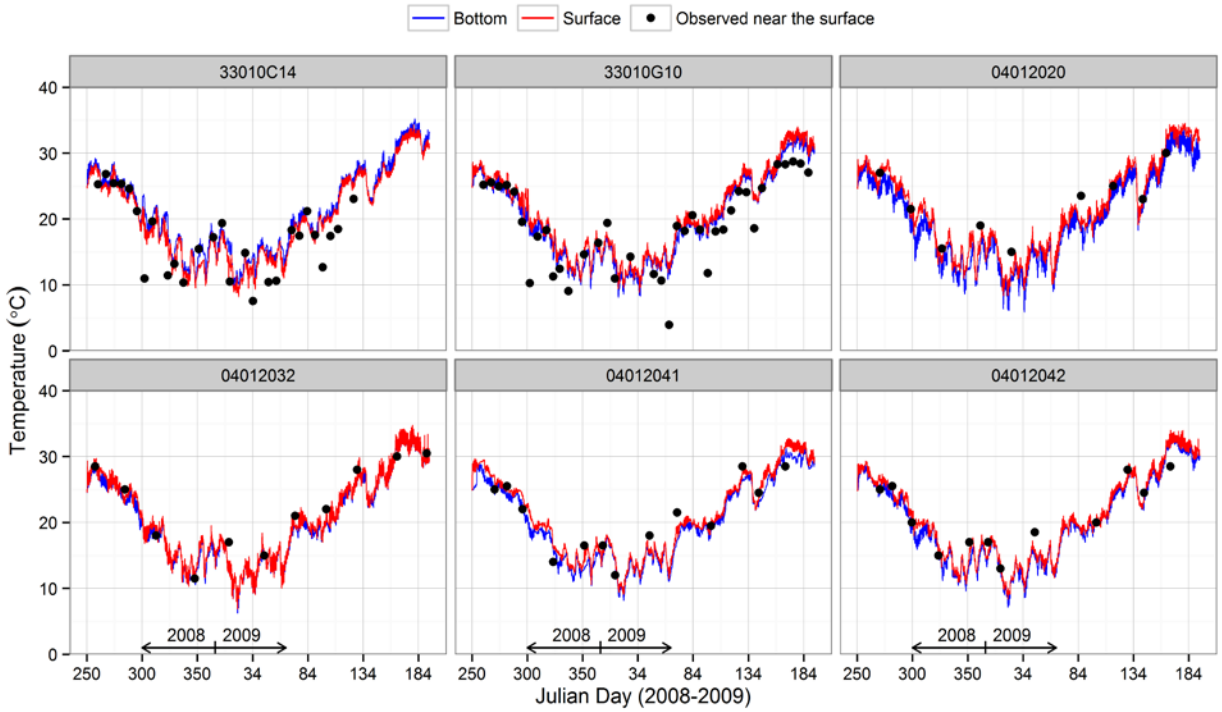

Fig. 2.5 Time-series plots of modeled surface and bottom water temperatures (lines) against observed surface temperatures (dots) at six monitoring stations (Fig. 2.1) in Wolf Bay and Perdido Bay

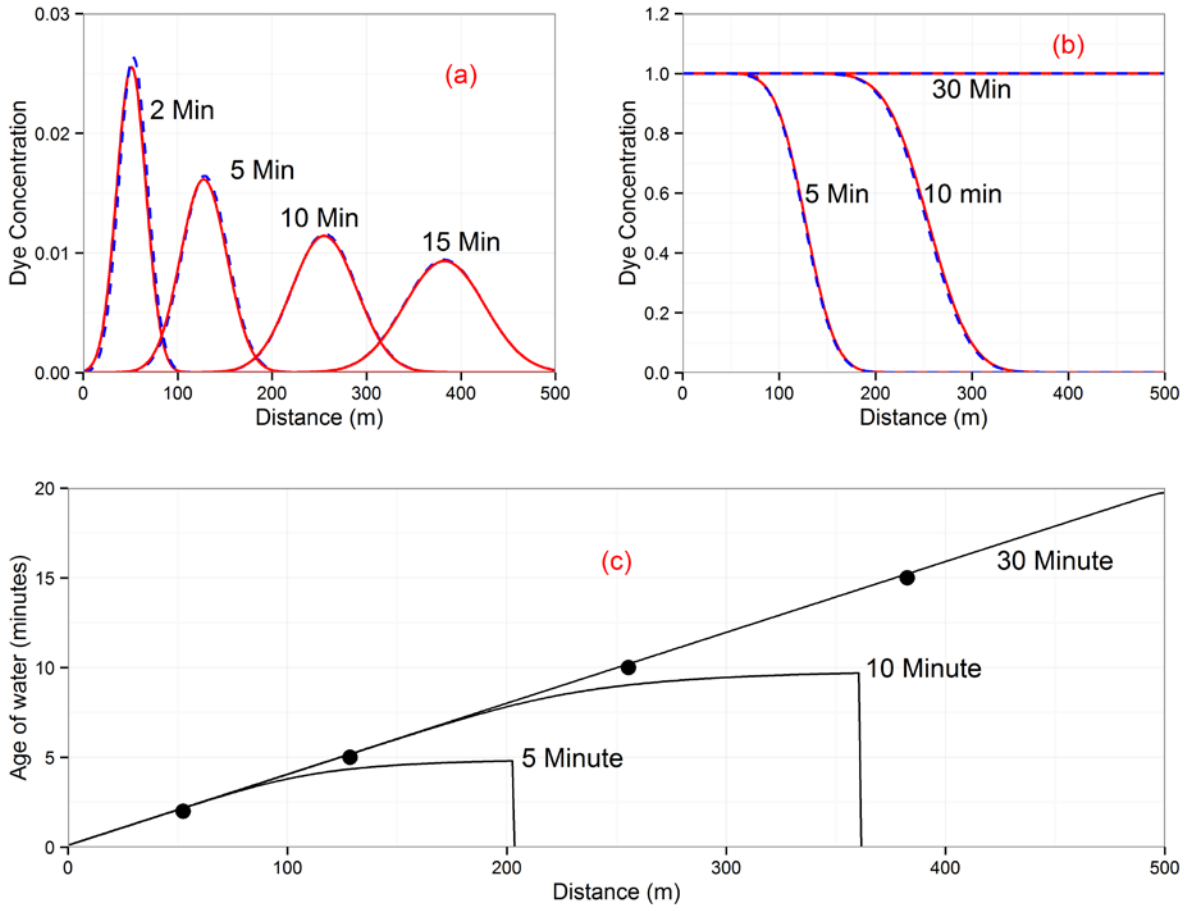

Fig. 2.6 Simulated dye concentrations plotted with analytical solutions for two idealized advection-diffusion experiments: (a) pulse dye release (b) continuous dye release. Age of water profiles calculated from the EFDC model at t = 5 min, 10 min, and 30 min for continuous release are given in (c) as solid lines, and the dots from left to right represent the age of dye calculated from the instantaneous pulse release at t = 2 min, 5 min, 10 min, and 15 min, respectively

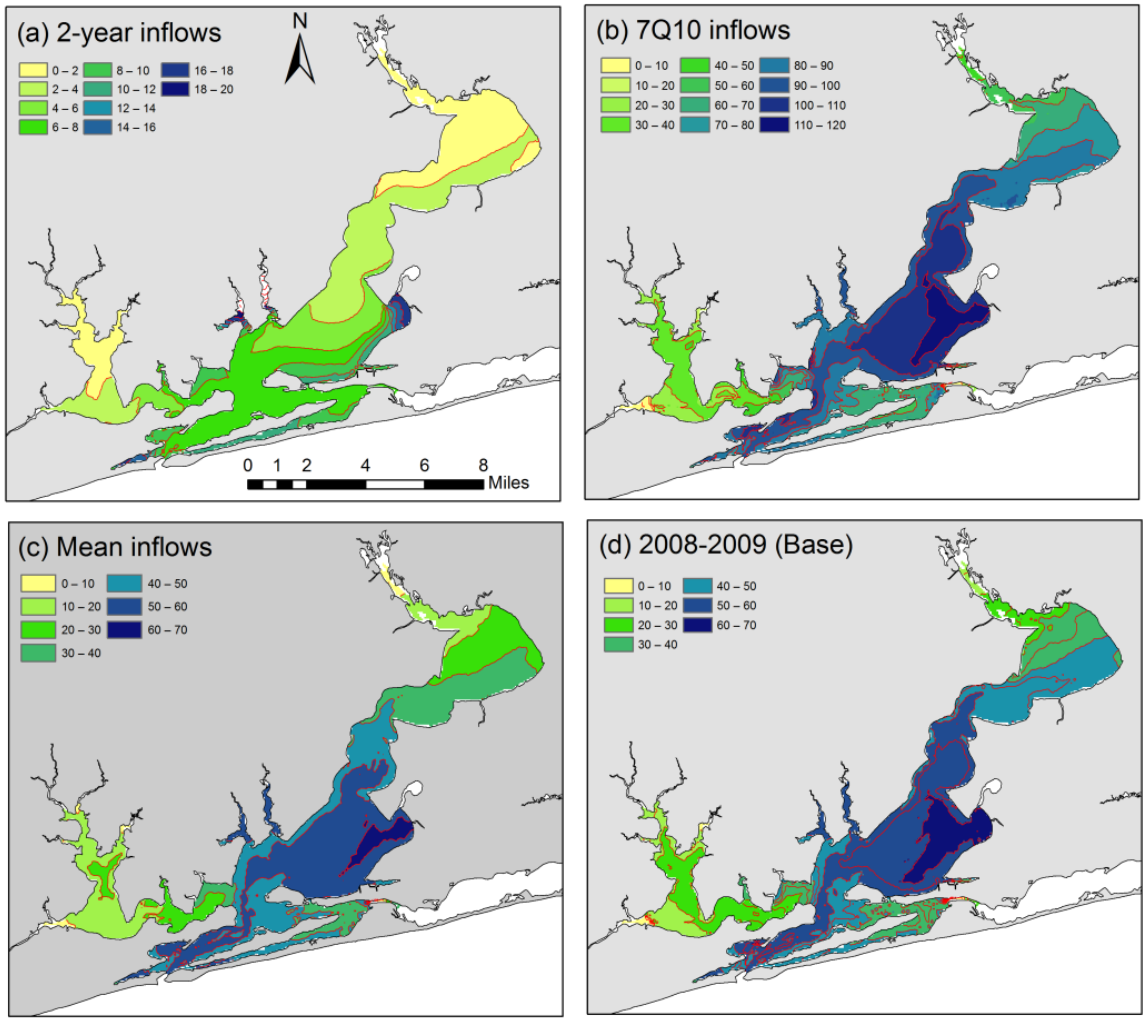

Fig. 2.7 Simulated age distributions in the Perdido and Wolf Bay system from all freshwater streams with constant tracer releases using (a) 2-year inflows, (b) 7Q10 low inflows, (c) mean inflows from 1998 to 2010, and (d) measured or SWAT simulated inflows in 2008–2009

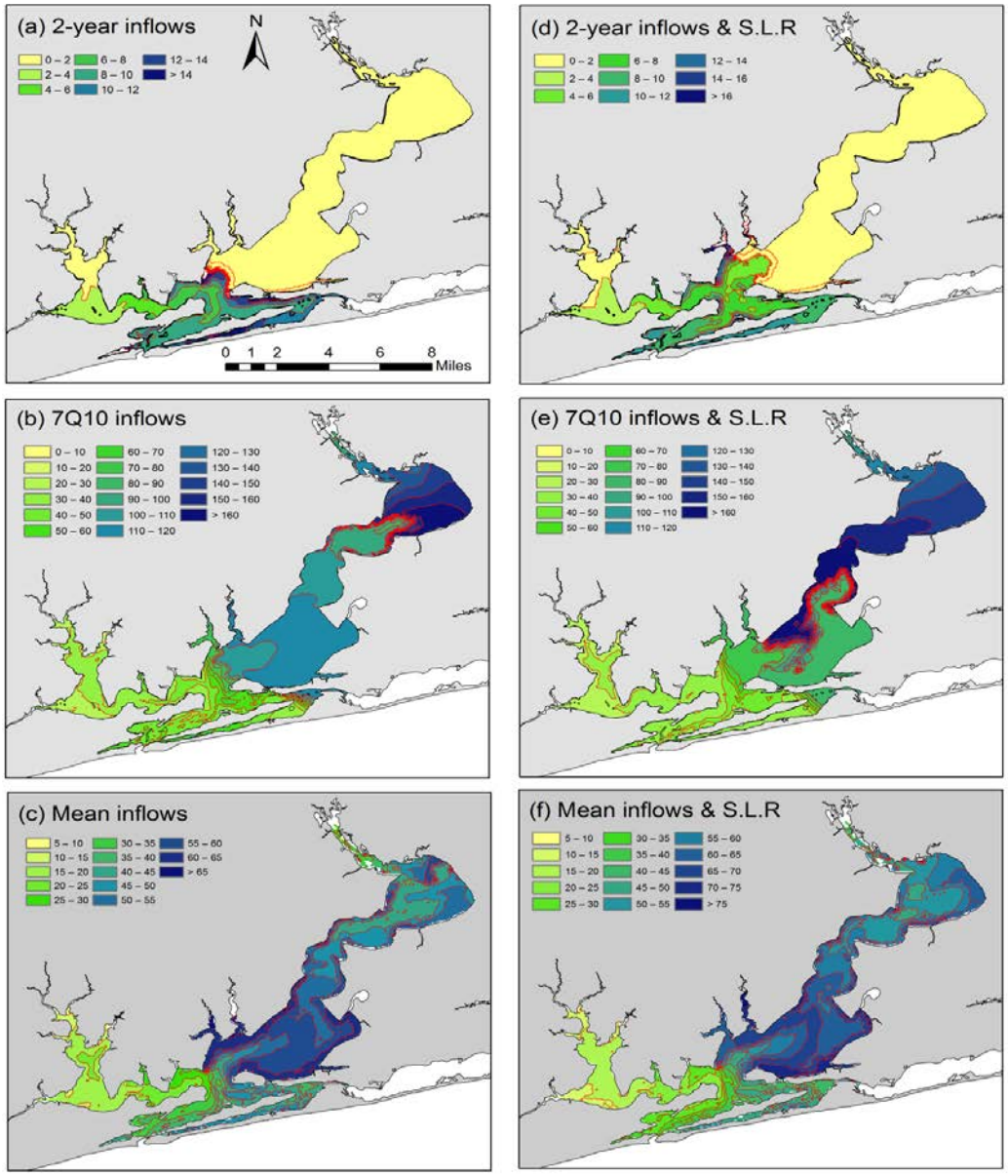

Fig. 2.8 Simulated age distributions in Wolf Bay and Perdido Bay when tracer is released only from streams in Wolf Bay watershed using (a) and (d) 2-year inflows, (b) and (e) 7Q10 low inflows, (c) and (f) mean inflows (1998–2010). Fig. 2.8a, 2.8b, and 2.8c were simulated under observed water levels, and Fig. 2.8d, 2.8e, and 2.8f are projected under the 2100 sea level rise (S.L.R.) scenario at the open boundaries (the Gulf, GIWW, and Dolphin Pass, Fig. 2.2)

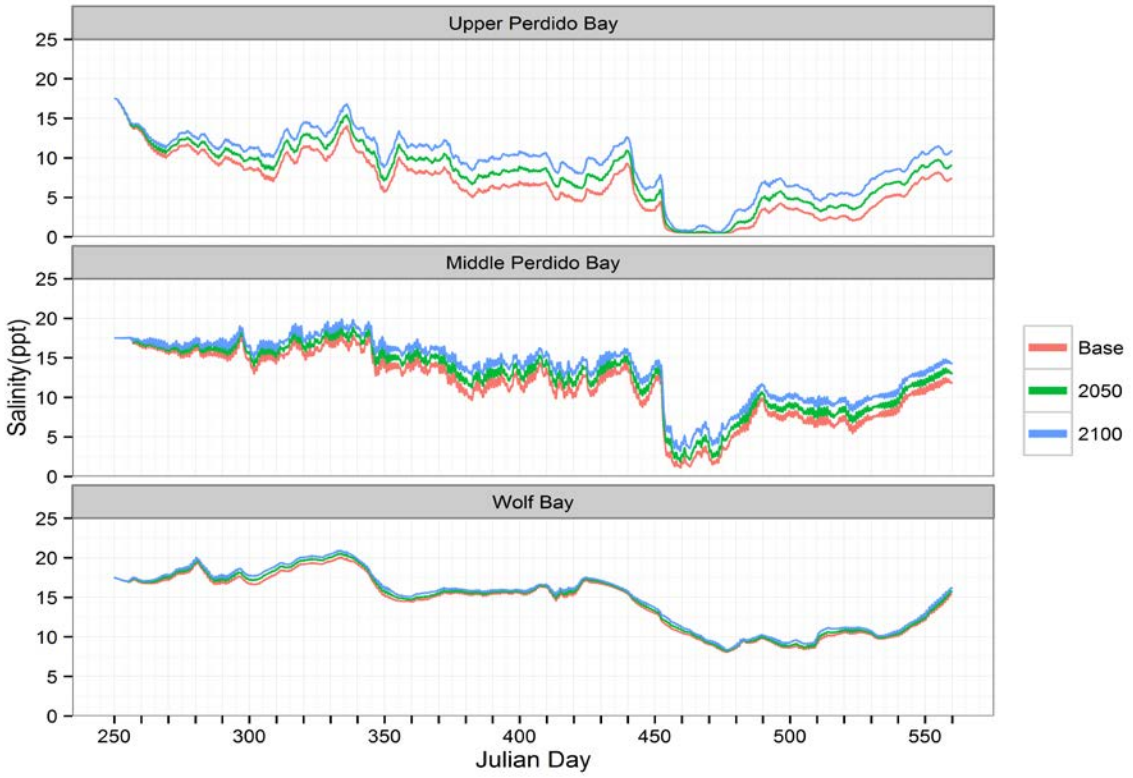

Fig. 2.9 Time series plots of mass-weighted salinities in the upper Perdido Bay, middle Perdido Bay, and Wolf Bay under the base run (2008 observed sea level) and the 2050 and 2100 sea level rise scenarios

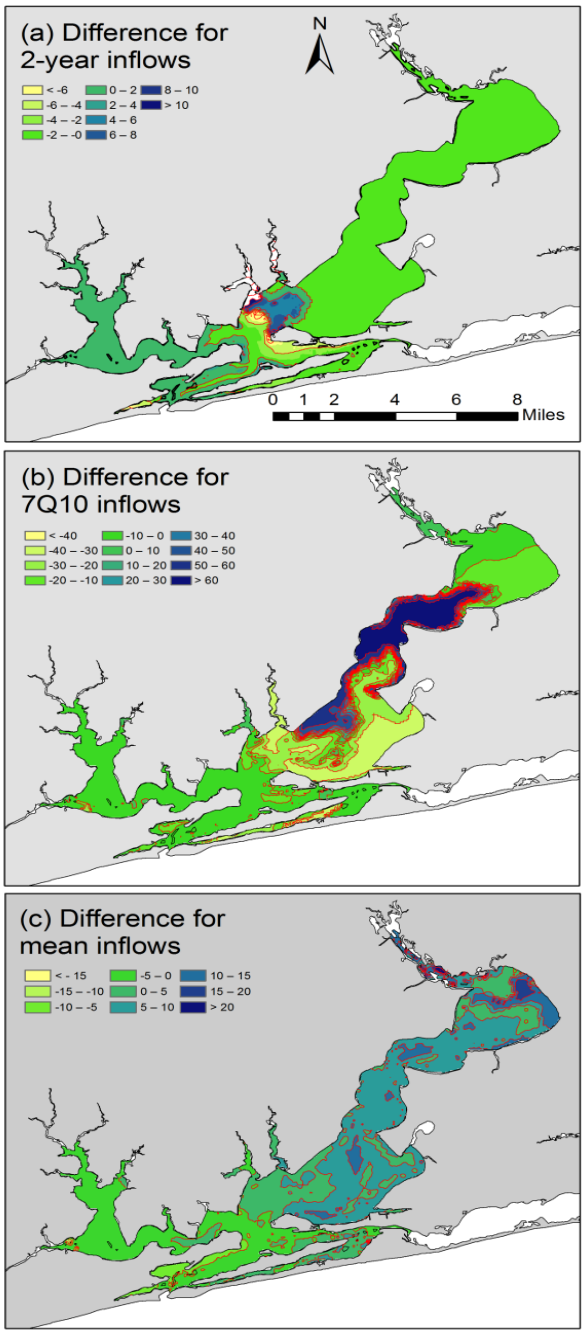

Fig. 2.10 Projected change on the age (2100 – Past) in Wolf Bay and Perdido Bay when tracer is released only from streams in Wolf Bay watershed for (a) 2-year inflows, (b) 7Q10 low inflows, and (c) mean inflows from 1998 to 2010

Chapter 3. Quantification of Water and Salt Exchanges in Perdido Bay and Wolf Bay system

3.1 Abstract

A calibrated three-dimensional hydrodynamic model was applied to the Perdido Bay and Wolf Bay system to study subtidal water and salt exchanges at various cross sections using the Eulerian and isohaline flux methods. Salt fluxes at Perdido Pass and Dolphin Pass were dominated by tidal oscillatory transport F_T whereas shear dispersive transport F_E was dominant at Perdido Pass complex, the Wolf-Perdido canal, and the lower Perdido Bay. The flow rate Q_F and salt transport rate F_S varied greatly in response to complex interactions between discharges from upstream rivers and tidal boundaries. Q_F and F_S ranged from -619 $m^3 s^{-1}$ (seaward) to 179 $m^3 s^{-1}$ (landward) and -13,480–6,289 kg s^{-1} at Perdido Pass when river discharges ranged 11.0–762.5 $m^3 s^{-1}$ in the 2008–2009 simulation period. Using the isohaline method, incoming (landward)/outgoing (seaward) flow rates from Perdido Pass were calculated and ranged from 0–210 and 0–619 $m^3 s^{-1}$ (averages of 83.6 and 131.1 $m^3 s^{-1}$). At the lower Perdido Bay, average incoming and outgoing salinity were 23.2 and 18.2 psu, respectively, with an average salinity stratification of 6.2 psu between surface and bottom layers. The decrease in salinity of outgoing flows indicated the dilution caused by the river inflows and weaker tidal influence. The isohaline method was robust compared to the Eulerian method because all time-dependent incoming and outgoing transport could be calculated and analyzed

separately (e.g. developing correlations with influencing factors) because different salt classes were used in the calculation of flux and salinity.

3.2 Introduction

Estuaries are extremely productive regions due to high flux of nutrients from the land and serve as breeding and nursery grounds for many species (Neilson and Cronin 1981). The impact of anthropogenic activity on the estuarine environment is a frequent concern because many major cities are located next to estuaries (Kennish 1986). Unfortunately, neither the estuaries nor the coastal ocean are capable of assimilating pollutants indefinitely and the environmental concerns now require that any pollutant released in coastal zone should be heavily regulated and properly managed (Bilgili et al. 2005). In studies of the ecology of tidal estuaries the exchanges of fresh and salt water are of primary importance in determining the characteristics of the environment (Ketchum 1951). Estuarine circulation and salinity distribution patterns are the result of several competing factors: river inflow pushing seaward, denser ocean water sliding landward, and tidal currents stirring and mixing the two (MacCready 2011). The “exchange flow” or “gravitational circulation”, which is characterized by deep inflow (denser salt intrusion in bottom layers) and shallow outflow (seaward freshwater flow in surface layers) through a cross section, dominates circulation in many estuaries (MacCready 2011). Mean circulation and the circulation with frequencies lower than the semidiurnal and diurnal tides are often collectively called the residual circulation (Lewis and Lewis 1983; Jay and Musiak 1996) because they are the residual of a time average over the principal periods.

The velocity and salinity determine the salt transport. The net outflow continually removes salt from the estuary. Generally salt is brought back into the estuary by the "estuarine salt transport", i.e., the vertical and lateral variations of tidally-averaged velocity and salinity; and "tidal dispersion", i.e., the tidal correlations of velocity and salinity (Fischer 1976). The magnitude of salt transport and the processes that contribute it depend on the bathymetry of the estuary and on the strength of the physical forcing (e.g., tides, freshwater inflows, wind, etc.). In strongly stratified estuaries, salt transport is predominantly due to advection by the net landward flow and the estuarine salt transport (Hansen and Rattray Jr 1966). Conversely, in relatively well-mixed estuaries, which are weakly stratified, tidal dispersion plays a larger role in the salt balance (Smith 1980). The stratification of partially stratified estuaries varies between these extremes.

Several methods of determining the flow and salt exchange in estuaries have been formulated and verified successfully by various scientists (Bilgili et al. 2005; MacDonald 2006; Gilcoto et al. 2007; Traynum and Styles 2008; Engqvist and Stenstrom 2009; Valle-Levinson et al. 2009; MacCready 2011; Chen et al. 2012). Ketchum (1951) presented an empirical method that describes the exchange across various cross sections and permits the calculation of the resulting average distribution of fresh and salt water in an estuary. Bilgili et al. (2005) used a Lagrangian particle tracking method embedded within a two-dimensional finite element model, to study the transport and ocean-estuary exchange processes in the relatively well-mixed Great Bay Estuarine System in New Hampshire, USA. Chen et al. (2012) used isohaline coordinate analysis to compare the exchange flow in two contrasting estuaries, the long (with respect to tidal excursion)

Hudson River and the short Merrimack River, using Regional Ocean Modeling System (ROMS).

Understanding the structure and variability of the salinity distribution in an estuary is critical to many ecological and engineering management decisions. The salinity distribution is governed by a balance between seaward advection of salt by river inflows and landward transport of salt by dispersive processes (Montani et al. 1998). These estuary fluxes can be divided into a subtidal component due to residual velocity and salinity and an oscillatory tidal component associated with correlations in velocity and salinity at tidal time scales (Fischer et al. 1979; Uncles and Stephens 1996).

This study uses a previously calibrated Environmental Fluid Dynamic Code (EFDC) model (Devkota et al. 2013) to investigate the flow and salt exchange across various cross sections to understand the underlying transport phenomena and mechanisms in the Perdido Bay and Wolf Bay (PBWB) system (Fig. 3.1). Xia et al. (2011a) used the EFDC model to understand distributions and dynamics of salinity and dissolved oxygen at Perdido Bay and the Gulf of Mexico. Xia et al. (2011b) studied the responses of estuarine plumes near the shoreline of the Gulf of Mexico under different wind conditions. They found that outflow from the estuary to the Gulf were strongest under northerly winds and could be stopped by southerly winds. Xia et al. (2011b) used the EFDC model to understand plume dynamics in the Perdido Bay using idealized sensitivity experiments to examine the influence of wind stress on the three-dimensional plume signatures. Devkota et al. (2013) developed and calibrated an EFDC model for the PBWB system to understand the age of water in the system under different inflows from the rivers flowing into Wolf Bay and Perdido Bay. The PBWB system is connected to

the Gulf of Mexico via three open boundaries (Fig. 3.1): Perdido Pass on the south, Dolphin Pass on the east that is connected to Big Lagoon and eventually to Pensacola Bay, and the Gulf Intracoastal Waterway (GIWW) to the west that is connected to the Mobile Bay and eventually to the Gulf of Mexico.

In this study, we tried to answer the following three flow and salt exchange related questions: 1) How much salt is imported into the Perdido Bay via Perdido Pass connection and how much fresh water is discharged from Perdido Bay to the Gulf of Mexico? 2) What factors are responsible for flow exchanges at different locations? 3) How much salt and water exchange takes place between Wolf Bay and Perdido Bay? In this paper we attempted to answer these questions by using the Eulerian salt decomposition method (Lerczak et al. 2006; MacCready 2011; Kim and Park 2012) and the isohaline salt flux technique (MacCready 2011) with the calibrated EFDC model.

3.3 Materials and Methods

3.3.1 Study Area

The PBWB system (Fig. 3.1) is a shallow to moderately deep inshore body of water that is approximately perpendicular to the Gulf of Mexico and oriented along a northeast-southwest axis (Livingston 2003). The PBWB system has the length of 53.4 km and an average width of 4.2 km. Perdido Bay has an average depth of 2.6 m that increases gradually from the Perdido River mouth via the lower Perdido Bay to the Gulf as indicated by elevation contours in Fig. 3.1. The water depth in Perdido Bay tends to increase southward with the deepest parts of the estuary located at the lower Perdido Bay, i.e., the cross section connecting Ross Point and Innerarity Point (Fig. 3.1). The

dissolved oxygen distribution in Perdido Bay as an indicator of water quality is a function of temperature, depth, salinity concentration, and the level of stratification (Livingston 2003). The major freshwater inflows into Perdido Bay are Perdido River, Styx River, Elevenmile Creek, and Bayou Marcus (Livingston 2003). The Perdido River combined with Styx River provide more than 70% of the freshwater input into the estuary and mean river discharge is 21 $m^3 s^{-1}$ recorded at U.S. Geological Survey (USGS) station at Barrineau Park, Florida (Xia et al. 2011b; Devkota et al. 2013). Perdido Pass is the primary pathway of salt water to Perdido Bay and controls salinity distributions in Perdido Bay (Livingston 2003). The U.S Army Corps of Engineers (USCOE) maintains the Perdido Pass navigation channel as part of the GIWW (USACE 1976; Livingston 2003). The width of Perdido Pass ranges from 200 to 500 m, and depth is around 5 m. The diurnal tidal range at Perdido Pass is about 0.2 m (Xia et al. 2011a; Devkota et al. 2013). The filtered water surface elevations at three open boundaries (GIWW, the Gulf of Mexico, and Big Lagoon, Table 3.1) have similar statistical characteristics during the calibration period. Wolf Bay is a sub-estuary of Perdido Bay with a connection of GIWW (Fig. 3.1) and has a contributing watershed area of 126 km^2 (Wang and Kalin 2011). The rivers that flow into Wolf Bay are Wolf Creek, Miflin Creek, Owens Bayou, Graham Bayou, and Hammock Creek, and combined flow into Wolf Bay ranged from 0.95 to 15.37 $m^3 s^{-1}$ with mean flow of 1.95 $m^3 s^{-1}$, which are very small in comparison to flows to Perdido Bay (Table 3.1). Wolf Bay and its surrounding waters are the most pristine estuarine waters in Alabama, granted 'Outstanding Alabama Water' status by the Alabama Department of Environmental Management in April, 2007 (Wang et al. 2013). Water in Wolf Bay flows through GIWW into either Perdido Bay or Mobile Bay,

depending on the moon, wind, and tide, and ultimately into the Gulf of Mexico (Beasley 2010).

3.3.2 Hydrodynamic Model

The calibrated EFDC model used for this study was developed by Devkota et al. (2013) for the PBWB system, called Perdido EFDC model. EFDC is a three-dimensional hydrodynamic model that solves continuity, momentum, salt and heat transport equations with hydrostatic and Boussinesq approximations. EFDC uses orthogonal curvilinear or Cartesian horizontal coordinates and a stretched sigma vertical coordinate. One of the unique features in the numerical solution of EFDC is an internal-external mode splitting for the momentum equation. EFDC solves both modes at the same time step by solving the external mode semi-implicitly with respect to barotropic pressure gradient term in depth-averaged momentum equations, which allows large time steps and facilitates the wetting and drying scheme (Hamrick 1992b; Hamrick and Mills 2000; Park et al. 2005). The Mellor and Yamada level 2.5 turbulence closure scheme is implemented in the model (Mellor and Yamada 1982; Galperin et al. 1988a). The EFDC model simulates density and topographically-induced circulation, tidal and wind-driven flows, and spatial and temporal distributions of salinity, and temperature (Hamrick 1992b; Gong et al. 2009). The Perdido EFDC model has a total of 4,878 curvilinear horizontal grids and 4 uniform spacing vertical sigma layers. The grid sizes for the model ranged from 27 m to 368 m and layer thicknesses ranged from 0.04 m to 1.78 m in the PBWP system (not including the small portion of the Gulf). The details of the model configurations are presented by Devkota et al. (2013).

Upstream boundaries for the Perdido EFDC model include inflows from the four rivers into Perdido Bay and the five streams into Wolf Bay (Devkota et al. 2013). The mean and maximum discharges from the rivers into Perdido Bay from 2005–2010 are 37.5 $m^3 s^{-1}$ and 801 $m^3 s^{-1}$, respectively. During the simulation period (2008–2009) of this study, the mean and maximum inflow rates from the rivers are 38.8 $m^3 s^{-1}$ and 762.45 $m^3 s^{-1}$ (Table 3.1), respectively. The maximum discharge during 2008–2009 was 95% of the maximum discharge from 2005–2010. Overall, the discharges from upstream rivers during the calibration period 2008–2009 represent the typical flows, which resulted from typical rainfall in 2008 and 2009 (49.84 inches in dry 2008 and 91.40 inches in wet 2009). The average annual rainfall from 2005–2010 was 58.4 inches. Wind speed plays an important role in Wolf Bay and Perdido Bay and ranged from 0 to 11.5 m s^{-1} with an average value of 2.9 m s^{-1} during the simulation period (2008–2009). The dominant winds during simulation periods are northerly, southerly and northeasterly winds. Southerly winds tend to push the water into the system via Perdido Pass whereas northerly and northeasterly winds push water out of the Bay. From 2002-2009 the wind speed varied from 0 to 27.7 m s^{-1} with an average value of 2.8 m s^{-1}.

3.3.3 Theoretical Formulation for Eulerian Decomposition Method

Eulerian decomposition approach can be used to study the salt flux in tidal rivers and estuaries and has been successfully used to predict the estuarine exchange (Lerczak et al. 2006; MacCready 2011; Chen et al. 2012; Kim and Park 2012). In this approach, the tidally averaged (subtidal) salt flux (F_S) through an estuarine cross section is decomposed into river flux (F_R), exchange flow flux (F_E), and tidal flux (F_T). The equation to

compute the subtidal salt flux F_S (mass flow rate in kg s^{-1}) are given below based on Lerczak et al. (2006):

$$F_S = \left\langle \int usdA \right\rangle \tag{3.1}$$

where $\langle\ \rangle$ denotes a low-pass, subtidal temporal filter that produces tidally averaged/integrated component, u is the velocity in m s^{-1} normal to the cross section as function of time and position on the cross section, s is the salinity in psu, and dA is the small area of integration in m^2. The subtidal volumetric flow rate Q_F (m^3 s^{-1}) through a cross-sectional area (A) is determined as

$$Q_F = \left\langle \int udA \right\rangle \tag{3.2}$$

To simplify the calculation of salt fluxes through a cross section, the area is divided into a number of the cells along the section with constant differential areas dA along depth, but dA varies with time (expands and contracts tidally) and cell location (bottom elevation change). Velocity, salinity, and salt flux are also separated (decomposed) into three components. They are a) tidally and cross-sectionally averaged, b) tidally averaged and sectionally varying, and c) tidally and sectionally varying remainder.

The tidally averaged properties are normalized using the tidally averaged, cross-sectional area $A_0 \equiv \left\langle \int dA \right\rangle$ (Lerczak et al. 2006). Therefore, the tidally and sectionally averaged velocity (u_0) and salinity (s_0) are given by

$$u_0 \equiv \frac{\left\langle \int udA \right\rangle}{A_0} = \frac{Q_F}{A_0}, \quad s_0 \equiv \frac{\left\langle \int sdA \right\rangle}{A_0} \tag{3.3}$$

Both u_0 and Q_F are negative when they are towards the ocean (seaward). The tidally averaged and sectionally varying velocity (u_E) and salinity (s_E) are defined as

$$u_E \equiv \frac{\langle udA \rangle}{dA_0} - u_0, \quad s_E \equiv \frac{\langle udA \rangle}{dA_0} - s_0 \tag{3.4}$$

where $dA_0 \equiv \langle dA \rangle$ is tidally averaged integration area. The exchange flow components (u_E and s_E) only include the vertically varying part of the gravitational circulation (MacCready 2011). The tidally varying and sectionally varying velocity (u_T) and salinity (s_T), which vary with time and over the cross section, are defined by Lerczak et al. (2006) as

$$u_T \equiv u - u_0 - u_E, \quad s_T \equiv s - s_0 - s_E \tag{3.5}$$

The components u_T and s_T vary predominantly on tidal scales, while u_0, s_0, u_E, and s_E vary only on subtidal scales.

Finally, the subtidal salt flux can be decomposed into three components (river, exchange, and tidal) as following:

$$\begin{aligned} F_S &= \left\langle \int (u_0 + u_E + u_T)(s_0 + s_E + s_T) dA \right\rangle \approx \left\langle \int (u_0 s_0 + u_E s_E + u_T s_T) dA \right\rangle \\ &\equiv Q_F s_0 + F_E + F_T \end{aligned} \tag{3.6}$$

In the above simplification, Lerczak et al. (2006) have made use of the following properties to eliminate six of the nine terms;

$$\int u_E dA_0 = 0, \ \int s_E dA_0 = 0, \ \langle u_T dA \rangle = 0, \ \langle s_T dA \rangle = 0 \tag{3.7}$$

The three fluxes in the right-hand side of Eq. 3.6 represent the subtidal salt fluxes due to cross-sectional average advective transport, shear dispersion due to vertical and

lateral shear transport, and tidal oscillatory salt transport due to temporal correlations between *u* and *s* (Lerczak et al. 2006).

3.3.4 Theoretical Formulation of Isohaline Salt Flux Method

The Eulerian analysis has the advantage that parts of it may be predicted from the known theory. For example, one may use theoretical solutions developed by Hansen and Rattray (1965) to predict u_1 and s_1 (Ralston et al. 2008; MacCready 2011). However, the current theories aimed at predicting size of tidal flux do not tell us what salinity classes are transported by tidal correlations between velocity and salinity (MacCready 2011). An alternate method to predict the subtidal estuarine salt flux is by averaging the transport as a function of salinity instead of as a function of spatial position within the cross section. Isohaline coordinate system has been used by scientists to study mass transformations in an idealized numerical simulation of estuary (MacCready and Geyer 2001; MacCready et al. 2002; MacCready 2011; Chen et al. 2012).

The theoretical equations used to calculate the salt exchange from the isohaline coordinate method developed by MacCready (2011) are briefly discussed below. The tidally averaged volumetric flux of water with salinity greater than *s* is defined as

$$Q(s) \equiv \left\langle \int_{A_s} u dA \right\rangle \tag{3.8}$$

where A_s is the tidally varying portion of the cross section with salinity greater than s. *Q(s)* can be defined for any cross section and for any salinity $0 \le s \le s_{ocean}$. *Q(x, s, t)* is referred as the isohaline transport function for a cross section with distance *x* from a reference point. By the definition of A_s, we can have $Q(s_{ocean}) = 0$, and $Q(s = 0) = Q_F$. To

find the tidally averaged volume flux in a specific salinity class, we differentiate *Q(s)* with respect to salinity,

$$-\frac{\partial Q}{\partial s} = -\lim_{\delta s \to 0} \frac{Q(s+\frac{\delta s}{2}) - Q(s-\frac{\delta s}{2})}{\delta s} \tag{3.9}$$

Here, we use finite salinity bins with ∂s of 1 psu to create the function $-\partial Q/\partial s$. If the fluxes coming in and going out through the cross section at salinity range ∂s are identical, then $-\partial Q/\partial s = 0$.

The exchange flow can be defined as

$$Q_{in} = \int \frac{-\partial Q}{\partial s}\Big|_{in} ds, \qquad Q_{out} = \int \frac{-\partial Q}{\partial s}\Big|_{out} ds, \tag{3.10}$$

where "*in*" means we only count $-\partial Q/\partial s$ in the integral when its sign (i.e., $-\partial Q/\partial s > 0$) indicates water flowing into the estuary and "*out*" means water going out of the estuary. Q_{in} and Q_{out} represent the net flux of water into and out of the estuary because both subtidal and tidal processes that occur in distinct salinity classes are included (MacCready 2011).

Similarly, salt fluxes and flux-weighted salinities can be defined as:

$$\begin{aligned} F_{in} &= \int s(-\frac{\partial Q}{\partial s})\Big|_{in} ds, \qquad F_{out} = \int s(-\frac{\partial Q}{\partial s})\Big|_{out} ds \\ s_{in} &\equiv \frac{F_{in}}{Q_{in}}, \qquad s_{\text{out}} \equiv \frac{F_{out}}{Q_{out}} \end{aligned} \tag{3.11}$$

The total volume and salt conservation are given by

$$\begin{aligned} Q_{in} + Q_{out} &= Q_F \\ F_S &= \frac{d}{dt}\int s dV = Q_{in}s_{in} + Q_{out}s_{out} \end{aligned} \tag{3.12}$$

From the above equations, it can be implied that the isohaline framework gives a group of fundamental estuarine quantities, Q_{in}, Q_{out}, s_{in}, and s_{out}, which are termed as total exchange flows (TEF) by MacCready (2011).

3.4 Results

The Perdido EFDC model was run from September 6, 2008 (Julian Day 250) to July 13, 2009 (Julian Day 560). The model was calibrated against measured water surface elevation, water temperature, and salinity at various monitoring stations. The details of the calibration are given by Devkota et al. (2013). In this paper, the observed and modeled time series of water surface elevations at Terry Cove and Blue Angels Park were revisited and subtidal components were studied using simulation outputs at each hour.

The tides in the PBWB system are dominated by diurnal tides: O1 and P1 tidal constituents (Devkota et al. 2013). It is essential to remove the tidal effects in the time series of water surface elevation and salinity to understand the underlying residual subtidal component. A 24-hour low-pass filter was tested first but was unable to remove the tidal effects completely. A 48-hour Godin low-pass filtering program (Godin 1972) was used by the USGS to remove tidal signals from observed discharges in Mobile River that links the Gulf of Mexico (USGS 2011). A 48-hour Lanczos low-pass filter was used by Kim and Park (2012) to study water and salt exchange for a micro-tidal, stratified northern Gulf of Mexico estuary. Therefore, a 48-hour Lanczos low-pass filter (Duchon 1979) was used to eliminate the tidal effects from the time series of water surface elevation at Terry Cove and Blue Angels Park. Fig. 3.2 shows the time series plot of subtidal observed and modeled water surface elevations at Blue Angels Park and Terry Cove from Julian Day 300 (October 26, 2014) to Julian Day 560 (July 13, 2009). The

observed and modeled subtidal water surface elevations match reasonably well. The mean absolute differences between observed and modeled subtidal water surface elevations at Blue Angels Park and Terry Cove from 300–560 days were 0.03 m and 0.04 m, respectively (Table 2). During the calibration period, there were no continuous time series data for other transport parameters such as temperature and salinity; therefore, time series comparison between observed and modeled subtidal temperature and salinity could not be made.

3.4.1 Salinity Distributions in Perdido Bay.

The temporal and spatial distributions of salinity in Perdido Bay are first illustrated using salinity profile distribution plots. The snapshots of salinity distribution in Perdido Bay along the centerline (Fig. 3.1) from Perdido Pass to Perdido River are plotted for six different times under low inflows (Fig. 3.3) on April 25–26 2009, and high inflows (Fig. 3.4) on March 30–31 2009. These specific times were chosen based on the upstream inflows from the rivers into Perdido Bay (Q_R in Fig. 3.5a) and water surface elevations at Perdido Pass (WSE in Fig. 3.5b). March 30–31, 2009 (Julian Days 455–456 in Fig. 3.5) had high inflows from upstream; and combined flow rate from all the rivers into Perdido Bay was about 250.0 $m^3 s^{-1}$. The inflows on April 25–26, 2009 (Julian Days 481–482 in Fig. 3.5) were low and about 19.5 $m^3 s^{-1}$. Under each inflow condition, three water surface elevations at Perdido Pass were chosen: ebb tide (seaward), the lowest elevation in the tidal cycle, and flood tide (landward).

Figs. 3.3 and 3.4 demonstrate varying salinity fields throughout Perdido Bay resulted from dynamic inflows, tides, and wind forcing. The x-axis in Figs. 3.3 and 3.4 represents the horizontal distance from the mouth of Perdido Pass (0 m) to Perdido River

(37,500 m) and the y-axis represents the depth elevations (m) of the computational grids along the centerline shown in Fig. 3.1. Salinity (psu) distributions along the depth and the centerline are represented using color contours with blue being the lowest salinity (0 psu) and red being the highest salinity (35 psu). Isohalines from 0 to 34 psu were also plotted in Figs. 3.3 and 3.4 using 2 psu increment. Various locations along the centerline such as Perdido River, Perdido River mouth, US Hwy 98 Bridge, DuPont Point, and Ross Point and Innerarity Point are shown using vertical dash lines that allow readers to visualize the temporal and spatial salinity distributions. Time series plots of flow rates from Perdido River and Styx River and water level at the Gulf of Mexico are also shown using small windows with the vertical line representing the corresponding time of the snapshot of salinity distribution.

Fig. 3.3 (a) shows that salt water was advancing towards the Gulf of Mexico due to the ebb tide (an arrow was used to indicate the flow direction) at the downstream boundary at 15:00 on April 25, 2009 under low inflows from upstream. The Perdido Pass complex includes the area from Perdido Pass (section A-A) to the section B-B in Fig. 3.1. The more or less well-mixed condition happened in the Perdido Pass complex with salinity about 34 psu throughout the depth. However, at the intersection of Ross Point and Innerarity Point (~7.5 km upstream from Perdido Pass), the vertical salinity stratification was strong and about 10 psu (11 and 21 psu at the surface and bottom, respectively). The salinity stratification decreased rapidly from Ross/Innerarity Point to DuPont Point and US Hwy 98 bridge due to the dilution created from the upstream freshwater inflows. In Fig. 3.3 (b) at 21:00 on April 25, 2009 reduced salinity towards Perdido Pass indicated that the salinity was greatly reduced from ebb tide to the lowest

water surface elevation at the downstream boundary. The Perdido Pass complex during lowest water surface elevation at downstream had a stronger stratification compared to the stratification under ebb tide (Fig. 3.3a). The strongest stratification occurred in the middle portion of the Perdido Pass complex where the surface salinity ranged from 14 to 18 psu and the bottom salinity from 28 to 30 psu (red region in Fig. 3.3b). A snapshot of salinity distribution at 05:00 on April 26, 2009 (Fig. 3.3c) shows that salinity was being introduced into the Perdido Bay by the flood tide from the Gulf of Mexico. During the flood tide, the stratification near Perdido Pass occurred at the lowest elevation (Fig. 3.3b) was destroyed because the water depth was relative small and flow momentum from tides was large, and flood tides from downstream eventually pushed high saline water into the system. Because the inflows were small on April 25–26 2009, salt water passed the US Hwy 98 Bridge (5–8 psu) and reached the upper Perdido Bay, but Perdido River mouth still had freshwater under both ebb and flood tides (Fig. 3.3) at Perdido Pass.

Fig. 3.4 (a) shows that salt water was passing the Perdido Pass complex towards the Gulf of Mexico due to the ebb tide from the downstream at 21:00 on March 30, 2009 under high inflows from upstream. Combined large inflows of 250.0 $m^3 s^{-1}$ from Perdido River and Styx River were clearly shown on small time-series plots and Fig. 3.5. The salinity distribution in the Perdido Pass complex was no longer more or less well-mixed condition with 34 psu salinity that happened at the low inflow condition (Fig. 3.3a) and had surface salinity ranged from 10 to 18 psu (bottom salinity about 14–28 psu). The large inflows generated high momentum which pushed the freshwater towards downstream and diluted and eventually flushed the saline water from Perdido Bay through Dolphin Pass and Perdido Pass. Freshwater with salinity less than 2 psu starting

from Perdido River passed the US Hwy 98 Bridge (Fig. 3.4) under both ebb and flood tides at Perdido Pass. Vertical salinity stratification (about 8 psu) was developed in DuPont Point with surface salinity of 5 psu and bottom salinity of 13 psu. Salinity distribution at 02:00 on March 30, 2009 for the lowest water surface elevation at the Gulf of Mexico (Fig. 3.4b) shows that the salinity in the Perdido Pass complex was largely reduced. The bottom salinity near Perdido Pass was ~16 psu and vertical salinity stratification was not strong (Fig. 3.4b). Fig. 3.4(c) shows the salinity profile under flood tide from downstream at 08:00 on March 31, 2009. The only noticeable difference from distribution shown in Fig. 3.4(b) was that ocean water with higher salinity was being introduced back into Perdido Bay through Perdido Pass. The arrow at the top of the panel indicates the direction of flow from downstream that was against the momentum of large upstream inflows, therefore, the region with high salinity was small in comparison to the low inflow condition shown in Fig. 3.3(c). At Perdido Pass, salinity at the surface layer was smaller than the bottom salinity, which indicated the water going out from the system through surface layers under high inflows and salt water from downstream coming back through the bottom layers under high water levels of the flood tides.

Thus, complex temporal and spatial stratification patterns in Perdido Bay resulted from interactions between different inflows and tidal variations. In the following sections, we present results of Eulerian salt flux decomposition and isohaline salt flux methods using hourly outputs from calibrated Perdido EFDC model to understand incoming/outgoing flows, and associated salt fluxes through five different cross sections shown in Fig. 3.1.

3.5 Water and Salt Exchange in the PBWB System

To explore the salt fluxes into the PBWB system, Eulerian and isohaline methods of salt flux decomposition were applied to hourly time series data of simulated velocity and salinity from calibrated Perdido EFDC model. The flux calculations were performed from September 26, 2008 (Julian Day 270) to July 3, 2009 (Julian Day 550). To avoid any effect of initial conditions, the first 20 simulation days were treated as model spin up period. The model forcing includes observed river inflows, ocean tides, and meteorological inputs as boundary conditions. Flow exchanges were calculated using both methods at five different cross sections (Fig. 3.1) in the PBWB system. For Eulerian flux method, Eqs. (3.1)–(3.7) were implemented to compute various flux components such as Q_F, F_S, s_0, $Q_F s_0$, F_E, F_T, u_E and s_E. For isohaline flux methods, Eqs. (3.8)–(3.12) were used to compute TEF Q_{in} , Q_{out} , s_{in}, and s_{out}. In this paper, all flows and fluxes moving from external boundary or Wolf Bay into Perdido Bay have positive values, and all flows and fluxes moving from Perdido Bay to external boundary or Wolf Bay have negative values for Figs. 3.5–3.10 and in Tables 3.3–3.6.

3.5.1 Eulerian Flux Decomposition

The 2008–2009 simulation period had a wide range of freshwater river discharges Q_R (Fig. 3.5a) flowing into Perdido Bay, which ranged from 11.05 to 762.45 $m^3 s^{-1}$ with an average inflow of 42.0 $m^3 s^{-1}$. The time series of filtered water surface elevation (WSE) at the Gulf of Mexico plotted in Fig. 3.5b exhibited the variation from -0.31 m up to 0.56 m with an average value of 0.15 m. Filtered WSE at the Big Lagoon (east boundary, Fig. 3.1) varied from -0.19 to 0.54 m with an average value of 0.14 m, and was mostly higher than filtered WSE at the Gulf before Julian Day 335 (November 31, 2008, Fig. 3.5b). Average values of subtidal volumetric flow rate Q_F (Fig. 3.5c) calculated from Eulerian flux method over the simulation period were -42.5 $m^3 s^{-1}$ and 16 $m^3 s^{-1}$ (Table 3.3) for Perdido Pass (cross section A-A, Fig. 3.1) and Dolphin Pass (cross section C-C, Fig. 3.1), respectively. The negative values of discharge Q_F and salt flux F_S indicate seaward flux from Perdido Bay, i.e., southward through Perdido Pass and eastward through Dolphin Pass. Both Q_F and F_S showed large temporal variations. Q_F through Perdido Pass ranged from -619 $m^3 s^{-1}$ to 180 $m^3 s^{-1}$ (Table 3.3). The subtidal salt flux F_S through Perdido Pass (Fig. 3.5d and Table 3.3) ranged from -13,480 to 6,289 kg s^{-1} (average of -527 kg s^{-1}) and -6,789 to 7,393 kg s^{-1} (average of 648 kg s^{-1}) through Dolphin Pass. With the range of variations 1–2 orders of magnitude larger than the corresponding means, the mean flux values are not representative of the water and salt exchange through Perdido Pass and Dolphin Pass.

Subtidal flow rate Q_F had relatively strong correlation with river discharge Q_R and filtered WSE at the Gulf (W_{gulf}) and Big Lagoon boundaries (W_{bl}). A multi-linear regression equation was developed, and it explains 76% variations of Q_F:

$$Q_{F\,(PerdidoPass)} = 6.92 - 0.77\,Q_R + 648\,W_{gulf} - 614\,W_{bl} \quad (R^2 = 0.76) \tag{3.13}$$

Because Q_F is negative for seaward flux and Q_R is positive for flows from upstream, the regression coefficient for Q_R is negative. The regression equation shows that the seaward flux at Perdido Pass is proportion to upstream river discharge and WSE at Big Lagoon but inversely proportion to WSE at the Gulf. The regression equation approximately indicates that a 100 $m^3\ s^{-1}$ of river discharge from upstream is balanced with a 0.12 m WSE increase at the Gulf. The equation shows complex interactions between river discharges from upstream and WSEs directly or indirectly influenced by tides in the Gulf of Mexico.

Fig. 3.5(e) shows the time series of tidally and sectionally averaged salinity (s_0) for Perdido Pass (solid line) and Dolphin Pass (dashed line). From Julian Day 270–330 s_0 at Dolphin Pass was comparable to the magnitude of s_0 at Perdido Pass. From Julian Days 330–550 s_0 at Perdido Pass was much higher. The salinity s_0 at Perdido Pass ranged from 14 to 34 psu with a mean value of 30.4 psu, whereas s_0 at Dolphin Pass ranged from 3 to 30 psu with a mean value of 22 psu. The reason s_0 is higher in Perdido Pass is because Perdido Pass is directly connected to the Gulf of Mexico but Dolphin Pass is connected to the Gulf through Big Lagoon and Pensacola Bay.

3.5.1.1 Exchange through Perdido Pass

The relative contribution of three components ($Q_F s_0$, F_E, and F_T in Eq. 3.6) to F_S varies as function of water column stratification (Kim and Park 2012). For Julian Days 270–450, F_S was almost entirely determined by $Q_F s_0$ (Fig. 3.5a), which indicates the stratification at Perdido Pass was relatively weak. However, for Julian Days 450–550,

the shear dispersive salt transport F_E and the tidal oscillatory salt transport F_T (Fig. 3.5b, different y-axis scale from Fig. 3.5a) were at least as important as $Q_F s_0$, which indicates a relatively strong stratification at Perdido Pass. The F_T at Perdido Pass (cross section A-A in Fig. 3.1) was dominant or important component of F_S in addition to $Q_F s_0$ because velocity and salinity components u_T and s_T were dominant or relatively large because it is close to the Gulf of Mexico and within a tidal excursion. Dronkers and van de Kreeke (1986) suggested that the larger magnitude of oscillatory flux, also called "nonlocal" salt transport whose magnitude is a function of a variation of topography within a tidal excursion, plays a significant role rather than processes representative of the overall salt transport in an estuary. Many theoretical and numerical studies of salt transport mechanisms have considered estuaries of a uniform cross section (Fischer 1972; Smith 1980; Scott 1994). The cross section A-A at Perdido Pass where the salt flux was studied doesn't have uniform cross section and is characterized by narrow width with deep channel and shallow overbank areas connecting Perdido Bay and the Gulf of Mexico. For Julian Days 450–560, F_T increased largely compared to F_T from 250–450 (Fig. 3.6b); this is due to the interaction of large inflows from upstream and variations of downstream tides. F_E at Perdido Pass was up to 346 kg s^{-1} (Fig. 3.6b) with an average value of 31 kg s^{-1} but F_T was up to 2,596 kg s^{-1} with an average value of 582 kg s^{-1}. F_T at Perdido Pass was on the average 19 times larger than F_E, and they are weakly correlated (correlation coefficient R = 0.34).

In Fig. 3.6 (c) and (d) exchange flow velocity and salinity (u_E and s_E) are displayed for surface and bottom layers at the deepest cell in the Perdido Pass cross section. These tidally averaged and sectionally varying velocities were dominantly

positive values in the bottom layer but negative values in the surface layer. It means that the exchange flow velocity was dominantly seaward at the surface and landward at the bottom. The exchange flow velocity at the surface was strongly correlated to the velocity at the bottom and the correlation coefficient between them was -0.88. The data analysis shows that the exchange flow salinity S_E at the bottom layer was always greater than the tidally and sectionally averaged salinity s_0 but S_E at the surface layer is less than s_0 because the interaction with freshwater from upstream rivers. The magnitude of exchange flow salinity at the bottom layer was similar to the salinity in the surface layer with a correlation coefficient of -0.96 (Fig. 3.6d). The estuarine salinity s_E at the deep channel of Perdido Pass varied with moderate variation in stratification. Maximum stratification at Perdido Pass occurred on Julian Days 450–560 with the bottom-surface salinity difference (Δs_E) as large as 9 psu whereas weak stratifications existed from Julian Days 270–450 with (Δs_E) ranging from 0 to 5.2 psu. Variation in stratification was largely determined by complex interactions of river discharges and tidal WSEs. The increase in river inflows from 450–560 increased the stratification in the Perdido Pass. The exchange flow (Δu_E) defined as the difference between the surface and bottom u_E had an average value of 0.06 m s^{-1} and a maximum value up to 0.19 m s^{-1}.

3.5.1.2 Exchange through the Perdido Pass complex and Dolphin Pass

Eulerian flow decomposition method was applied to determine the flow exchange components through the cross sections B-B (Perdido Pass complex), C-C (Dolphin Pass), D-D (the Wolf-Perdido canal), and E-E (the lower Perdido Bay) in Fig. 3.1 that would allow us to investigate the underlying factors that govern salt flux exchange through these

cross sections. The distributions of salt flux components F_E and F_T are different in the Perdido Pass complex (Fig. 3.7a) compared to the components in Perdido Pass (Fig. 3.6b). The dominance of tidal oscillatory flux F_T was greatly reduced and exchange flux F_E became dominant in the Perdido Pass complex. The salinity and momentum differences between the incoming water flux from the Gulf and outgoing water flux from upstream controlled the amount of flow exchange through the cross section B-B. The water and salt exchange at the Perdido Pass complex was also affected by western/eastern fluxes from Dolphin Pass (Fig. 3.1) in addition to seaward/landward fluxes from Perdido Pass. Subtidal averaged Q_F through the cross section B-B varied from 139 $m^3 s^{-1}$ (incoming flux) to -873 $m^3 s^{-1}$ (outgoing flux, Table 3.3). The average value of Q_F from Julian Days 270–550 through the cross section B-B was -34 $m^3 s^{-1}$ that was slightly smaller than average Q_F at Perdido Pass (Fig. 3.5c). The salt flux F_S through the cross section B-B ranged from -14,810 to 4,020 kg s^{-1} (average of 113 kg s^{-1}). In comparison to F_E (ranged from -27.9 to 14.0 kg s^{-1} with an average value of -0.5 kg s^{-1}) through the cross section C-C (Dolphin Pass, Fig. 3.7b), F_T was dominant (ranged from -134.7 to 61.1 kg s^{-1} with an average value of -5.6) and flow exchange occurred in the east-west direction. F_T was dominant because the salinities of incoming and outgoing water through Dolphin Pass were not much different, which were directly influenced by the Big Lagoon boundary which is far away from the Gulf of Mexico. Subtidal Q_F through the cross section C-C (Dolphin Pass) varied from -286 $m^3 s^{-1}$ (western flux) to 272 $m^3 s^{-1}$ (eastern flux) with a small average value of 16 $m^3 s^{-1}$ (Table 3.3) in 2008–2009. It means that there were relatively large flows back and forth in the east-west directions through Dolphin Pass but the net flow was not significant.

3.5.1.3 Exchange through the Wolf-Perdido canal and the lower Perdido Bay

The flow exchanges at the Wolf-Perdido canal (cross section D-D in Fig. 3.1), which connects Perdido Bay and Wolf Bay, and in the lower Perdido Bay (cross section E-E) take place in the east-west direction. At the Wolf-Perdido canal, F_E was dominant (ranged from -472.2 to 407.7 kg s^{-1} with an average value of -20.5 kg s^{-1}) and negative value of F_E indicated that the flow was moving from Perdido Bay to Wolf Bay (Fig. 3.7c) due to inflows from upstream rivers into Perdido Bay. Q_F at the Wolf-Perdido canal varied from -127.2 m^3 s^{-1} (towards Wolf Bay) to 51.1 m^3 s^{-1} (towards Perdido Bay). It means that a small portion of river discharges Q_R from Perdido River and Styx River could flow through the cross section C-C into Wolf Bay. On average there were more days for flows from Perdido Bay to Wolf Bay through the cross section C-C because average Q_F at C-C was -14 m^3 s^{-1}. Q_F at the Wolf-Perdido canal was typically smaller than Q_F at Perdido Pass and Dolphin Pass. The salt-water intrusion from Perdido Bay towards Wolf Bay mostly occurred when there were large inflows from upstream and large incoming flows via Dolphin Pass and Perdido Pass boundaries. The amount of flow entering Wolf Bay from Perdido Bay was of small magnitude that might be one of the reasons that Wolf Bay is pristine and less polluted than Perdido Bay. At the lower Perdido Bay, F_E was dominant with mean value of 556.3 kg s^{-1} and mean F_T was -15.7 kg s^{-1}. Q_F at the lower Perdido Bay ranged from -776.5 to 93.5 m^3 s^{-1} with an average value of -49.5 m^3 s^{-1} (75% of Q_F is less than -10.0 m^3 s^{-1} or seaward outflows). The salt flux F_S at lower Perdido Bay ranged from -11,430 kg s^{-1} to 2,198 kg s^{-1} with an average value of -360 kg s^{-1} (Table 3.3).

A data analysis was performed to examine possible correlations of salt and flow fluxes F_E, F_S, and Q_F through different cross sections. Fig. 3.1 shows that the sum or combined salt and flow fluxes through the Perdido Pass complex (section B-B) and the Wolf-Perdido canal (section D-D) would possibly correlate with corresponding fluxes through the lower Perdido Bay (section E-E). It is also possible that the sum or combined salt and flow fluxes through Perdido Pass (section A-A) and Dolphin Pass (section C-C) would correlate with corresponding fluxes through the Perdido Pass complex (Fig. 3.1). Derived correlation coefficients of F_E, F_S, and Q_F between above mentioned cross sections are summarized in Table 3.4. The interaction among exchange salt fluxes F_E through the Perdido complex, Dolphin Pass, and Perdido Pass was complex. Therefore, the correlation coefficient between the sum of F_E through Perdido Pass and Dolphin Pass and F_E through the Perdido Pass complex was very small (only 0.06) because tidal oscillatory flux F_T was dominant at Perdido Pass. Other correlation coefficients ranged from 0.91–0.99 (Table 3.4) indicating that strong correlations of F_E, F_S, and Q_F indeed exist between these cross sections.

3.5.2 Isohaline Flux Method

Although Eulerian method gave us the indication of incoming and outgoing water and salt fluxes, we were not able to quantify what salinity classes were being introduced into the PBWB system. Therefore, isohaline method was also used to further quantify the incoming and outgoing salinity classes under different flow conditions in 2008–2009. The incoming/outgoing flow and salinity through the five cross sections (Fig. 3.1) were computed using equations 7–10 for isohaline method.

3.5.2.1 Flow exchanges through cross sections

Incoming and outgoing flows through the five cross sections are presented in Fig. 3.8. It was checked and confirmed that the summation of incoming flow Q_{in} and outgoing flow Q_{out} through all cross sections is equal to Q_F calculated using Eulerian flux method (Eq. 3.12). Because Q_{in} is always positive and Q_{out} is negative, for easy comparison, "$-Q_{out}$" was plotted for all cross sections in Fig. 3.8. The incoming/outgoing flows through the cross sections A-A (Perdido Pass) and B-B (the Perdido Pass complex) occurred towards the north and south directions, i.e., landwards and seawards, respectively. The incoming/outgoing flows through the cross sections C-C (Dolphin Pass), D-D (the Wolf-Perdido Canal), and E-E (the lower Perdido Bay) occurred along the east-west directions but Q_{in} always means the flow moving into Perdido Bay. The mean incoming flows at Perdido Pass and Perdido Pass complex were 83.6 $m^3 s^{-1}$ and 100 $m^3 s^{-1}$ with maximum flows up to 210.6 $m^3 s^{-1}$ and 218.4 $m^3 s^{-1}$, respectively. The 25% of incoming flows at Perdido Pass were less than 57.8 $m^3 s^{-1}$ at Perdido Pass and 66.2 $m^3 s^{-1}$ at the Perdido Pass complex (Table 3.5). At Julian Day 453.2 (March 29, 2009 5:00 AM), the largest peaks of outflow ($-Q_{out}$) occurred were 877.9 $m^3 s^{-1}$ at the Perdido Pass complex and 619 $m^3 s^{-1}$ at Perdido Pass because of the large upstream river inflows (Fig. 3.5a). For Julian Days 270–335, the outgoing discharges (maximum value of 349.4 $m^3 s^{-1}$) at Perdido Pass were larger than the incoming flow (Fig. 3.8a). This large outflow through Perdido Pass was primarily contributed by the incoming flux into Perdido Bay from the Dolphin Pass (Fig. 3.8c) because of higher water levels at Big Lagoon (Fig. 3.5b and 3.5c) from Julian Days 270–335. The average inflow through Dolphin Pass for Julian Days 270–335 was 181 $m^3 s^{-1}$ with smaller average outflow of 6.6 $m^3 s^{-1}$ leaving the system (Fig. 3.8c). However,

after Julian Day 335, average incoming and outgoing flows through the cross section C-C were 25.2 $m^3 s^{-1}$ and 59.8 $m^3 s^{-1}$, respectively. Under large inflows from upstream rivers on March 29, 2009, the peak outflow through Dolphin Pass to Big Lagoon reached 293.5 $m^3 s^{-1}$ also.

At the cross section D-D (the Wolf-Perdido canal), Q_{in} represents the flows from Wolf Bay towards Perdido Bay and Q_{out} for the flows from Perdido Bay towards Wolf Bay. In 2008–2009, Q_{in} varied from 0 to 91.6 $m^3 s^{-1}$ with an average value of 14.6 $m^3 s^{-1}$ (Table 3.5). In contrary, a relatively large outflow (Q_{out}) occurred through the Wolf-Perdido canal that varied from 0 to 133.8 $m^3 s^{-1}$ (Fig. 3.8d and Table 3.5) with an average value of 26.8. It was found that for Julian Days 270–335, both outgoing flows through the Wolf-Perdido canal and incoming flows through the lower Perdido Bay were contributed due to the incoming flows from Dolphin Pass (Fig 3.8d). The flows moving towards Perdido Bay from Wolf Bay were mainly contributed from the tidal inflows at GIWW because the freshwater inflows from tributaries in Wolf Bay were very small (Table 3.1) and WSEs at GIWW were of similar magnitude as WSEs at Gulf of Mexico. Therefore, the tidal boundary at GIWW (west) is the major driving force which controls the flow from Wolf Bay towards Perdido Bay. A regression analysis performed between Q_{out}, filtered water surface elevation, and filtered wind stress at east-west direction described 44% of the variation in Q_{out} at the Wolf-Perdido canal (Table 3.7).

At the lower Perdido Bay (cross section E-E), the average and maximum incoming flows were 75 $m^3 s^{-1}$ and 192 $m^3 s^{-1}$ (Julian day 414.87), respectively. The incoming flows at the lower Perdido Bay resulted from interaction of incoming flows from Perdido Pass, Dolphin Pass, and the Wolf-Perdido canal. However, the outgoing

flows were more controlled by inflows from upstream rivers into Perdido Bay but also affected by ebb/flood tides at the Gulf of Mexico and Big Lagoon. The average and maximum outflows through the lower Perdido Bay were 124.3 $m^3 s^{-1}$ and 777.4 $m^3 s^{-1}$ (Julian day 453.25), respectively. The maximum outflows through the cross sections A-A, B-B, C-C, and E-E occurred almost at the same time (Julian day 453.25) when there was a maximum inflow from upstream rivers into Perdido Bay (Fig. 3.5a).

The correlation coefficients of incoming and outgoing flows Q_{in} and Q_{out} and salt fluxes F_{in} and F_{out} through different cross sections were also derived and listed in Table 3.4. The correlation coefficients between combined flows through Perdido Pass and Dolphin Pass and corresponding flows through Perdido Pass complex were 0.38 for Q_{in} and 0.84 for Q_{out}. These correlation coefficients were smaller than correlation coefficients between combined flows through the Perdido Pass complex and the Wolf-Perdido canal and corresponding flows through the lower Perdido Bay (Table 3.4). The smaller correlations of Q_{in} and F_{in} for the sections (A-A, B-B, and C-C) inside the Perdido Pass complex were because the incoming flow from Dolphin Pass could leave the system as outflow at Perdido Pass. The relatively stronger correlations of Q_{out} and F_{out} through cross sections were due to strong connections to upstream inflows (Fig. 3.8). These correlation coefficients were smaller than correlation coefficients of F_E, F_S, and Q_F except the correlation coefficient of combined F_E through the section A-A and C-C versus F_E through the section B-B (Table 3.4).

3.5.2.2 Salinity exchanges through cross sections

The incoming salinity at Perdido Pass was typically at 33–34 psu because it is directly connected to the Gulf of Mexico. The average incoming salinity from Perdido Pass was

33.5 psu and varied from 13 psu to 34 psu (Table 3.6) in 2008–2009. The sharp drops of incoming salinity at Julian Days 453.2 (March 29, 2009) was 13 psu which resulted from the large flows from upstream. The outgoing salinity at Perdido Pass ranged from 11.8 psu to 34 psu with an average value of 27.7 psu. For majority of the time, the outgoing salinity was smaller than the incoming salinity (Fig. 3.9a) in Perdido Pass. The smaller outgoing salinity resulted from the freshwater dilution from the upstream rivers and relatively less saline water from Big Lagoon. The average and maximum differences between incoming (bottom layers) and outgoing (surface layers) salinity at Perdido Pass were 5.7 psu and 20.4 psu, respectively (Table 3.6).

Though the magnitudes of incoming/outgoing flows through the cross section B-B (Perdido Pass complex) were similar to the flows at Perdido Pass (Figs. 3.8a and 3.8b), incoming/outgoing salinities were largely reduced compared to salinity at Perdido Pass (Fig. 3.9a). The incoming salinity at B-B had relatively large variations because 75% of salinity varied from 23.4 to 34.0 psu, while 75% of salinity at Perdido Pass only varied from 33.3 to 34.0 psu. This was because the dilution and mixing in the Perdido Pass complex was increased by complex interaction of flows from Wolf Bay, freshwater inflows from Perdido Bay, and inflows from Big Lagoon. The average incoming and outgoing salinity through the cross section B-B were 25.3 psu and 19.1 psu, respectively, which were about 8 psu smaller than the corresponding salinities at Perdido Pass. The average and maximum differences between incoming and outgoing salinity at B-B were 6.2 psu and 15.4 psu, respectively. The incoming salt flux due to TEF (i.e., F_{in}, Eq. 3.11) at Perdido Pass ranged from 0 to 6,911 kg s^{-1} with an average value of 2,785 kg s^{-1} and the outgoing salt flux (F_{out}, Eq. 3.11) at Perdido Pass ranged from 0 to 13,805 kg s^{-1} with

an average of 3,538 kg s^{-1}. Therefore, in 2008–2009, due to large inflows, on average there was more salt removed from Perdido Pass than salt introduced through it. For other dry years with less inflows from upstream rivers, the situation could be reversed.

At the cross section C-C (Dolphin Pass), incoming and outgoing salinities exhibited similar magnitudes and variations that implied salinity inside Perdido Bay near Dolphin Pass similar to salinity in Big Lagoon. The average incoming and outgoing salinities at Dolphin Pass were 22.1 and 22.4 psu, respectively (Table 3.6). The maximum difference between incoming and outgoing salinity at Dolphin Pass was 9.7 psu with an average difference of 0.3 psu. The incoming salt flux due to TEF at Dolphin Pass ranged from 0 to 8,080 kg s^{-1} with an average value of 1,511 kg s^{-1} and the outgoing salt flux at Dolphin Pass ranged from 0 to 7,050 kg s^{-1} with an average value of 965 kg s^{-1}. This is because there was more salt introduced into Perdido Bay from Julian Days 270-335 due to higher WSEs at Big Lagoon.

The flow exchange between Wolf Bay and Perdido Bay determines the fate and transport of the nutrients and pollutants. Therefore, identifying flows and nutrients from Perdido Bay that would intrude into Wolf Bay would be very important. To quantify the flow exchange between Wolf Bay and Perdido Bay, an approximate middle point (cross section D-D in Fig. 3.1) of the navigation channel connecting Wolf Bay and Perdido Bay was chosen. The average incoming (to Perdido Bay) salinity (19.9 psu) was slightly smaller than the average outgoing salinity (20.8 psu) which implies that Wolf Bay is less saline than Perdido Bay, as Fig. 3.9d also shows that s_{in} was typically smaller than s_{out}.

At the lower Perdido Bay, the average and maximum incoming salinities were 23.2 and 30 psu, respectively. The maximum incoming salinity at the Lower Perdido

Bay was ~4 psu smaller than the maximum salinity at Perdido Pass and the Perdido Pass complex. The outgoing salinity ranged from 5.5 psu to 28.3 psu with an average salinity of 18.2 psu (Table 3.6). The minimum and maximum outgoing salinity occurred on Julian Days 460.4 (April 5, 2009) and 296.6 (October 23, 2008), respectively, which were shortly after the periods with maximum and minimum inflows from upstream rivers (Fig. 3.5a).

Thus, using the isohaline flux decomposition method, we were able to quantify the exact incoming and outgoing salinity classes through different cross sections of Perdido Bay. The difference in incoming and outgoing salinities inferred the amount of dilution occurred at different locations. The lower average outgoing salinity resulted at the lower Perdido Bay indicated that the impact of tides from the Gulf of Mexico and Dolphin Pass was attenuated as tides traveled towards upstream. Comparing Fig. 3.5 (a) and Fig. 3.9 one can see the direct correlation between flows and salinities at different locations in Perdido Bay. Sharp drops shown in Fig 3.9(a) were the response from the large flows from the tributaries in Perdido Bay.

3.5.2.3 Linear regressions of total exchange flows (TEF)

Multi-linear regression analysis was performed at all cross sections to find the correlation and relations of incoming and outgoing flows with river inflows (Q_R), water surface elevations at the Gulf of Mexico (W_{gulf}), Big Lagoon (W_{bl}), and GIWW (W_{giww}), wind stresses in the north-south direction (τ_{NS}) and the east-west direction (τ_{EW}) for the simulation period. Average wind stresses were on order of ~1.6×10^{-6} Pa and were calculated using formulas that Hamrick (1992b) proposed for EFDC. Table 3.7 shows the linear regression equations developed to predict Q_{in} and Q_{out} at Perdido Pass, the Perdido Pass complex, the Wolf-Perdido canal, and the lower Perdido Bay. Not all independent variables were used for each regression equation, and only variables that had smaller p values ($p < 0.00001$) and significantly improved adjusted R^2 were included. Wind had the influence on the outgoing and incoming flows through all the cross sections (Table 3.7). It was found that outgoing flows Q_{out} through all cross sections had correlations with the east-west wind. This is related to the orientation of Perdido Bay (Fig. 3.1) and might be because outgoing flows through other cross sections are ultimately related to Q_{out} at the lower Perdido Bay, which was correlated strongly with the east-west wind (Table 3.7). The incoming flows had stronger correlations with the wind that is perpendicular to the cross section (Table 3.7), i.e., the north-south wind for Perdido Pass and the Perdido Pass complex and the east-west wind for the Lower Perdido Bay and the Wolf-Perdido canal.

It was found that 78%, 75%, and 79% of the variations in Q_{out} at Perdido Pass, the Perdido Pass complex, and the lower Perdido Bay were explained by independent variables Q_R, W_{gulf}, W_{bl}, and τ_{EW}, respectively. It means that river inflows and water

surface elevations at the Gulf and Big Lagoon are important to Q_{out} in addition to wind. Q_R had the similar effect on Q_{out} at these three cross sections (similar coefficient values and the same sign, i.e., Q_{out} increases with increase in Q_R), but W_{gulf} and W_{bl} had somewhat different effects on Q_{out} depending on the location based on the regression coefficient values and signs. At the Wolf-Perdido canal, 62% of the variations in Q_{out} (flows from Perdido Bay to Wolf Bay) were explained by Q_R, W_{giww}, W_{bl}, W_{gulf} and τ_{EW} (Table 3.7), but the influence of Q_R was smaller in comparison to other three cross sections. Upstream river inflows to Wolf Bay were relatively small (Table 3.1) and did not affect Q_{in} at the Wolf-Perdido canal when inflow momentum was dissipated in Wolf Bay. Q_{out} modeled (solid line) from EFDC and predicted (dashed line) from regression equations at three cross sections (Perdido Pass, the Perdido Pass complex, and the lower Perdido Bay) are shown in Fig. 3.10. Overall, the predicted Q_{out} at the three cross sections agree reasonably well with the modeled Q_{out}. The predicted Q_{out} accurately mimicked the large outflow on Julian Day 453 when there was very large inflow from upstream.

Since Q_{in} and Q_R are greater than zero, Q_R had negative correlation on Q_{in} at the Lower Perdido Bay and the Perdido Pass complex (Table 3.7). However, Q_R was not an influencing factor to Q_{in} at Perdido Pass because it is directly connected to the Gulf. The correlation coefficient was relatively low for the correlation of Q_{in} at Perdido Pass with W_{gulf}, W_{giww}, W_{bl}, and τ_{NS}, because effects on Q_{in} due to W_{gulf} are opposite of W_{giww} and W_{bl}, which are indicated by opposite signs of regression coefficients (Table 3.7). At the Perdido Pass complex, 60% of incoming flow variations were explained by Q_R, W_{gulf}, W_{bl}, and τ_{NS}. At the Wolf-Perdido canal, Q_{in} had correlation with W_{giww} and τ_{EW} only but not

correlated with Q_R, W_{gulf}, and W_{bl}; it means that the outflow from Wolf Bay to Perdido Bay was more influenced by or dependent on water levels at GIWW (west boundary) and the east-west wind (R^2 = 0.44, Table 3.7). Overall, these regression equations reveal complex correlations and interactions among independent variables on total exchange flows, and allows us to make estimations of incoming and outgoing flows through these cross sections.

3.6 Summary and Conclusions

A previously calibrated three-dimensional hydrodynamic EFDC model was used to simulate flow and salinity distributions in the Perdido Bay and Wolf Bay system under unsteady flows from rivers, tides from three open boundaries, and atmospheric forcing in 2008–2009. The calibrated EFDC model provided simulated hourly velocities and salinity at different layers (depths) for all grids in five cross sections. Eulerian and isohaline flux methods were applied to determine the water and salt fluxes through these cross sections using hourly model outputs. From the isohaline flux method, the incoming and outgoing flux and salinity were calculated at five cross sections A-A, B-B, C-C, D-D, and E-E (Fig. 3.1). The sum of incoming and outgoing flows from isohaline Flux method was exactly equal to Q_F calculated from Eulerian flux method. The summaries of key findings from the study are as follows:

a. The salinity at Perdido Bay varied largely with upstream inflows (low and high inflows) and tides at open boundaries (ebb and flood tides). During the large inflows from upstream (Fig. 3.4) the salinity at the Perdido Pass complex was relatively small regardless of ebb or flood tides at the Gulf of Mexico. Inflow of highly saline

water at the bottom layers and outflow of relative low salinity water at the surface layers resulted from the interaction of flood tide at the Gulf of Mexico and large inflows from upstream. Salinity was always small from the US Hwy 98 Bridge towards Perdido River. During low inflows from upstream and flood tides from the Gulf of Mexico, maximum salinity up to 32 psu reached Ross/Innerarity Point (the lower Perdido Bay).

b. From Eulerian analysis it was found that at Perdido Pass (cross section A-A) and Dolphin Pass (section C-C), tidal oscillatory flux (F_T) was dominant compared to exchange flow component F_E, whereas at the cross sections B-B (Perdido Pass complex), D-D (Wolf-Perdido canal), and E-E (lower Perdido Bay) the exchange flows F_E were dominant.

c. During the simulation period, both Eulerian and isohaline flux methods indicated that small amount of flow exchange occurred between Wolf Bay and Perdido Bay. During the high inflows from rivers in Perdido Bay and higher tides from the Gulf and Big Lagoon, the water from Perdido Bay moved towards Wolf Bay, however, during normal flows and gentle tides the water from Wolf Bay moved towards Perdido Bay. It means the influences from Perdido Bay and the Gulf of Mexico was relatively small in Wolf Bay under normal inflows.

d. Total exchange flows (Q_{in} and Q_{out},) and salinity classes (s_{in} and s_{out}) extracted from the isohaline method allowed us to identify the effect and interaction of low and high inflows, winds, and tides. The isohaline method can quantify/separate incoming/outgoing flows and salinities through a cross section when both flows occurred through the same cross section (different layers) and at the same time. The

sharp drops of incoming salinity at Perdido Pass were affected by large inflows from upstream rivers and further controlled the incoming salinity to Perdido Bay.

e. Multi-linear regression analysis was performed to explore the correlations and relations of Q_{in} and Q_{out} at all five cross sections with river inflows, water surface elevations at open boundaries, and wind stresses. More than 75% of the variations of Q_{out} at Perdido Pass, the Perdido Pass complex, and the lower Perdido Bay were explained by the regression equations. Wind had certain influences on the incoming and outgoing flows at all the cross sections (Table 3.7). River inflows Q_R influenced all total exchange flows except Q_{in} in Perdido Pass and Q_{out} at the Wolf-Perdido canal. Q_{in} has relatively weaker correlations with independent variables. All regression equations reveal complex interactions among influencing factors.

Table 3.1 Statistical summary of river inflows into Wolf Bay and Perdido Bay and filtered water surface elevations at GIWW (Gulf Intracoastal Waterway, west boundary), the Gulf of Mexico (south boundary), and Big Lagoon (east boundary)

	Discharges ($m^3 s^{-1}$)		Water Surface elevation (m)		
Statistical Parameters	Wolf-Bay rivers	Perdido-Bay rivers	GIWW	Gulf of Mexico	Big Lagoon
Minimum	0.95	11.05	-0.29	-0.31	-0.19
Maximum	15.37	762.45	0.58	0.56	0.54
Mean	1.95	38.81	0.10	0.10	0.14
Standard Deviation	1.97	66.05	0.14	0.15	0.17
1st Quartile	1.11	14.61	0.019	0.01	0.00
Median	1.24	16.56	0.11	0.11	0.13
3rd Quartile	1.74	32.83	0.20	0.20	0.25

Table 3.2 Statistical summary of the differences (Observed - Modeled) and absolute differences (|Observed - Modeled|) between observed and modeled subtidal water surface elevations (m) at the monitoring stations Terry Cove and Blue Angeles Park.

Statistical Parameters	Blue Angels Park		Terry Cove	
	Observed - Modeled	|Observed - Modeled|	Observed - Modeled	|Observed - Modeled|
Minimum	-0.13	0.00	-0.1	0.00
Maximum	0.18	0.18	0.05	0.10
Mean	0.00	0.03	-0.02	0.02
Standard Deviation	0.04	0.03	0.03	0.02
1st Quartile	-0.02	0.01	-0.04	0.01
Median	0.00	0.02	-0.02	0.02
3rd Quartile	0.02	0.04	0.00	0.04

Table 3.3 Statistical summary of Q_F (m^3 s^{-1}) and F_S (kg s^{-1}) computed using Eulerian decomposition method through five cross sections (Fig. 3.1): Perdido Pass (section A-A), the Perdido Pass complex (section B-B), Dolphin Pass (section C-C), the Wolf-Perdido canal (section D-D), and the lower Perdido Bay (section E-E) .

Statistical Parameters	Perdido Pass		Perdido Pass complex		Dolphin Pass		Wolf-Perdido canal		Lower Perdido Bay	
	Q_F	F_S	Q_F	F_S	Q_F	F_S	Q_F	F_S	Q_F	F_S
Minimum	-619	-13480	-873	-14810	-286	-6789	-127	-2181	-777	-11430
Maximum	180	6289	139	4020	272	7393	51	804	94	2198
Mean	-42	-527	-34	113	16	648	-14	-309	-50	-360
Standard Deviation	98	2787	95	1862	121	2924	25	472	76	1302
1st Quartile	-101	-2114	-66	-713	-75	-1474	-29	-570	-71	-921
Median	-40	-506	-15	430	3	44	-12	-231	-36	-125
3rd Quartile	18	1118	21	1153	89	1852	2	11	-10	327

Table 3.4 Correlation coefficients of F_E (kg s^{-1}), F_S (kg s^{-1}), Q_F (m^3 s^{-1}), Q_{in} (m^3 s^{-1}), Q_{out} (m^3 s^{-1}), F_{in} (kg s^{-1}), and F_{out} (kg s^{-1}) through different cross sections (Fig. 3.1).

Cross sections \ Variables	F_E	F_S	Q_F	Q_{in}	Q_{out}	F_{in}	F_{out}
Combined through section A-A and C-C versus through section B-B	0.06	0.95	0.97	0.38	0.84	0.45	0.75
Combined through section B-B and D-D versus through section E-E	0.91	0.98	0.99	0.75	0.93	0.79	0.89

Note: The cross section A-A is Perdido Pass, B-B is the Perdido Pass complex, C-C is Dolphin Pass, D-D is the Perdido-Wolf canal, and E-E is the lower Perdido Bay (Fig. 3.1).

Table 3.5 Statistical summary of the filtered incoming (Q_{in}, m^3 s^{-1}) and outgoing flows (Q_{out}, m^3 s^{-1}) through five cross sections (Fig. 3.1): Perdido Pass, the Perdido Pass complex, Dolphin Pass, the Wolf-Perdido canal, and the lower Perdido Pass.

Statistical Parameters	Perdido Pass		Perdido Pass complex		Dolphin Pass		Wolf-Perdido canal		Lower Perdido Bay	
	Q_{in} [1]	$-Q_{out}$ [2]	Q_{in}	$-Q_{out}$	Q_{in}	$-Q_{out}$	Q_{in}	$-Q_{out}$	Q_{in}	$-Q_{out}$
Minimum	0.0	0.0	0.0	9.7	0.0	0.0	0.0	0.0	0.0	3.4
Maximum	210.6	619.0	218.4	877.9	289.7	293.5	91.6	133.8	192.0	777.4
Mean	83.6	131.1	100	133.1	59.3	48.2	14.6	26.8	75.0	124.3
Standard deviation	39.0	71.8	46.8	74.8	77.9	58.0	19.7	16.9	38.6	71.4
1st Quartile	57.8	82.8	66.2	92.3	3.2	4.6	1.7	15.8	45.2	84.0
Median	86.0	123.9	105.3	123.8	21.4	20.6	8.5	22.5	76.9	116.5
3rd Quartile	110.4	181.8	129.7	154.9	85.8	81.1	21.2	34.9	103.0	148.9

Note: [1] = flow moving from outside boundary or Wolf Bay into Perdido Bay, [2] = flow moving out from Perdido Bay to outside boundary or Wolf Bay.

Table 3.6 Statistical summary of the filtered incoming (s_{in} in psu) and outgoing salinity (s_{out} in psu) through five cross sections (Fig. 3.1): Perdido Pass, Dolphin Pass, the Perdido Pass complex, the Wolf Perdido canal, and the lower Perdido Bay.

Statistical Parameters	Perdido Pass		Perdido Pass complex		Dolphin Pass		Wolf-Perdido canal		Lower Perdido Bay	
	s_{in}	s_{out}	s_{in}	s_{out}	s_{in}	s_{out}	s_{in}	s_{out}	s_{in}	s_{out}
Minimum	13.0	11.8	9.7	6.8	4.1	5.6	8.6	6.9	7.0	5.5
Maximum	34.0	34.0	34.0	27.0	31.0	31.0	30.0	28.2	30.0	28.3
Mean	33.5	27.7	25.3	19.1	22.1	22.4	19.9	20.8	23.2	18.2
Standard deviation	1.2	2.8	3.5	4.2	5.4	4.8	4.1	4.3	3.8	4.4
1st Quartile	33.3	26.1	23.4	15.7	19.6	20.0	17.1	19	20.8	14.9
Median	33.8	28.1	26.0	20.3	22.7	23.0	20.1	22.3	24.1	19.4
3rd Quartile	34.0	29.5	27.7	22.1	26.0	25.9	22.8	23.7	26.1	21.3

Table 3.7 Linear regression equations developed to predict Q_{in} (m^3 s^{-1}) and Q_{out} (m^3 s^{-1}) through Perdido Pass (cross-section A-A), the Perdido Pass complex (cross-section B-B), the Wolf-Perdido canal (cross-section C-C), and the lower Perdido Bay (cross-section E-E) with regression variables river inflow $(Q_R, m^3 s^{-1})$ from Perdido Bay, filtered water surface elevations at the Gulf of Mexico (W_{gulf}, m), Big Lagoon (W_{bl}, m), and GIWW (W_{giww}, m), and filtered wind stress in the north-south (τ_{NS}, Pa) and east-west (τ_{EW}, Pa) directions

Location	Incoming flow ($Q_{in} > 0$)	Outgoing flow ($Q_{out} < 0$)
Perdido Pass	$Q_{in} = 84.45 + 268.2W_{gulf} - 76.52W_{bl} - 174.4W_{giww} + 8.2 \times 10^5 \tau_{NS}$ $R^2 = 0.36$	$Q_{out} = -84.62 - 0.62\ Q_R + 343.2W_{gulf} - 419.1\ W_{bl} - 1.42 \times 10^6\ \tau_{EW}$ $R^2 = 0.78$
Perdido Pass complex	$Q_{in} = 91.81 - 0.24Q_R + 87.2W_{bl} + 1.95 \times 10^6 \tau_{NS}$ $R^2 = 0.6$	$Q_{out} = -97.85 - 0.83Q_R - 242.8W_{gulf} + 119.3W_{bl} - 1.76 \times 10^5\ \tau_{EW}$ $R^2 = 0.75$
Wolf-Perdido canal	$Q_{in} = 10.58 - 7.78 \times 105\tau_{EW} + 29.02W_{giww}$ $R^2 = 0.44$	$Q_{out} = -15.57 - 0.1Q_R + 2.5 \times 10^5\ \tau_{EW} + 104.6W_{giww} - 89.87W_{bl} + 162.3W_{gulf}$ $R^2 = 0.62$
Lower Perdido Bay	$Q_{in} = 68.1 - 0.19Q_R + 112.3W_{gulf} + 1.49 \times 106\tau_{NS} + 1.08 \times 106\tau_{EW}$ $R^2 = 0.62$	$Q_{out} = -90.57 - 0.75Q_R - 209.9W_{gulf} + 80.92W_{bl} - 2.77 \times 10^6 \tau_{EW}$ $R^2 = 0.79$

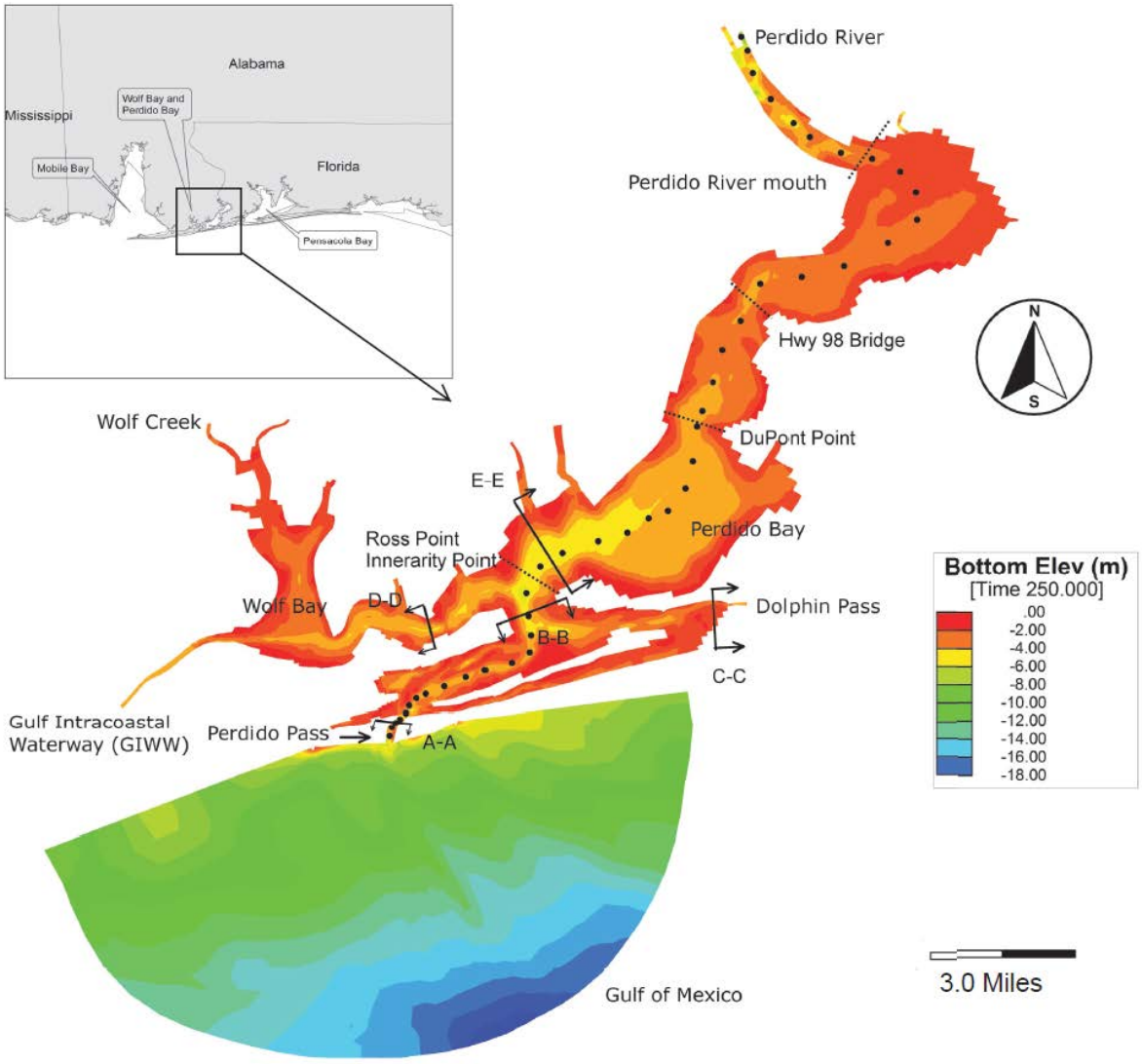

Fig. 3.1 EFDC model domain for Wolf Bay and Perdido Bay showing the colored contours of bottom elevation and five cross sections (A–A, B–B, C–C, D–D, and E–E) where water and salt fluxes were calculated. A centerline from Perdido Pass to Perdido River is represented using a series of dots for studying the salinity profile.

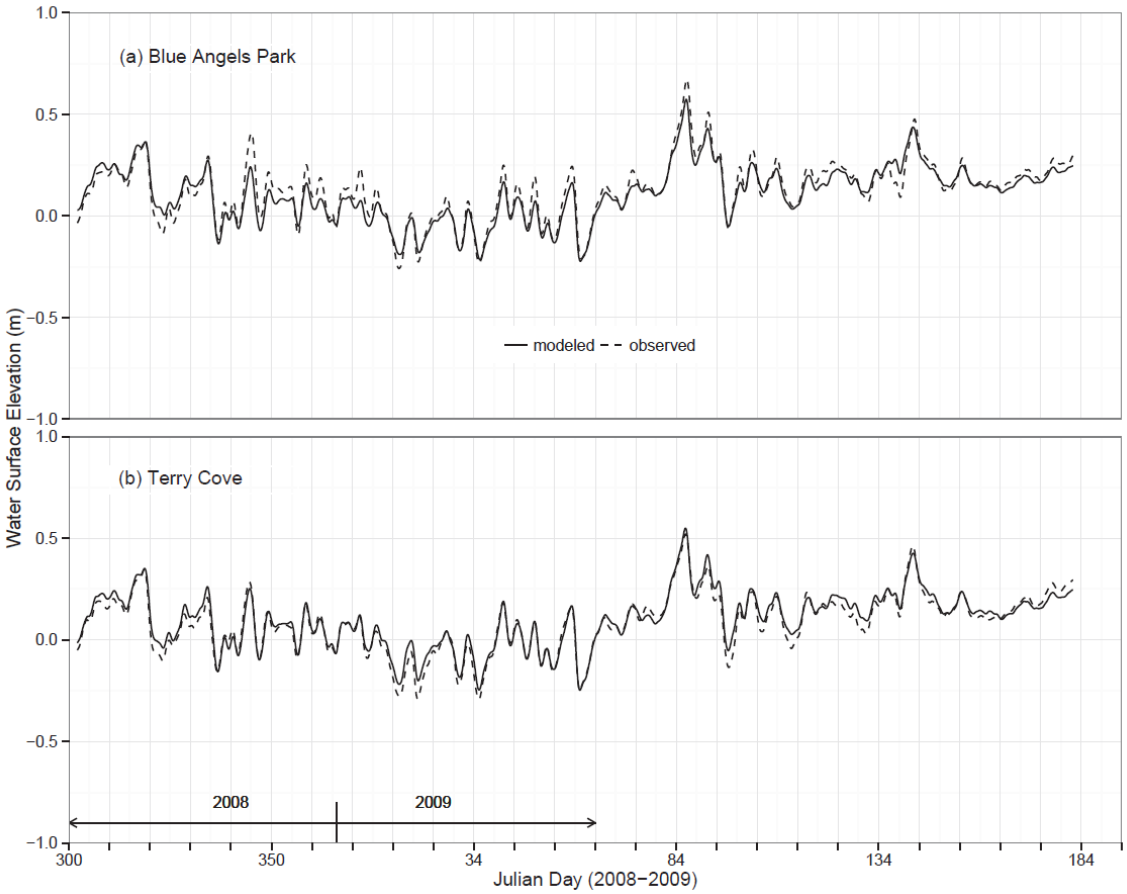

Fig. 3.2 Modeled and observed filtered water surface elevations at station (a) Blue Angels Park and (b) Terry Cove from October 27, 2008 (Julian Day 300) to July 3, 2009 (Julian Day 184).

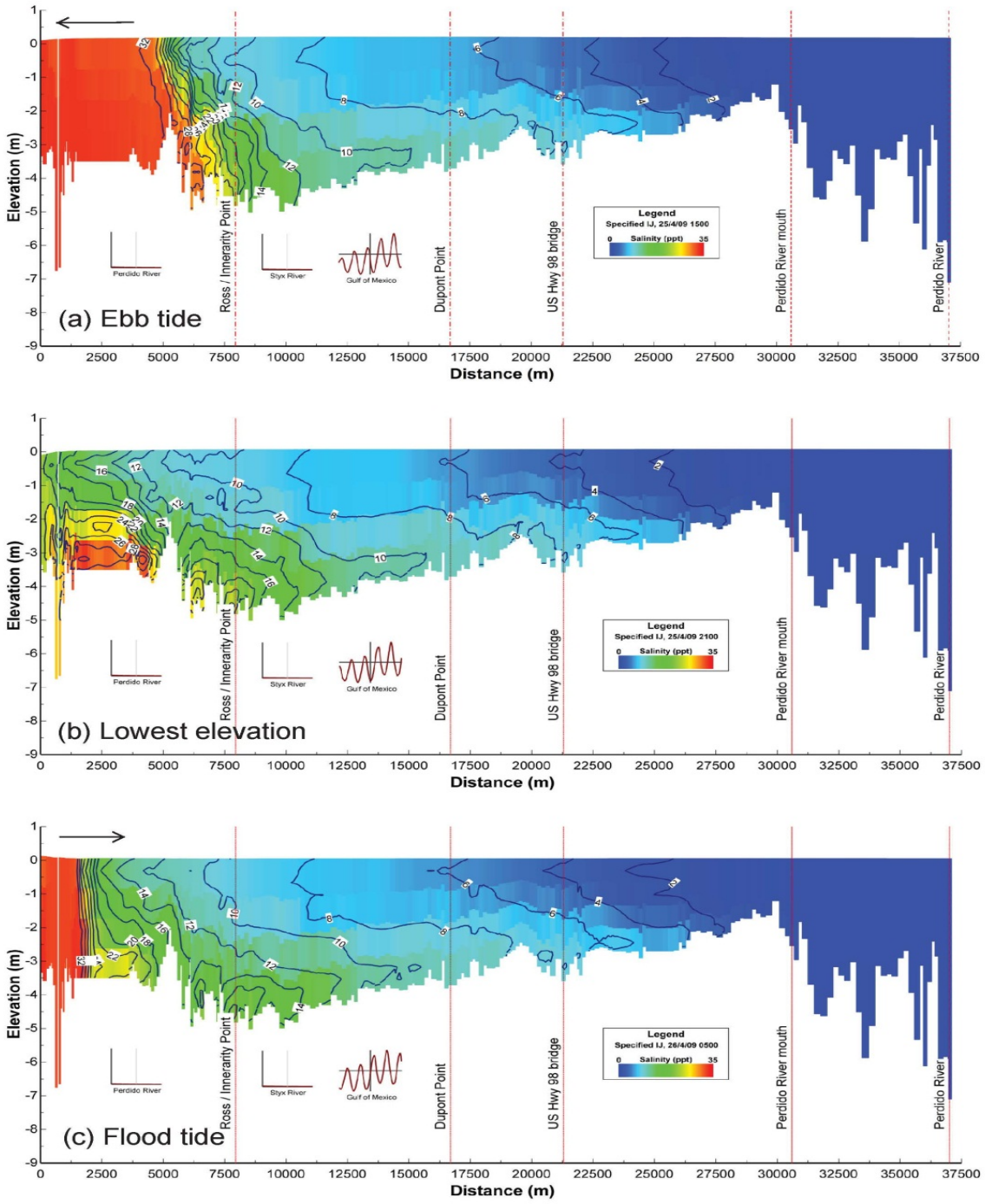

Fig. 3.3 Simulated salinity profile contour plots through the centerline (Fig. 3.1) from Perdido Pass to Perdido River during **low flows** from upstream under (a) ebb tide (15:00 April 25, 2009) (b) lowest water surface elevation (21:00 April 25, 2009), and (c) flood tide (05:00 April 26, 2009) at the Gulf of Mexico.

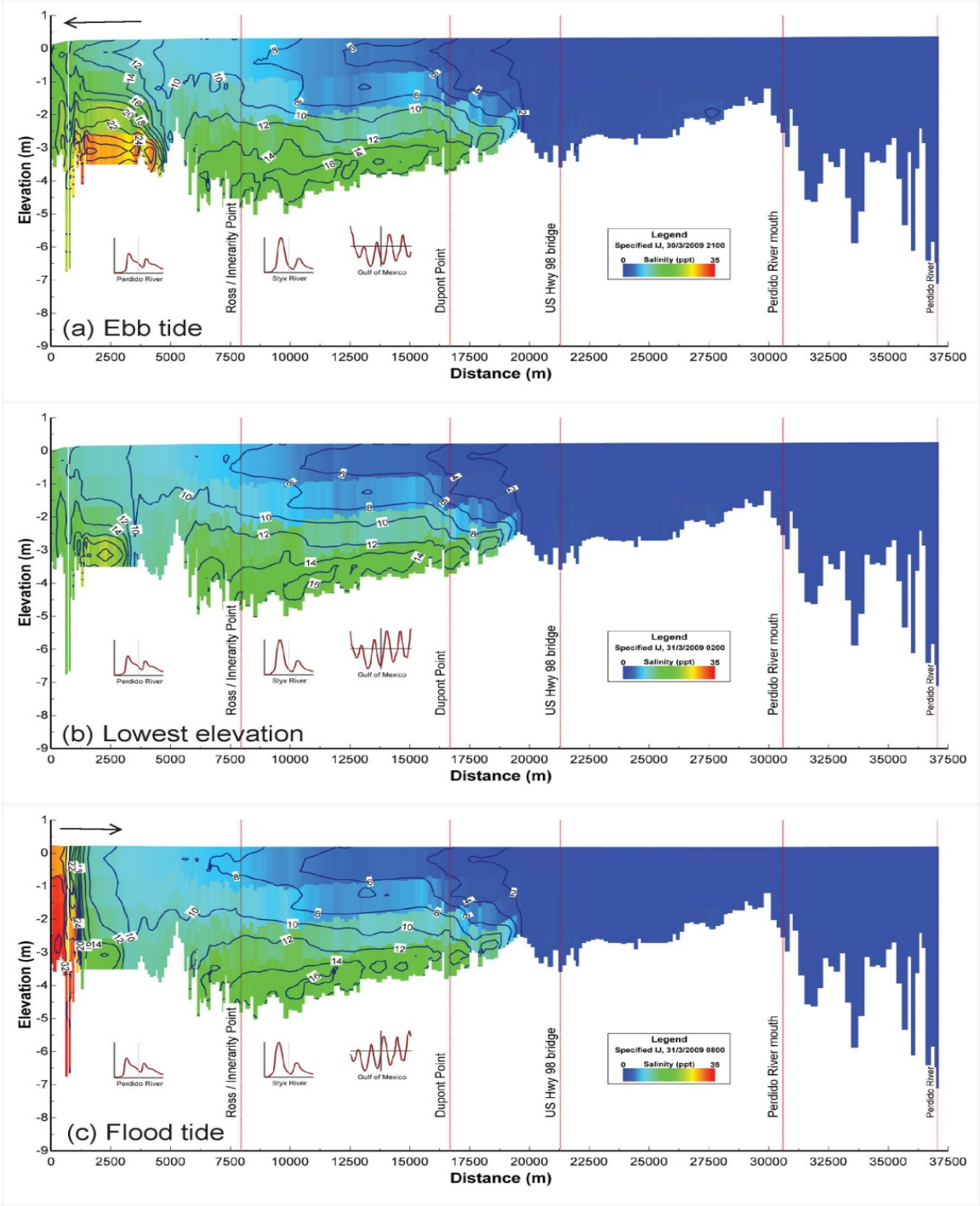

Fig. 3.4 Simulated salinity profile contour plots through the centerline (Fig. 3.1) from Perdido Pass to Perdido River during **high flows** from upstream rivers in Perdido Bay under (a) ebb tide (21:00 March 30, 2009), (b) the lowest water surface elevation (02:00 March 31, 2009) , and (c) flood tide (08:00 March 31, 2009) at the Gulf of Mexico.

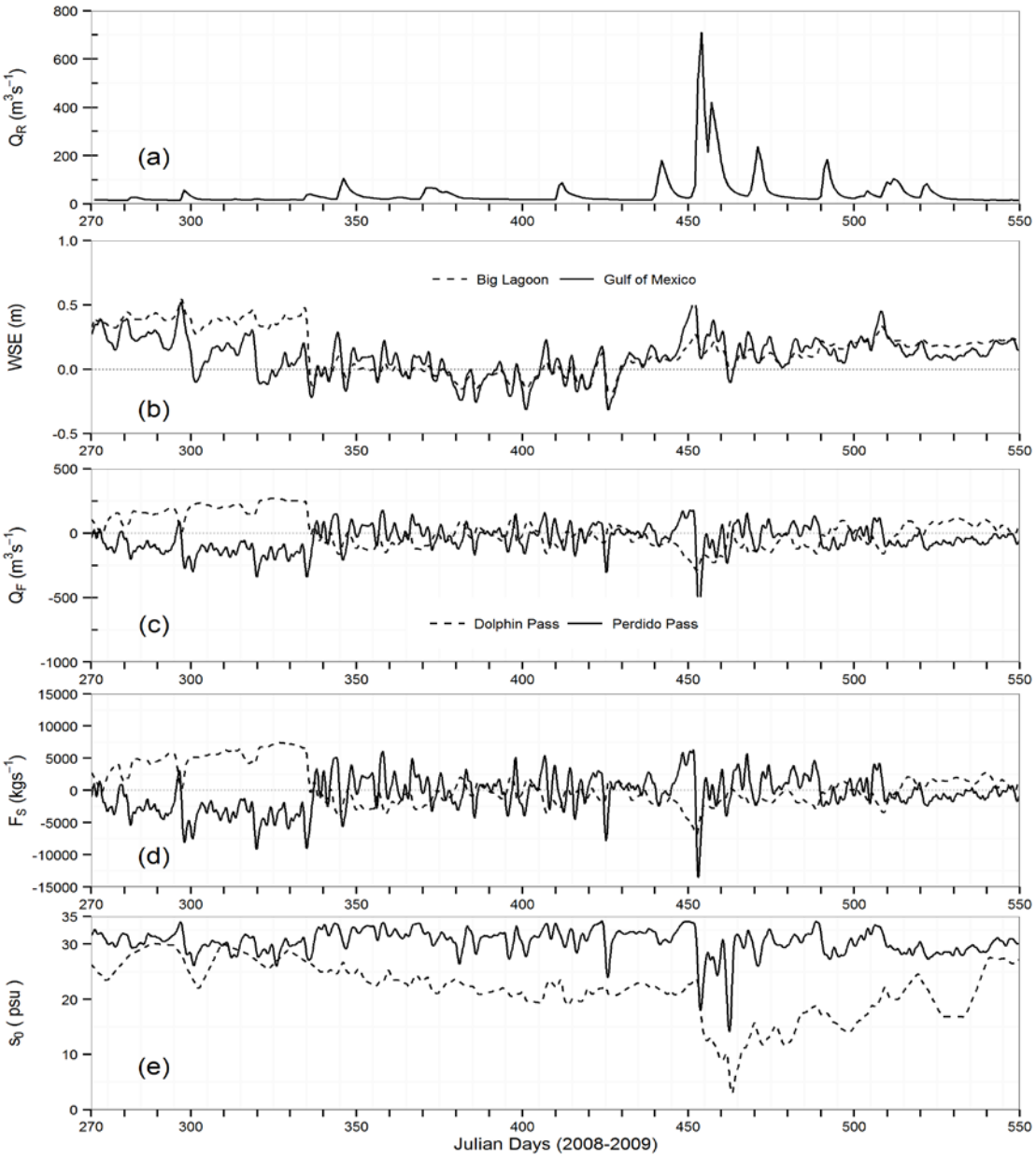

Fig. 3.5 Time series of (a) discharge Q_R (m^3 s^{-1}) from Perdido River and Styx River, (b) water surface elevation (WSE, m) at the Gulf of Mexico (solid line) and Big Lagoon (dashed line), (c) volumetric flow rate Q_F (m^3 s^{-1}), (d) salt transport rate F_S (kg s^{-1}), and (e) cross-sectional average salinity s_0 (psu) at Perdido Pass and Dolphin Pass. Positive and negative fluxes in (c) and (d) indicate flow into and out of the Perdido Bay.

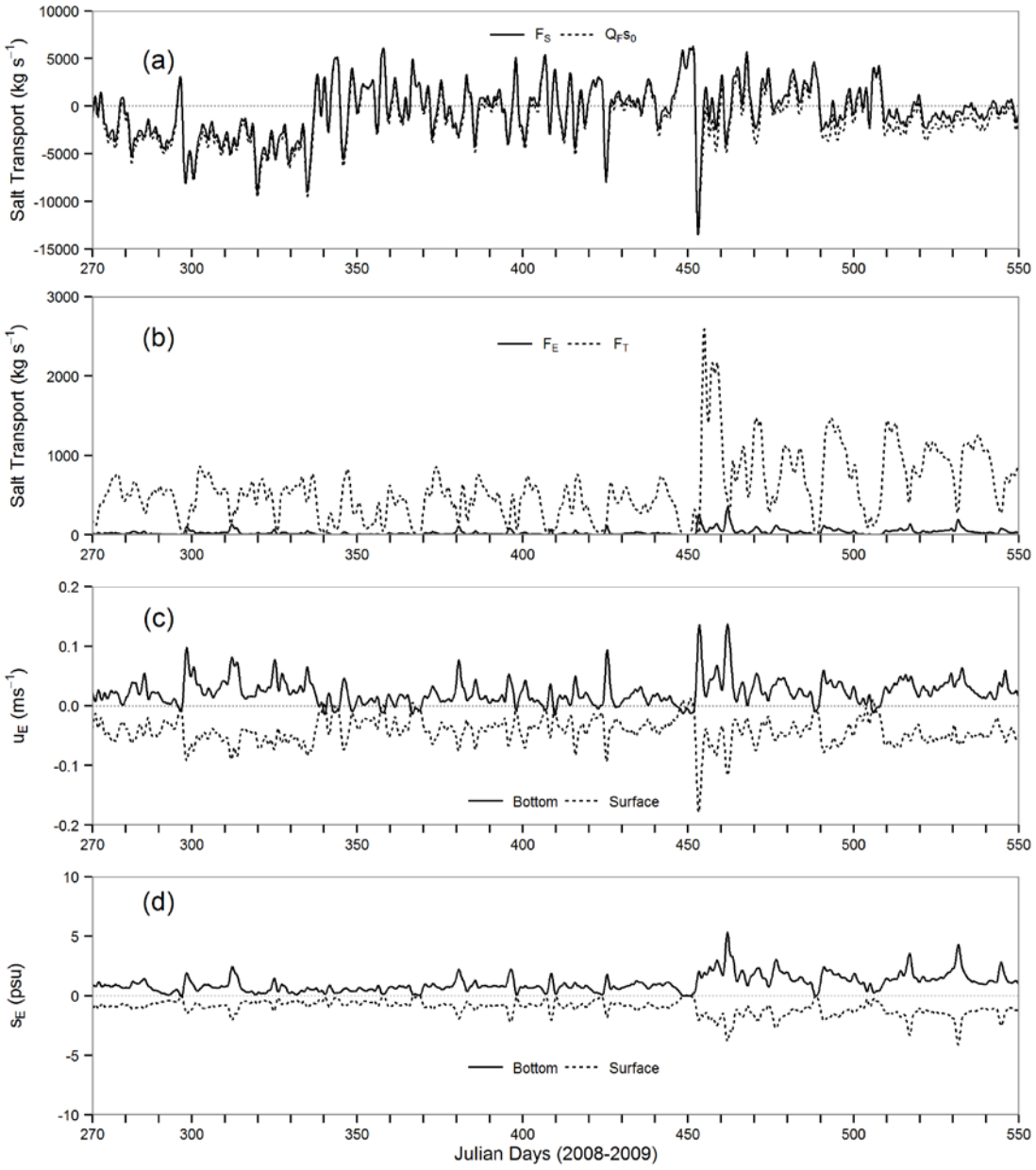

Fig. 3.6 (a) Salt transport rate F_S (kg s^{-1}) and river flow flux component $Q_F s_o$, (b) salt transport components F_E and F_T through the cross section A-A (Perdido Pass), (c) subtidal estuarine exchange flow u_E (m s^{-1}), and (d) salinity s_E (psu) in the surface and bottom layers at the deepest channel cell of Perdido Pass.

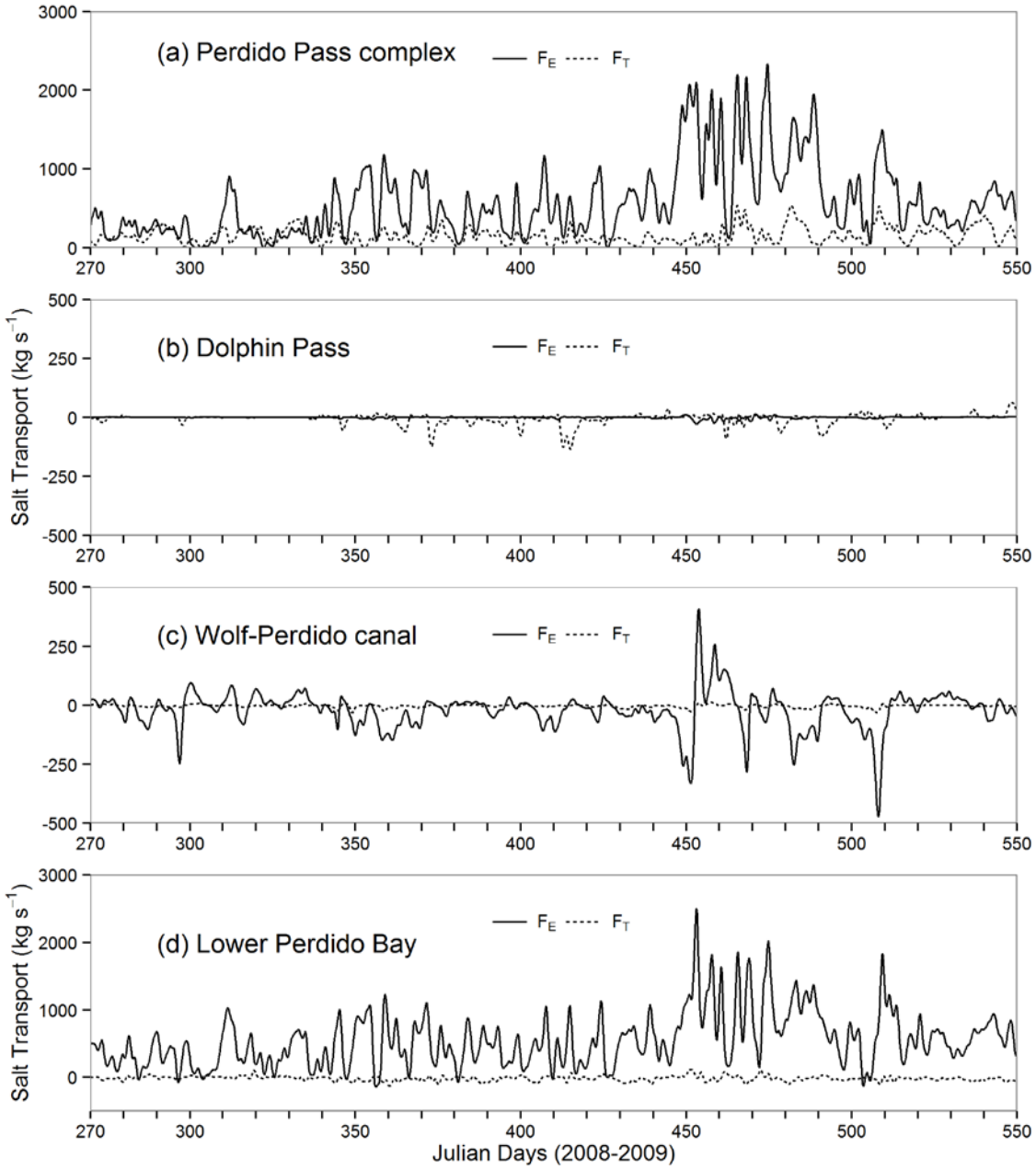

Fig. 3.7 Shear dispersion (F_E) and tidal oscillatory salt transport (F_T) through four cross sections (Fig. 3.1): (a) Perdido Pass complex (section B-B), (b) Dolphin Pass (section C-C), (c) Wolf-Perdido canal (section D-D), and (d) Lower Perdido Bay (section E-E).

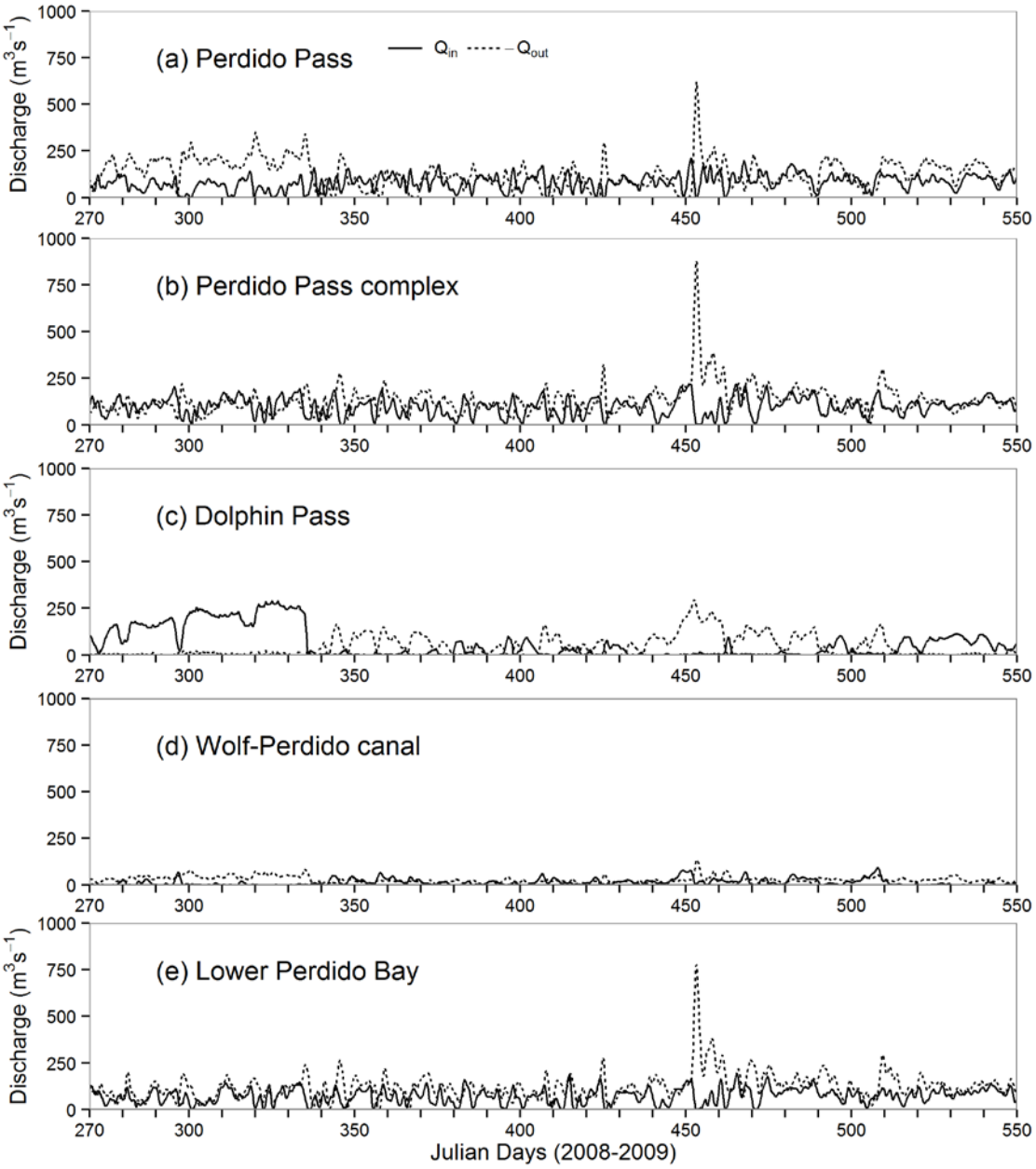

Fig. 3.8 Low-pass filtered isohaline total exchange flow (TEF) transport (Q_{in} and $-Q_{out}$ in $m^3\ s^{-1}$) through five cross sections (Fig. 3.1): (a) Perdido Pass (section A-A), (b) Perdido Pass complex (section B-B), (c) Dolphin Pass (section C-C), (d) Wolf-Perdido canal (section D-D), and (e) Lower Perdido Bay (section E-E).

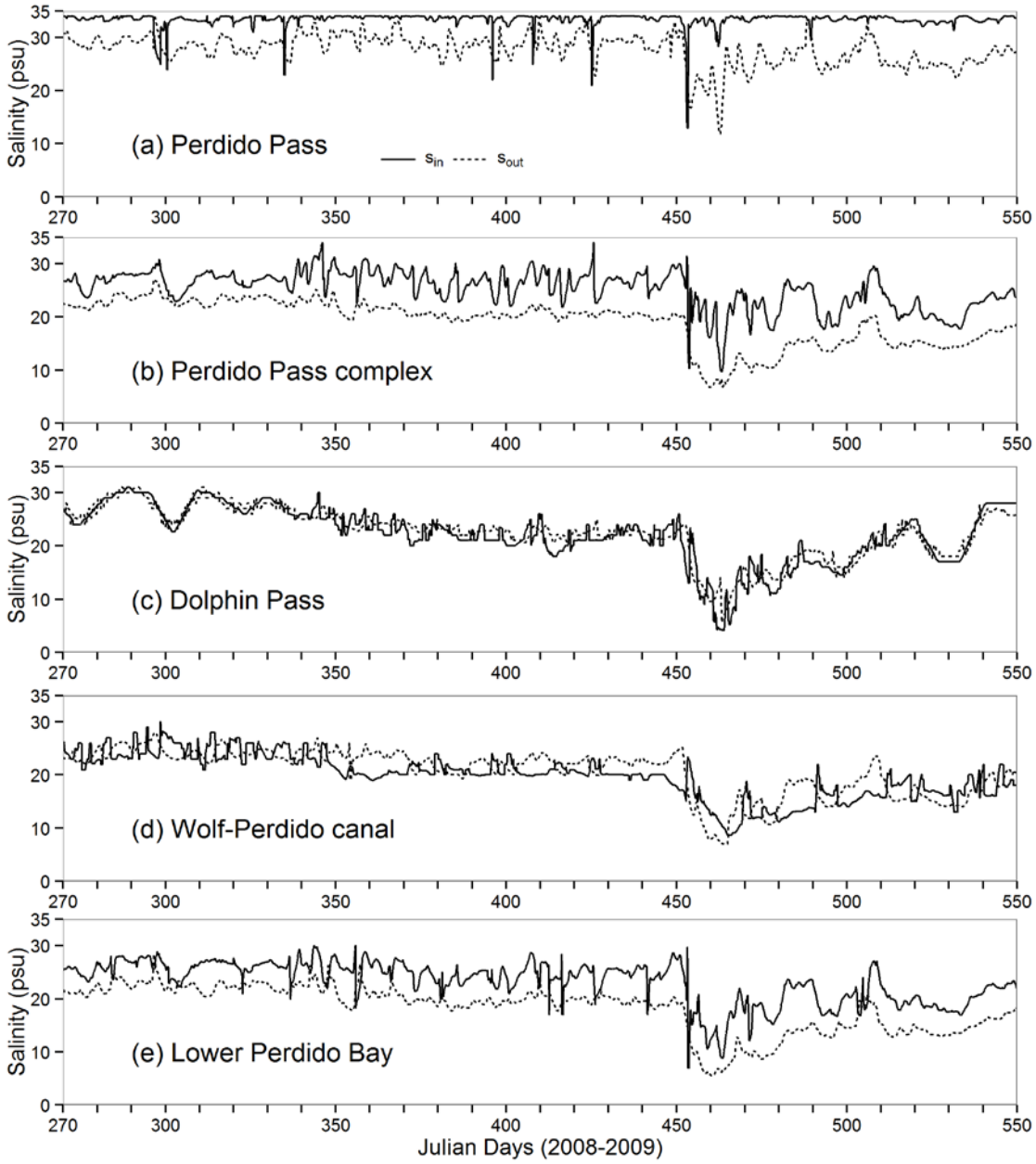

Fig. 3.9 Low-pass filtered isohaline total exchange flow (TEF) salinity (s_{in} and s_{out} in *psu*) through five cross sections (Fig. 3.1): (a) Perdido Pass (section A-A), (b) Perdido Pass complex (section B-B), (c) Dolphin Pass (section C-C), (d) Wolf-Perdido canal (section D-D), and (e) lower Perdido Bay (section E-E).

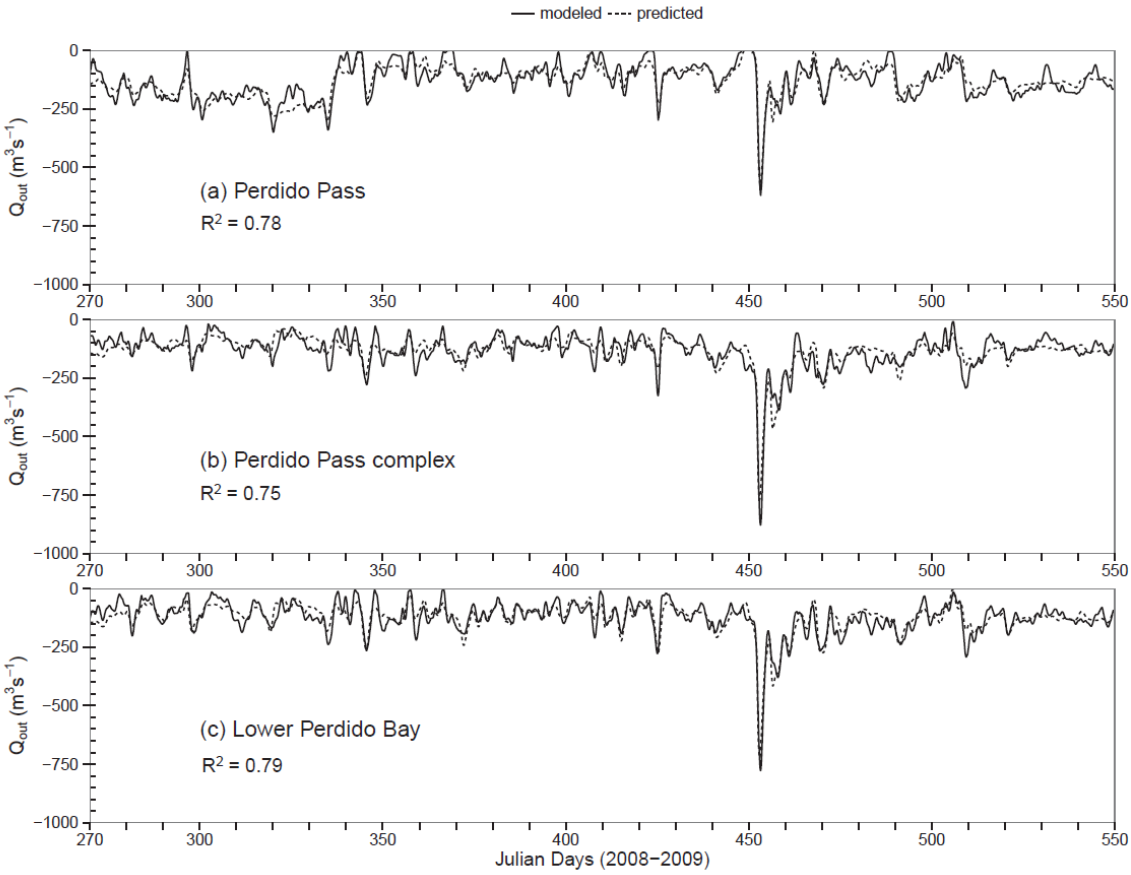

Fig. 3.10 Q_{out} calculated from EFDC model output (solid) and predicted (dashed) from regression equations (Table 3.6) through three cross sections (Fig. 3.1): (a) Perdido Pass (section A-A), (b) Perdido Pass complex (section B-B), and (c) lower Perdido Bay (section E-E).

Chapter 4. Numerical Simulation of Flow Dynamics in a Tidal River under various Upstream Hydrological Conditions

4.1 Abstract

A three-dimensional Environmental Fluid Dynamics Code model was developed for a 17 km segment of the Mobile River. The model external forcing factors include river inflows from upstream, tides from downstream and atmospheric conditions. The model was calibrated against measured water levels, velocities, and temperatures from 26 April to 29 August 2011. The Nash-Sutcliffe coefficients for water levels were greater than 0.94 and for water temperatures ranged from 0.88 to 0.99. The calibrated model was extended approximately 13 km upstream for simulating unsteady flow, dye, and temperature distributions in the Mobile River under different upstream inflows and downstream harmonic tides. Velocity profiles and distributions of flow, dye, and temperature at various locations were analyzed and show that flow recirculation could only occur under small inflow (50 $m^3 s^{-1}$) when downstream tides control the flow pattern in the Mobile River. The model results reveal complex interactions among discharges from a power plant, inflows, and tides.

4.2 Introduction

Tides are the major forcing in an estuary and, along with freshwater inflows, control the vertical and horizontal distributions of salinity (Ji 2008). The tide entering into rivers behaves as a wave progressing upstream, increasingly distorted and eventually extinguished by bottom friction (Godin 1999). The impact of tides on a tidal river depends on various factors such as the distance from river mouth (where it meets the ocean), the water depth, the channel geometry, and the duration and magnitude of a tidal cycle. Because of the variations in those factors from one river to another, tides may influence the water levels for just a mile to as much as several dozen miles. In tidally influenced rivers, the tides from the ocean control the overall flow pattern in the river and the periodic motion is observed in the river. During the flood tide (rising tide), estuary receives water from the ocean and water level rises (Ji 2008) and increases salinity in the tidal river. On a time scale of hours, advection of freshwater during the ebb tide and salt water intrusion during the flood tide determine dynamics of fundamental parameters of the water column in an estuary, such as salinity (Uncles and Stephens 1996; Montani et al. 1998), nutrients (Hernandez-Ayon et al. 1993). Therefore, oceans where the environmentally influenced events such as oil spill have occurred would pose a threat to the river system connected to it where tidal impacts are detected. The winds play a major role in influencing the salinity distribution, circulation, and primary productivity in a tidal estuary (Mann and Lazier 1996; Yin et al. 2004; Xia et al. 2007), but the wind effects on a narrow tidal river segment far upstream from river mouth may not be significant. Xia et al. (2007) studied the impact of winds on the salinity plume in the Cape Fear River estuary and reported that strong winds reduced the surface plume size whereas moderate

winds could reverse the flow direction of plume. Xia et al. (2011b) studied the effect of wind on the Gulf of Mexico estuary plume orientation, area, width, length, and depth, and reported that the plume is largest for northerly (offshore) winds. The wind blowing against the river flow direction would act as a catalyst to the tides and as a result the tidal effects can be observed at a significant distance from the river mouth.

The Mobile River is a tidally influenced river in the southern Alabama, USA. The Mobile River is formed from Tombigbee River and Alabama River and is approximately 72.4 km long before it discharges into the Mobile Bay and the Gulf of Mexico (Fig. 4.1). Schroeder et al. (1990) examined the roles of both river runoff and wind stress on stratification-destratification patterns in the Mobile Bay, Alabama. Schroeder et al. (1990) reported that the principal source of river runoff is the Mobile River system, which enters at the northern end of the bay and accounts for approximately 95% of the freshwater input. Chadwick and Feminella (2001) studied the influence of salinity and temperature on the growth and production of a freshwater mayfly in the Lower Mobile River. Field observations and laboratory experiments were used to understand the production of mayfly. Kim and Park (2012) studied the water and salt exchange in the Mobile Bay and the Gulf of Mexico estuary using the Environmental Fluid Dynamics Code (EFDC) model. Their EFDC model was primarily focused on the Mobile Bay and adjacent portion of the northern Gulf of Mexico and included the Mobile River to represent the freshwater inflows into the Mobile Bay. The grid cells used to represent the Mobile River were very coarse and didn't include the withdrawal and return flow of an existing power plant operation. Hamrick and Mills (2000) developed and used

an EFDC model to simulate water temperature distributions in Conowingo Pond that has thermal discharges from the Peach Bottom atomic power plant.

In the United States, 90 percent of electricity comes from thermoelectric power plants that boil water to create steam and then spins turbines to generate electricity. The heat used to boil water can come from burning a fuel such as coal, natural gas, and oil; and from nuclear reactions. Therefore, a cooling system is required to cool steam back into water before it can be reused to produce more electricity or discharged to adjacent water body (e.g., rivers, lakes, estuaries, or the ocean). The once-through cooling systems were initially the most popular and widespread in the eastern U.S.A. The once-through cooling system withdraws the ambient water from the intake canal and releases warmer water into the discharge canal connecting to nearby water body. Colder water cools the steam more effectively and allows more efficient electricity generation (U.S. DOE 2008). It is essential to understand whether there is any recirculation of warmer water from the discharge canal to the intake canal. There are several questions that need to be answered for the power plant design and operations using cooling water from nearby tidal rivers. 1) Is there any warmer water recirculation from the discharge canal back to the intake canal during normal flow conditions? 2) Under what upstream inflows does the recirculation occur? 3) Is there any recirculation caused by the tides from downstream? In this paper, we attempt to answer these three recirculation related questions by examining the flow rates, velocity profiles, temperatures, and dye distributions in Mobile River using calibrated EFDC model.

To accurately simulate tidal and residual circulation in coastal seas and estuaries driven by tides, winds, and density gradients, the numerical model must be able to

accurately and efficiently resolve the dynamics of various vertical boundary layers and the complex geometry and bottom topography (Liu et al. 2007). This paper presents the application of a calibrated three dimensional (3D) EFDC hydrodynamic model to investigate the flow patterns in a 17 km segment of the Mobile River near a power plant (Figs. 4.1 and 4.2) and possible recirculation of warmer water from the discharge canal back to the intake canal under various freshwater inflows at the upstream boundary and tidal water surface elevations at the downstream boundary. The power plant has a once-through cooling system that withdraws the ambient water from the intake canal and releases warmer water into the discharge canal (Fig. 4.2) connecting to the Mobile River. The discharge from the power plant is eventually dispersed and diluted with a large volume of the water from upstream inflow in the Mobile River. Two separate EFDC models were developed; one was used for the model calibration and another for the sensitivity (scenario) analysis. The calibrated EFDC model was extended about 13 km upstream and used to explore flow circulation patterns in the Mobile River near the intake and discharge canals of a power plant under different hydrological (inflow) scenarios. Dye simulation experiments were conducted and dye was continuously released from discharge canal to trace the path of the dye released. The flow patterns and dye distributions in the river simulated for different scenario runs revealed the complex flow interaction between the downstream tides and upstream inflows during the high and low inflow conditions. The existence of a power plant in this tidally influenced Mobile River adds an interesting perspective to the overall study. During the low inflow conditions, the tides from the downstream may push the water towards upstream and as a result warmer water from the discharge canal may reach the intake canal (recirculation) thereby

decreasing the overall efficiency of the power plant. This paper quantifies specific hydrologic conditions when and where the flow recirculation might occur.

4.3 Materials and Methods

4.3.1 Study Area

The 3D EFDC model was developed to simulate unsteady flow patterns and temperature distributions in the Mobile River where a power plant is located nearby (Fig. 4.1). The EFDC model was developed for a segment (about 17 km, Fig. 4.1) of the Mobile River near Bucks, Alabama, including the intake canal and discharge canal of the power plant, and for the model calibration. The upstream boundary of the calibration model was at the river cross section (Upstream-1 in Fig. 4.1b) where the U.S. Geological Survey (USGS) streamflow gauging station at Bucks, Alabama, is located. The downstream boundary is located at the intersection of the Mobile River and the I-65 Bridge and approximately 33.8 km upstream from the Mobile Bay. For the sensitivity (scenario) analysis, the upstream boundary was extended about 13 km northwards to the Upstream-2 cross section (Fig. 4.1b) where the Tensaw River is split from the Mobile River. The river width in the study area ranged from about 160 to 260 m, and the water depth ranged from about 1 to 18 m.

Although the Mobile River is highly tidally dominant during the summer period, the part of the Mobile River used in this study didn't exhibit distinct salinity influences during the calibration period. The formula relating the salinity and conductivity (UNESCO 1983) was used to calculate the salinity from observed conductivity data. Calculated salinity was about 0.1 PSU during the monitoring period of 2010 and 2011.

Thus, salinity module in EFDC model was not activated; quantification and interpretation of the salinity intrusion in Mobile River were beyond the scope of this study.

The study river is tidally influenced because of its connection to the Mobile Bay and the Gulf of Mexico at the downstream. The hydrodynamic conditions in the Mobile River are influenced by fluctuations of the water levels in the Mobile Bay, which result from the interaction of tides and river discharges. Two distinct flow patterns can be detected in the Mobile River during spring and summer. Under the large inflows from upstream in spring season, there is minimal tidal impact from downstream that results in fast flushing of freshwater in the Mobile River towards downstream. However, under the low inflows in summer season, the downstream tides dominate and control the flow pattern and a periodic tidal pattern is observed in the Mobile River. The presence of tidal influence on the study area is supported by observed water surface elevations in the Mobile River. Harmonic analysis was performed on the time series of water surface elevation at three monitoring stations (Bucks station, discharge canal, and intake canal) in 2010 and 2011. It was found that the dominant tidal constituents on the monitoring stations during the summer season were lunar diurnal constituents [O1, K1, (Pugh 1996), Kim and Park (2012)] and were consistent with the constituents of the tides in the Mobile Bay.

4.3.2 Numerical Model

Two site specific 3D EFDC hydrodynamic models were developed and applied in this study to understand the hydrodynamics and transport of temperature and dye in the Mobile River (called Mobile EFDC model). The EFDC model is a general purpose

modeling package for simulating 3D flow, transport, and biogeochemical processes in various surface water systems including rivers (Shen and Lin 2006; Jeong et al. 2010), lakes (Ji and Jin 2006), estuaries (Martin et al. 2001; Wang et al. 2010; Kim and Park 2012; Devkota et al. 2013), reservoirs (Caliskan and Elci 2009), wetlands, and coastal regions. The EFDC model was originally developed at the Virginia Institute of Marine Science. The model solves the vertically hydrostatic, free-surface, turbulent-averaged equations of motions for a variable-density fluid. The EFDC model uses sigma vertical coordinate and curvilinear orthogonal horizontal coordinates. The Mellor-Yamada level 2.5 turbulence closure scheme (Mellor and Yamada 1982) is used to calculate turbulence parameters; vertical turbulent momentum diffusion (A_v) and mass diffusion coefficient (A_b). EFDC employs a second order accurate spatial finite difference scheme on a staggered or C grid to solve the momentum equations (Hamrick 1992b). The time integration is implemented using a second-order accurate three-time level, semi-implicit finite difference scheme with an internal-external mode splitting scheme to separate the internal shear or baroclinic mode from external free surface gravity wave or barotropic mode (Hamrick 1992b). The EFDC model implements a second-order, accurate in space and time, mass conservation, fractional step solution scheme for the Eulerian transport equations for salinity, temperature, and other constituents. Details of governing equations and numerical schemes for EFDC hydrodynamic model are given by Hamrick (1992a). The updated EFDC version with the graphic user interface EFDC-Explorer from the Dynamic Solutions International, LLC (http://efdc-explorer.com/) was used for the study. The horizontal eddy viscosity, A_H is calculated using the Smagorinsky subgrid

scale scheme (Smagorinsky 1963), which can be written in the two-dimensional Cartesian coordinate as:

$$A_H = C\Delta x\Delta y\left[\left(\frac{\partial u}{\partial x}\right)^2 + \left(\frac{\partial v}{\partial y}\right)^2 + \frac{1}{2}\left(\frac{\partial u}{\partial y} + \frac{\partial v}{\partial x}\right)^2\right]^{\frac{1}{2}} \tag{4.1}$$

where C is horizontal mixing constant, Δx and Δy are model grid sizes in x and y directions.

The EFDC model has features specifically designed for thermal simulation of a power plant cooling systems. In EFDC, the cooling water withdrawal from a nearby river or lake and discharge from the plant are represented by the withdrawal and return boundaries and can be represented by specifying the flow rate Q at the withdrawal and return cells (Hamrick and Mills 2000):

$$\begin{aligned} Q &= -Q_{cool} \quad \text{for the intake} \\ Q &= Q_{cool} \quad \text{for the outlet (discharge canal)} \end{aligned} \tag{4.2}$$

where Q_{cool} is the flow rate for the once-through cooling system of a power plant.

The thermal sinks and sources Q_H are specified in the transport equation for heat:

$$\begin{aligned} Q_H &= -Q_{cool}\,\rho_w\,c_{pw}\,T_1 \quad \text{for the intake} \\ Q_H &= Q_{cool}\,\rho_w\,c_{pw}\,(T_1 + \Delta T) \quad \text{for the outlet (discharge canal)} \end{aligned} \tag{4.3}$$

where ρ_w is the density of the water, c_{pw} is the specific heat of the water, T_1 is the ambient intake temperature and ΔT is the temperature rise of a power plant.

4.4 Model Setup

The horizontal model grids developed for the Mobile EFDC model were based on NAVD 1988 horizontal datum and Universal Transverse Mercator (UTM) projection coordinates system. The horizontal grids were developed using the shoreline GIS shapefile of the Mobile River downloaded from AlabamaView (http://www.alabamaview.org/). The shoreline data were further validated using AutoCAD data and hydrographic data developed by the U.S. Army Corps of Engineers.

The EFDC model developed for model calibration has a total of 2,454 horizontal grids and six horizontal layers along depth direction (a total of 14,724 3D computational cells). Bottom elevations of model grids are shown as color contours in Fig. 4.1, and ranged from -17.8 to -0.8 m below mean sea level (MSL) using NAVD 1988 datum. There are a total of 2,297 horizontal grids in the Mobile River. The intake canal and discharge canal of the power plant were modeled using additional 77 and 80 horizontal grids or 462 and 480 3D computational cells (Fig. 4.2), respectively. The grid size Δx along the cross section ranged from 9.4 to 74.1 m and Δy along the flow direction ranged from 10 to 114 m. The average Δx is 30 m and the average Δy is 49 m for the Mobile EFDC model.

4.4.1 Boundary Conditions

The upstream boundary for the model calibration, located at the Bucks USGS gauging station (Upstream-1 in Fig. 4.1), includes time series of measured discharges and temperatures (provided by an independent field sampling group). The operation of the power plant is included in the EFDC model using the withdrawal and return boundaries, which include the inflows withdrawn from the intake canal, the discharges of warm water

to the discharge canal, and the temperature rises between the discharge canal and the intake canal. The temperatures at the intake canal and discharge canal were measured at two depths: near the surface and near the bottom. The power plant has five generating units, the intake 1 (W1 in Fig. 4.2) withdraws the cooling water for the two units and the intake 2 (W2 in Fig. 4.2) for remaining three units. The intakes W1 and W2 are located at the separate locations in the intake canal (Fig. 4.2). Therefore, the withdrawal of cooling water and discharge of warmer water from the power plant were modeled using two withdrawal and return boundaries for the separate intake and discharge locations (Fig. 4.2). The downstream boundary of the EFDC model was located at the I-65 Bridge and included the time series of measured water surface elevations and temperatures as hydrostatic pressure (water level) and temperature boundaries.

4.4.2 Atmospheric Forcing

The meteorological parameters required by the EFDC model are atmospheric pressure (millibars), air temperature (^{o}C), dew point temperature (^{o}C) or relative humidity (decimal), rainfall (mm), cloud cover (decimal), evaporation (mm, optional), solar radiation (W/m^2), wind speed (m s^{-1}), and wind direction (degree from the north). The meteorological data recorded at the Mobile Regional Airport (Fig. 4.1) were used for the Mobile EFDC model. The hourly data from the airport were obtained from the Southeast Regional Climate Center (SERCC). The data obtained from SERCC didn't include the solar radiation data that are required to run the EFDC model. Solar radiation data for the study were obtained from the Agricultural Weather Information Service, Inc. in Alabama. The hourly weather data allow the EFDC model to accurately compute heat exchange

through the water surface (heating or warming during the day and cooling during the night) at a short time interval.

4.5 Model Calibration Results

The EFDC model developed for the Mobile River was calibrated from 26 April (Julian day 115) to 28 August 2011 (Julian day 240). The calibration period was chosen based on the available measured flow, temperature, meteorological, and power plant operation data. Observed streamflow data at Bucks from 2008 to 2012 were obtained and analyzed. The data analysis shows that probability distributions of observed streamflow in 2011 and from 2008 to 2012 were similar and statistical parameters of streamflow have similar magnitudes. It was concluded that 2011 used for model calibration was a typical year in terms of streamflow at Bucks. The model was calibrated for velocity (m s^{-1}), water surface elevation (m), and temperature (°C) using observed data collected at several monitoring stations (Fig. 4.1) throughout the Mobile River. Two commonly used calibration parameters; bottom roughness coefficient and the dimensionless horizontal momentum coefficient were calibrated to obtain the best match between observed and modeled water surface elevations. In this study, the roughness coefficient of 0.01 m was found by calibration and falls in the same range of the coefficient values used by other studies (Bai and Lung 2005; Zou et al. 2008) . The dimensionless horizontal momentum coefficient (*C* in Equation 4.1) was calibrated to be 0.2 for the Mobile EFDC model and used to compute the horizontal momentum diffusion coefficient using the Smagorinsky formula (Smagorinsky 1963).

4.5.1 Model Evaluation Criteria

Several statistical parameters can be used to evaluate the performance of model calibration (Ji 2008), and three error parameters were used in this study: (a) mean absolute error (MAE), (b) root-mean-square error (RMSE), and (c) Nash-Sutcliffe Coefficient [NSE, McCuen et al. (2006), Nash and Sutcliffe (1970)].

The MAE is defined as the mean of absolute differences between observed and predicted values:

$$MAE = \frac{1}{N}\sum_{n=1}^{N}|O^n - P^n| \tag{4.4}$$

where N is the number of observation and predication data pairs, O^n is the value of the nth observed data, and P^n is the nth predicted value from the model.

The RMSE is a good measure of model accuracy that is commonly used to evaluate model performance. The RMSE is defined as the square root of the mean squared errors or differences between observed and predicted values:

$$RMSE = \sqrt{\frac{1}{N}\sum_{n=1}^{N}(O^n - P^n)^2} \tag{4.5}$$

The NSE is typically used to assess the predictive power of hydrological models. It is defined as:

$$NSE = 1 - \frac{\sum_{n=1}^{N}(O^n - P^n)^2}{\sum_{n=1}^{N}(O^n - \overline{O})^2} \tag{4.6}$$

The NSE can range from -∞ to 1. An efficiency of 1 (NSE = 1) corresponds to a perfect match between modeled values and observed data. An efficiency of 0 (NSE = 0) indicates that the model predictions are as accurate as the mean of the observed data, whereas as efficiency less than zero (NSE < 0) occurs when the observed mean is a better predictor than the model. The closer the model efficiency is to 1, the more accurate the model is.

4.5.2 Water Level Calibration

Fig. 4.3 shows the time series plot of measured and simulated water surface elevations (WSE) at the WS1 monitoring station from 30 April to 28 August (Julian day 120 to 240) 2011. The bottom elevation at WS1 is -3.95 m below MSL, therefore, the water depth at WS1 varied from 3.8 to 5.7 m from Julian day 126 (6 May 2011) to 240 (28 August) when downstream tides primarily controlled the variations of the water level (Fig. 4.3). The average absolute difference (|Observed - Modeled| in Table 1) between observed and modeled WSE at WS1 is 0.04 m with a maximum difference of 0.50 m. Seventy-five percent of the absolute differences of WSE are less than 0.06 m (Table 4.1). The root mean square error (RMSE) for WSE at the WS1 monitoring station is 0.06 m. Water surface elevations at WS2 were measured near the mouth of the discharge canal (Fig. 4.1). The average difference (Observed – Modeled in Table 4.1) between observed and modeled WSE at WS2 is -0.07 m (or modeled is slightly larger than observed) with a maximum difference of 0.34 m. The NSE values for both monitoring stations (WS1 and WS2) are greater than 0.94 (Table 4.3). The statistical summary for the observed and modeled WSE at the monitoring stations WS1 and WS2 is presented in Table 4.1.

4.5.3 Temperature Calibration

The temperature data available for model calibration were not measured continuously but only collected for 4 weeks during each of three seasons (spring, summer, and fall) in 2011. Spring data were measured from 9 May to 7 June 2011. Summer data were measured from 12 June to 9 August 2011, and fall data were measured from 19 September to 18 October 2011. Because the model simulation period was from 26 April to 29 August 2011, only the spring and summer data sets were used for the model calibration. The approximate depth of these temperature measurements at the temperature monitoring stations was -2.0 m below MSL, and typically water surface elevations in the simulation domain ranged from 0 to 0.5 m above MSL. Therefore, temperatures measured at the monitoring stations were compared with modeled temperatures at the surface or top layers (Layer 6) at the corresponding grids of the Mobile EFDC model. Fig. 4 shows a time-series plot of observed and modeled surface-layer temperatures at the T1 monitoring station (Fig. 4.1). Overall, the agreement between observed and modeled temperatures at the monitoring stations was good (Fig. 4.4 and Table 4.2). Statistical summary of the differences or absolute differences between observed and modeled temperatures at T1 and T2 (Fig. 4.1) are given in Table 4.2. Median absolute errors between observed and modeled temperatures at T1 and T2 are 0.20 °C and 0.47 °C, respectively.

4.5.4 Velocity Calibration

Acoustic Doppler Current Profiler (ADCP) instruments were used twice (June and August) in 2011 at the Upstream-1 (Fig. 4.1) and a cross section just upstream I-65 bridge (the downstream boundary location). Because the elevation boundary condition (*i.e.*, time-series data of water surface elevations) was used in the downstream boundary of the Mobile EFDC model, the velocity data measured by ADCP were compared with simulated velocities (Fig. 4.5) as part of model calibration.

In June 2011, the velocities near the downstream boundary were measured from 29 June, 9:20 AM, to 30 June, 9:05 AM (approximately one day or 24-hour period). The ADCP data were processed using a VMS user interface module (Kim et al. 2009). Velocity measurements in both June and August were compared with modeled velocities (Fig. 4.5). For the velocity comparison, modeled velocities were extracted at the center grid (where the maximum depth is) in the cross section that is just one row above the downstream boundary of the Mobile EFDC model. Visually, modeled velocities matched reasonably well with observed velocities during 29–30 June and 24–25 August 2011 (Fig. 4.5).

4.6 Model Applications under Different Inflow Scenarios

In order to examine the response of the Mobile River system to different freshwater inflows, and tides, calibrated EFDC model was extended further 13 km upstream from the Bucks station (Upstream-1) to the Upstream-2 cross section (Fig. 4.1), where Tensaw River is split from the Mobile River. Additional 1020 horizontal grids were added into the Mobile EFDC model that was used for the model calibration. The reasons for

extending the upstream boundary northward were availability of bathymetry data from Bucks to Upstream-2 and smaller or no tidal impact at the new boundary. The primary objectives of the scenario studies are to understand possible flow recirculation in the Mobile River, where the power plant has a once-through cooling system that withdraws the cooling water required for its operation from the intake canal.

A data analysis was first performed for the long-term discharges measured at the USGS Bucks gauging station (Upstream-1 in Fig. 4.1). The astronomical tides of the Mobile Bay cause significant tidal cycles of water levels at the Bucks station (approximate period of 24.84 hours). Filtered flow data at Bucks from 2008–2012 were also obtained from the USGS web site. A Godin low-pass filtering program (Godin 1972) was used by the USGS to remove tidal signals from observed discharges (USGS 2011). The filtered data were available at an hourly interval and observed data were available in a 15-minute interval. Summary of observed and filtered discharges ($m^3 s^{-1}$) at Bucks during 2008–2012 is presented in Table 4.4. Positive discharges in Table 4.4 indicate the flow at Bucks is from upstream to downstream towards the Mobile Bay, and negative discharges reflect tidal effects, i.e., flow from downstream towards upstream. The statistical summary of discharge data at Bucks was performed separately for spring (January to April) and summer (May to September) periods. The mean and median discharges during the summer were about one third of the ones during the spring (Table 4.4). The one percentiles of the summer filtered discharges in both 2011 and 2008–2012 were about 50 $m^3 s^{-1}$ (Table 4.4), which was about one seventh of the mean filtered discharges. Statistical summary in Table 4.4 shows that 2011 used for model calibration was a typical year in terms of observed and filtered discharges at Bucks.

There are two USGS gauging stations with discharge data available that are upstream of the boundary Upstream-2 (Fig. 4.1). The first gauging station is located at Clairborne L&D (lock and dam) near Monroeville in Alabama River and the second one is located at Coffeville L&D in Tombigbee River. The Mobile River is formed from Alabama River and Tombigbee River. However, these gauging stations are very far from the Upstream-2 and the combined discharges measured at those two locations may not be representative freshwater discharges at the Upstream-2 boundary for the scenario runs. Discharges in the Mobile River at the Upstream-2 should be combined discharges for those two rivers excluding discharges to the Tensaw River, which are also not measured. Therefore, the selected inflows based on filtered discharges (Table 4.4) at the USGS Bucks station were used for the scenario runs because of the short distance from Upstream-2 to Bucks. The extended model for scenario runs was tested using 2011 filtered discharges from the USGS Bucks station for the Upstream-2 boundary and keeping all other inputs, model parameters, and boundary conditions unchanged (same as in calibrated model). During the summer months, simulated water surface elevations at WS1 by the extended model were almost the same as simulated elevations (Fig. 4.3) by the calibrated model. The mean absolute errors (Eq. 4.4) for simulated elevations at WS1 from the extended and calibrated models are 0.06 and 0.04 m, respectively, from 1 June to 30 June (Julian Day 151 to 181 for all scenario runs), 2011. Statistical summaries of all error parameters for simulated elevations at WS1 and WS2 and simulated temperatures at T1 and T2 from the extended model are almost the same as results presented in Table 4.1 and Table 4.2 for the calibrated model; therefore, the extended model was well calibrated with observed data also.

Numerical experiments for all scenario runs were performed under various assumed upstream constant inflow conditions and harmonic boundary condition at the downstream. The lowest inflow scenario, 50 $m^3 s^{-1}$ constant inflow from the Upstream-2, was used as the base case for model experiments. The system responses to different inflow conditions were assessed by varying inflow rate from the base case in the other scenario runs. Freshwater inflows were varied from 50 $m^3 s^{-1}$ to 900 $m^3 s^{-1}$ to represent a very low inflow (1 percentile of filtered discharges, Table 4.4) to a relatively high flow (about mean filtered discharge during the spring and roughly 92 percentile during the summer, Table 4.4) from upstream. Harmonic constituents with amplitude of 0.3 m were specified at the downstream boundary (I-65 Bridge on the Mobile River) in the model. Harmonic constituents used for the downstream boundary were derived from the 2010-2011 water surface elevations at the Mobile State Docks NOAA station (http://tidesandcurrents.noaa.gov/waterlevels.html?id=8737048). The water surface elevation calculated from harmonic constituents of the Mobile State Dock station with the amplitude of 0.3 m matched reasonably well with the measured water surface elevations at the I-65 Bridge for the year 2011.

A data analysis of power plant operation and temperatures measured in the intake canal and discharge canal was performed. Based on the data analysis, the flow rates and the temperature increases (temperature differences between the discharge and the intake) through the power plant were assumed constant during the study period for the scenario runs. For the withdrawal and return boundaries of the power generating units supported by the intake 1, a constant flow of 29.3 $m^3 s^{-1}$ and a temperature rise of 8°C were used for scenario runs. Similarly, a constant flow of 20.6 $m^3 s^{-1}$ and a temperature rise of 4°C

were used for withdrawal and return boundaries for the units supported by the intake 2 (Fig. 4.2).

All of the numerical experiments were run for 36 days (Julian day 145 to 181, 25 May to 30 June) with constant inflow at the upstream boundary (Upstream-2 in Fig. 4.1) and constant withdrawal and return flow boundaries. All model results are reported from 151 to 181 (30 days) after six days of the model spin-up period. The initial water temperatures of all grid cells were assigned as 22 °C, and the simulation typically reaches quasi equilibrium after a few simulation days. The model grid for the scenario analysis was extended from Bucks to the intersection of the Mobile River and Tensaw River (Upstream-2 Fig. 4.1).

4.6.1 Discharge Distributions under Different Scenarios

Thermal recirculation is characterized by the movement of heated water released from a power plant through the discharge canal towards the intake location (Bai and Lung 2005). During the thermal recirculation, there is a possibility of 2 layer flow; the bottom layer moving towards downstream and the surface layer moving towards upstream. In the power plant, the cooling water is withdrawn from the deeper layers of the water column (W1 and W2 in Fig. 4.2). Such withdrawal arrangements are common in the coastal regions where the dominant current is tidal driven (Baur 2008). The flow distributions in the Mobile River near the intake canal and discharge canal are complex due to the interactions of intake withdrawal for the power plant, discharge from the power plant, upstream inflows, and downstream tides. Flow rates across different cross sections for scenario runs with different inflows from upstream boundary were extracted to investigate possible recirculation in the Mobile River.

Fig. 4.6(a) shows the location of the cross section *A* in the intake canal and two cross sections *B* and *C* in the Mobile River where discharges through the surface layer and bottom layer were determined from EFDC simulation results. The surface and bottom discharges reported in Figs. 4.6 and 4.7 are the summation of flow rates through the surface layer and bottom layer in all grid cells across the defined cross sections *A*, *B*, and *C* shown in Fig. 4.6(a). Figs. 4.6(b), (c), and (d) show time series plots of simulated surface and bottom discharges (flow rate in $m^3 s^{-1}$) across the cross section *A* inside the intake canal for three scenario runs with upstream inflow of 50 $m^3 s^{-1}$, 250 $m^3 s^{-1}$, and 900 $m^3 s^{-1}$, respectively. The inflow of 250 $m^3 s^{-1}$ is approximately equal to the median filtered discharge during the summer (Table 4.4) in 2011 and 2008–2012. The negative flow rates in Fig. 4.6 indicate that the flow is moving from the Mobile River towards the intake canal. The flow moving towards the intake canal is due to the combined effect of upstream inflows and downstream tides under the constant withdrawals of cooling water by the power plant through the intake 1 (29.5 $m^3 s^{-1}$) and the intake 2 (20.6 $m^3 s^{-1}$). Fig. 4.6 shows that the surface and bottom discharges at the intake canal cross section differ in patterns and magnitudes under different upstream inflows. When the inflow from the upstream boundary is assumed to be 50 $m^3 s^{-1}$, flow across the bottom layer of the intake canal cross section varies from -7.19 $m^3 s^{-1}$ to -3.75 $m^3 s^{-1}$ with a mean value of -5.71 $m^3 s^{-1}$ and flow at the surface layer ranges from -11.69 $m^3 s^{-1}$ to -5.72 $m^3 s^{-1}$ with a mean value of -8.72 $m^3 s^{-1}$. The flows through other four layers (2^{nd}, 3^{rd}, 4^{th}, and 5^{th}) are not shown in Fig. 4.6 (b), and when flows across all the layers are added together, the total flow across the intake canal cross section ranges from -51.5 $m^3 s^{-1}$ to -47.83 $m^3 s^{-1}$ with a mean value of -49.97 $m^3 s^{-1}$. The mean total flow across the cross section *A* is equal to

the total withdrawal (-49.9 $m^3 s^{-1}$) by the power plant, however, the variations of surface and bottom flows across the cross section (Fig. 4.6) indicate the interaction with upstream inflows and tides from downstream. The flow patterns at both surface and bottom layers in Fig. 4.6 (c) for 250 $m^3 s^{-1}$ inflow from upstream differ from the ones in Fig 4.6 (b) for 50 $m^3 s^{-1}$ inflow. The surface and bottom flows on Fig. 4.6 (b) and (c) for 50 and 250 $m^3 s^{-1}$ inflows have peaks in the opposite directions that indicate the complex and frequent interaction of the inflow from upstream and downstream tides. The correlation coefficients developed between surface and bottom flows are -0.52, -0.94, and 0.06 for 50, 250, and 900 $m^3 s^{-1}$ inflows from upstream, respectively. The variations of the surface and bottom flows across the intake canal for 900 $m^3 s^{-1}$ inflow (Fig. 4.6 d) are much smaller compared to the ones for 50 and 250 $m^3 s^{-1}$. The smaller variation of the flows in the intake canal under large upstream inflow (Fig. 4.6 d) indicates the dominance of the upstream inflow over tides from downstream, which reflects through the small positive correlation coefficient between surface and bottom flows.

Fig. 4.7 shows the time series of simulated surface and bottom flows ($m^3 s^{-1}$) across the cross sections *B* (left panels) and *C* (right panels) in the Mobile River between the intake canal and discharge canal (Fig. 4.6 a) under 50 (top panels), 250 (middle panels), and 900 $m^3 s^{-1}$ (bottom panels) inflow from upstream. The cross section *B* was chosen at the downstream of the intake canal and the cross section *C* immediately upstream of the discharge canal (Fig. 4.6 a). The cross section *B* was chosen to examine the interaction of the upstream inflow and downstream flows (including tides and possible flow recirculation from the discharge canal) before reaching the intake canal. The flow across the cross section *C* can help us to understand the complex interaction of

the discharge from the power plant, upstream inflow, and downstream tides. The black dotted lines in Fig 4.7 indicate the line of zero flow that separates positive and negative flows. The positive flows in Fig. 4.7 indicate that the flows are moving towards upstream (because of downstream tides and flow recirculation), and the negative flows are moving from upstream to downstream (due to inflow momentum).

Under 50 $m^3 s^{-1}$ constant inflow from upstream, the discharges across the cross section *B* through the surface layer are dominantly positive and through the bottom layer all negative. The positive surface flows under 50 $m^3 s^{-1}$ inflow indicate that the warmer water from the downstream and discharge canal is moving towards the intake canal, this phenomenon is called flow recirculation. The negative flows at the bottom layer indicate that the flow from upstream is moving towards downstream. Therefore, two-layer flows with recirculating flow on the surface layers and downward flow from upstream at the bottom layers are developed under very low inflows from upstream. The surface layer flow ranges from -17.65 to 35.12 $m^3 s^{-1}$ (93% are positive flows) with a mean value of 15.26 $m^3 s^{-1}$ whereas the bottom layer flow ranges from -45.69 $m^3 s^{-1}$ to -21.31 $m^3 s^{-1}$ with a mean value of -31.42 $m^3 s^{-1}$. Both simulated surface and bottom flows across the cross section *B* under 250 and 900 $m^3 s^{-1}$ inflows, however, have all negative magnitudes. This indicates that the flows from the downstream do not reach the intake canal under upstream inflows 250 and 900 $m^3 s^{-1}$, i.e., no recirculation in the system. The correlation coefficients between bottom and surface flows at the cross section *B* are 0.72, 0.58, and 0.99 for 50, 250, and 900 $m^3 s^{-1}$ inflows from upstream, respectively. The slightly weaker correlation coefficient between bottom and surface flows under the medium inflow (250 $m^3 s^{-1}$) indicates the complex interaction between the inflow and downstream tides.

However, the stronger and positive correlation coefficients under the very small or quite large inflows are because the flow dynamics in the Mobile River is controlled by either downstream tides (for 50 $m^3 s^{-1}$) or upstream inflows (for 900 $m^3 s^{-1}$), and the interaction between the inflow and tides is relatively weak.

The discharges across the cross section *C* (Fig. 4.7 b, immediately upstream of the discharge canal) through the surface layer are all positive and through the bottom layer all negative under 50 $m^3 s^{-1}$ inflow from upstream. The surface flow rates range from 9.3 $m^3 s^{-1}$ to 34.72 $m^3 s^{-1}$ with a mean value of 24.45 $m^3 s^{-1}$ and the bottom flow rates from -27.98 $m^3 s^{-1}$ to -5.53 $m^3 s^{-1}$ with a mean value of -15.96 $m^3 s^{-1}$. The momentum of 50 $m^3 s^{-1}$ inflow from the Upstream-2 boundary (Fig. 4.2) is completely diminished at the surface layer of the cross section *C* when acts against tidal waves from the downstream boundary; this is why all surface flows are positive (Fig. 4.7 b top panel). The positive surface flows at the cross section *C* are also contributed by heated water released from the discharge canal that has smaller density than upstream inflow. In contrast to the flow distribution at the cross section *B* under 250 $m^3 s^{-1}$ inflow, simulated surface flows across the cross section *C* show occasional positive peaks and have larger variations than the bottom flows do. The larger variation of surface discharge occurs when flood tides from downstream is coupled with the flow from the discharge canal but the momentum of upstream inflow is relatively small at the cross section *C* under 250 $m^3 s^{-1}$ inflow. However, the momentum from tides at downstream is not large enough to reach cross sections *A* and *B* (Fig. 4.6 a). The surface flows at the cross section *C* range from -67.56 $m^3 s^{-1}$ to 26.44 $m^3 s^{-1}$ with a mean value of -8.72 $m^3 s^{-1}$ and the bottom flows range from -24.56 $m^3 s^{-1}$ to -47.49 $m^3 s^{-1}$ with a mean value of -34.87 $m^3 s^{-1}$ under 250 $m^3 s^{-1}$ inflows

from upstream. Simulated surface and bottom flows at the cross section *C* under constant inflow of 900 $m^3 s^{-1}$ (Fig. 4.7 b bottom panel) from upstream show similar variations compared to flows at the cross section *B*. Surface layer flows (magnitude) are larger than the bottom layer flows at both cross sections *B* and *C* under upstream flow of 900 $m^3 s^{-1}$. The correlation coefficients between bottom and surface flows at the cross section *C* were 0.62, -0.16, and 0.91 for 50, 250, and 900 $m^3 s^{-1}$ inflows from upstream, respectively. The interactions of all influencing forces under 250 $m^3 s^{-1}$ inflow are complex and result in a negative correction between the surface and bottom flows.

4.6.2 Velocity Distributions under Different Upstream Inflows

Simulated velocity profiles from numerical experiments with 50 $m^3 s^{-1}$ and 100 $m^3 s^{-1}$ inflows from upstream are presented in Fig. 4.8 to illustrate the recirculation phenomenon in the Mobile River in the vicinity of the power plant. The three locations Cell D, Cell E and Cell F shown in Fig. 4.2 were selected to represent the velocity profiles just downstream of the intake canal, about the midway between the intake canal and the discharge canal, and upstream of the discharge canal, respectively. Simulated velocity profiles at six layers (surface to bottom) under ebb tide on Julian day 159.583 (9 June 14:00, 2011) and flood tide on Julian day 166.458 (16 June 11:00, 2011) at the downstream boundary were plotted at each cell (Fig. 4.8). Positive velocities in Fig. 4.8 represent the flow moving towards upstream and negative velocity represents flow moving towards downstream.

Fig. 4.8 shows that positive velocities prevail in the top two layers and negative velocities in the bottom four layers at all three locations for both ebb and flood tides when the inflow is 50 $m^3 s^{-1}$. The presence of both positive and negative velocities along

the depth of the channel suggests the presence of recirculation, i.e., flow towards upstream via top layers and flow moving towards downstream from some bottom layers under small inflows from upstream. However, under 100 $m^3 s^{-1}$ inflow from upstream, velocities in all the layers are negative in magnitude for both ebb and flood tides at Cell D and for ebb tide at Cell E. This suggests flow moving towards downstream at all depths that implies no recirculation reaching the intake canal. Under 100 $m^3 s^{-1}$ inflow, both positive and negative velocities occur for flood tide at Cell E and for both ebb and flood tides at Cell F. It means that flow recirculation can propagate to Cell E under flood tide but not under ebb tide, but cannot reach to the intake canal as demonstrated by velocity profiles at Cell D under both ebb and flood tides. When inflow is 900 $m^3 s^{-1}$, Fig. 4.7 shows that there is no flow recirculation just upstream of the discharge canal.

4.6.3 Dye Distributions under Different Upstream Inflows

For the model simulations under different upstream inflow scenarios, the dye was continuously released from the power plant after the model spin-up period to track the flow path of the heated water released into the discharge canal. For the dye simulations, dye concentrations were initialized to zero at all the grid cells (initial condition). The dye concentrations at the upstream and downstream boundaries were assigned to be zero at all times, i.e., the dye was not introduced into the system from the upstream and downstream boundaries. The dye was only introduced into the simulation domain through the withdrawal and return boundaries (Fig. 4.2). In the withdrawal and return boundary, the rise of dye concentration was set to be 1 (arbitrary units) which implies the dye released into the discharge canal would have a dye concentration of 1 plus the dye concentration at the intake withdrawal location. The dye concentrations at the discharge points (Fig.

4.2) would always be 1 as long as the concentrations of dye at the intake withdrawal locations were zero, i.e., there is no heated water from the discharge canal that has been recirculated back to the withdrawal point. When the dye concentrations are greater than zero in the intake locations for the intake 1 and intake 2 (Fig. 4.2), it would indicate the recirculation of heated water from the discharge canal to the intake canal, and then the dye concentrations at the discharge points would be greater than 1.

The model experiments of dye simulations with upstream inflows of 50 $m^3 s^{-1}$, 100 $m^3 s^{-1}$ and 250 $m^3 s^{-1}$ were performed and reported from Julian days 151 (1 June) to 181 (30 June) to investigate any possible recirculation from the discharge canal to the intake canal. The inflow of 100 $m^3 s^{-1}$ is a relatively small flow rate from upstream because it is approximate 6 percentile of the filtered discharges during the summer in 2011 and 2008–2012 (Table 4.4). At the downstream boundary, water surface elevations (WSE) were calculated from harmonic constituents with amplitude of 0.3 m (Fig. 4.9a). The atmospheric forcing for the same period in 2011 was used for model experiments, and Fig. 4.9b shows air temperature variations from Julian day 151 to 181. Air temperature varied from 20.0 to 39.4 ^oC with a 30-day average value of 28.4 ^oC (Fig. 4.9b). This simulation period was selected because of the highest 30-day average air temperature and solar radiation, and it is the most challenging operational periods of the power plant where the once-through cooling system is used. Fig. 4.9(c) shows the time series of simulated dye concentrations at the discharge points R1 and R2 (Fig. 4.2) under 50, 100, and 250 $m^3 s^{-1}$ inflows. There are small differences in simulated dye concentrations at R1 and R2 under 50 $m^3 s^{-1}$ inflow. Simulated dye concentrations at both R1 and R2 are equal to 1 under both 100 and 250 $m^3 s^{-1}$ inflows, which means no

recirculation of heated water from the discharge canal to the intake canal under these large inflows, but they are greater than 1 under 50 $m^3 s^{-1}$ inflow from upstream. Simulated dye concentrations at R1 and R2 under 50 $m^3 s^{-1}$ inflow become greater than 1 after one and half days of the simulation that indicate how long the recirculation of heated water from the discharge canal takes to reach the intake canal. The dye concentrations at R1 and R2 range from 1.0 to 1.27 with a mean value of 1.12. Simulated dye concentrations fluctuate with time (Fig. 4.9c), and the variation of simulated dye concentrations at R1 and R2 follows the variations of the WSE at the downstream boundary.

Time series of simulated dye concentrations were extracted from W1 (the withdrawal location for the intake 1), Cell E (Fig. 4.2), and the discharge exit (Fig 4.2) and plotted in Fig. 4.10. Cell E refers to a point on the Mobile River (Fig. 4.2) about the midway between the intake canal and the discharge canal. For 50 $m^3 s^{-1}$ inflow from upstream, the periodic variations of water surface elevation (not shown by graphs) are simulated near the intake canal of the power plant because the flow dynamics in the simulation domain are controlled by the tides from the downstream when upstream inflow is small. Therefore, Figs. 4.10 (a) and (b) show that the dye concentrations are greater than zero in the bottom and surface layers at W1 (Fig. 4.2) after one and half days of the simulation. The dye concentration at W1 vary from 0 to 0.22 with a mean value of 0.10 at the bottom layer and from 0 to 0.48 with a mean value of 0.22 at the surface layer under 50 $m^3 s^{-1}$ inflow from upstream (Table 4.5). Because the withdrawal for the power plant are from the bottom three layers at the withdrawal points W1 and W2 (Fig. 4.2), dye concentration at the discharge canal would depend on the dye concentration of the

bottom three layers. Based on the mean dye concentration (0.12) in the three bottom layers at W1, one may conclude that there is about 12% recirculation of heated water from the discharge canal. The presence of dye concentration at W1 under an upstream inflow of 50 $m^3 s^{-1}$ supports that under very small inflows (1 percentile, Table 4.4) from upstream, flow recirculation is observed in the intake canal. Fig. 4.10 (a) and (b) show that there is more heated water from the discharge canal present in the surface layer than in the bottom layer at W1 because of the density stratification in the Mobile River. The simulated dye concentrations for 100 $m^3 s^{-1}$ and 250 $m^3 s^{-1}$ inflows from upstream are zero (Table 5, Figs. 4.10a and 4.10b) at W1, i.e., the dye doesn't reach the W1 withdrawal point under these larger inflows.

Figs. 4.10 (c) and (d) show the time series of dye concentrations in the surface and bottom layers at Cell E (Fig. 4.2). At this location, dye is found under the upstream inflows of 50 $m^3 s^{-1}$ and 100 $m^3 s^{-1}$ but the dye is not detected under the inflow of 250 $m^3 s^{-1}$. The 250 $m^3 s^{-1}$ inflow from upstream is large enough compared to the tides from downstream and prevents the heated water released at the discharge canal from reaching (flowing back to) Cell E. The surface dye concentrations (Fig. 4.10 d) at Cell E are higher than the dye concentrations at the bottom layer (Fig. 4.10 c). The dye concentrations simulated under 50 $m^3 s^{-1}$ inflow range from 0 to 0.57 (mean value of 0.45) in the bottom layer and from 0 to 0.89 (mean value of 0.74) in the surface layer (Table 4.5). The dye concentrations simulated under 100 $m^3 s^{-1}$ inflow are projected to be smaller in magnitude compared to the ones under 50 $m^3 s^{-1}$ and range from 0 to 0.03 in the bottom layer and from 0 to 0.26 (mean value of 0.05). Under 100 $m^3 s^{-1}$ inflow the dye concentrations at the bottom layer are very small at Cell E (Fig. 10c) and the dye

doesn't reach the intake canal (Figs. 4.10a and 4.10b). A distinct stratification of dye concentrations between the top and bottom layer was detected at Cell E under both 50 $m^3 s^{-1}$ and 100 $m^3 s^{-1}$ inflows from upstream.

Fig. 4.10 (e) and (f) show the time series of dye concentrations at the discharge exit point (Fig. 4.2, the confluence of the discharge canal and the Mobile River). At the discharge exit, the surface dye concentration under 50 $m^3 s^{-1}$ inflow is larger than 1 after two and half days of the simulation because the dye has reached the intake canal after about 1.5 days due to recirculation. The presence of dye concentration at the intake canal would cause the dye concentration at the discharge canal to be greater than 1. Dye concentrations at the discharge exit under 50 $m^3 s^{-1}$ inflow range from 0.07 to 1.06 (mean value of 0.93) at the bottom layer and from 0.09 to 1.20 (mean value of 1.07) at the surface layer. Dye concentrations at the discharge exit under 100 $m^3 s^{-1}$ inflow have mean values of 0.48 and 0.87 at the bottom and surface layer, respectively (Table 4.5). Even though dye concentrations at the discharge points R1 and R2 (Fig. 4.2) are equal to 1, the dye concentrations under 100 and 250 $m^3 s^{-1}$ inflows are less than 1 (Fig. 4.10e and 4.10f) at the discharge exit in the Mobile River because of the dilution effect of flows from the discharge canal and the Mobile River. Dye concentrations at the discharge exit location under 250 $m^3 s^{-1}$ inflow are smaller in magnitude than ones under 50 $m^3 s^{-1}$ and 100 $m^3 s^{-1}$ inflows because the larger inflow of 250 $m^3 s^{-1}$ has larger momentum to push heated water towards downstream. Dye concentrations at the discharge exit under 250 $m^3 s^{-1}$ range from 0.05 to 0.19 (mean value of 0.14) at the bottom layer and range from 0.22 to 0.75 (mean value of 0.60) at the surface layer (Table 4.5).

Sensitivity model runs with no temperature rises in the withdrawal and return boundaries for the intake 1 and intake 2 were also performed for upstream 50 $m^3 s^{-1}$, 100 $m^3 s^{-1}$ and 250 $m^3 s^{-1}$ inflow scenarios. No temperature rise through the power plant is a hypothetical operational condition, and the model results can help us to identify any flow recirculation due to the interactions of upstream inflow, downstream tides, and solar heating of the atmosphere only. The model results with no temperature rise through the withdrawal-return boundary show that the dye is still found at W1 under 50 $m^3 s^{-1}$ inflow from upstream. However, the dye concentrations are projected to be very small with maximum values of 0.05 and 0.13 in the bottom and surface layers at W1 as shown in Figs. 4.10 (a) and (b). Without temperature rises there is no dye projected to present at Cell E under 100 $m^3 s^{-1}$ and 250 $m^3 s^{-1}$ inflows (not shown in Figs. 4.10c and 4.10d). In summary, model simulation results with and without temperature rises indicate that the recirculation is enhanced by the temperature rise created by the power plant, compared to recirculation driven by low inflows, tidal forces and solar heating only.

The calibrated EFDC model was also used to simulate dye distributions in the Mobile River under 2011 measured unsteady inflows from upstream and measured tides from downstream as model boundary conditions. Dye concentrations in the surface and bottom layers at W1, Cell E, and the discharge exit were extracted and a statistical analysis of dye greater than 0.01 (1% the released dye) was performed. Dye concentrations at W1 and Cell E location were zero most of the times in the 2011 simulation period (25 April to 29 August) and were greater than zero when the inflows from upstream were small. It was found that the dye concentrations greater than 0.01 in the bottom layer at W1 were detected for 97 hours (~4.0 days, 3.2% of the total

simulation time, 125 days) and had a mean value of 0.056 and a maximum value of 0.24, and in the surface layer for 136 hours (5.7 days, 4.5% of the total simulation time, Table 6). Dye concentrations greater than 0.01 in the surface and bottom layers of Cell E were detected 13.2% and 18.2% of the total simulation time, respectively (Table 4.6). This indicates the overall efficiency of the power plant was high because very low possibility of flow recirculation would maintain lower withdrawal temperatures at the intake canal.

4.6.4 Temperature Distributions under Different Inflows

Simulated temperatures were extracted to further understand the impact of recirculation in the Mobile River near the power plant. Simulated temperature distributions for the model runs with 50 $m^3 s^{-1}$, 250 $m^3 s^{-1}$, and 900 $m^3 s^{-1}$ inflows are presented in Figs. 4.11 and 4.12. The temperatures at the upstream and downstream boundaries during the simulation period were the actual measured temperatures at the USGS Bucks station and I-65 bridge location. Water temperatures at the upstream boundary (dashed lines in Fig. 4.12) ranged from 28.1 to 32.1 °C with a mean value of 30.5 °C and at downstream (dotted dashed lines in Fig. 4.12) ranged from 28.9 to 33.9 °C with a mean value of 32.1 °C. The absolute differences between upstream and downstream temperatures ranged from 0.52 to 2.5 °C with a mean value of 1.55 °C from 1 June to 30 June 2011. In the spring months (e.g., from Julian days 115 to 130 or 26 April 26 to 11 May), the absolute differences between upstream and downstream temperatures only ranged from 0.0 to 0.6 °C with a mean value of 0.14 °C. This was because inflow was colder and evaporation under low air temperatures lost more heat in the spring.

The snapshots of 3D temperature distributions and two dimensional (2D) temperature profiles (along depth) were plotted at Julian days 166.458 (16 June 11:00

am) and 166.92 (16 June 10:00 pm) for the river segment of the Mobile River near the intake canal and the discharge canal of the power plant (Fig. 4.11) to demonstrate possible recirculation under 50 $m^3 s^{-1}$ inflow from upstream. These two specific times were chosen to represent the flood tide (Figs. 4.11a and b) and ebb tide (Figs. 4.11c and d) from the downstream. Figs. 4.11 (a) and (b) show the extent or how far the warmer water from the discharge canal moves towards the intake canal under harmonic tides from downstream and the very low inflow condition from upstream. From Fig. 4.11 it can be observed that the heated water from the discharge canal reaches the intake canal under both flood and ebb tide conditions under 50 $m^3 s^{-1}$ inflow. Simulated temperatures at the intake canal during the flood tide condition are higher than temperatures under the ebb tide condition. Figs. 4.11 (b) and (d) show temperature contours along the channel centerline using the distance from the downstream boundary and the elevation above MSL as x and y axes, and the locations of the intake canal, the discharge canal, and the middle channel location are clearly marked by red vertical lines. Water temperatures at the discharge canal are more than 39.5 ^oC [Figs. 4.11 (a) and (c)], but inflow temperatures in the river bottom layers near the intake canal were about 32 ^oC [Figs. 4.11 (b) and (d)]. The temperature stratification between the surface and bottom layers is stronger under the flood tide (due to recirculation) than under the ebb tide. The heated water from the discharge canal is pushed by downstream tides against the inflow momentum from upstream inflow. Fig. 4.11 shows the output of the model run with an upstream inflow of 50 $m^3 s^{-1}$ because the recirculation between the discharge and intake canals is only simulated and present under very small inflows. The 50 $m^3 s^{-1}$ inflow is

about one percentile of filtered flow during the summer (Table 4.4) and is a very small freshwater inflow from upstream.

In order to complement the findings from dye distribution on flow recirculation in the intake canal from discharge canal, temperature time-series at W1 (Fig. 4.2) for the upstream inflows of 50 $m^3 s^{-1}$, 250 $m^3 s^{-1}$, and 900 $m^3 s^{-1}$ were plotted in Fig. 4.12 from Julian day 151 (1 June) to 181 (30 June). W1 was chosen as the comparison location because it is the withdrawal location for the intake 1. Simulated water temperatures in the surface layer (solid lines in Fig. 4.12b) range from 29.3 to 35.0 °C with a mean value of 32.2 °C and in the bottom layer (dotted lines in Fig. 4.12) range from 28.7 to 32.4 °C with a mean value of 31.2 °C under 50 $m^3 s^{-1}$ inflow. Time series of upstream inflow temperature (dashed lines) and downstream water temperature (dotted dashed lines) were plotted in the top panel of Fig. 4.12 to show the temperature time series applied at the boundaries. The strong stratification of temperatures between the surface and bottom layers for 50 $m^3 s^{-1}$ inflow from upstream is projected to occur at the withdrawal location (W1) due to the recirculation of heated water from the discharge canal to the intake canal and diurnal solar heating of the atmosphere. Simulated temperature differences between the surface and bottom layers at W1 are projected to vary from 0.01 to 3.57 ^oC with a mean value of 1.06 ^oC under 50 $m^3 s^{-1}$ inflow. The withdrawal and return boundaries for all scenario runs use the constant temperature rises, and simulated temperatures at the discharge points R1 and R2 are totally dependent on temperatures at the intake canal. If the flow recirculation occurs, temperatures at the intake canal are increased and heated water with the higher temperature is released at the discharge canal and continues its pathway for further recirculation when inflow from upstream is very small.

Temperature simulations with hypothetical no temperature rise in withdrawal and return boundaries (intake 1 and intake 2) were also performed to investigate the possibility of the flow recirculation induced due to downstream tides and diurnal heating only. Without temperature rise from the power plant, projected temperatures in the bottom layer at W1 range from 27.8 to 31.63 °C with a mean value of 30.5 °C and in the surface layer range from 27.8 to 33.1 °C with a mean value of 31.0 °C. Therefore, on average, the temperature rises specified on the withdrawal and return boundary contribute to an average temperature increase of 0.7 °C in the bottom layer and 1.2 °C in the surface layer at W1. Simulated temperature peaks at W1 are due to solar heating and typically occur a few hours after the noon. Diurnal heating is influenced by meteorological parameters such as air temperature, relative humidity, solar radiation, and cloud cover.

In contrast to Fig. 4.12 (b), simulated temperatures in the surface and bottom layers under 250 $m^3 s^{-1}$ shown in Fig. 4.12 (c) closely follow the patterns of temperatures at the upstream boundary, and the differences between them are small. Fig 4.12 (c) shows that surface temperatures at W1 vary from 28.1°C to 33.3°C with a mean value of 31.0°C and bottom temperatures from 28.1°C to 32.3°C with a mean value of 30.8°C. Absolute differences of simulated temperatures between the surface and bottom layers at W1 are projected to vary from 0.0 to 1.5 ^oC with a mean value of 0.2 ^oC under 250 $m^3 s^{-1}$ inflow. Temperature peaks in the surface layer (Fig. 4.12c) are consistent with surface temperature peaks at Fig. 4.12 (b) which are due to diurnal heating. For 900 $m^3 s^{-1}$ inflow from upstream, there are small differences between surface, bottom, and upstream temperatures. Diurnal effect is hardly recognized (Fig. 4.12d) because of the large inflow from upstream that controls the overall flow dynamics in the system. Heated water from

the discharge canal is flushed out through the downstream boundary due to higher momentum from upstream inflow.

Differences of simulated temperatures in the bottom and top layers at the intake canal (W1) for model experiments between 50 $m^3 s^{-1}$ and 250 $m^3 s^{-1}$ inflow from upstream were calculated to understand the effect of the flow recirculation on intake temperatures, because flow recirculation was predicted to occur under 50 $m^3 s^{-1}$ but not under 250 $m^3 s^{-1}$ inflow. The average temperature increase due to flow recirculation was 0.4 °C with a maximum value up to 1.1 °C in the bottom layer at W1 and 1.22 °C with a maximum value up to 2.6 °C in the surface layer at W1 during 30 days of simulation. The power plant withdraws cooling water from bottom layers; therefore, the impact of the flow recirculation to the power plant operation is minor. It should be noted that simulated temperature increases in the intake canal due to flow recirculation do not cumulatively increase the intake temperatures because discharged warmer water loses more heat to the environment through heat exchange with the atmosphere and river bed. Both temperature increases over time in the surface and bottom layers shown in Fig. 4.12 are primarily due to naturally warming over season.

4.7 Conclusion

Two three-dimensional hydrodynamic EFDC models were developed for the Mobile River to simulate flow, dye, and temperature distributions under various upstream flows, downstream tides, power plant operations and atmospheric forcing. The first EFDC model domain included a 17.0 km segment of the Mobile River from Bucks USGS gauging station to I-65 Bridge and calibrated against observed water surface elevations, temperatures, and velocities at the monitoring stations with good agreement (Tables 4.1, 4.2, 4.3, and 4.4). The second EFDC model domain was extended approximately 13 km upstream to the Upstream-2 (Fig. 4.1) to investigate the possible recirculation patterns in the Mobile River from the discharge canal to the intake canal of the power plant under various upstream inflow scenarios and fixed downstream boundary derived from harmonic constituents at the Mobile State Docks. Overall, Mobile EFDC model was able to predict the temporal and spatial distributions of flow, dye, and temperature and revealed complex interactions due to upstream inflows, withdrawals and discharges of the power plant, downstream tides, and solar heating from atmosphere. The major findings of the study are summarized as follows:

a. Velocity profiles and distributions of flow, dye, and temperature at different locations (cross sections or interesting points) throughout the Mobile River from the intake canal to discharge canal were studied in detail to understand the possible occurrence of recirculation. The dye simulations and velocity profiles provided the very useful information on understanding the thermal recirculation in the Mobile River. It was identified that only under a very small inflow from upstream (50 $m^3 s^{-1}$), the warmer water in the discharge canal could travel up to

the intake canal. When the upstream inflow reached 100 $m^3 s^{-1}$, the dye was discovered in Cell E (Fig. 4.2) but did not reach the withdrawal location in the intake canal. Inflows larger or equal to 250 $m^3 s^{-1}$ from upstream would flush the warmer water released from the discharge canal towards downstream and prohibit any recirculation in the system.

b. Recirculation of smaller magnitudes (Fig. 4.10) was also identified for hypothetical conditions–no temperature rise at the withdrawal-return boundary of the power plant; and this is because of the dominant control from downstream tides when the inflow is small. Model simulation results with and without temperature rise scenario indicate that the recirculation is enhanced by the temperature rise created by the power plant, compared to recirculation driven by low inflows, tidal forces and solar heating only.

c. For the model calibration period (25 April to 29 August 2011), it was found that the dye concentrations greater than 0.01 in the bottom layer at the withdrawal point W1 were detected for 97 hours (~4.0 days, 3.2% of the total simulation time, 125 days) and in the surface layer were detected for 136 hours (5.7 days, 4.5% of the total simulation time, Table 4.6). This indicates the overall efficiency of the power plant was high because very low possibility of flow recirculation would maintain lower withdrawal temperatures at the intake canal.

In summary, temperatures in the intake canal under very small inflows from upstream would rise due to the interaction of the inflows, downstream tides, temperature rises in the discharge canal and solar heating. If the upstream inflow is small in the range of 50 $m^3 s^{-1}$ and lasts for a few days, then there is a possibility of thermal recirculation

from the discharge canal to the intake canal. It should, however, be noted that 50 $m^3 s^{-1}$ inflow is 1 percentile of filtered flows at the Bucks gauging station (Table 4.4). These scenario model runs provide valuable information for us to understand the dynamics of the system and possible conditions when and where the recirculation would occur.

Table 4.1 Statistical summary of the differences (Observed - Modeled) and absolute differences (|Observed - Modeled|) between observed and modeled water surface elevations (m) at the monitoring stations WS1 and WS2 (Fig. 4.1).

Statistical Parameters	Station WS1		Station WS2	
	Observed - Modeled	|Observed - Modeled|	Observed - Modeled	|Observed - Modeled|
Minimum	-0.20	0.00	-0.29	0.00
25 Percentile	-0.02	0.02	-0.10	0.04
Median	0.01	0.04	-0.06	0.06
75 Percentile	0.05	0.06	-0.04	0.10
Maximum	0.50	0.50	0.34	0.34
Average	0.01	0.04	-0.07	0.07
Standard Deviation	0.06	0.04	0.05	0.04

Table 4.2 Statistical summary of the differences (Observed - Modeled) and absolute differences (|Observed - Modeled|) between observed and modeled water temperatures (^{o}C) at the temperature monitoring stations T1 and T2 (Fig. 4.1).

	Station T1		Station T2	
Statistical Parameters	Observed - Modeled	|Observed - Modeled|	Observed - Modeled	|Observed - Modeled|
Minimum	-5.707	0.000	-2.333	0.000
25 Percentile	-0.604	0.056	0.052	0.223
Median	-0.012	0.201	0.367	0.472
75 Percentile	0.090	0.929	0.873	0.929
Maximum	2.942	5.707	4.334	4.334
Average	-0.288	0.595	0.551	0.728
Standard Deviation	0.931	0.772	0.876	0.736

Table 4.3 Statistical summary of model performance evaluation of water surface elevation (m) time series at the WS1 and WS2 stations and water temperature (^{o}C) time series at the T1 and T2 stations.

Station ID	Starting Date/Time	Ending Date/Time	#Pairs	*MAE*	*RMSE*	*NSE*
WS1	4/26/2011	8/28/2011	2 974	0.04	0.06	0.98
WS2	4/26/2011	8/28/2011	35 997	0.07	0.08	0.94
T1	5/9/2011	8/9/2011	16 303	0.60	0.97	0.93
T2	5/10/2011	8/9/2011	16 125	0.70	1.04	0.89

Note: *MAE* – Mean absolute error (Eq. 4.4), *RMSE* – Root-mean-square-error (Eq. 4.5), and *NSE* – Nash-Sutcliffe efficiency (Eq. 4.6).

Table 4.4 Statistical summary of observed and filtered flow rate (m^3 s^{-1}) at Bucks gauging station in 2011 and from 2008 to 2012.

Observed/Filtered Streamflow	Statistical Parameters	2011		2008–2012	
		Spring	Summer	Spring	Summer
Observed Discharge (m^3 s^{-1})	Minimum	-102	-473	-320	-504
	1 Percentile	84	-272	51	-230
	25 Percentile	530	100	651	126
	Mean	925	343	1030	395
	Median	997	306	1073	343
	Maximum	1894	1410	2064	1826
Filtered Discharge (m^3 s^{-1})	Minimum	221	28	64	-151
	1 Percentile	309	52	233	55
	25 Percentile	493	183	616	184
	Mean	925	343	1028	395
	Median	994	250	1075	263
	Maximum	1872	1382	2025	1803

Table 4.5 Statistical summary of simulated dye concentrations (arbitrary units) in the surface and bottom layers at W1, Cell E, and the discharge exit (Fig. 4.2) under 50 $m^3 s^{-1}$, 100 $m^3 s^{-1}$, and 250 $m^3 s^{-1}$ inflows from upstream.

Inflow	Location / Layer	Minimum	1st Quartile	Mean	Median	3rd Quartile	Maximum	Standard Deviation
50 $m^3 s^{-1}$	W1 / bottom	0.00	0.06	0.10	0.11	0.14	0.22	0.06
	W1 / surface	0.00	0.13	0.22	0.24	0.31	0.48	0.12
	Cell E / bottom	0.00	0.47	0.45	0.50	0.52	0.57	0.13
	Cell E / surface	0.00	0.72	0.74	0.79	0.84	0.89	0.18
	Discharge exit / bottom	0.07	0.91	0.93	0.96	1.00	1.06	0.13
	Discharge exit / surface	0.09	1.02	1.07	1.08	1.12	1.20	0.09
100 $m^3 s^{-1}$	W1 / bottom	0.00	0.00	0.00	0.00	0.00	0.00	0.00
	W1 / surface	0.00	0.00	0.00	0.00	0.00	0.00	0.00
	Cell E / bottom	0.00	0.00	0.00	0.00	0.01	0.03	0.01
	Cell E / surface	0.00	0.00	0.05	0.00	0.10	0.26	0.08
	Discharge exit / bottom	0.06	0.45	0.48	0.49	0.51	0.56	0.05
	Discharge exit / surface	0.08	0.86	0.87	0.87	0.88	0.90	0.03
250 $m^3 s^{-1}$	W1 / bottom	0.00	0.00	0.00	0.00	0.00	0.00	0.00
	W1 / surface	0.00	0.00	0.00	0.00	0.00	0.00	0.00
	Cell E / bottom	0.00	0.00	0.00	0.00	0.00	0.00	0.00
	Cell E / surface	0.00	0.00	0.00	0.00	0.00	0.00	0.00
	Discharge exit / bottom	0.05	0.12	0.14	0.14	0.15	0.19	0.02
	Discharge exit / surface	0.22	0.54	0.60	0.62	0.70	0.75	0.11

Table 4.6 Statistical summary of simulated dye concentrations (arbitrary units, greater than 0.01 i.e. 1% released dye) in the surface and bottom layers at W1, Cell E, and the discharge exit (Fig. 4.2) for the calibration run (measured inflows from upstream).

Location / Layer	Occurrence (hrs)	Mean	Median	Maximum	Percentage of occurrence
W1 / bottom	97	0.056	0.048	0.239	3.2%
W1 / surface	136	0.088	0.065	0.288	4.5%
Cell E / bottom	396	0.091	0.070	0.285	13.2%
Cell E / surface	547	0.232	0.247	0.463	18.2%
Discharge exit / bottom	2985	0.222	0.193	0.612	99.5%
Discharge exit / surface	2985	0.589	0.681	1.009	99.5%

Note: Maximum occurrence hours = 3000 hours (125 days)

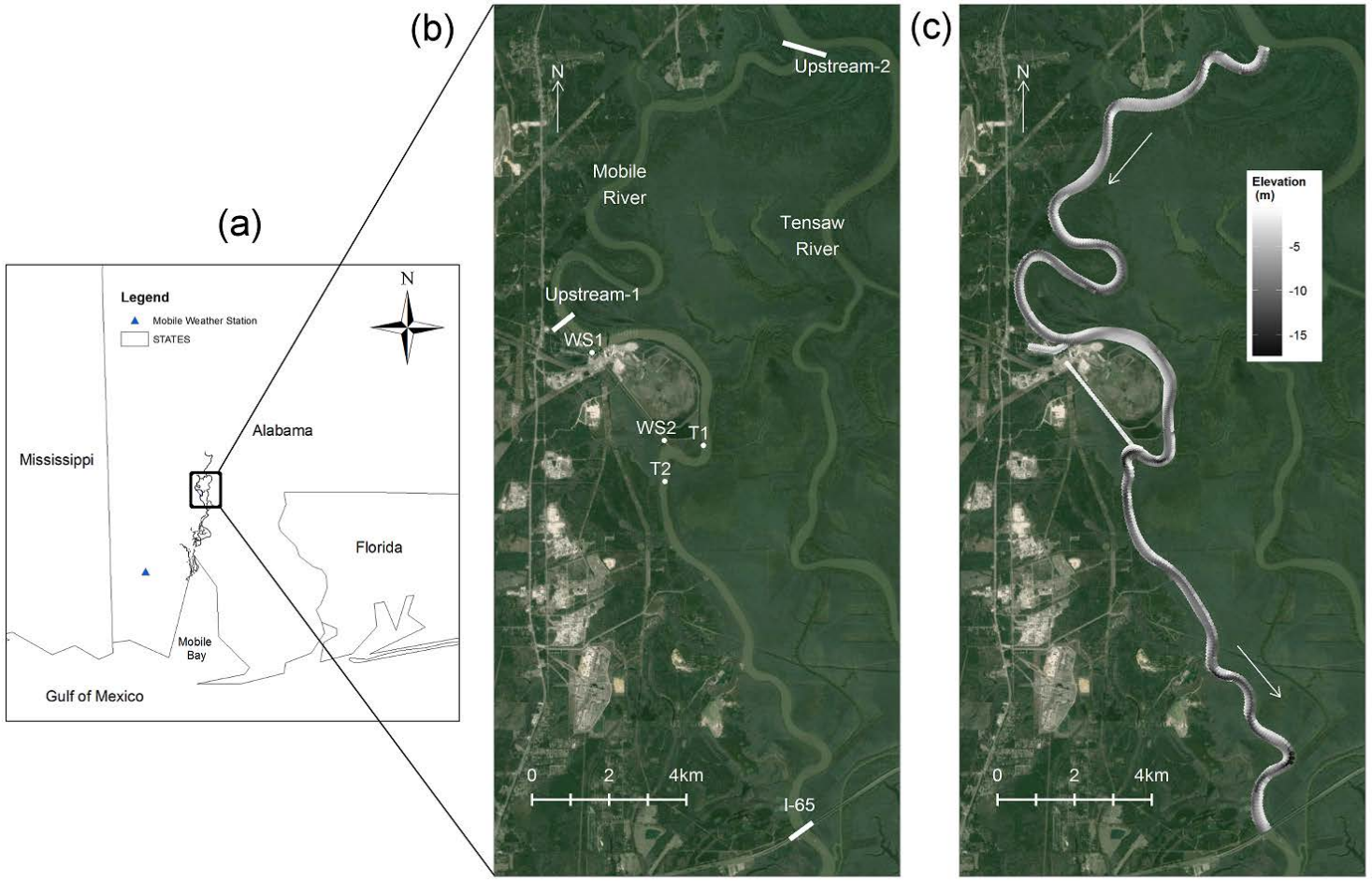

Fig. 4.1 (a) Geographic location of the study area including the location of weather station, (b) satellite images showing monitoring stations (WS1, WS2, T1, and T2), downstream (I-65), and upstream boundary locations for calibration (Upstream-1) and for sensitivity runs (Upstream-2), and (c) model domain showing channel bathymetry

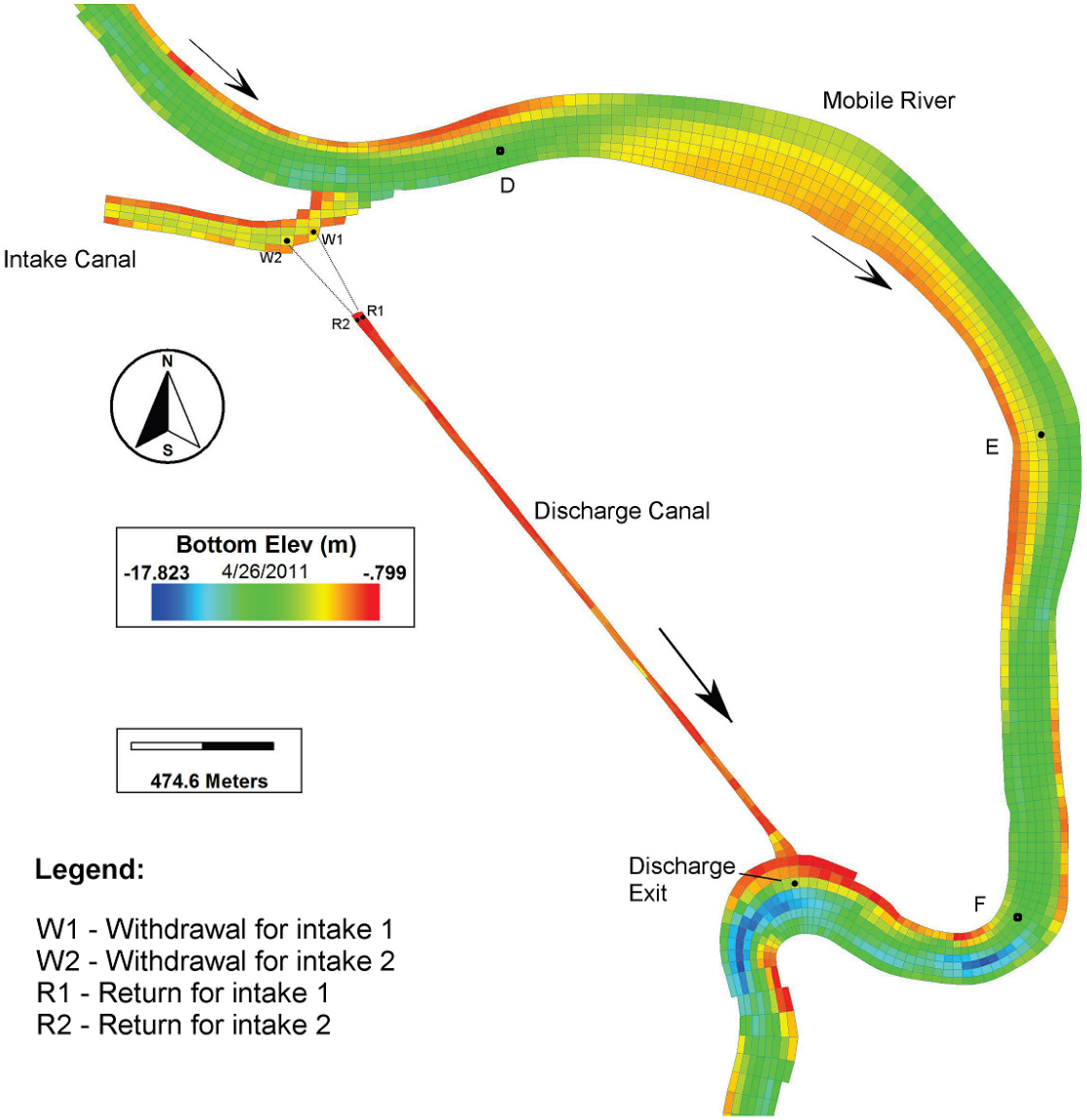

Fig. 4.2 The EFDC model grid with bottom elevation zoomed to show the intake canal and discharge canal. Withdrawal locations (W1 and W2) and discharge points (R1 and R2) for the power plant are shown along with three locations (Cell D, Cell E, and Cell F) where velocity profiles were studied in detail. At the Cell E and discharge exit point, dye concentration and water temperatures were studied.

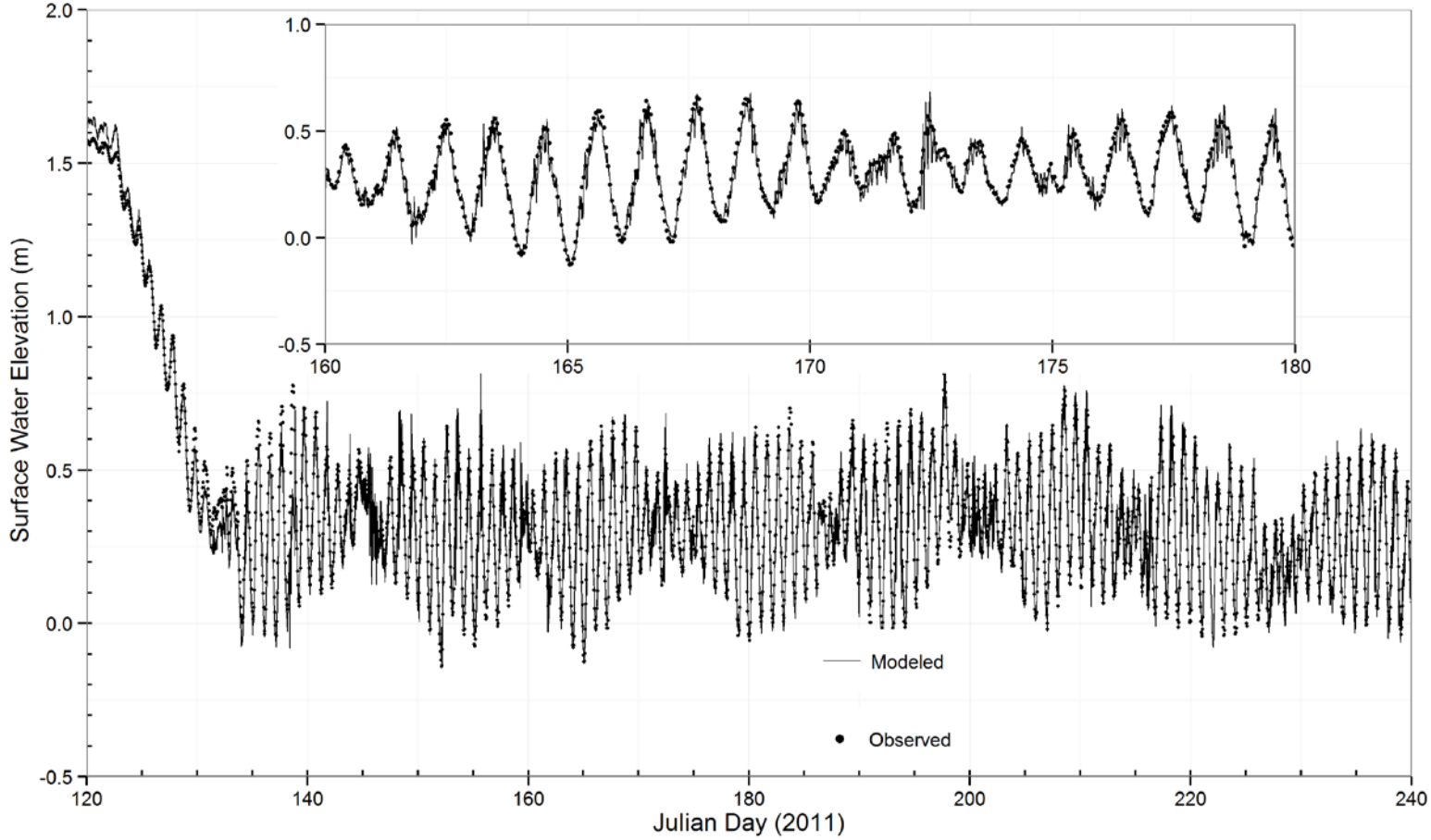

Fig. 4.3 Time-series plot of observed and modeled water surface elevations (m) at the monitoring station WS1 from 26 April to 28 August 2011 (Julian day 115 to 240).

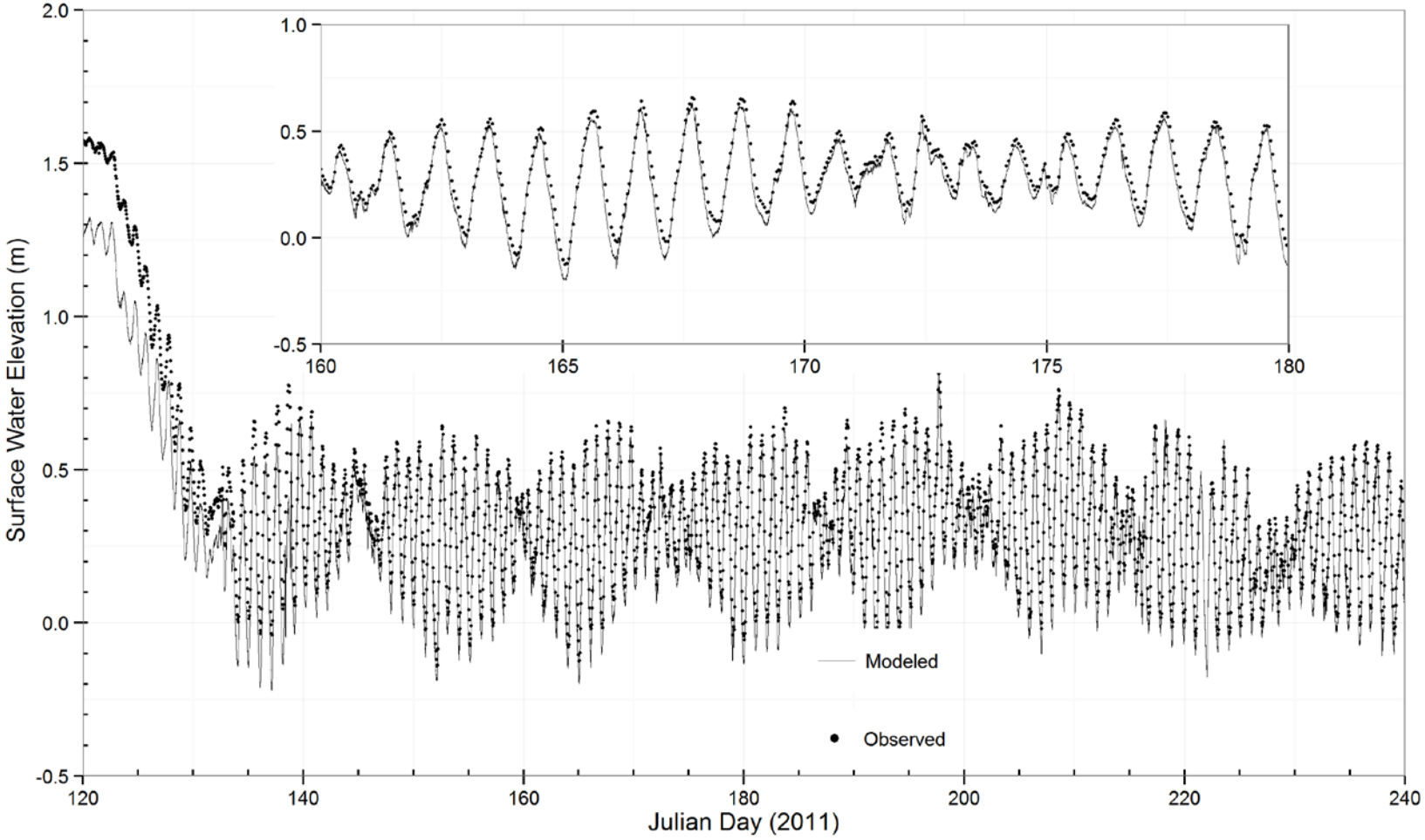

Fig. 4.4 Time-series plots of observed and modeled water surface temperature (°C) at the shallow depth of the temperature monitoring station T1 from 26 April to 28 August 2011 (Julian day 115 to 240).

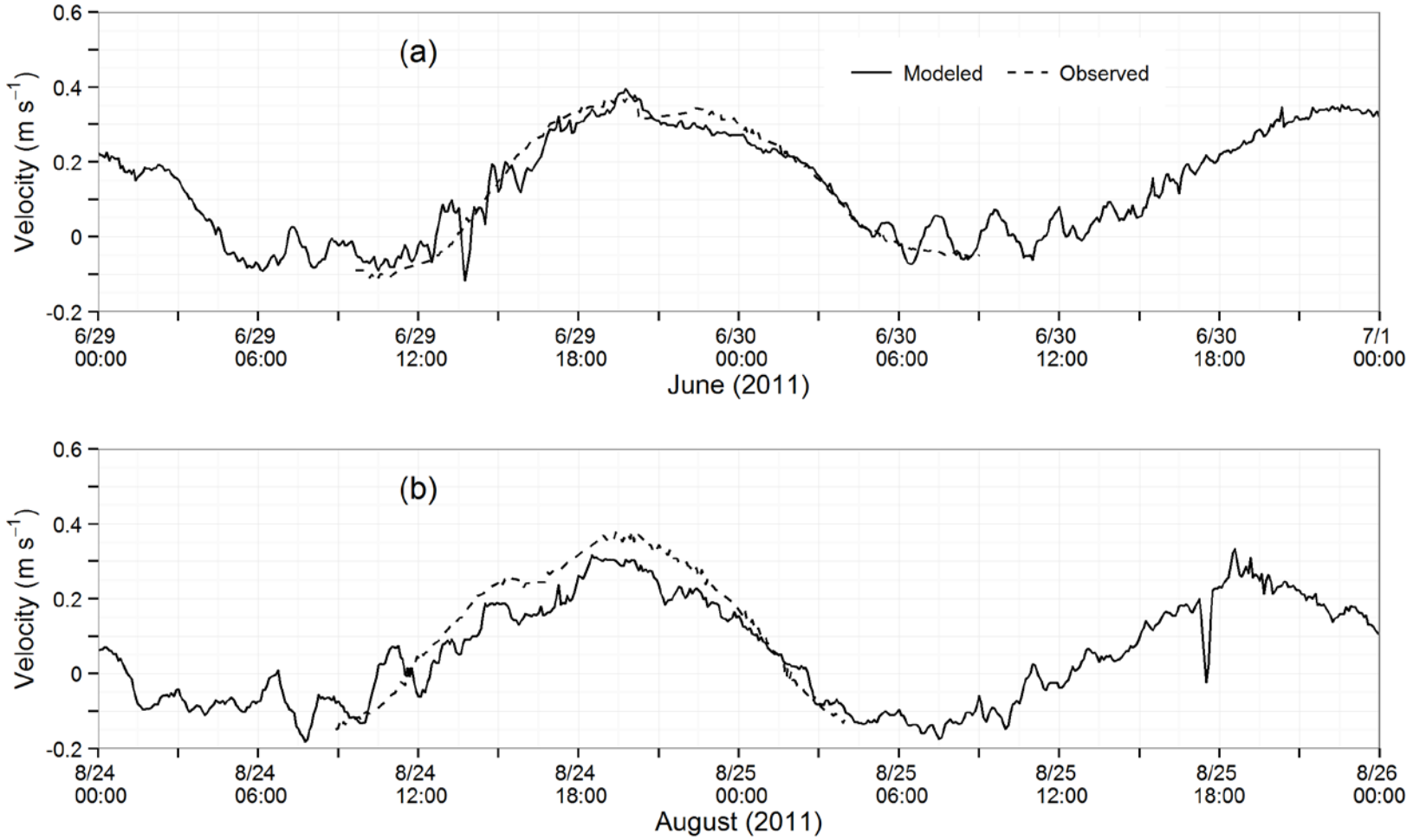

Fig. 4.5 Time-series plots of observed (dashed lines) and simulated (solid lines) depth-averaged velocities at the downstream of the EFDC model on 29–30 June and 24–25 August 2011

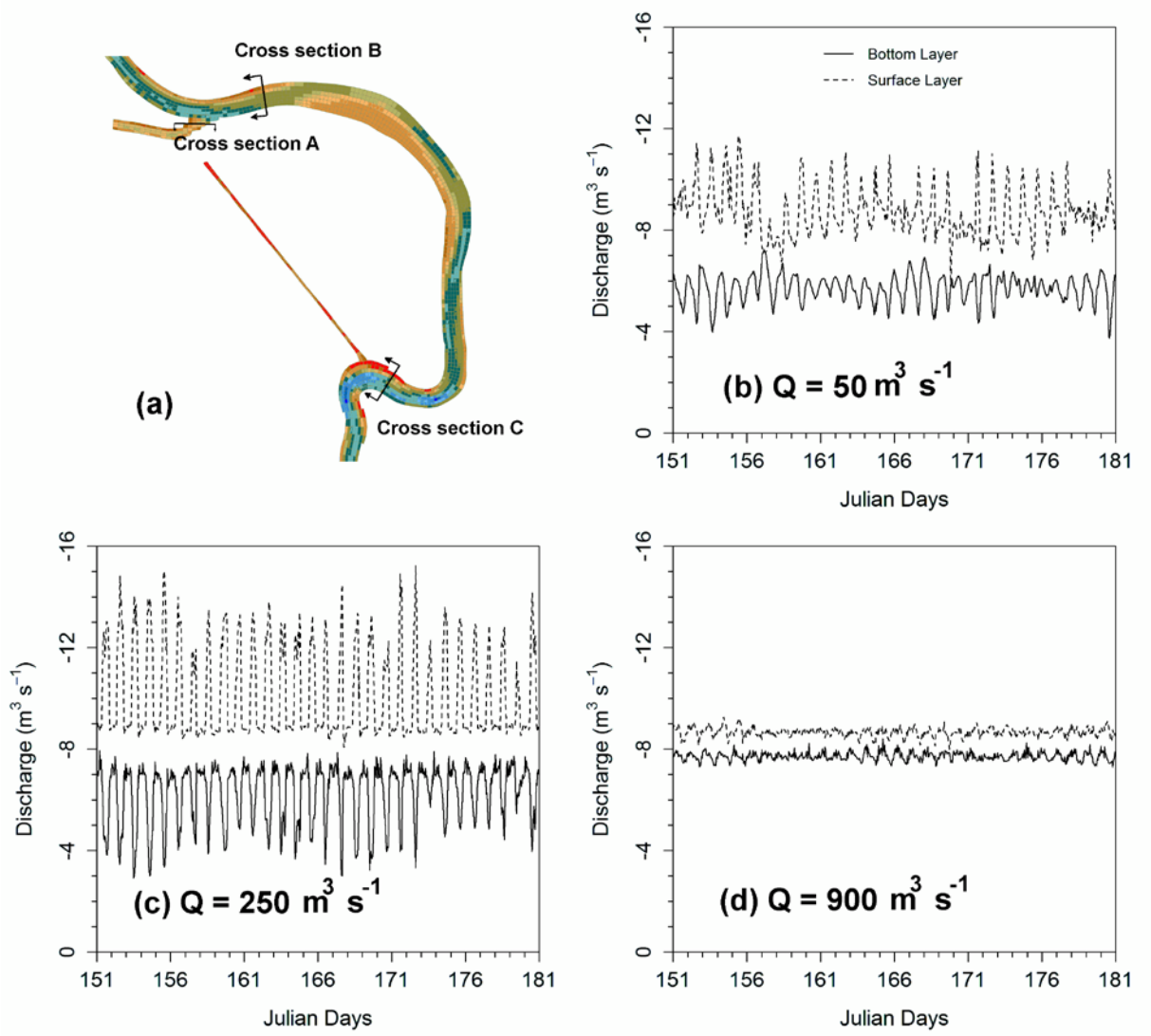

Fig. 4.6 (a) Location of the three cross sections *A*, *B*, and *C* (used in Figs. 4.6 and 4.7) from the intake canal to the discharge canal. Simulated discharges through the bottom layer (solid lines) and the surface layer (dashed lines) at the cross section *A* under (b) 50 $m^3 s^{-1}$, (c) 250 $m^3 s^{-1}$, and (d) 900 $m^3 s^{-1}$ inflows from upstream, respectively.

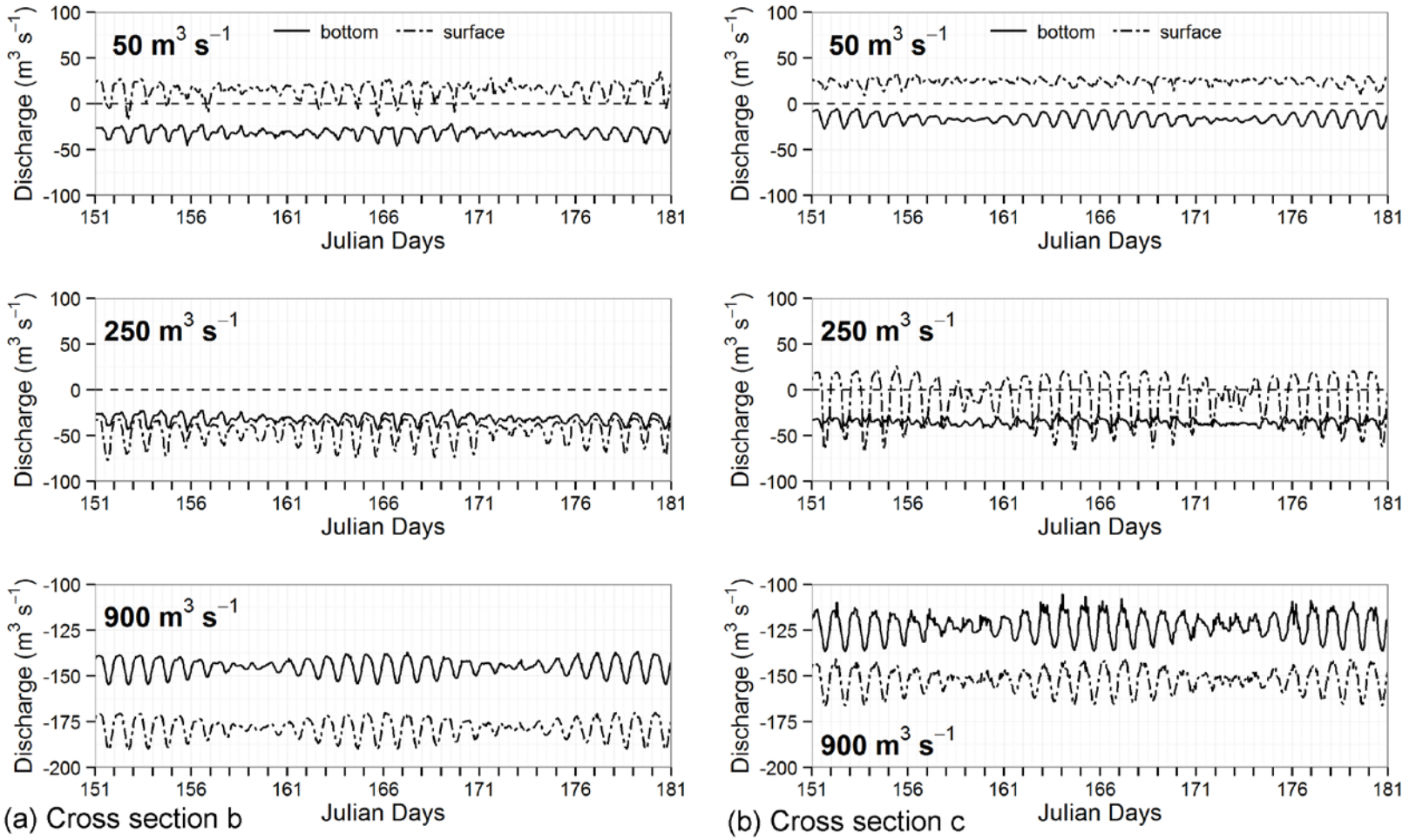

Fig. 4.7 Time series of simulated discharges (m^3 s^{-1}) at the (a) downstream of the intake canal (cross section *B* in Fig. 4.6a), and (b) upstream of the discharge canal (cross section *C* in Fig. 4.6a) for numerical experiments with 50 m^3 s^{-1} (top panels), 250 m^3 s^{-1} (middle panels), and 900 m^3 s^{-1} (bottom panels) inflows from upstream, respectively.

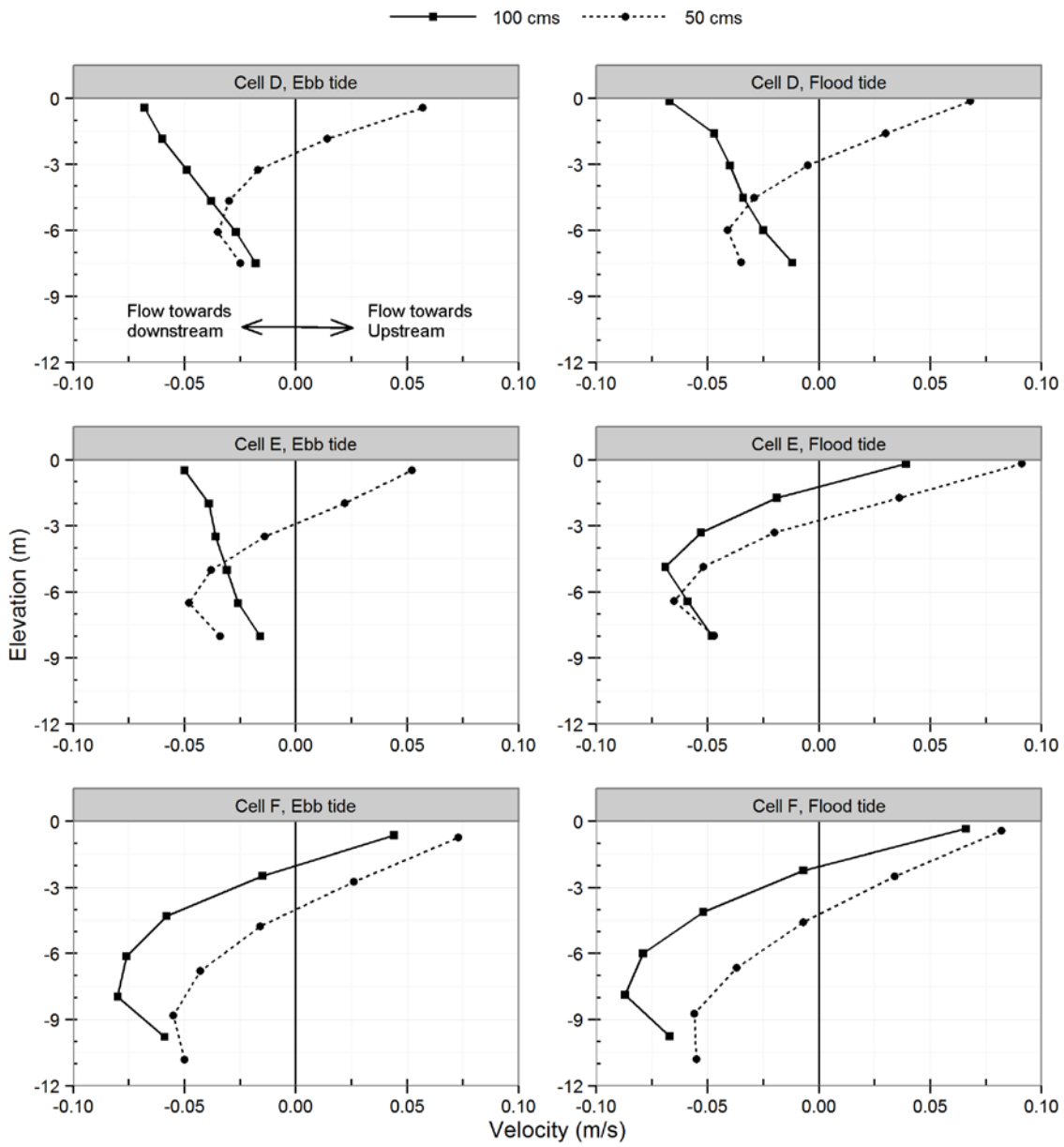

Fig. 4.8 Simulated velocity profiles at the Cell D (top panels), Cell E (middle panels) and Cell F (bottom panels) for numerical experiments with upstream inflow 50 m^3s^{-1} and 100 m^3s^{-1} under ebb tide (left panels) and flood tide (right panels) from the downstream boundary.

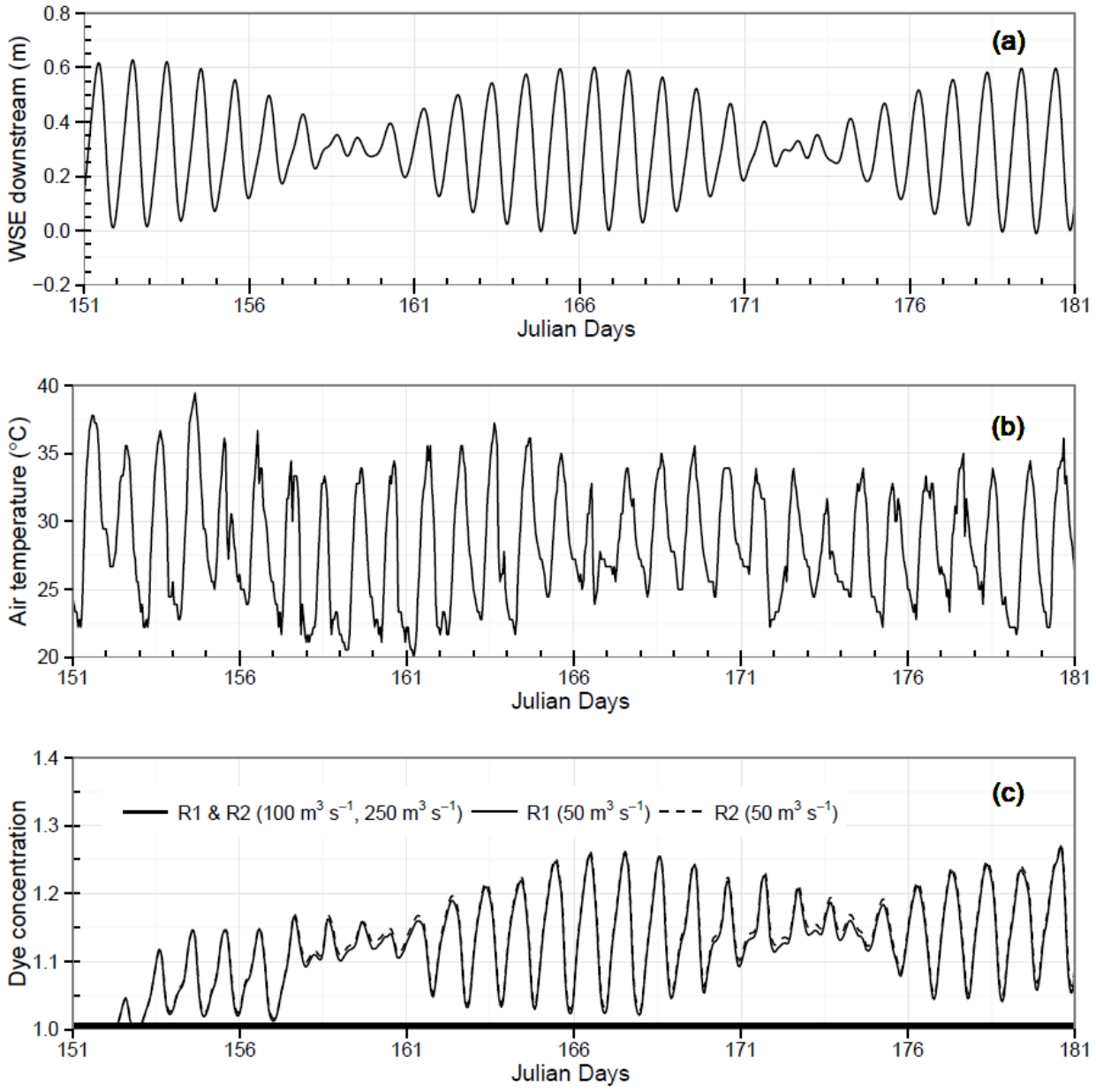

Fig. 4.9 Time series of (a) water surface elevation (WSE) at the downstream boundary (b) air temperature (°C), and (c) simulated dye concentration at R1 and R2 (Fig. 2) from Julian day 151 to 181 (1–30 June) under three different inflows (50, 100, and 250 $m^3 s^{-1}$).

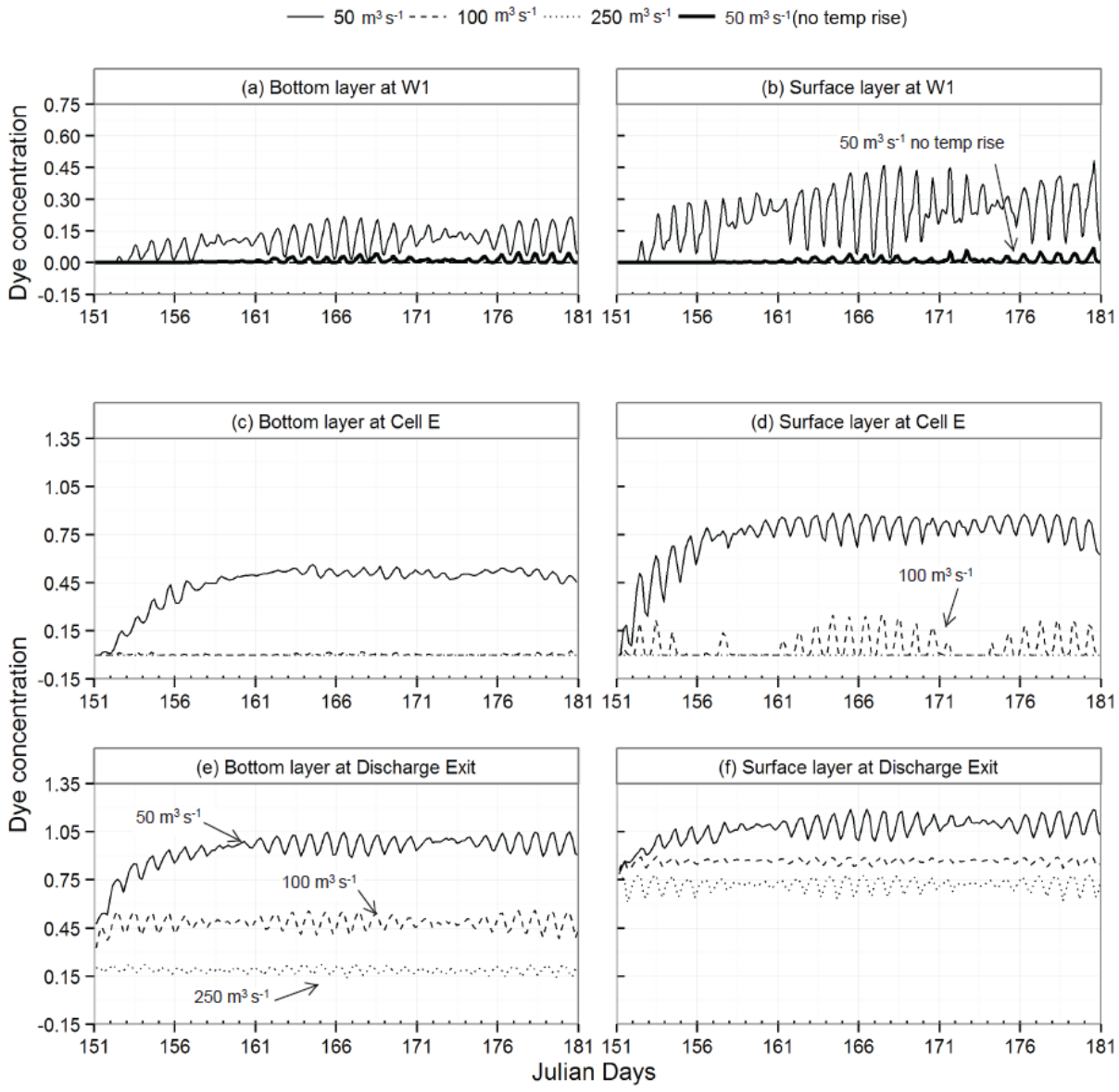

Fig. 4.10 Time series of simulated dye concentrations in the surface layer (right panels) and bottom layer (left) at the withdrawal location W1, Cell E, and discharge exit under 50 m^3 s^{-1}, 100 m^3 s^{-1}, and 250 m^3 s^{-1} inflows with temperature rises, and 50 m^3 s^{-1} inflows without temperature rises in the intakes/discharges 1 and 2.

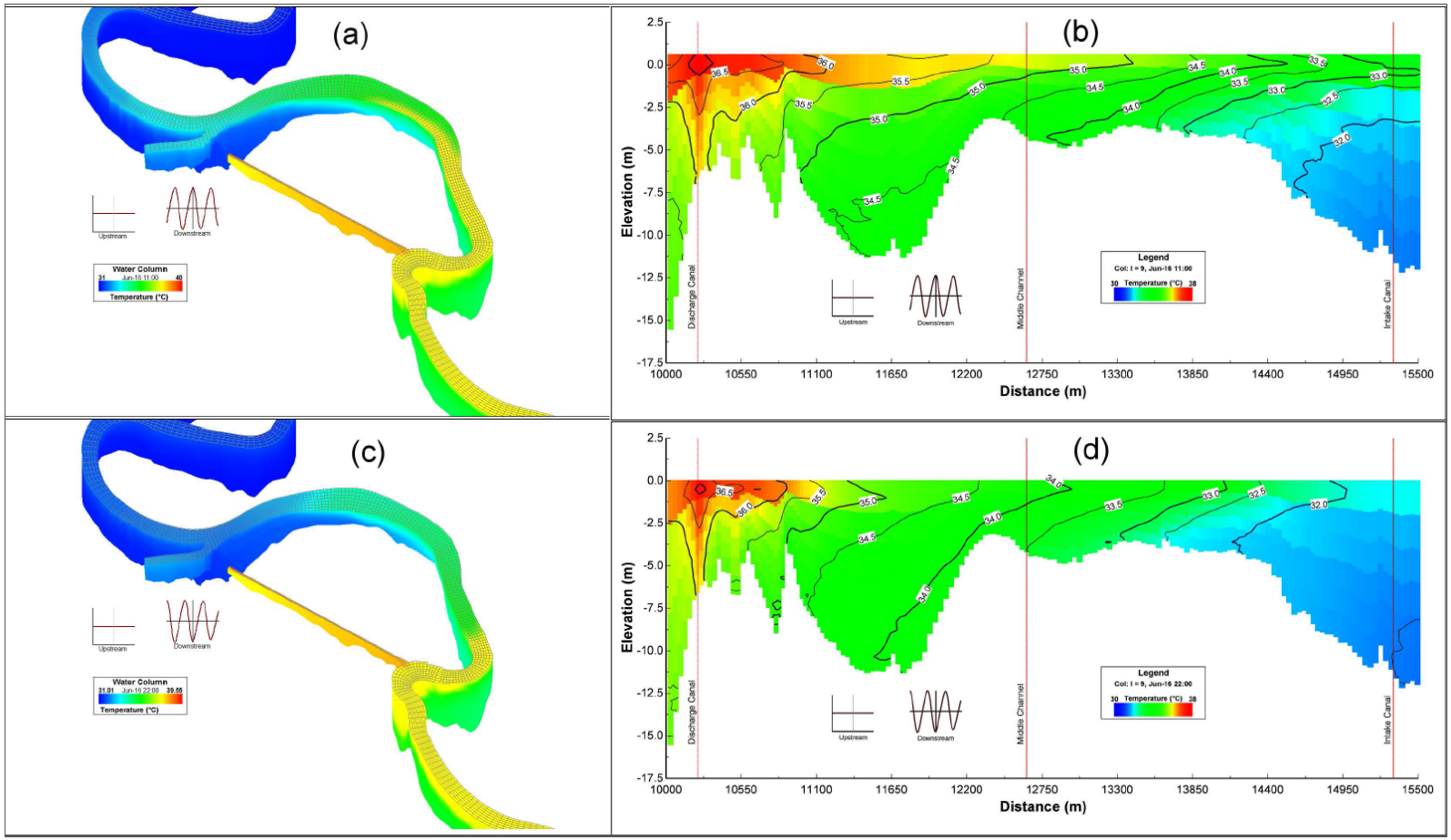

Fig. 4.11 Simulated three-dimensional temperature distributions at (a) 11:00 and (c) 22:00 on 16 June, and two-dimensional temperature profile contours along the river centerline of the Mobile River in the vicinity of the intake canal and discharge canal at (b) 11:00 and (d) 22:00 on 16 June under 50 m^3 s^{-1} inflow from upstream.

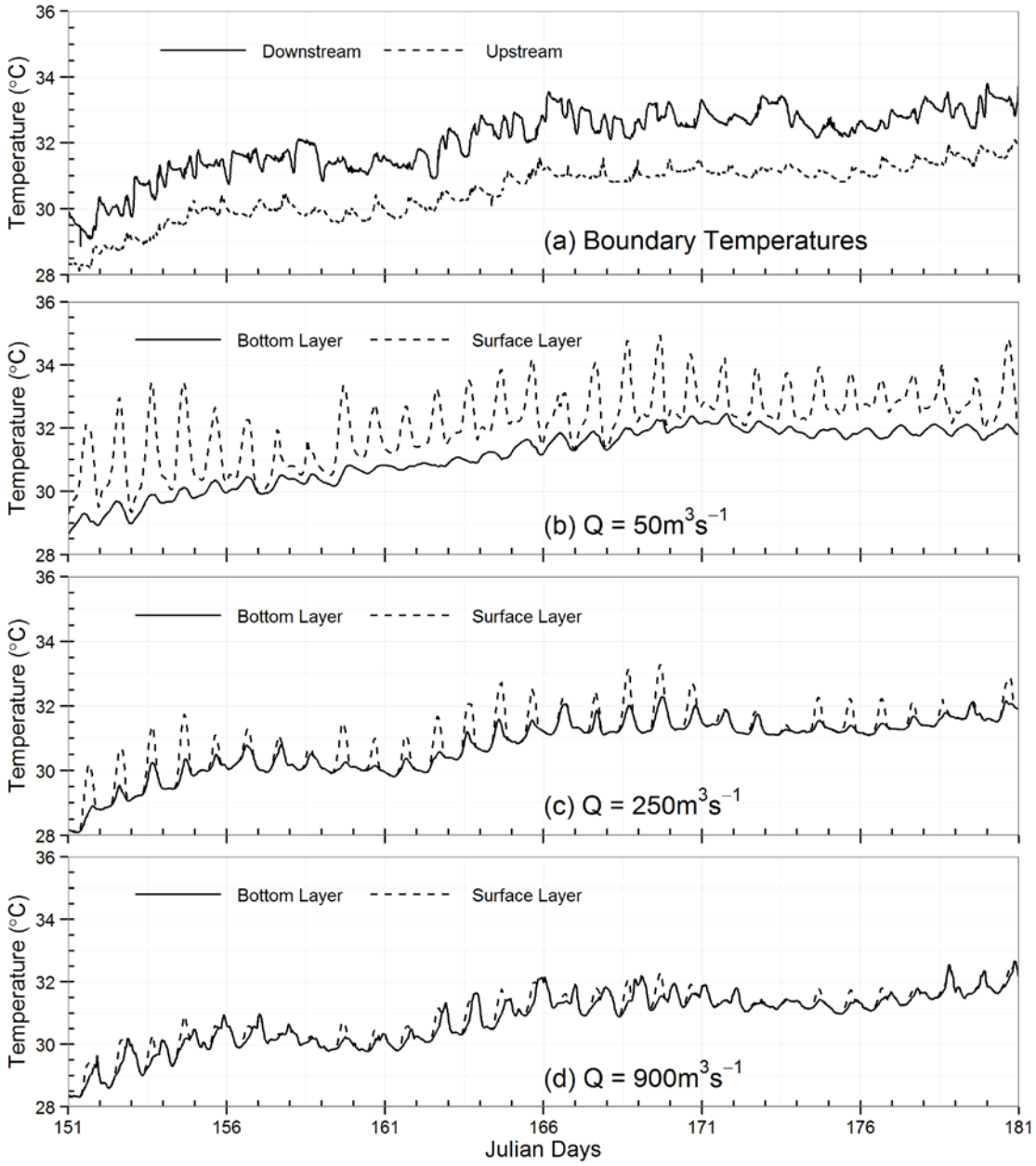

Fig. 4.12 Time series of simulated surface and bottom temperatures at the withdrawal location W1 under (a) 50 m^3 s^{-1}, (b) 250 m^3 s^{-1}, and (c) 900 m^3 s^{-1} inflows from upstream, respectively, with time series of measured temperatures at the downstream (I-65 bridge) and upstream (Bucks station) boundaries from 151–181 Julian days (1–30 June).

Chapter 5. Conclusions and Recommendations

5.1 Summary and Conclusions

This research work is part of Auburn University Water Resources Center Project "Impacts of human activities and climate change on water resource and ecosystem health in the coastal Wolf Bay Basin: A Coastal Diagnostic and Forecast System (CDFS) for integrated assessment". The fourth chapter of the dissertation was related to another funded project. The objective of the overall study is to develop three-dimensional hydrodynamic and water quality models to simulate flow, temperature, salinity, dye and age of water in the coastal regions in Alabama. These numerical models allow us to study the spatial and temporal distributions of flow, salinity, and dye; and provide useful information such as salt and water flux, age of water and recirculation of warm water.

Age of water or pollutants cannot be directly measured in the field or in the lab. Age is a derived concept. However, the dye or pollutant concentration can be measured in the lab and in the field. The cost of the dye experiment in the field is expensive. If measured dye concentration is available, one can verify his model comparing simulated dye concentration with measured concentration from the field. However, because it is expensive it is not feasible to conduct the dye experiment always. Instead the practice of researchers and scientists has been to use the calibrated flow model for the dye study. There are several reasons to predict the age even if we cannot measure it directly in the field. Age of water helps to understand the impact of various hydrologic conditions such

as river inflows, density-induced circulation, and wind-induced transport (Shen and Wang 2007). Without the age of water and tracer concentration we would not be able to understand how the flow from a particular river affects the system. In other words with the age concept we can track the transport path and the pollutant distribution in the system from a source. Age of water and age of tracer have been used as a tool to understand the ventilation timescale in the ocean by various scientists (Thiele and Sarmiento 1990; England 1995; Khatiwala et al. 2001).

For the first phase of the study, EFDC model was developed which included Wolf Bay and Perdido Bay estuary and a part of the Gulf of Mexico to simulate flow, temperature, dye and age of water. Age of water were determined using the equations developed by Delhez et al. (1999). The EFDC model was calibrated and validated against observed data (water surface elevations, temperatures, and salinity) at different locations in 2008–2009 using measured or simulated flows of tributaries from Wolf Bay and Perdido Bay, measured tides at Gulf of Mexico, Big Lagoon and Gulf Intracoastal Waterway (GIWW), and atmospheric data at Jay station from Florida Automated Weather Network (FAWN) as boundary conditions. Mean age of water in a computational cell was computed as the ratio of age concentration and dye concentration. Age of water was used as the transport time scale parameter to understand the transport and fate of pollutants released from all the rivers in Wolf Bay and Perdido Bay and the pollutants released from rivers in Wolf Bay only. For the model scenario runs with 2-year return inflows, 7Q10 low inflows and mean inflows, the constant flow rates were used in rivers throughout the simulation period. Model runs were also performed for the sea level

rise scenarios in 2050 and 2100 using the procedure proposed by Titus and Narayanan (1995). The key conclusions of the first objective from Chapter two (Paper 1) are:

- The steady-state mean age of water computed by solving dye and age concentration equations in a one dimensional (1-D) rectangular channel experiment with constant dye release from upstream was very similar to the age of water computed for the 1-D channel with pulse release. The dye concentrations at various locations for these two experiments were compared with analytical solutions and matched perfectly which suggested that age of water obtained by solving two equations is reliable to find the age of water in real systems.
- Simulated age of water in the Wolf Bay and Perdido Bay system indicated that it would take about 60 days for the substances that are discharged into the system to completely flush out of the system under historic mean (from 1998 to 2010 data) and 2008-2009 inflow conditions. Under 2-year high inflow conditions, simulated age of water was significantly less compared to the historic inflow conditions.
- Under projected sea level rises in 2050 and 2010, salinity in upper Perdido Bay was projected to increase up to 4.3 ppt. The projected change on age of water was about 10 days under 2-year return inflows when sea level rise scenarios were included using tidal boundary at the Gulf of Mexico, Big Lagoon and GIWW.

For the second phase of the study, calibrated EFDC model developed in phase 1 were used to study the water and salt fluxes at various locations in Wolf Bay and Perdido Bay. The five cross sections for studying salt and water exchanges were chosen such that we would be able to quantify the flow and salt exchanges between PBWB and the Gulf of

Mexico, PBWB and Big Lagoon, the Perdido Pass complex and Perdido Bay, and Wolf Bay and Perdido Bay. The subtidal salt exchange was computed using Eulerian and isohaline methods at these five cross sections in the PBWB system. Salinity distributions at Perdido Bay showed the large variation with river inflows and ebb and flood tides at open boundaries. Salinity was typically high in the Perdido Pass complex area where the complex interactions of tides from the Gulf of Mexico and Big Lagoon took place. However, salinity in the upper Perdido Bay, i.e., from US Highway 98 Bridge to Perdido River, had small magnitude under both low and high inflows from upstream and ebb and flood tides from downstream. The key conclusions from Chapter 3 (Phase 2) are:

- From Eulerian analysis, it was found that at Perdido Pass (cross section A-A in Fig. 3.1) and Dolphin Pass (section C-C) tidal oscillatory flux (F_T) was more dominant than the exchange flow (F_E) because these cross sections were closer to the open boundary conditions near the Gulf. However, at the Perdido Pass complex (section B-B), Wolf-Perdido canal (section D-D), and lower Perdido Bay (section E-E) the exchange flow was dominant due to interaction of freshwater from upstream and saline water from the Gulf.
- The flow exchange at the Wolf-Perdido canal was relatively smaller than the flow exchanges at other four cross sections. It was found that under high inflows from Perdido Bay and higher tides from Big Lagoon and the Gulf of Mexico, the flow can move towards Wolf Bay from Perdido Bay. The smaller amount of flow exchange between Perdido Bay and Wolf Bay might be one of the reasons that Wolf Bay is more pristine compared to Perdido Bay.

- The average outgoing salinity at the lower Perdido Bay (18.2 psu) was smallest among the five cross sections: Perdido Pass (27.7 psu), Perdido Pass complex (19.1 psu), Dolphin Pass (22.4 psu), and Wolf-Perdido canal (20.8 psu) . This indicates that the lower Perdido Bay is typically less saline than other four cross sections because the salt intrusion resulted from incoming flows from the Gulf of Mexico and Big Lagoon is attenuated as the tides travel towards upper Perdido Bay and also mixed with freshwater from upstream rivers.
- From Julian Days 270 to 335, the outgoing flows (maximum 349.4 $m^3 s^{-1}$) were larger than the incoming flows at Perdido Pass and the incoming flow into the Perdido Bay from Big Lagoon was significantly larger than the outgoing flows. This was happened because water surface elevation at Big Lagoon was higher than the water surface elevation at Perdido Pass. The large influx of water from Big Lagoon caused the large outflux at Perdido Pass.
- Multi-linear regression analysis was performed to explore the correlations of Q_{in} and Q_{out} at all five cross sections with possible influencing factors: river inflows, water surface elevations at open boundaries, and wind stresses. Wind had influences on the outgoing and incoming flows at all the cross sections. The outgoing flows at Perdido Pass, Perdido Pass complex and lower Perdido Bay had the correlation coefficient greater than 0.75, i.e., the measured inflows, tides and wind stresses explained 75% of the outgoing flows.

For the third phase of the study, two EFDC models were developed for the calibration and sensitivity analysis for the Mobile River in south Alabama. The study area

was influenced by the operation of a once-through cooling system of a power plant, which withdraws ambient water from the deeper depth in the intake canal and discharges warm water at the surface of the discharge canal. Distributions of discharge, velocity, temperature, and dye were analyzed to determine the flow conditions from upstream when the recirculation of warm water from the discharge canal to intake canal would take place. The key conclusions of Chapter 4 (phase 3) are:

- From the dye and velocity profiles, it was found that for 50 $m^3 s^{-1}$ constant inflow from upstream and harmonic boundary at downstream (intersection of I-65 Bridge and Mobile River), the warmer water in the discharge canal could reach up to the intake canal. However, for the model run with 100 $m^3 s^{-1}$ from upstream, the dye was detected up to Cell E (the mid-point between intake canal and discharge canal) but not up to the intake canal. This indicated that recirculation did not occur for 100 $m^3 s^{-1}$ inflow from upstream.
- Model simulation results with and without temperature rise scenario indicate that the recirculation is enhanced by the temperature rise created by the power plant, compared to recirculation driven by low inflows, tidal forces, and solar heating only.
- For the model run with 50 $m^3 s^{-1}$ from upstream, at cross section B the flows with negative magnitude (mean flow -31.4 $m^3 s^{-1}$) were present at the bottom layers and flow with positive magnitude (mean flow 15.3 $m^3 s^{-1}$) were present at the surface layers. This indicated that two layer flows with recirculating flow on the surface layers and downward flow from upstream at the bottom layers are developed under very low inflows from upstream.

5.2 Limitations of the Study

The EFDC model considered in this study is not a completely three dimensional model. In the *z*-direction (along the depth), the water depth is divided into number of horizontal layers and momentum equations (*x* and *y* directions) are solved at each layer. A vertical sigma coordinate and a horizontal orthogonal-curvilinear coordinate are used in the EFDC model. However, it has been well known that sigma-coordinate transformation also induces numerical errors in the horizontal pressure gradient force in the case of stratified flow over steep topography (Liu and Huang 2008). The EFDC model was adequate for the analysis performed in the study because bathymetries in the PBWB system and in Mobile River have relative smooth changes on bottom elevations, i.e. without steep topography. All the models developed were first calibrated and validated with the observed data before performing any scenario analysis.

In all the EFDC model runs, ground water and surface water interaction was not considered. The reason for not including ground water in model simulation was that there is not significant interaction of ground water with surface water. Previous numerical studies (Xia et al. 2011a; Xia et al. 2011b) done in Perdido Bay haven't reported any ground water interaction with surface water and haven't included ground water in their studies.

In the second phase of study, some small tributaries such as inflow at Tarklin Bayou in the Perdido Bay and Soldier Creek in the navigation canal joining Wolf Bay and Perdido Bay were not included in the EFDC model. The impacts of these small rivers were negligible as the calibration process indicated. However, for the age of water study,

the results in small regions nearby the rivers might be slightly different from reported results when there is water release from these locations. From the age of water study, it was found that it would take long time for water released at Perdido Bay to reach the area near Tarklin Bayou. This happened because those flow boundaries for small rivers were not considered in the model. For model runs with 2-year return inflows, not including small rivers might have a relatively larger impact when 2-year return flows from small rivers are not very small.

The third phase of study, i.e., recirculation study in Mobile River didn't use salinity as a model parameter. The reason that salinity was not used as a model parameter was because during the study period there were no large flows coming from Mobile Bay towards the model domain. Harmonic constituents with amplitude of 0.3 m were specified at the downstream boundary (I-65 Bridge on the Mobile River) in the model. Harmonic constituents used for the downstream boundary were derived from the 2010-2011 water surface elevations at the Mobile State Docks NOAA station. The water surface elevation calculated from harmonic constituents of the Mobile State Dock station with the amplitude of 0.3 m matched reasonably well with the measured water surface elevations at the I-65 Bridge for the year 2011. However, during the periods with larger tides from downstream, salinity was observed in the Mobile River segment in the study area in the past. In 2010–2011, there were no larger tides during summer months. Impacts of extreme storm events, which create significant large tides at Mobile Bay, on salinity and temperature distributions in the study area will be investigated in the future.

The Perdido EFDC model has a total of 4,878 curvilinear horizontal grids and 4 uniform spacing vertical sigma layers. The grid sizes for the model ranged from 27 m to

368 m and layer thicknesses ranged from 0.04 m to 1.78 m in the PBWP system (not including the small portion of the Gulf). To obtain better and more accurate model results, it is always better to make the grid size and layer thickness smaller, but at the same time, the computational time will increase for each model run. Spatial resolutions for all 3-D models developed are adequate for the study.

5.3 Future Study

Extending the model developed for tidal Mobile River in the third phase of current study (Chapter 4) is a part of future study. In the third phase of current study, the Mobile River EFDC model domain covers the Mobile River segment from the confluence of Mobile River and Tensaw River at the upstream to the intersection of Mobile River and I-65 Bridge at the downstream. The model used in this current study doesn't consider salinity as a model variable. However, a new EFDC model has been developed to use the larger simulation domain in Mobile River, i.e., from the current upstream location to Mobile Bay on the downstream. The new model thus developed would allow us to directly compare the effects on water surface elevations and salinity in the river domain due to flow and salinity condition at Mobile Bay, especially during extreme storm events (e.g., tropical storms or hurricanes). The model would account for the density differences caused due to the combined effect of salinity and temperature differences in the River. The key objectives of the future study are as follows:

- As a tidal river, it would be very interesting to understand the salt water intrusion in the Mobile River. Several numerical experiments have been designed to represent the flow conditions at Mobile Bay by modifying the water surface

elevations and salinity based on the historic observed data at Mobile Bay to investigate their impacts on the upstream of Mobile River close to the power plant.

- The extreme flow conditions such as hurricane analysis and sea level rise study based on historic flow data would also be explored in the future study. Tidally influenced rivers are always a threat due to flooding due to their connection to oceans and seas. The inundation study of the Mobile River would also be studied.
- The isohaline analysis used in phase 2 (Chapter 3) would be extended to the newly developed Mobile River model to quantify the incoming (towards land) and outgoing (towards ocean) flows at several sections in Mobile River. The numerical experiments with varying upstream inflows and downstream tides are designed that would allow us to better understand the flow and salt exchange that occur in Mobile River under different flow and tidal conditions.
- Another area that would be explored is the analysis of transport and fate of oil spilled in the Gulf of Mexico. A deep oil spill occurred in 2010 in deep horizons in the Gulf of Mexico and had a huge impact in the coastal regions in Alabama, Florida, and Mississippi. The study would be extended to study the impacts of an oil spill by using particle tracking method. Since Mobile River is connected to the Gulf of Mexico and a nursery for several aquatic lives, it would be essential to understand the threat that such oil spill poses to the aquatic and human life.

The isohaline method used in phase 3 (paper 3) is a robust method to calculate the flux through any cross section. In this method, incoming and outgoing flux are first calculated for each salinity class and then positive and negative fluxes at any cross

section are computed. The sum of incoming and outgoing flows calculated from isohaline method for phase 3 was exactly equal to the flow Q_F from the Eulerian decomposition method. Therefore, the method can be extended beyond water and salt exchange. Currently, we are working on another project on a river bounded by two dams on upstream and downstream of the river segment. The upstream dam regulates the water from the reservoir upstream of the river by releasing cold water to the system to support the electricity generation through a power plant located on the river bank approximately midway between the upstream and the downstream. The power plant being considered is also a once-through cooling system. When there is large amount of river inflows from upstream tributaries contributing to the river and high flow releases from upstream reservoir, some of water arriving the downstream dam leaves the system through spillways, at the same time it creates a backwater effect: the rise in water level upstream from flow obstruction (such as dam). Usually, the water is also removed from the system at downstream dam through water turbines. Some interesting phenomena occur in such complex system. Because of cold water releases from upstream, a strong density current flowing along river bottom is developed in the system. At the downstream when the turbines are closed, flow releases are ceased, and then due to the momentum of upstream inflows created during the turbine release, there will be a backwater effect created at the downstream boundary. Because of the backwater effect, water flows backwards towards the upstream in the surface layers and then interacts with flow releases from upstream when the flow releases last reasonably long.

Isohaline method can be modified as isothermal and can be used to calculate the incoming (upstream) and outgoing (downstream) isothermal flux at any cross section for

any temperature range or class. Using isothermal approach, when the water is going towards upstream due to backwater effect or flow recirculation from the power plant, we can find out the exact amount of flows going towards upstream and downstream and temperatures associated with flow moving upstream and downstream. It is very important to understand underlying processes that contribute the flow movement towards upstream or downstream in such complex system where the power plant requires the cold water for the efficient electricity generation. Several release experiments at upstream and downstream will be performed and isothermal fluxes at several cross sections will be studied which allow us to understand the amount of flow moving upwards due to backwater effect and temperature associated with it. We would eventually try to create regression equations relating the outflow/inflow and T_{in}/T_{out} at any cross section with magnitude of flow release, flow release duration at upstream and downstream, water elevation at downstream dam, and air temperature, which would be very useful to provide guidance on flow releases for the efficient production of electricity.

Appendix A: Calibration Parameters in EFDC model

For any numerical model to be able to predict dependent unknown variables accurately, the model should be calibrated using reliable observed data. EFDC model is not a self-calibrated model. The modeler needs to adjust the model parameters based on the study area and hydrologic and hydrodynamic conditions. There are several parameters one may adjust to get the good calibration results. However, before tweaking any calibration parameters, it is very important and essential to represent the study area with appropriate model grid, bathymetry resolution, and boundary conditions. The tuning of model parameters in the calibration process is a recursive process. The values of the model parameters are generally obtained through direct measurement, estimation from other measured data, literature values, and model calibration. Based on literature review the parameters can be selected from a feasible range and adjusted to minimize differences between model results and measured data. For EFDC hydrodynamic models, the parameter determining the bottom friction, such as bottom roughness is often the first model parameter most often adjusted in the model calibration (Ji 2008). The turbulent parameters of Mellor-Yamada model (Mellor and Yamada 1982) are usually not adjusted in the model calibration process, unless there are well-justified reasons. The parameters that are usually adjusted in EFDC hydrodynamic models are as follows:

a. Parameter determining bottom friction, such as bottom roughness height.
b. Horizontal momentum diffusion coefficient

Bottom roughness height, is the one adjusted first and most in EFDC hydrodynamic calibration. According to literature the bottom roughness of the bed is frequently set to 0.02 m with a typical range between 0.01 and 0.1 m. In EFDC model, one needs to

specify the empirical parameter C, when using Smagorinsky formula to compute the horizontal momentum diffusion coefficient. The typical values for the empirical parameter C range from 0.1 to 0.2.

A.1 Calibration Parameters and their Ranges

The calibration parameters used in Perdido EFDC model and EFDC model for Mobile River are shown in table A.1.

Table A.1 Calibration parameters used in Perdido EFDC model, EFDC model for Mobile River and the calibration range for calibration parameters

Calibration Parameters	Perdido EFDC Model	EFDC (Mobile River)	Calibration Range
Smagorinsky Coefficient (empirical parameter c)	0.15	0.2	0.1 – 0.2
Roughness height	0.02 m	0.01 m	0.01 m – 0.1 m
Vertically Eddy viscosity	0.00001 m^2/s	0.00001 m^2/s	$1.0E^{-7} - 1.0E^{-3}$ m^2/s
Horizontal Eddy Viscosity	0.5 m^2/s	2 m^2/s	Usually $10^2 - 10^7$ greater than vertical eddy viscosity

Before adjusting any parameters of EFDC models for the study areas “Wolf Bay and Perdido Bay” and “Mobile River” many iterative runs were performed initially to make sure the grid and the bathymetry used are representative for the study area. Grid cells and bathymetry were revised number of times because the topography of the study area is quite complex. After the higher degree of accuracy was attained in the grid cells and bathymetry, boundary conditions for flow (used in rivers inflows) and water surface elevation (used to represent the ocean boundary) were analyzed and compared with the

data from other nearby stations to check whether the data being used are consistent with the data observed nearby.

In DSI-EFDC model temperature is solved using CEQUAL-W2 approach (Craig 2011). For the temperature simulation the input parameters are atmospheric pressure (millibars), solar radiation (W/m^2), rainfall (m/day), air temperature (°C), evaporation (m/day), relative humidity (dimensionless), and cloud cover (dimensionless). In the models for Perdido Bay and Wolf Bay, and Mobile River evaporation was internally calculated by model from air and dewpoint temperature and wind speed. The model parameters that can be adjusted are minimum fraction of solar radiation absorbed in the top layer, clear water light extinction coefficient (1/m), wind sheltering coefficient, initial bed temperature etc.

Table A.2 Temperature calibration parameters used in Perdido EFDC model, EFDC model for Mobile River

Calibration Parameters	Perdido EFDC Model	EFDC (Mobile River)	Calibration Range
Minimum fraction of solar radiation absorbed in surface layer	0.3	0.35	0.3-0.45
Clear water extinction coefficient (1/m)	0.6	1.2	0.2-1.68
Wind sheltering coefficient	1	1	0.5-1.5
Evaporation transfer coefficient	1.5	1.5	Depends on water body

There were no separate model parameters for salinity calibration. Therefore, the model parameters mentioned in the Tables A.1 and A.2 were adjusted to have the best possible matches between the observed data and modeled water surface elevation, salinity, temperature, and velocity.

Appendix B: Age of Water Theory

In support of the theory of the age of water or pollutants used in Phase 1 the detailed evolution of age of tracer/water equations are presented here. The theory and concepts of age of water presented here is based on the study by Delhez et al. (1999), Deleersnijder et al. (2001), and Delhez and Deleersnijder (2002). Age of tracer / pollutant can be defined as the time elapsed since the parcel under consideration left the region in which its age is prescribed to be zero (Delhez et al. 1999). The basic assumptions for the age of water / pollutants are as follows:

1. The constituents inside of a water or seawater volume element is regarded as the mixture of I+1 constituents, i.e., pure water, dissolved salts, pollutants, plankton etc. that can be identified by the index i $(0 \leq i \leq I)$.
2. Tracer / freshwater is modeled as the continuous medium an approach adopted in most fluid mechanics problems.
3. Boussinesq approximation is used.
4. State variables of the flow under study, i.e., water velocity, pressure, temperature, constituent concentration, etc. are assumed to be defined at every time and location in the domain of interest.

The age theory being introduced uses the Eulerian approach and accounts for advection, mixing, and production / destruction terms of tracer. The method described can be implemented directly to the numerical model using Eulerian discretization.

Let us assume a fluid parcel of volume (ΔV) and *x*, *y*, and *z* denote Cartesian coordinates such that position vector of any point in the domain of interest is given by a vector:

$\boldsymbol{x} = (x, y, z)$. Concentration distribution function of the i-th constituent (Fig. B.1) is defined such that the mass of the particles contained in a parcel of volume ΔV, i.e., $\left(x - \frac{\Delta x}{2}, y - \frac{\Delta y}{2}, z - \frac{\Delta z}{2}\right) \leq (x, y, z) \leq \left(x + \frac{\Delta x}{2}, y + \frac{\Delta y}{2}, z + \frac{\Delta z}{2}\right)$ and the age interval $\left[\tau - \frac{\Delta \tau}{2}, \tau + \frac{\Delta \tau}{2}\right]$ tends to $\rho \Delta V \Delta \tau c_i(t, x, \tau)$ where ρ is a density of seawater and is assumed constant according to Boussinesq approximation. The idea is simply to split the concentration of a tracer into continuous age classes: the concentration distribution function $c(t, \boldsymbol{x}, \tau)$ represents then the contribution of the material with an age of τ to the total concentration $C(t, \boldsymbol{x})$ (Delhez and Deleersnijder 2002).

In the above definition, age τ is an independent variable and it is different from the mean age a which will be introduced later.

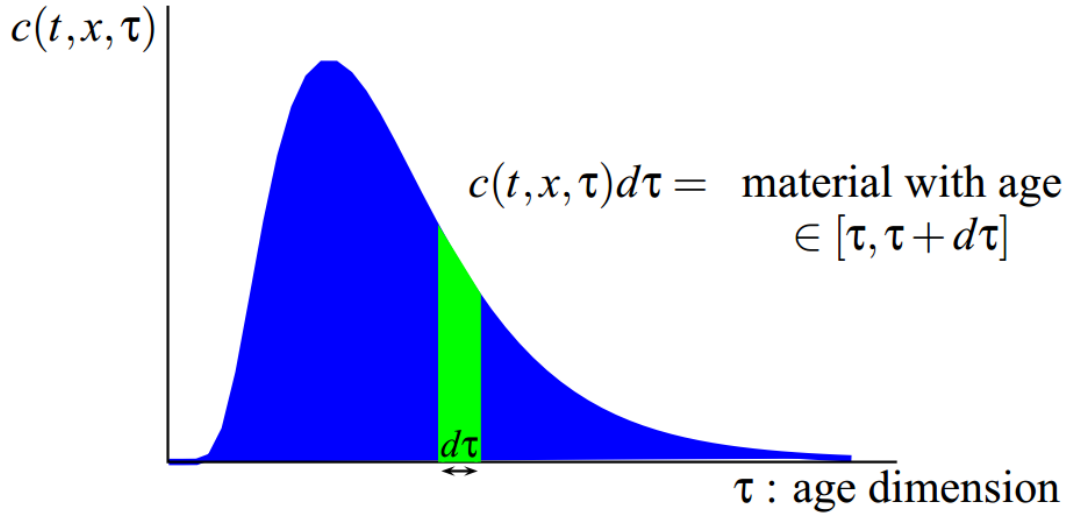

Fig. B.1 Concentration distribution function of a fluid parcel in the age direction (Delhez and Deleersnijder 2002)

If we consider a fluid parcel of volume that at time t has its center at location **x,** the total mass of the particles of the i-th constituent contained in this fluid parcel, of which the age

lies in the interval $\tau - \Delta\tau/2, \tau + \Delta\tau/2$, is asymptotic to $\rho\Delta V\Delta\tau c_i(t,x,\tau)$ as $\Delta V \to 0$ and $\Delta\tau \to 0$. The $c_i(t,x,\tau)$ is the concentration distribution function (Fig. B.1) of the i-th constituents and this definition holds true for any fluid parcel in the domain of interest.

Mass of i-th constituent with different ages contained in the fluid parcel under consideration $m_i(t,\boldsymbol{x},\Delta V)$ can be expressed in terms of concentration distribution function as follows:

$$m_i(t,\boldsymbol{x},\Delta V) \sim \rho\Delta V \int_0^\infty c_i(t,\boldsymbol{x},\tau)d\tau \,, \Delta V \to 0 \qquad \text{(B.1)}$$

The reason for integrating the above integral from $0 - \infty$ is to include all the i-th constituent from age zero to infinity. The mass of fluid constituents is dependent on 5 different independent variables, i.e., *x*, *y*, *z*, *t*, and τ. The dependency of the distribution function on the age τ can be explained as follows. In the vicinity of the source, the main contribution to the tracer concentration is made of material that has been released recently in the system. At a larger distance from the source, the tracer concentration is a mixture of young and old material with a minimum corresponding to the advection time scale from the source. When the tracer is continuously released into the system, there is no material that is older than time *t*. There are some tracers that have the age between the minimum advection time scale and the release time *t* due to diffusion and possible complex hydrodynamics resulting from the detour of these tracers.

Similarly, the mass $m(t,\boldsymbol{x},\Delta V)$ of the fluid parcel is obtained by integrating the masses of several constituents in the water (constituents as previously described vary from i = 0 to $i = I$) as follows:

$$m_i(t,\boldsymbol{x},\Delta V) \sim \sum_{i=0}^{I} m_i(t,\boldsymbol{x},\Delta V) \,, \Delta V \to 0 \qquad \text{(B.2)}$$

Dimensionless concentration $C_i(t,x)$ of the i-th constituent is defined as the mass of the i-th constituent divided by the total mass of all constituents in the volume ΔV and is given by:

$$C_i(t,x) = \int_0^{\infty} c_i(t,x,\tau)\ d\tau \tag{B.3}$$

Now, let us consider a four dimensional volume element $\Delta\Omega$, comprising three-dimensional space coordinates *x*, *y*, and *z*, and age as the fourth dimension which is associated with coordinate τ .The volume element considered consists of the physical volume element given by $\left[x-\frac{\Delta x}{2}, x+\frac{\Delta x}{2}\right]\times\left[y-\frac{\Delta y}{2}, y+\frac{\Delta y}{2}\right]\times\left[z-\frac{\Delta z}{2}, z+\frac{\Delta z}{2}\right]$. The mass of the i-th constituents may vary as a result of local production / destruction, chemical reactions or radioactive decay, and transport through the boundaries. So, considering all of the possible processes, the mass budget of volume element is given by:

$$\begin{aligned}
&\rho\Delta\,x\,\Delta\,y\,\Delta\,z\,\Delta\,\tau\frac{\partial}{\partial t}c_i(t,x,\tau)\\
&\quad=\rho\,\Delta\,x\,\Delta\,y\,\Delta\,z\,\Delta\,\tau\,(p_i-d_i)\\
&\quad-\rho\,\Delta\,y\,\Delta\,z\,\Delta\tau\left[q_{\{i,x\}}(t,x+\Delta x/2,y,z,\tau)\right.\\
&\quad-\left.q_{\{i,x\}}(t,x-\Delta x/2,y,z,\tau)\right]\\
&\quad-\rho\Delta x\,\Delta z\,\Delta\tau\left[q_{\{i,y\}}(t,x,y+\Delta y/2,y,z,\tau)\right.\\
&\quad-\left.q_{i,y}\,(t,x,y-\Delta y/2,z,z,\tau)\right]\\
&\quad-\rho\,\Delta\,x\,\Delta\,y\,\Delta\tau\left[q_{i,z}\,(t,x,y,z+\Delta z/2,\tau)\right.\\
&\quad-\left.q_{\{i,z\}}(t,x,y,z-\Delta z/2,\tau)\right]\\
&\quad-\rho\,\Delta\,x\,\Delta\,y\,\Delta z\left[q_{i,\tau}\,(t,x,y,z,\tau+\Delta\tau/2)\right.\\
&\quad-\left.q_{\{i,\tau\}}(t,x,y,z,\tau-\Delta\tau/2,\tau)\right]
\end{aligned} \tag{B.4}$$

where $p_i(\geq 0)$ and $d_i(\geq 0)$ are rates of production and destruction, respectively, i.e., sources and sink terms, $q_{i,x}, q_{i,y}, q_{i,z}, and\ q_{i,\tau}$ represent the fluxes in the x, y, z, and τ directions.

Now, taking the limit $\Delta x, \Delta y, \Delta z, \Delta\tau \rightarrow 0$, Equation B.4 can be written as

$$\frac{\partial\, \mathrm{c_i}}{\partial\, \mathrm{t}} = \mathrm{p_i} - \mathrm{d_i} - \nabla . \mathbf{q_i} - \frac{\partial \mathrm{q_{i,\tau}}}{\partial \tau} \qquad \text{(B.5)}$$

where $\boldsymbol{q_i} = \left(q_{i,x}, q_{i,y}, q_{i,z}\right)$ is a flux vector that accounts for the transport of mass in the three-dimensional physical space, and ∇ is nabla or del vector operator in physical space.

So, we can write $\nabla . \boldsymbol{q_i} = \frac{\partial q_{i,x}}{\partial x} + \frac{\partial q_{i,y}}{\partial y} + \frac{\partial q_{i,z}}{\partial z}$

The flux (q_i) represents the transport of mass in the physical mass in the physical space which is assumed to be independent of the age of the particles being transported. The flux $(\boldsymbol{q_i})$ consists of an advective part, due to the fluid velocity **u** and the diffusivity tensor (**K**) which is given by:

$$\boldsymbol{q_i} = \boldsymbol{u} c_i - \boldsymbol{K} . \nabla c_i \qquad \text{B. 6}$$

The flux $q_{i,\tau}$ is related to ageing, i.e., the process by which age of every particle tends to increase by a certain amount of time as time progresses. It is typically assumed to increase the same amount of time which can be viewed as advection with a unit velocity in age direction. So, flux $q_{i,\tau}$ can be written as $q_{i,\tau} = c_i$

Now, Equation B.5 can be further simplified as follows:

$$\frac{\partial c_i}{\partial t} = p_i - d_i - \nabla . (\boldsymbol{u} c_i - \boldsymbol{K} . \nabla c_i) - \frac{\partial c_i}{\partial \tau} \qquad \text{B.7}$$

The above equation should be solved in a five dimensionless space because it has five independent variables, i.e, *x*, *y*, *z*, *t*, and τ. So, instead of solving in 5 dimensional space, which is difficult to accomplish, it can be integrated over τ and use the boundary of

concentration distribution function that the concentration distribution function would be zero when τ reaches infinity, i.e.

$li\, m_{\tau\to\infty}\, c_i(t, x, \tau) = 0$

Now, Equation B.7 can be written in the simplified form as follows:

$$\frac{\partial C_i}{\partial t} = P_i - D_i - \Delta.(\boldsymbol{u}C_i - \boldsymbol{K}.\nabla \mathrm{C_i}) \qquad \text{B.8}$$

It should be noted that from now onwards C_i will be used in place of c_i. P_i and D_i are integrated production and destruction terms.

If there are no production and destruction terms involved (i.e., if passive tracer is considered), then the above equation can be written as:

$$\frac{\partial C(t,\ \vec{x})}{\partial t} + \nabla\big(uC(t,\vec{x}) - K\nabla C(t,\vec{x})\big) = 0 \qquad \text{B.9}$$

B.1 Age Averaging Hypothesis and Age of Tracer

An age averaging hypothesis is introduced by Delhez et al. in 1999 to derive the mean age of particles from the concentration distribution function. Age averaging hypothesis states that, "The mean age of a set of particles is defined as the mass-weighted, arithmetic average of the ages of the particles considered; that is valid for particles of the same constituents or for particles of different constituents."

If we assume two particles, identified by superscript "A", and "B" and the masses and ages of which are m^A, m^B and τ^A, τ^B, the mean age τ^{A+B} according to age averaging hypothesis is given by:

$$\tau^{A+B} = \frac{\mathrm{m^A}\tau^{\mathrm{A}} + m^{\mathrm{B}}\tau^{\mathrm{B}}}{(\mathrm{m^A} + \mathrm{m^B})} \qquad \text{B.10}$$

where $m^{A+B} = m^A + m^B$ (because mass is additive quantity) and age is not a additive quantity.

Now, Equation B.10 can be written as follows:

$$m^{A+B}\tau^{A+B} = m^A\tau^A + m^B\tau^B \qquad \text{B.11}$$

The left hand side (L.H.S) of the above equation might be called **age content** – an appellation inspired from the fact mass is a measure of the matter content of the system.

In the real systems there are more than two particles, therefore, to deal with a system consisting of more than two particles, the formula can be extended translating the Lagrangian expressions (Equations B.10 and B.11) into Eulerian equation B.12 easily. The mean age $a_i(t,x)$ of the i-th constituent at time *t* and location $\boldsymbol{x}$ is given by:

$$a_i(t,x) = \frac{\int_0^\infty \tau c_i(t,x,\tau)\partial\tau}{\int_0^\infty c_i(t,x,\tau)d\tau} = \frac{\alpha_i(t,x)}{C_i(t,x)} \qquad \text{B.12}$$

Where the new variable $\alpha_i(t,x) = \int_0^\infty \tau c_i(t,x,\tau)\partial\tau$ is the age concentration (time unit seconds or hours or days) and $C_i(t,x) = \int_0^\infty c_i(t,x,\tau)\partial\tau$ is the dye concentration defined before.

Age concentration is closely associated with the concept of age content as tracer concentration was associated with the mass. Consider, the fluid parcel of volume ΔV at time *t* and has its center at location *x*. Then adopting the concept used to Equation B.1 to this present case, age content $A_i(t,x,\Delta V)$ of the i-th constituent of the fluid parcel satisfies:

$$A_i(t,\boldsymbol{x},\Delta V) \sim \rho\Delta V\alpha_i(t,\boldsymbol{x}), \qquad \Delta V \to 0 \qquad \text{B.13}$$

Hence, the age content being an additive quantity, the total age content of the fluid parcel under study is

$$A(t,\boldsymbol{x},\Delta V)\sim \sum_{i=0}^{I} A_i(t,\boldsymbol{x},\Delta V), \qquad \Delta V \to 0 \qquad \text{B.14}$$

Comparing Equations B. 13 and B. 14 with mass of the fluid constituents and mass of fluid parcels, it appears that the role played by the age concentration in the calculation of the age content is similar to that of the concentration in the measure of the matter content – i.e. the calculation of the mass. Therefore, we can derive the equations for the age concentration similar to the governing equations of the concentration.

Now, we can write,

$$\lim_{\tau\to 0} \tau c_i(t,x,\tau) = 0 \qquad \text{B.15}$$

$$\lim_{\tau\to \infty} \tau c_i(t,x,\tau) = 0 \qquad \text{B.16}$$

Multiplying Equation B.7 by τ, integrating over τ from 0 to infinite (the reason for integrating τ from 0 to infinite is because the concentration of the particles is the summation of the concentration distribution function from age 0 to infinity), taking into account the above boundary conditions, we get,

$$\frac{\partial \alpha_i}{\partial t} = C_i + \pi_i - \delta_i - \boldsymbol{\nabla}.(\boldsymbol{u}\alpha_i - \boldsymbol{K}.\nabla\alpha_i) \qquad \text{B.17}$$

With

$$\pi_i(t,x) = \int_0^{\infty} \tau p_i(t,x,\tau)d\tau \qquad \text{B.18}$$

$$\delta_i(t,x) = \int_0^{\infty} \tau d_i(t,x,\tau)d\tau \qquad \text{B.19}$$

As expected, the age concentration satisfies an equation similar to the equation B.7 governing the evolution of the concentration of every constituent, hence its name.

The equation governing every constituent concentration and its age concentration are derived from the same equation, i.e., the equation obeyed by the concentration distribution function. Therefore, the sub grid-scale parameterizations in the equations governing the dye or tracer concentration and the age concentration, respectively, are consistent with each other.

As the differential terms in the concentration and age concentration equations (B.7 and B.17) have a similar form, there is no need to develop new numerical schemes for the purpose of estimating the age concentration. Instead, those implemented for computing the concentration can be used to obtain the age concentration. The implementation using EFDC to solve for the age concentration is described in the section 1.4.2.

B.2 Special Case: Passive Tracer

The source/sink terms appearing in the equation governing the concentration distribution function of a passive constituent – i.e. a constituent that is neither produced nor destroyed are obviously zero:

$$p_p = 0 = d_p \qquad \text{B.20}$$

Hence, the corresponding production and destruction rates of concentration and age concentrations are also zero:

$$P_p = 0 = D_p \qquad \text{B.21}$$

and in Equation B.17, $\pi_p = 0 = \delta_p$ B.22

Therefore, the expressions of governing equations for the passive tracer are as follows:

$$\frac{\partial C(t,\vec{\boldsymbol{x}})}{\partial t} + \nabla(uC(t,\vec{\boldsymbol{x}}) - K\nabla C(t,\vec{\boldsymbol{x}}) = 0 \qquad \text{B. 23}$$

$$\frac{\partial \alpha(t,\vec{\boldsymbol{x}})}{\partial t} + \nabla(u\alpha(t,\vec{\boldsymbol{x}}) - K\nabla \alpha(t,\vec{\boldsymbol{x}}) = C(t,\vec{\boldsymbol{x}}) \qquad \text{B. 24}$$

$$a(t,\vec{\boldsymbol{x}}) = \frac{\alpha(t,\vec{\boldsymbol{x}})}{C(t,\vec{\boldsymbol{x}})} \qquad \text{B. 25}$$

Equations B.23 and B.24 will be used to solve for the dye (passive tracer) concentration and age concentration. The mean age "a" is calculated by Equation B. 25 where C is the tracer concentration, α is the age concentration, $\boldsymbol{u}$ is the velocity field (u, v, w for three dimensional velocities in x, y, and z directions), K is the diffusivity tensor, and t is time and $\vec{x}$ is spatial coordinates.

In the research study performed in Phase 1 the dye considered is a passive tracer, i.e., it does not decay with time, therefore, the equations B.23–B.25 were used to find the age of tracer. The limitations of age of water are as follows:

1. In the real systems, the dye used may be radioactive tracer which may decay with time or may be changed into another tracer after reaction so one might need to include the production and destruction terms so the assumption of passive tracer wouldn't be valid. Equations that need to be solved for radioactive tracer is given in Deleersnijder et al. (2001).
2. The concept of age in case of pure diffusion (no advection) is not valid (Delhez and Deleersnijder 2002)

References

Bai, S., and Lung, W.-S. (2005). "Modeling sediment impact on the transport of fecal bacteria." *water Research*, 39(20), 5232-5240.

Bales, J., Tomlinson, S., and Tillis, G. (2006). *Flow and salt transport in the Suwannee River Estuary, Florida, 1999-2000: Analysis of data and three-dimensional simulations*, US Department of the Interior, US Geological Survey, Reston, VA.

Baur, T. (2008). "Location and design of cooling water intake and outlet structures for power plants in Germany's coastal area." Chinese-German Joint Symposium on Hydraulic and Ocean Engineering, Darmstadt.

Beasley, L. R. (2010). "Interaction of groundwater, surface water and seawater in Wolf Bay, Weeks Bay, and Dauphin island coastal watersheds, Alabama," Auburn University.

Bhuiyan, M., and Dutta, D. (2012). "Analysis of flood vulnerability and assessment of the impacts in coastal zones of Bangladesh due to potential sea-level rise." *Natural Hazards*, 61(2), 729-743, doi:10.1007/s11069-011-0059-3.

Bilgili, A., Proehl, J. A., Lynch, D. R., Smith, K. W., and Swift, M. R. (2005). "Estuary/ocean exchange and tidal mixing in a Gulf of Maine Estuary: A Lagrangian modeling study." *Estuarine, Coastal and Shelf Science*, 65(4), 607-624, doi:10.1016/j.ecss.2005.06.027.

Blumberg, A., Galperin, B., and O'Connor, D. (1992). "Modeling vertical structure of open-channel flows." *Journal of Hydraulic Engineering*, 118(8), 1119-1134, doi:doi:10.1061/(ASCE)0733-9429(1992)118:8(1119).

Caliskan, A., and Elci, S. (2009). "Effects of selective withdrawal on hydrodynamics of a stratified reservoir." *Water resources management*, 23(7), 1257-1273.

Chadwick, M. A., and Feminella, J. W. (2001). "Influence of salinity and temperature on the growth and production of a freshwater mayfly in the Lower Mobile River, Alabama." *Limnology and Oceanography*, 46(3), 532-542.

Chapra, S. C. (1997). *Surface water-quality modeling*, McGraw-Hill series in water resources and environmental engineering, McGraw-Hill, New York, 844 p.

Chen, S. N., Geyer, W. R., Ralston, D. K., and Lerczak, J. A. (2012). "Estuarine Exchange Flow Quantified with Isohaline Coordinates: Contrasting Long and Short Estuaries." *Journal of Physical Oceanography*, 42(5), 748-763, doi:10.1175/jpo-d-11-086.1.

Chuang, Y.-L., Yang, H.-H., and Lin, H.-J. (2009). "Effects of a thermal discharge from a nuclear power plant on phytoplankton and periphyton in subtropical coastal waters." *Journal of Sea Research*, 61(4), 197-205.

Craig, P. M. (2011). "User's Manual for EFDC_Explorer 6: A Pre/Post processor for the Environmental Fluid Dynamics Code." Dynamic Solutions, LLC, Knoxville, TN.

Deleersnijder, E., Campin, J.-M., and Delhez, E. J. M. (2001). "The concept of age in marine modelling: I. Theory and preliminary model results." *Journal of Marine Systems*, 28(3–4), 229-267, doi:10.1016/s0924-7963(01)00026-4.

Delhez, E. J. M., Campin, J.-M., Hirst, A. C., and Deleersnijder, E. (1999). "Toward a general theory of the age in ocean modelling." *Ocean Modelling*, 1(1), 17-27, doi:10.1016/s1463-5003(99)00003-7.

Delhez, E. J. M., and Deleersnijder, E. (2002). "The concept of age in marine modelling: II. Concentration distribution function in the English Channel and the North Sea." *Journal of Marine Systems*, 31, 279-297.

Deltares. (2010). "Delft3D-RGFGRID: Generation and manipulation of curvilinear grids for FLOW and WAVE: User manual." Netherland.

Deng, J. S., Wang, K., Hong, Y., and Qi, J. G. (2009). "Spatio-temporal dynamics and evolution of land use change and landscape pattern in response to rapid urbanization." *Landscape and urban planning*, 92(3–4), 187-198, doi:http://dx.doi.org/10.1016/j.landurbplan.2009.05.001.

Devkota, J., Fang, X., and Fang, V. Z. (2013). "Response characteristics of Perdido and Wolf Bay system to inflows and sea level rise." *British Journal of Environment and Climate Change*, 3(2), 229-256, doi:10.9734/BJECC/2013/3516.

Dronkers, J., and van de Kreeke, J. (1986). "Experimental determination of salt intrusion mechanisms in the Volkerak estuary." *Netherlands Journal of Sea Research*, 20(1), 1-19, doi:http://dx.doi.org/10.1016/0077-7579(86)90056-6.

Duchon, C. E. (1979). "Lanczos Filtering in One and Two Dimensions." *Journal of Applied Meteorology*, 18(8), 1016-1022, doi:10.1175/1520-0450(1979)018<1016:lfioat>2.0.co;2.

Dyer, K. R. (1973). *Estuaries: A Physical Introduction*, John Wiley & Sons, New York, NY, USA, l40 p, 140.

Engqvist, A., and Stenstrom, P. (2009). "Flow regimes and long-term water exchange of the Himmerfjarden estuary." *Estuarine Coastal and Shelf Science*, 83(2), 159-174, doi:10.1016/j.ecss.2007.11.029.

Fischer, H. B. (1972). "Mass transport mechanisms in partially stratified estuaries." *Journal of Fluid Mechanics*, 53(4), 671-687, doi:doi:10.1017/S0022112072000412.

Fischer, H. B. (1976). "Mixing and dispersion in estuaries." *Annual Review of Fluid Mechanics*, 8(1), 107-133, doi:10.1146/annurev.fl.08.010176.000543.

Fischer, H. B., List, E. J., Koh, R. C. Y., Imberger, J., and Brooks, N. H. (1979). "Mixing in Inland and Coastal Waters." Academic Press, San Diego.

Flemer, D., Livingston, R., and McGlynn, S. (1998). "Seasonal growth stimulation of sub-temperate estuarine phytoplankton to nitrogen and phosphorus: An outdoor microcosm experiment." *Estuaries*, 21(1), 145-159, doi:10.2307/1352553.

Galperin, B., Kantha, L. H., Hassid, S., and Rosati, A. (1988a). "A Quasi-equilibrium Turbulent Energy Model for Geophysical Flows." *Journal of the Atmospheric Sciences*, 45(1), 55-62, doi:10.1175/1520-0469(1988)045<0055:aqetem>2.0.co;2.

Galperin, J., Kantha, L. H., Hassid, S., and Rosati, A. (1988b). "A quasi-equilibrium turbulent energy model for geophysical flows." *Journal of the Atmospheric Sciences*, 45(1), 55-62.

Gilcoto, M., Pardo, P. C., Alvarez-Salgado, X. A., and Perez, F. F. (2007). "Exchange fluxes between the Ria de Vigo and the shelf: A bidirectional flow forced by remote wind." *Journal of Geophysical Research-Oceans*, 112(C6), doi:10.1029/2005jc003140.

Godin, G. (1972). *The analysis of tides*, University of Toronto Press, Toronto, 264 pp.

Godin, G. (1999). "The Propagation of Tides up Rivers With Special Considerations on the Upper Saint Lawrence River." *Estuarine, Coastal and Shelf Science*, 48(3), 307-324, doi:http://dx.doi.org/10.1006/ecss.1998.0422.

Gong, W., Shen, J., and Reay, W. G. (2007). "The hydrodynamic response of the York River estuary to Tropical Cyclone Isabel, 2003." *Estuarine, Coastal and Shelf Science*, 695-710.

Gong, W., and Shen, J. (2009). "Response of sediment dynamics in the York River Estuary, USA to tropical cyclone Isabel of 2003." *Estuarine, Coastal and Shelf Science*, 84(1), 61-74.

Gong, W., Shen, J., and Hong, B. (2009). "The influence of wind on the water age in the tidal Rappahannock River." *Marine Environmental Research*, 68(4), 203-216.

Gong, W., and Shen, J. (2010). "A model diagnostic study of age of river-borne sediment transport in the tidal York River Estuary." *Environmental Fluid Mechanics*, 10(1), 177-196, doi:10.1007/s10652-009-9144-5.

Grubbs, J., and Pittman, J. R. (1997). "Application of acoustical methods for estimating water flow and constituent loads in Perdido Bay, Florida." *Water-Resources Investigations Report*, 97-4101.

Hamrick, J. M. (1992a). "Estuarine environmental impact assessment using a three-dimensional circulation and transport model." "Estuarine and Coastal Modeling" The 2nd International Conference, M. L. Spaulding, K. Bedford, A. Blumberg, R. Cheng, and C. Swanson, eds., ASCE, New York, 292-303.

Hamrick, J. M. (1992b). "A three-dimensional environmental fluid dynamics computer code: Theoretical and computational aspects." Special Report 317, Virginia Institute of Marine Science, College of William and Mary, Gloucester Point, VA.

Hamrick, J. M. (1994). "Linking hydrodynamic and biogeochemical transport models for estuarine and coastal waters." *Proceedings of the 3rd International Conference on Estuarine and Coastal Modeling*, American Society of Civil Engineers, New York, 591-608.

Hamrick, J. M. (1995). "Calibration and verification of the VIMS EFDC model of the James River, Virginia." The College of William and Mary, Virginia Institute of Marine Science.

Hamrick, J. M., and Mills, W. B. (2000). "Analysis of water temperatures in Conowingo pond as influenced by the Peach Bottom atomic power plant thermal discharge." *Environmental Science & Policy*, 3(Supplement 1), 197-209.

Hansen, D. V., and Rattray, M. (1965). "Gravitational circulation in straits and estuaries." *J. Mar. Res.*, 23, 104-122.

Hansen, D. V., and Rattray Jr, M. (1966). "New dimensions in estuary classification." *Limnology and Oceanography*, 319-326.

Hernandez-Ayon, J. M., Galindo-Bect, M. S., Flores-Báez, B. P., and Alvarez-Borrego, S. (1993). "Nutrient concentrations are high in the turbid waters of the Colorado River Delta." *Estuarine, Coastal and Shelf Science*, 37(6), 593-602, doi:http://dx.doi.org/10.1006/ecss.1993.1075.

Huang, W., and Liu, X. (2009). "Effects of reducing river flow on pulse residence time in Little Manatee River, USA." *Transactions of Tianjin University*, 15(2), 95-100.

Huang, W., Liu, X., and Chen, X. (2009). "Hydrodynamic modeling of residence time in Little Manatee River, USA." *Advances in Water Resources and Hydraulic Engineering*, 1330-1334.

Ilus, E. (2009). "Environmental effects of thermal and radioactive discharges from nuclear power plants in the boreal brackish-water conditions of the northern Baltic Sea," University of Helsinki.

Jay, D. A., and Musiak, J. D. (1996). "Internal tidal asymmetry in channel flows: Origins and consequences." *Coastal and Estuarine Studies*, 211-249.

Jeong, S., Yeon, K., Hur, Y., and Oh, K. (2010). "Salinity intrusion characteristics analysis using EFDC model in the downstream of Geum River." *Journal of Environmental Sciences*, 22(6), 934-939.

Ji, Z.-G. (2008). *Hydrodynamics and water quality: modeling rivers, lakes, and estuaries*, John Wiley and Sons, Inc., New Jersey, 676.

Ji, Z., Hu, G., Shen, J., and Wan, Y. (2007). "Three-dimensional modeling of hydrodynamic processes in the St. Lucie Estuary." *Estuarine, Coastal and Shelf Science*, 73(1-2), 188-200.

Ji, Z. G., Morton, M., and Hamrick, J. (2001). "Wetting and drying simulation of estuarine processes." *Estuarine, Coastal and Shelf Science*, 53(5), 683-700.

Ji, Z. G., and Jin, K. R. (2006). "Gyres and seiches in a large and shallow lake." *Journal of Great Lakes Research*, 32(4), 764-775.

Jiang, H., and Shen, Y. (2009). "Numerical study of salinity stratification in the Oujiang River Estuary." *Journal of Hydrodynamics*, 21(6), 835-842.

Kennish, M. J. (1986). "Ecology of Estuaries, Volume I: Physical and Chemical Aspects." *CRC Press, Inc., Boca Raton FL. 1986. 254*.

Kennish, M. J. (2002). "Environmental threats and environmental future of estuaries." *Environmental Conservation*, 29(01), 78-107, doi:doi:10.1017/S0376892902000061.

Ketchum, B. H. (1951). "The exchanges of fresh and salt waters in tidal estuaries." *Journal of Marine Research*, 10(1), 18-38.

Kim, C.-K., and Park, K. (2012). "A modeling study of water and salt exchange for a micro-tidal, stratified northern Gulf of Mexico estuary." *Journal of Marine Systems*, 96–97(0), 103-115, doi:10.1016/j.jmarsys.2012.02.008.

Kim, D., Muste, M., Mueller, D., and Winkler, M. (2009). "VMS ADCP velocity mapping software." Coastal & Hydraulics Laboratory, Engineer Research and Development Center, US Army Corps of Engineers, Vicksburg, MS 39180.

Langford, T. (1990). *Ecological effects of thermal discharges*, Springer.

Lerczak, J. A., Geyer, W. R., and Chant, R. J. (2006). "Mechanisms driving the time-dependent salt flux in a partially stratified estuary." *Journal of Physical Oceanography*, 36(12), 2296-2311.

Lewis, R. E., and Lewis, J. O. (1983). "The principal factors contributing to the flux of salt in a narrow, partially stratified estuary." *Estuarine, Coastal and Shelf Science*, 16(6), 599-626, doi:10.1016/0272-7714(83)90074-4.

Li, X., Wang, Y., and Zhang, S. (2009). "Numerical simulation of water quality in Yangtze Estuary." *Water Science and Engineering*, 2(4), 40-51.

Li, Y., Acharya, K., Chen, D., and Stone, M. (2011a). "Modeling water ages and thermal structure of Lake Mead under changing water levels." *Lake and Reservoir Management*, 26(4), 258 - 272.

Li, Y., Acharya, K., and Yu, Z. (2011b). "Modeling impacts of Yangtze River water transfer on water ages in Lake Taihu, China." *Ecological Engineering*, 37(2), 325-334.

Liu, X., and Huang, W. (2008). "An Effective Algorithm to Reduce Horizontal Pressure Gradient Errors in σ-Coordinate in EFDC Hydrodynamic Model." *Journal of Coastal Research*, 193-204, doi:10.2112/1551-5036-52.sp1.193.

Liu, X., and Huang, W. (2009). "Modeling sediment resuspension and transport induced by storm wind in Apalachicola Bay, USA." *Environmental Modelling & Software*, 24(11), 1302-1313.

Livingston, R. J. (2003). *Trophic organization in coastal systems*, CRC Press.

Macauley, J. M., Engle, V. D., Summers, J. K., Clark, J. R., and Flemer, D. A. (1995). "An assessment of water quality and primary productivity in Perdido Bay, a Northern Gulf of Mexico Estuary." *Environmental Monitoring and Assessment*, 36(3), 191-205, doi:10.1007/bf00547901.

MacCready, P., and Geyer, W. R. (2001). "Estuarine salt flux through an isohaline surface." *J. Geophys. Res.*, 106(C6), 11629-11637, doi:10.1029/2001jc900006.

MacCready, P., Hetland, R. D., and Geyer, W. R. (2002). "Long-term isohaline salt balance in an estuary." *Continental Shelf Research*, 22(11–13), 1591-1601, doi:10.1016/s0278-4343(02)00023-7.

MacCready, P. (2011). "Calculating estuarine exchange flow using isohaline coordinates." *Journal of Physical Oceanography*, 41(6), 1116-1124, doi:10.1175/2011jpo4517.1.

MacDonald, D. G. (2006). "Estimating an estuarine mixing and exchange ratio from boundary data with application to Mt. Hope Bay (Massachusetts/Rhode Island)." *Estuarine, Coastal and Shelf Science*, 70(1–2), 326-332, doi:10.1016/j.ecss.2006.06.025.

Mann, K. H., and Lazier, J. (1996). *Dynamics of marine ecosystems*, Blackwell Science Cambridge, Massachusetts.

Martin, J. L., Tillman, D., Cerco, C., Hendrickson, J., and Dortch, M. (2001). "A three-dimensional water quality model for estimating TMDLs in a Blackwater river estuary, the lower St. Johns river, FL." Proceedings of 8th International Conference on Estuarine and Coastal Modeling, ASCE, 15.

Mason, R. R., King, J. N., and Thomas, W. O. (1998). "The National Flood-Frequency Program - Methods for estimating flood magnitude and frequency in rural and urban areas in Alabama." U.S. Geological Survey Fact Sheet 088-97, U.S. Geological Survey Fact Sheet 088-97, 3.

McCuen, R., Knight, Z., and Cutter, A. (2006). "Evaulation of the Nash-Sutcliffe efficiency index." *Journal of Hydrologic Engineering*, 11(6), 597-602.

Mellor, G. L., and Yamada, T. (1982). "Development of a turbulence closure model for geophysical fluid problems." *Reviews of geophysics and space physics*, 20(4), 851-875.

Monsen, N. E., Cloern, J. E., Lucas, L. V., and Monismith, S. G. (2002). "A comment on the use of flushing time, residence time, and age as transport time scales." *Limnology and Oceanography*, 1545-1553.

Montani, S., Magni, P., Shimamoto, M., Abe, N., and Okutani, K. (1998). "The effect of a tidal cycle on the dynamics of nutrients in a tidal estuary in the Seto Inland Sea, Japan." *Journal of Oceanography*, 54(1), 65-76, doi:10.1007/bf02744382.

Nash, J. E., and Sutcliffe, J. V. (1970). "River flow forecasting through conceptual models part I - A discussion of principles." *Journal of Hydrology*, 10(3), 282-290.

Neilson, B. J., and Cronin, L. E. (1981). *Estuaries and nutrients*, Humana Press.

Park, K., Jung, H.-S., Kim, H.-S., and Ahn, S.-M. (2005). "Three-dimensional hydrodynamic-eutrophication model (HEM-3D): application to Kwang-Yang Bay, Korea." *Marine Environmental Research*, 60(2), 171-193.

Pilgrim, J. M., Fang, X., and Stefan, H. G. (1998). "Stream temperature correlations with air temperatures in Minnesota: Implications for climate warming." *JAWRA Journal of the American Water Resources Association*, 34(5), 1109-1121.

Pugh, D. T. (1996). *Tides, surges and mean sea-level (reprinted with corrections)*, John Wiley & Sons Ltd.

Ralston, D. K., Geyer, W. R., and Lerczak, J. A. (2008). "Subtidal Salinity and Velocity in the Hudson River Estuary: Observations and Modeling." *Journal of Physical Oceanography*, 38(4), 753-770, doi:10.1175/2007jpo3808.1.

Schroeder, W. W., Dinnel, S. P., and Wiseman, W. J. (1990). "Salinity stratification in a river-dominated estuary." *Estuaries*, 13(2), 145-154.

Schropp, S., Calder, F., Slone, G., Swanson, K., Carlton, J., Halcomb, G., Windom, H., Huan, F., and Taylor, R. (1991). "A report on physical and chemical processes affecting the management of Perdido Bay." *Results of the Perdido Bay Interstate Project. Mobile, Alabama Alabama Department of Environmental Management, and Tallahassee, Florida: Florida Department of Environmental Regulation, Coastal Zone Management Section*.

Scott, C. F. (1994). "A numerical study of the interaction of tidal oscillations and non-linearities in an estuary." *Estuarine, Coastal and Shelf Science*, 39(6), 477-496, doi:http://dx.doi.org/10.1016/S0272-7714(06)80004-1.

Selesnick, I. W., and Burrus, C. S. (1998). "Generalized digital Butterworth filter design." *Signal Processing, IEEE Transactions on*, 46(6), 1688-1694, doi:10.1109/78.678493.

Sellner, K. G., Doucette, G. J., and Kirkpatrick, G. J. (2003). "Harmful algal blooms: causes, impacts and detection." *Journal of industrial microbiology & biotechnology*, 30(7), 383-406.

Shen, J., and Haas, L. (2004). "Calculating age and residence time in the tidal York River using three-dimensional model experiments." *Estuarine, Coastal and Shelf Science*, 61(3), 449-461.

Shen, J., and Lin, J. (2006). "Modeling study of the influences of tide and stratification on age of water in the tidal James River." *Estuarine, Coastal and Shelf Science*, 68(1-2), 101-112.

Shen, J., and Wang, H. V. (2007). "Determining the age of water and long-term transport timescale of the Chesapeake Bay." *Estuarine, Coastal and Shelf Science*, 74(4), 585-598, doi:10.1016/j.ecss.2007.05.017.

Sheng, Y. P. (1990). "Evolution of a three-dimensional curvilinear-grid hydrodynamic model for estuaries, lakes and coastal waters: CH3D." *Estuarine and Coastal Modeling (1989)*, ASCE, 40-49.

Shu, C.-W., and Osher, S. (1988). "Efficient implementation of essentially non-oscillatory shock-capturing schemes." *Journal of Computational Physics*, 77(2), 439-471, doi:http://dx.doi.org/10.1016/0021-9991(88)90177-5.

Smagorinsky, J. (1963). "General circulation experiments with the primitive equations." *Monthly Weather Review*, 91(3), 99-164.

Small, C., Gornitz, V., and Cohen, J. E. (2000). "Coastal hazards and the global distribution of human population." *Environmental Geosciences*, 7(1), 3-12.

Smith, R. (1980). "Buoyancy effects upon longitudinal dispersion in wide well-mixed estuaries." *Philosophical Transactions of the Royal Society of London. Series A, Mathematical and Physical Sciences*, 296(1421), 467-496.

Team, R. C. (2005). "R: A language and environment for statistical computing." *R foundation for Statistical Computing*.

Tetra Tech Inc. (1998). "Three-dimensional hydrodynamic and water quality model of Peconic Estuary." A report to the Peconic Estuary Program, Suffolk County, NY, Tetra Tech, Inc., Fairfax, VA.

Titus, J. G., and Narayanan, V. K. (1995). *The probability of sea level rise*, US Environmental Protection Agency, Washington, D.C.

Tralli, D. M., Blom, R. G., Zlotnicki, V., Donnellan, A., and Evans, D. L. (2005). "Satellite remote sensing of earthquake, volcano, flood, landslide and coastal inundation hazards." *ISPRS Journal of Photogrammetry and Remote Sensing*, 59(4), 185-198, doi:http://dx.doi.org/10.1016/j.isprsjprs.2005.02.002.

Traynum, S., and Styles, R. (2008). "Exchange flow between two estuaries connected by a shallow tidal channel." *Journal of Coastal Research*, 24(5), 1260-1268, doi:10.2112/07-0840r.1.

U.S. DOE. (2008). " Estimating freshwater needs to meet future thermoelectric generation requirements." U.S. Department of Energy (DOE), Washington, DC.

Uncles, R. J., and Stephens, J. A. (1996). "Salt intrusion in the Tweed Estuary." *Estuarine, Coastal and Shelf Science*, 43(3), 271-293, doi:http://dx.doi.org/10.1006/ecss.1996.0070.

UNESCO. (1983). "Algorithms for computation of fundamental properties of seawater." *UNESCO technical Papers in Marine Science*, 44, 53.

USACE. (1976). "Statement of Findings: Perdido Pass Channel (maintenance dredging), Balwdin County, AL."

USGS. (2011). "Processing and publication of discharge and state data collected in tidally-influenced areas."

Valle-Levinson, A., Gutierrez de Velasco, G., Trasviña, A., Souza, A., Durazo, R., and Mehta, A. (2009). "Residual Exchange Flows in Subtropical Estuaries." *Estuaries and Coasts*, 32(1), 54-67, doi:10.1007/s12237-008-9112-1.

Walters, R. A., and Heston, C. (1982). "Removing Tidal-Period Variations from Time-Series Data Using Low-Pass Digital Filters." *Journal of Physical Oceanography*, 12(1), 112-115, doi:10.1175/1520-0485(1982)012<0112:rtpvft>2.0.co;2.

Wang, R. (2010). "Modeling hydrologic and water quality responses to changing climate and land use/cover in the Wolf Bay Watershed, South Alabama," M.S. thesis, Auburn University, Auburn, AL.

Wang, R., and Kalin, L. (2011). "Modelling effects of land use/cover changes under limited data." *Ecohydrology*, 4(2), 265-276, doi:10.1002/eco.174.

Wang, R., Kalin, L., Kuang, W., and Tian, H. (2013). "Individual and combined effects of land use/cover and climate change on Wolf Bay watershed streamflow in southern Alabama." *Hydrological Processes*, doi:10.1002/hyp.10057.

Wang, Y., Shen, J., and He, Q. (2010). "A numerical model study of the transport timescale and change of estuarine circulation due to waterway constructions in the Changjiang estuary, China." *Journal of Marine Systems*, 82(3), 154-170.

Warner, J. C., Geyer, W. R., and Lerczak, J. A. (2005). "Numerical modeling of an estuary: A comprehensive skill assessment." *Journal of Geophysical Research*, 110(C5), doi:10.1029/2004JC002691.

Xia, M., Xie, L., and Pietrafesa, L. J. (2007). "Modeling of the Cape Fear River Estuary plume." *Estuaries and Coasts*, 30(4), 698-709.

Xia, M., Craig, P. M., Wallen, C. M., Stoddard, A., Mandrup-Poulsen, J., Peng, M., Schaeffer, B., and Liu, Z. (2011a). "Numerical simulation of salinity and dissolved oxygen at Perdido Bay and adjacent coastal ocean." *Journal of Coastal Research*, 27(1), 73-86.

Xia, M., Xie, L., Pietrafesa, L. J., and Whitney, M. M. (2011b). "The ideal response of a Gulf of Mexico estuary plume to wind forcing: Its connection with salt flux and a Lagrangian view." *Journal of Geophysical Research*, 116(C8), C08035.

Xu, H., Lin, J., and Wang, D. (2008). "Numerical sutdy on salinity stratification in the Pamlico River Estuary." *Estuarine, Coastal and Shelf Science*, 80, 74-84.

Yin, K., Zhang, J., Qian, P.-Y., Jian, W., Huang, L., Chen, J., and Wu, M. C. S. (2004). "Effect of wind events on phytoplankton blooms in the Pearl River estuary during summer." *Continental Shelf Research*, 24(16), 1909-1923, doi:http://dx.doi.org/10.1016/j.csr.2004.06.015.

Zimmerman, J. T. F. (1976). "Mixing and flushing of tidal embayments in the western Dutch Wadden Sea part I: Distribution of salinity and calculation of mixing time scales." *Netherlands Journal of Sea Research*, 10(2), 149-191, doi:10.1016/0077-7579(76)90013-2.

Zou, R., Bai, S., and Parker, A. (2008). "Hydrodynamic and eutrophication modeling for a tidal marsh impacted estuarine system using EFDC." *Coastal and Estuary Modeling*, 561-589.